A sensitivity study on the aerodynamic performance of a wingtip-mounted tractor propeller-wing system

Roger Willemsen

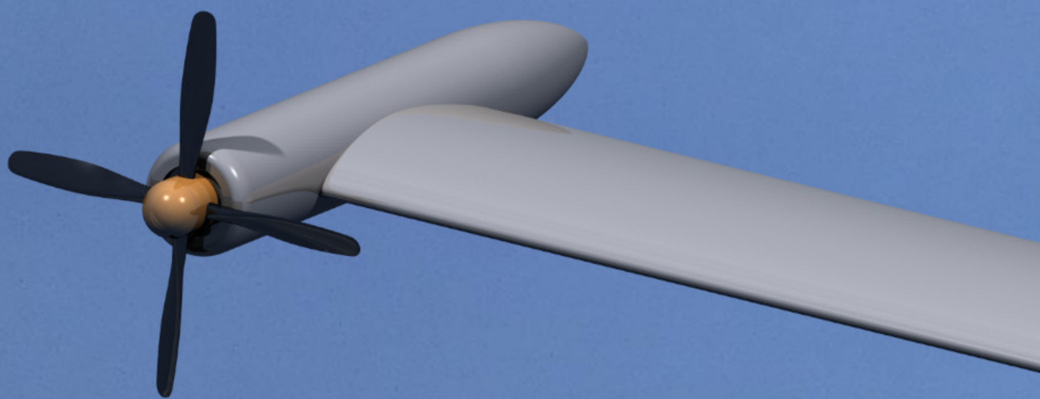

Technische Universiteit Delft

TU Delft

A sensitivity study on the aerodynamic performance of a wingtip-mounted tractor propeller-wing system

by

Roger Willemsen

to obtain the degree of Master of Science
at the Delft University of Technology,
to be defended publicly on Friday November 27, 2020 at 9:30 AM.

Student number:	4290674	
Project duration:	September 2019 – November 2020	
Thesis committee:	Dr. ir. T. Sinnige,	TU Delft, supervisor
	Prof. dr. ir. L. L. M. Veldhuis,	TU Delft, chairman
	Dr. F. Avallone,	TU Delft

An electronic version of this thesis is available at `http://repository.tudelft.nl/`.

TU Delft

Preface

This thesis marks the end of my time as a student at the faculty of Aerospace Engineering at Delft University of Technology. While the path to get here was often challenging, it has brought me many great opportunities and experiences. It has allowed me to pursue many of my interests and to work on many amazing projects. This thesis has provided me with my greatest challenge so far and I could not have completed it without help. I would like to express gratitude for those who supported me during my thesis.

First of all, I would like to thank by daily supervisor Tomas for his feedback and ideas on my work. His investigative and critical attitude always propelled my research forward. Throughout my research he would always be available when I needed assistance.

I would also like to thank the members of the propeller research group for providing me with feedback when I presented my research to them. Also, thanks to my fellow students in room N1.09, for fostering interesting discussions and providing help when I ran into problems. Special thanks to my friends who took the time to read parts of this report and provide their feedback.

Roger Willemsen
Delft, November 2020

Summary

With rising concern about the environmental impact of aviation, propellers are considered as an alternative, more efficient propulsion method compared to jet engines. Using (hybrid) electric propulsion, even further emission reduction can be achieved. Electric engines also offer more flexibility in design, since they are relatively low-weight and can be scaled easily without performance drawbacks. This opens up new design possibilities with regard to aero-propulsive integration. One of the promising ways of beneficial aero-propulsive integration is wingtip-mounted propellers. For a tractor configuration with inboard-up rotating propeller, the swirl in the propeller can be used to counteract the wingtip vortex. Doing so leads to an increase in effective aspect ratio, increasing wing performance.

The aerodynamic interaction of wingtip-mounted propellers is very complex. There are multiple mechanisms that change the relative benefit of the propeller-wing interaction. While research into wingtip-mounted propellers has been increasing over the last years, guiding design principles for optimum system efficiency are still lacking. Thus, this research aims to quantify the sensitivity of the aerodynamic performance of a wingtip-mounted tractor propeller-wing system. The analysis is done using a low-order numerical model. Using this model, the performance of the propeller-wing system is calculated throughout the defined design space. To minimize the number of numerical model evaluations, a metamodel is created on top of the numerical model, which approximates the numerical model response.

The numerical model consists of two parts: a propeller model and a wing model. The propeller model consists of a blade element method (BEM). Using this BEM code the propeller is analyzed at different advance ratios to create a performance map. This performance map is then used to calculate the propeller performance for an arbitrary non-uniform inflow field. This inflow field is determined by wing induced velocities. The slipstream of the propeller is modelled by a slipstream tube model. The original slipstream tube model assumes a straight wake and a propeller in uniform inflow. The slipstream tube model was improved by adding slipstream deflection, slipstream contraction and by allowing an azimuthal circulation distribution. Next, the wing model consists of a vortex lattice method (VLM). The VLM code allows for spanwise non-uniform inflow. However, the increased dynamic pressure jet induced by the propeller has a finite height. This means that the circulation increase on the wing is a function of the dynamic pressure increase and of the slipstream height. The effect of the slipstream height is accounted for by a jet correction. The induced drag of the wing model is calculated using a Trefftz plane analysis. Furthermore, using 2D wing section analysis, corrections were calculated to account for non-linear effects.

The described propeller model is dependent on the induced velocities of the wing, while the wing model is dependent on the induced velocities of the propeller. So, to calculate the performance of the propeller-wing system, an iterative scheme is used. It was found that the model shows convergent behaviour most of the time, only at high thrust settings there is a chance that convergence is not reached. Validation of the numerical model was done using data from windtunnel experiments. It was found that the main trends in the data were all predicted well by the numerical model.

The results are obtained by creating three metamodels. The first two metamodels investigate the interaction between lift distribution, propeller size and propeller position. This is done by varying aspect ratio, outboard wing twist, propeller diameter-to-span ratio, propeller vertical position and propeller horizontal position. This was done at constant lift coefficient and thrust. The thrust for metamodel 2 was doubled with respect to metamodel 1, to compare the effect of thrust. To investigate the effect of the relative magnitude of thrust and the propeller swirl with respect to the lift, a third metamodel was created. This metamodel varies design lift coefficient, design thrust, the amount of swirl and the wing aspect ratio.

From the data it was found that the drag of the propeller-wing system mainly depends on the spanwise wing lift distribution. The reduction in drag due to beneficial propeller-wing interaction is typically an order of magnitude lower than the value of drag. Thus, the drag is mainly determined by the amount of drag of the clean wing. Furthermore, the increase in wing performance, given by an increase in lift-to-drag ratio, was found to be mainly dependent on the total drag and the change in drag due to propeller-wing interaction. Thus, lowering the drag with propeller-wing interaction should be prioritized over a lift increase to obtain better performance. For a low total drag, the same decrease in drag gives a higher increase in lift-to-drag ratio. Since the change in drag is not highly dependent on the wing lift distribution, a wing with low drag would also benefit the most from propeller-wing interaction in terms of lift-to-drag ratio. For a realistic thrust level of $T_C = 0.05$, a maximum drag reduction of about $2 \cdot 10^3$ or 20 drag counts could be obtained. This would be translated to an increase in lift-to-drag ratio of about 6 for the a wing with aspect ratio 16.

It was found that increasing thrust is beneficial for both lift and drag. On the other hand, the horizontal position of the propeller requires a trade-off. Increasing the propeller horizontal position is beneficial for the drag, but disadvantageous for lift. Furthermore, it was found that propeller vertical position mainly affects lift and the diameter-to-span ratio mainly affects drag.

Throughout the analyzed design space, a thrust increase was obtained due to propeller-wing interaction, mainly due to a wing induced angle of attack on the propeller. However, this thrust increase was always paired with a proportional increase in power, thus propeller efficiency is not affected by the propeller-wing interaction with a tractor propeller. Furthermore, this thrust increase is relatively low in magnitude, a relative increase of about 1% in thrust is typically found.

Lastly, a total system efficiency was calculated by multiplying propeller efficiency with lift-to-drag ratio. It was found that with increasing thrust, lift-to-drag ratio increases. However, this would only lead to an increase in system efficiency if propeller efficiency would also increase. In other words, if thrust is increased, this gives a benefit in lift-to-drag ratio, but this increase is relatively small compared to the change in propeller efficiency due to the change in thrust. Thus, the propeller should be designed to maximize efficiency and not to maximize the gain in lift-to-drag ratio from propeller-wing interaction.

Contents

List of Symbols

a	Axial induction factor	[-]
a'	Tangential induction factor	[-]
AIC	Aerodynamic Influence Coefficient matrix	[-]
b	Wing span	[m]
B	Number of propeller blades	[-]
c	Chord	[m]
C	Circulation-induced velocity correlation	[-]
C_d	Sectional drag coefficient	[-]
C_D	Total drag coefficient	[-]
C_l	Sectional lift coefficient	[-]
C_L	Total lift coefficient	[-]
C_P	Power coefficient $\left(=\frac{P}{\rho n^3 D^5}\right)$	[-]
C_Q	Torque coefficient	[-]
C_T	Propeller thrust coefficient $\left(=\frac{T}{\rho n^2 D^4}\right)$	[-]
d	distance	[m]
D	Drag	[N]
D	Propeller diameter	[m]
f	Prandtl's tip loss factor exponent	[-]
f_i	Modelled response at point	[-]
F	Prandtl's tip loss factor	[-]
F	Force	[N]
g	Airfoil camberline	[m]
G	Jet correction	[-]
h	height	[m]
J	Advance ratio	[-]
k	Number of levels	[-]
l	Length	[m]
l	Sectional lift	[N]
L	Lift	[N]
n	Rotational speed	[Hz]
n	Normal vector	[-]
n	Number of dimensions	[-]
N	Number (discrete)	[-]
M	Mach number	[-]
P	Power	[W]
P_C	Propeller-wing power coefficient $\left(=\frac{P}{\frac{1}{2}\rho U_\infty^3 S_{ref}}\right)$	[-]
r	Radial position	[m]
R	Propeller radius	[m]
R^2	R-squared, coefficient of determination	[-]
Re	Reynolds number	[-]
S	Surface	[m^2]
SF	Scaling factor	[-]
SMF	Swirl multiplication factor	[-]
SS	Sum of squares	[-]
T	Thrust force	[N]

T_C	Propeller-wing thrust coefficient $\left(= \frac{T}{\frac{1}{2}\rho U_\infty^2 S_{ref}}\right)$	[-]
Q	Torque	[Nm]
u	Induced velocity	[m/s]
U	Velocity	[m/s]
W	Total velocity at propeller blade	[m/s]
x, y, z	Cartesian coordinates	
y	Spanwise coordinate	[m]
y_i	True response at point	[-]
z	Propeller-wing horizontal distance	[m]
z'	Distance center propeller slipstream to wing	[m]
α	Angle of attack	[deg]
β	Propeller twist	[deg]
γ	Circulation of element	[m^2/s]
Γ	Circulation	[m^2/s]
η	Efficiency	[-]
θ	Wing twist	[deg]
λ	Axial inflow advance ratio	[-]
λ	Jet correction integration variable	[-]
ρ	Density	[kg/m^3]
ϕ	Blade pitch	[deg]
ϕ	Propeller azimuth position	[deg]
ϕ	Disturbance velocity potential	[-]
Φ	Velocity potential	[-]
ψ	Iteration dummy variable	[-]
Ω	Rotational speed	[rad/s]

Subscripts

a	Axial
$clean$	Clean, without propeller
$corr$	Correction
deg	Polynomial degree
des	Design
D	At the propeller disk
e	Even solution
E	Error
eff	Effective
hub	Propeller hub
i	Induced
i	At position i
inv	Inviscid
iso	Isolated
j	Jet/inside jet
o	Odd solution
o	Outside jet
p	Propeller
p	At a point
p	Profile (drag)
$prop-on$	With the propeller installed
pts	Of points
r	Radial
ref	Reference
R	At the propeller blade tip
R	Regression
t	Tangential
t	Total (pressure)
T	Total
up	Upper bound
$visc$	Viscous
w	Wake
w	Wing
x	x-component
y	y-component
z	z-component
∞	Freestream
0	Initial

List of Figures

List of Tables

1

Introduction

With increasing environmental awareness, there has been a great push to make aircraft more efficient. One of the means to achieve this is by means of propeller propulsion, which accelerates a large volume of air with a low velocity, making it more efficient than jet propulsion. By placing the propeller at the wingtip, even higher efficiencies can be reached. This chapter will describe the developments in wingtip-mounted propellers, from which a research gap will be identified. From this research gap a research objective is formulated, which will form the basis of this thesis.

1.1. Background information

This section will provide some background information on the research presented in this thesis. It describes the historical background and an overview of the main developments in research on wingtip-mounted propellers.

1.1.1. History of propeller propulsion

Propeller propulsion has been used since the inception of heavier-than-air aircraft. Propeller propulsion was first successfully introduced in 1852 to propel an airship and in 1903 the Wright Flyer took off using propeller propulsion. The first propellers were not very sophisticated and had a low efficiency [1]. But in 1917 Durand [2] published his extensive experimental research on propellers, greatly advancing propeller design, leading to efficiencies of around 75 to 80%. However, low fuel prices and the desire to fly at high Mach numbers led to the success of the turbojet and turbofan engines, and research in propeller propulsion slowed down after the mid-1950s. Interest in propeller propulsion was regained after the oil crisis in 1973. Fuel efficiency of aircraft had to be increased due to the high fuel prices. In 1975 an open rotor concept called *propfan* was published by Rohrbach and Metzger [3]. The propfan promised better efficiency than turbofan engines, even at Mach numbers around $M = 0.8$, as seen in Figure 1.1. By the time all problems regarding the propfan design and implementation were overcome, oil prices dropped again. Also, turbofan engines were made increasingly more efficient by increasing bypass ratio. This removed the incentive to further develop the propfan concept and halted further research.

With the rising fuel prices and increasing environmental awareness in the 21st century, there is again a need to make aircraft more fuel efficient. To address climate change, ambitious goals have been set by multiple institutions. The International Air Transport Association (IATA) aims for carbon neutral growth from 2020 onwards, with a reduction in CO_2 emissions of 50% in 2050 compared to 2005 levels [4]. Other institutions like the Advisory Council for Aviation Research and innovation in Europe (ACARE)[1] and National Aeronautics and Space Administration (NASA) [5] have also set goals for emissions and noise reduction. Propellers are one of the solutions for this problem, as they provide a higher propulsive efficiency with respect to turbofan engines [6][7]. While propeller propulsion is generally associated with higher noise compared to turbofan engines, new technologies can provide noise reduction, such as propeller cowling [8] and propeller blade sweep [9]. This has increased the

[1] `https://www.acare4europe.org/sria/flightpath-2050-goals/protecting-environment-and-energy-supply-0`, Retrieved on: 27 July 2018

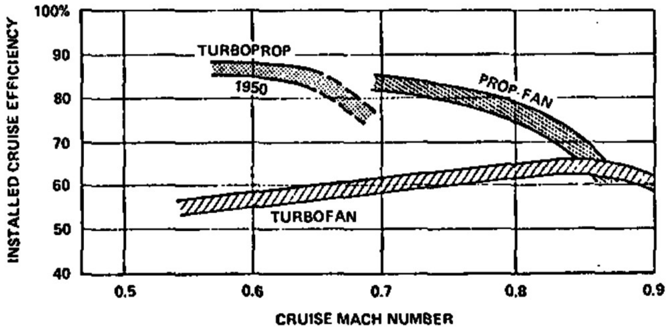

Figure 1.1: Comparison of different propulsion technologies in 1975 [3]

research in open rotor propulsion. One of the ongoing projects investigating open rotor concepts is Clean Sky 2[2], the successor of the successful Clean Sky project. In this project research on open rotor concepts is done in collaboration with influential companies like Airbus, GKN and Safran.

1.1.2. Electric propulsion

With hybrid electric or full electric propulsion, even further emission reductions can be achieved [10]. Electric motors are relatively low weight and can be scaled without major efficiency decrease. Thus, electric propulsion also allows for more flexibility in the placement of the propellers. This can lead to new propulsion architectures and aircraft configurations. Distributed propulsion can for example replace the high lift system of an aircraft, if it is integrated properly [11]. It is also possible to further increase aerodynamic performance by placing propellers at the wingtips [12][13]. Furthermore, air properties like temperature and pressure have limited effect on the performance of electric engines. This means that, when sizing for take-off conditions, an aircraft with electric propulsion system needs less power and less wing area compared to one with an air breathing system. With the many benefits of electrical propulsion, the aircraft efficiency, noise, safety and operating costs can be improved compared to aircraft with conventional propulsion systems [14].

In Europe research on (hybrid) electric propulsion is done by projects like Modular Approach to Hybrid-Electric Propulsion Architecture (MAHEPA)[3] and Distributed Propulsion and Ultra-high by-pass Rotor Study at Aircraft Level (DisPURSAL)[4], while NASA is working on several concept planes with distributed electric propulsion like the X-57 and N3-X [15]. Furthermore, distributed electric propulsion is already being implemented in the on-demand air taxi Lilium[5], shown in Figure 1.2. The Lilium jet performed its first successful full-scale test flight in 2019 and it is planned to be operational in 2025. And wingtip-mounted electric propulsion is being applied in the Eviation Alice[6], shown in Figure 1.3, which is planned to enter service in 2023.

1.1.3. History of wingtip-mounted propellers

When looking at propeller placement, wingtip-mounted propellers could lead to major performance benefits. Propellers that rotate in opposite direction of the wingtip vortex (inboard up) can have beneficial interaction between the propeller swirl and the wingtip vortex. This can lead to increased wing and/or propeller efficiency.

The first implementation of wingtip-mounted propellers happened already in the 1930s. The V-173 and XF5U-1, designed by Charles H. Zimmerman, were very low aspect ratio aircraft with counter-rotating propellers mounted on the wingtips, as seen in Figures 1.4 and 1.5. The unconventional design allowed for low approach and landing speeds [16]. The design featured wingtip-mounted counter-rotating propellers, in opposite direction of the wing-tip vortices to decrease induced drag. In wind-tunnel experiments on the V-173 it was concluded that the beneficial interaction of the propeller with the wingtip vortex could increase the effective aspect ratio of the wing [16][17]. However, when the

[2]`https://www.cleansky.eu`, Retrieved on: 27 July 2018
[3]`https://mahepa.eu`, Retrieved on: 27 July 2018
[4]`https://www.dispursal.eu`, Retrieved on: 27 July 2018
[5]`https://lilium.com`, Retrieved on: 27 July 2018
[6]`https://www.eviation.co/`, Retrieved on: 4 August 2020

rotational direction of the propellers was reversed, it only resulted in a small decrease in performance, contrary to the designer's hypothesis. Furthermore, during aerodynamic testing of the XF5U-1, it was recognized that the propellers increased lift coefficient due to higher dynamic pressure in the propeller slipstream and the upwards directed component of the propeller thrust [18].

Figure 1.2: Lilium jet

Figure 1.3: Eviation Alice

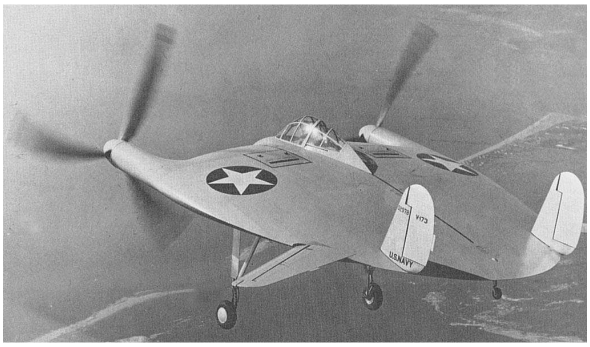

Figure 1.4: Vought V-173[7]

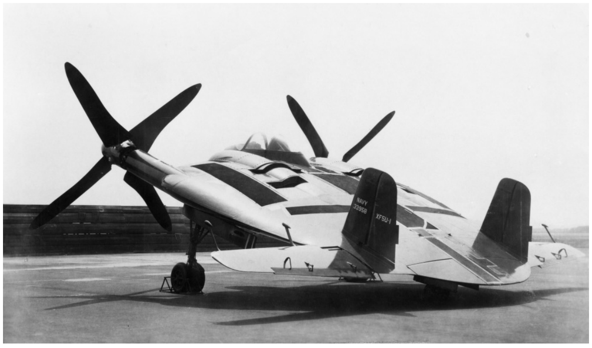

Figure 1.5: Vought XF5U-1[8]

In 1968 Snyder and Zumwalt [19][20] started systematically testing the effects of wingtip-mounted tractor propellers by conducting windtunnel experiments. Here the effects of rotational speed and spanwise position of different propellers were investigated. Propellers rotating opposite the wingtip vortex move the vortex core outboard, as shown in Figure 1.6. This decreases induced drag. Furthermore, the high dynamic pressure in the slipstream increases the wing lift coefficient. This combined effect leads to a higher effective aspect ratio of the wing, based on the drag polar. In Figure 1.7 it can be seen that these effects are most favorable when the propeller is positioned at the wingtip. When moving the propeller inboard, the effective aspect ratio decreases. The worst performance is obtained when the propeller is rotating with the wingtip vortex at the wingtip.

In 1970 Patterson and Flechner [21] performed windtunnel experiments to investigate the effect of a fan-jet engine at the wingtip. The results suggest that some of the vortex energy can be dissipated by a high-energy non-rotating wake, leading to a decrease in induced drag. However, it was also suggested that a counter-vortex rotating engine wake could be more effective. In 1985 and 1987 Patterson and Bartlett [22][23] conducted windtunnel experiments on wingtip mounted pusher propellers. From this research it was concluded that a propeller immersed in the wingtip vortex needs less power for the same amount of thrust. This is due to the vortex velocity seen by the propeller blade (as shown in Figure 1.8), leading to a more streamwise directed lift component on the propeller blade. Also, the induced drag is decreased by having a propeller at the wingtip. The drag decreases even more when the nacelle was placed under an incidence angle, which places the propeller above the wing chord plane. This leads to better alignment between the propeller and wingtip vortex, further reducing induced drag.

[7]SDASM Archives www.flickr.com/photos/sdasmarchives/4822056685/, Retrieved on: 28 July 2018
[8]SDASM Archives www.flickr.com/photos/sdasmarchives/16318271846/, Retrieved on: 28 July 2018

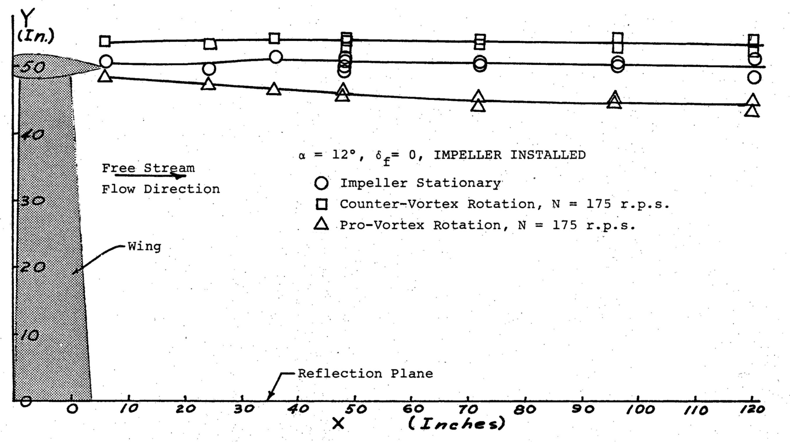

Figure 1.6: Trailing vortex core trajectory in the plane of the wing [19]

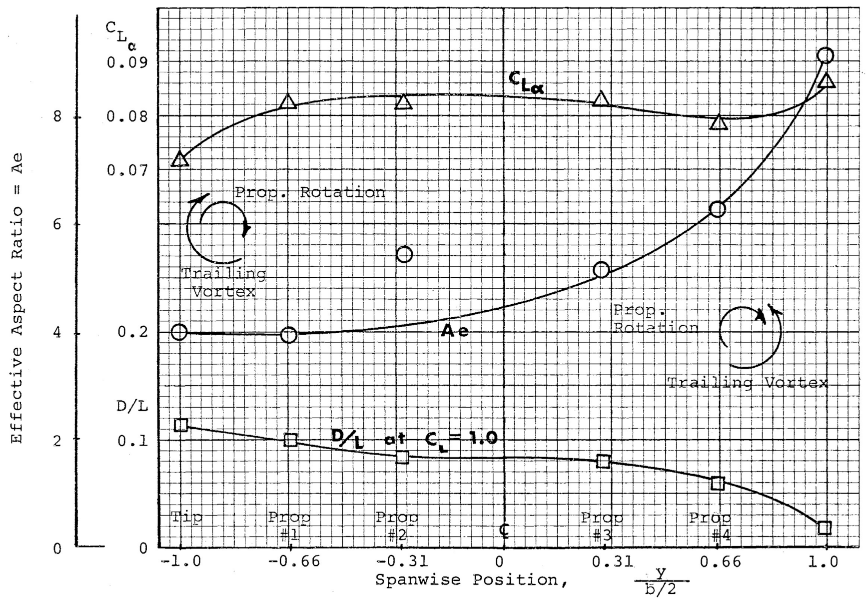

Figure 1.7: Influence of the spanwise position of the propeller on wing lift and drag [19]

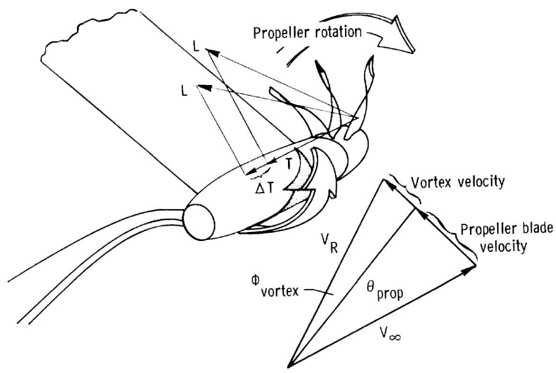

Figure 1.8: The induced velocity on a propeller due to a wingtip vortex [22]

Tip mounted propellers have also been investigated using mathematical models by Loth and Loth [24], Miranda and Brennan [12], and Kroo [13]. Loth and Loth observed that wingtip-mounted propellers could induce upwash on the wing and downwash beyond the wing span. This could lead to reduced drag. However, Miranda and Brennan pointed out that the model used by Loth and Loth was incorrect. In Loth and Loth's model, the propeller wake was modelled as a vortex which induces velocities up to infinity. However, in reality only the domain within the slipstream tube of the propeller is affected by the propeller. Miranda and Brennan and Kroo found that the same efficiency is obtained for both the tractor and pusher configurations, based on Munk's Stagger Theorem [25]. For a tractor configuration mainly the wing induced drag is decreased, while for a pusher configuration the propeller thrust is increased, as visualized in Figure 1.9. Furthermore, Kroo notes that the aerodynamic benefits of wingtip-mounted propellers could be overshadowed by factors like the One Engine Inoperative (OEI) condition and the added structural weight due to reinforcement to account for the moment created by the thrust force.

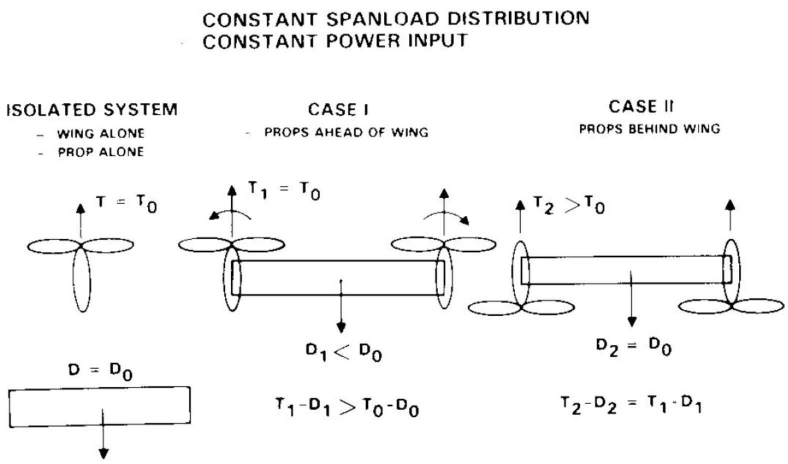

Figure 1.9: Munk's Stagger Theorem applied to wingtip-mounted propellers [12]

1.1.4. Recent research on wingtip-mounted propellers

In 2014 NASA started research on an all-electric experimental plane, the X-57 Maxwell[9], shown in Figure 1.10. This aircraft is a modified Tecnam P2006T. At the wingtips two propellers are located, providing thrust during cruise. There are an additional 12 tractor propellers along the wing span, providing high-lift during take-off and landing. During cruise, these propellers will be folded into the nacelle to reduce drag. The latest configuration of the X-57 has a 2.5x reduction in wing area and a 4.8x reduction in energy consumption compared to the original aircraft [26]. From a CFD analysis a 7.5% reduction in induced drag during cruise conditions is predicted compared to a wing without wingtip-mounted propellers [27].

There is also a lot of research done on propeller-wing interaction and wingtip-mounted propellers by the Flight Performance research group at Delft University of Technology. In 2004 and 2005 Veldhuis [28][29] published the results of his research on propeller-wing interaction. By means of experimental and numerical analysis a good overview of the different propeller-wing interaction mechanisms and phenomena was provided. And over the last few years, research has been done on different aerodynamic interaction phenomena for propellers. Some of the researched topics are: propeller-pylon interaction [30][31][32][33], swirl recovery vanes [34][35][36] and non-uniform inflow [37][38]. Furthermore, several studies have been conducted completely focusing on wingtip-mounted propellers. Van Arnhem et al. [39] investigated the aerodynamic interaction effects of propellers mounted on the horizontal tailplane. A study on the accuracy and capability of the use of a RANS solver for the simulation of wing-tip mounted propellers was investigated by Stokkermans et al. [40]. The latest study is performed by Sinnige et al. [41], where aerodynamic interaction effects of a wingtip-mounted propeller

[9]NASA `www.nasa.gov/centers/armstrong/news/FactSheets/FS-109.html`, Retrieved on: 16 August 2018

Figure 1.10: X-57 Maxwell [27]

are thoroughly investigated. Furthermore, the performance of a wing with wingtip-mounted propeller is compared to a conventional configuration where the propeller is mounted inboard of the wing. Lastly, there are several Master's theses investigating wingtip-mounted propellers [42][43][44].

Although there is understanding of the aerodynamic interaction principles regarding wingtip-mounted propellers, there is little known on the design principles for wingtip-mounted propellers. For an isolated propeller and isolated wing it is known which design parameters to change to achieve an optimal distribution of circulation/force to achieve the highest possible efficiency. However, when there is strong interaction, such as for a wingtip-mounted propeller, these design principles could change and the sensitivity of the design parameters is not known. This is the focus of this thesis. Since the interaction effects for tractor and pusher propellers are very different, it was chosen to focus on only one of these configurations. Pusher propellers see a non-uniform inflow, which alters the performance of the propeller. Furthermore, a non-uniform inflow on the propeller could lead to significant vibrations and noise. On the other hand, the non-uniform inflow seen by the wing for a tractor configuration is less critical to the design and it can be better modelled with lower order tools. Thus, it was chosen to investigate the tractor configuration.

1.2. Research aim and objectives

The research consists of finding design principles to get the best performance of a wingtip-mounted tractor propeller-wing system. This is done by varying design parameters and determining the sensitivity for these design parameters on the performance. From this the main objective is formulated:

To quantify the sensitivity of the aerodynamic efficiency of the whole propeller-wing system for the main design parameters for a wingtip-mounted tractor propeller-wing system by means of a low-order numerical model

A low-order model was chosen, since it is expected that many evaluations are needed to map the design space. While low-order models are generally less sophisticated than higher-order models, they still provide accurate results in the near-linear regime. Low-order models can also provide direct aerodynamic interaction properties, such as induced velocity, which can provide insightful information about propeller-wing interaction. These aerodynamic properties can not be directly obtained from higher-order models. A the basic geometry for the model that will be investigated is shown in Figure 1.11. Furthermore, from this main objective, the following sub-objectives were derived:

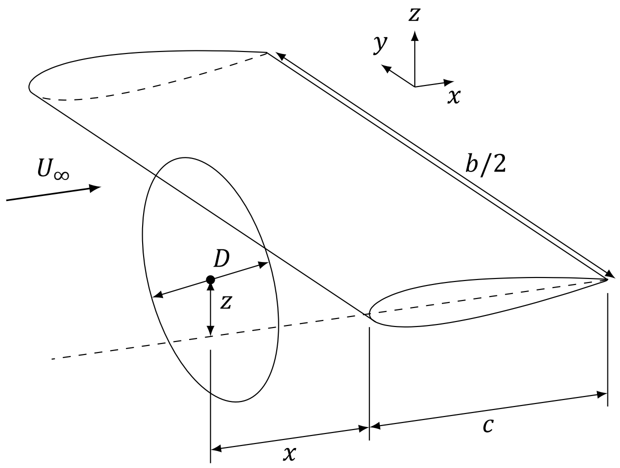

Figure 1.11: Propeller-wing system geometry

- **To create a low-order model that can accurately capture the aerodynamic interaction phenomena for a wingtip-mounted tractor propeller-wing system**
Low-order models have been used in the past to model propeller-wing interaction, but some interaction effects could use improved modelling. An example is the frequently used *swirl recovery factor*, which has a large effect on the wing lift distribution, but is not based on any physical flow phenomena. Also, slipstream contraction is usually calculated using an assumed shape, while more physical ways of modelling are possible here.

- **To determine the influence of the wing spanwise lift distribution on the aerodynamic performance of a wingtip-mounted propeller-wing system**
Since the propeller-wing interaction is driven by the wingtip vortex, it is assumed that the lift distribution should play a significant role in the performance of the propeller-wing system. It was decided to vary lift distribution by means of aspect ratio and linear twist to the wing. Sweep and taper were not included, since this would complicate modelling and it would make results hard to compare due to the more complex geometry.

- **To determine the influence of the linear and angular momentum distribution of the propeller on the aerodynamic performance of a wingtip-mounted propeller-wing system**
This sub-objective concerns the design parameters of the propeller. By changing the propeller design, a different distribution of linear and/or angular momentum can be found, which has a different interaction effect with the wing.

- **To determine the influence of the main design parameters on the aerodynamic performance of a wingtip-mounted propeller-wing system**
This sub-objective includes the design parameters that are not specific to either the propeller or wing. To investigate this sub-objective, three design variables were chosen: propeller diameter to span ratio, and the horizontal and vertical distance between wing and propeller. This leads to three non-dimensional parameters: D/b, x/c and z/D.

- **To find a relation between the main aerodynamic performance parameters of the wing and propeller**
The main performance parameters of the propeller-wing system are defined as lift, drag, thrust and power (C_L, C_D, T_C and P_C respectively). By evaluating many design, a correlation could be found between some of these parameters. By understanding these correlations, more conscious decisions can be made about trade-offs or beneficial interaction effects.

1.3. Thesis outline

The theory used in this thesis is presented in Chapter 2. Chapter 3 describes the implementation of the theory to create a numerical propeller model, while Chapter 4 describes a numerical wing model. The models are integrated in Chapter 5, to create a model that can predict the aerodynamic performance of a wingtip-mounted propeller-wing system. This model is subsequently validated in Chapter 6. In Chapter 7 the process of metamodelling is described, which makes it possible to evaluate the numerical model within the design space in an efficient way. In Chapter 8 the results of the evaluation of the model are discussed. The results found here lead to conclusions and recommendations, which are presented in Chapter 9.

2
Theoretical background

This chapter aims to provide an understanding of the aerodynamic principles at work when dealing with propeller-wing interaction. The chapter is divided in three parts. Section 2.1 provides a description of wing aerodynamics, mainly focusing on potential flow models. Section 2.2 describes propeller aerodynamics and slipstream modelling. Finally, in Section 2.3 the interaction effects of the wing and propeller are discussed.

2.1. Wing aerodynamics

This section describes the main principles of wing aerodynamics by means of potential flow models. Section 2.1.1 provides information on the basics wing modelling in potential flow. In Section 2.1.2 the aerodynamics for a wing in a jet are introduced, which will be important when modelling propeller-wing interaction.

2.1.1. Potential flow models

The wing produces lift by creating a pressure difference between the upper and lower surface. At the wingtips air flows from the high pressure (bottom) to the low pressure (top) area, which leads to wingtip vortices. A common low-order way to describe these phenomena on the wing is by using potential flow models. Potential flow assumes that the velocity field can be described as the gradient of a scalar function, which is referred to as the potential function. The flow described by a potential function is irrotational. When this flow is also assumed to be incompressible, the flowfield should satisfy Laplace's equation. A vortex is one of the flow elements that satisfies this equation. In Equation 2.1 the formal definition is given for the circulation Γ. In the case of a vortex, Γ is the strength of the vortex. Γ is the integral of the local velocity $\overline{U}$ along a closed contour C. Furthermore, the Kutta-Joukowski theorem relates circulation to lift, as shown in Equation 2.2. Here it can be seen that the upstream velocity U_∞ determines the lift per unit span l. Note that the Kutta-Joukowski theorem is derived in 2D, so this U_∞ is the upstream velocity at a certain 2D section.

$$\Gamma = -\oint_C \overline{U} \cdot \overline{ds} \tag{2.1}$$

$$l = \rho_\infty U_\infty \Gamma \tag{2.2}$$

In Figure 2.1 a simple representation of a wing is shown. On the wing the bound vortex produces lift. According to Helmholtz's theorem a vortex has a constant strength and a vortex can not end, meaning that a vortex must always form a closed loop. This leads to the starting vortex, which is shed when the wing starts producing lift. This starting vortex is connected to the bound vortex by tip vortices or trailing vortices. In reality the tip and starting vortex dissipate after some time, but the wing still experiences induced velocity from the tip vortices, this induced velocity is called downwash. This leads to lift induced drag, which is dependent on the strength of the tip vortices and thus the magnitude of the wing lift and lift distribution.

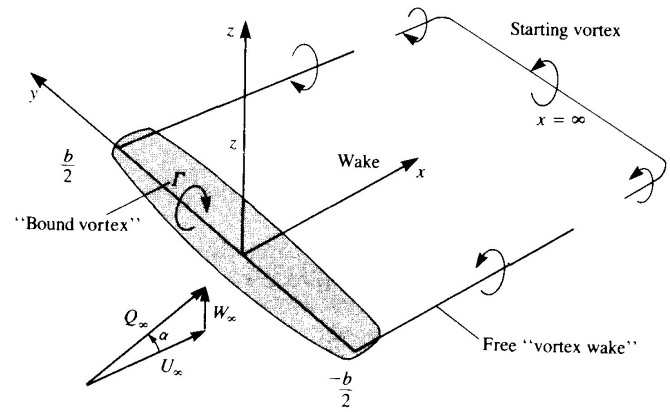

Figure 2.1: A simplified vortex representation of a wing [45]

In reality the wing does not consist of a single vortex line with constant strength. Circulation will be distributed over the wing surface, leading to a continuous vortex sheet in the wake. Different potential flow models represent this continuous vortex distribution differently. A lifting line model has a spanwise distribution of circulation on a single line. A Vortex Lattice Method (VLM) model adds a chordwise distribution of circulation, with the vortices lying on the camberline. Finally, a panel method puts circulation on the surface of the wing, actually modelling the wing volume. Another benefit of the panel method is that it is able to model any geometry, thus it is relatively easy to model other parts of the aircraft, while this is not possible for the other previously described methods. These potential flow methods all require a relatively low computational cost, while still producing accurate and useful results for many applications.

A downside is that viscous effects are not captured by potential flow models. Due to the no-slip condition at a surface, there exists a thin layer of air with a high velocity gradient, which is the boundary layer. Inside the boundary layer the flow is considered viscous, while outside the boundary layer the flow is considered inviscid [46]. Thus, the flow outside the boundary layer can be modelled using potential flow models. However, drag is highly dependent on the boundary layer. The velocity gradient at the surface leads to a shear stress, which results in friction drag. This drag is dependent on the development of the boundary layer, which determines the velocity gradient at the surface. The velocity gradient is also dependent on the state of the boundary layer. Here a distinction is made between laminar (smooth and regular) and turbulent (random and irregular) flow. So, to correctly estimate drag using potential flow models, friction drag should be added. The boundary layer can also influence the lift, mainly through separation. Separated flow is mainly associated with stall, where the flow separation leads to a large decrease in lift. Furthermore, separation gives rise to pressure drag. In normal flight conditions separation occurs at high angles of attack, thus the potential flow models are less accurate here.

2.1.2. Wing in jet

For conventional analysis methods for a wing, the wing usually sees a freestream velocity which is completely uniform. Using conventional methods the response of the wing to (small) disturbances in angle of attack or dynamic pressure with respect to this uniform freestream velocity can still be predicted. However, when the wing is submerged in a jet, as shown in Figure 2.2, conventional ways of analyzing the wing do not hold anymore when using potential flow models. When the freestream velocity U_∞ is doubled, the lift is expected to increase by a factor of four, since lift scales quadratically with the velocity. However, when this area of increased dynamic pressure has a finite height, this relation is no longer valid. Due to the finite height of the jet, the increase in lift is less than expected. This is shown in Figure 2.3, based on the theory presented by Ting and Liu [47]. Here the blue line shows the relation for $U_j = 2U_\infty$ and the red line shows it for $U_j = 1.5U_\infty$. The lift ratio K_l is defined as the the lift for a certain jet height divided by the lift without jet or with a uniform inflow of the freestream velocity U_∞.

While Figure 2.3 is valid for a 2D airfoil or infinite wing with an infinitely wide jet, something similar happens when a circular jet is applied to the wing. Due to the finite height of the jet, the increase in

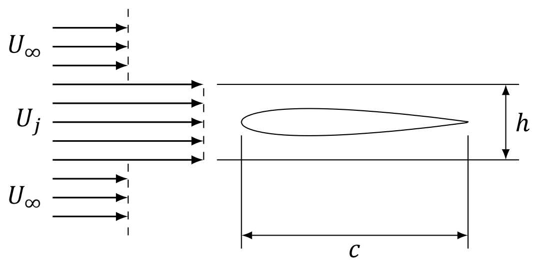

Figure 2.2: Schematic of a wing in a jet with finite slipstream height

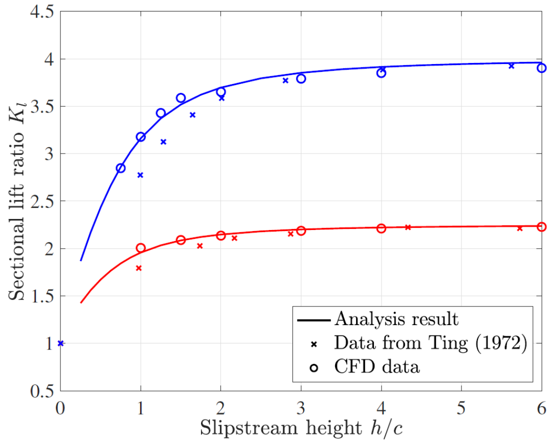

Figure 2.3: The lift of an airfoil section for different jet heights [48]

lift is less than what is expected from predictions from conventional potential flow models. This has been shown by Nederlof [48], as shown in Figure 2.4, based on the theory by Rethorst [49][50]. Here a case is shown with a circular jet in the middle of the wing and $U_j = 1.5U_\infty$. It can be seen that by simply applying the velocity increase in the jet region as boundary conditions to the lifting line model, the lift is highly overestimated when compared to the CFD data. With a correction for the jet applied, the increase in lift is lower and it matches the CFD data. This reduction in lift has sometimes been modelled for propeller-wing interaction as a reduction in swirl or swirl recovery, this will be further discussed in Section 2.3.2.

Lastly, the circulation distribution requires some attention. As shown in Figure 2.5 the circulation distribution exhibits a step change at the jet boundary. While this seems unusual for a wing, it still follows the definition of circulation and Kutta-Joukowski theorem, as given in Equation 2.1 and 2.2 respectively. For pressure, and thus lift, to be spanwise continuous, the circulation must show a step change when there is a spanwise step change in inflow velocity.

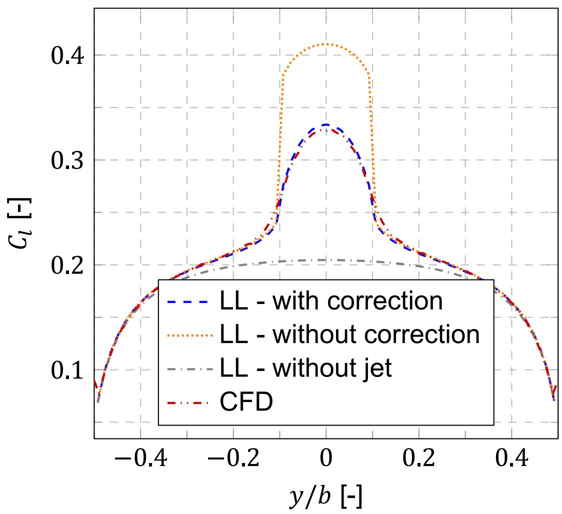

Figure 2.4: The lift distribution for a wing with a circular jet at the center [48]

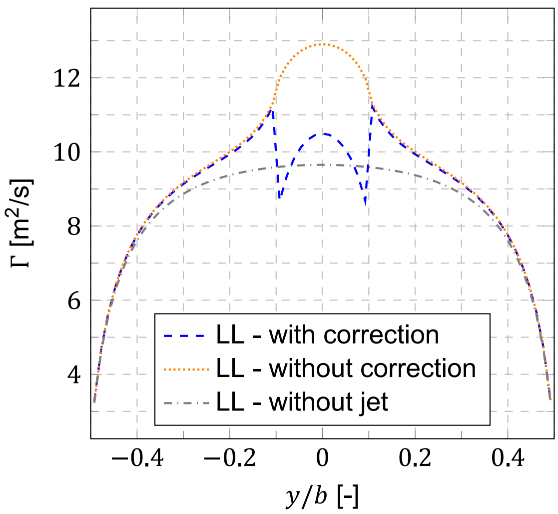

Figure 2.5: The circulation distribution for a wing with a circular jet at the center [48]

2.2. Propeller aerodynamics

The main purpose of a propeller is to provide thrust. This is done by rotating the propeller blades, which results in a forward force, called the thrust, and a tangential force, which causes torque. The thrust, torque and subsequent power can be non-dimensionalized, resulting in Equations 2.3, 2.4, 2.5.

$$C_T = \frac{T}{\rho n^2 D^4} \tag{2.3}$$

$$C_Q = \frac{Q}{\rho n^2 D^5} \tag{2.4}$$

$$C_P = \frac{P}{\rho n^3 D^5} \tag{2.5}$$

An important propeller parameter is the advance ratio J, given in Equation 2.6. The advance ratio is useful for scaling propellers, because at the same advance ratio, a propeller experiences the same angle of attack on its blades if the pitch distribution is the same, neglecting propeller wake induced velocities. By dividing the effective propulsive power by the input power, the efficiency can be obtained, as shown in Equation 2.7.

$$J = \frac{U_\infty}{nD} \tag{2.6}$$

$$\eta = \frac{TU_\infty}{P} = \frac{C_T}{C_P}J \tag{2.7}$$

When looking at propeller-wing interaction, it might be useful to compare forces to the aircraft forces. In this case forces can be non-dimensionalized in the same way as the aircraft forces. This leads to Equation 2.8 for the thrust coefficient, where S_{ref} is a reference surface area on the aircraft, usually the wing area.

$$T_C = \frac{T}{\frac{1}{2}\rho U_\infty^2 S_{ref}} \tag{2.8}$$

2.2.1. Actuator disk model

A simple way to analyse the behaviour of a propeller is by using the actuator disk model. In this model the flow affected by the propeller is captured by the streamtube. Subsequently it is assumed that the flow in the streamtube is an axial flow, uniform across its cross section, so without any rotational velocities. With these assumptions a one dimensional analysis can be done using the continuity and momentum equations.

Such a simple analysis already provides a good insight of the aerodynamic phenomena around the propeller, as visualized in Figure 2.6. The pressure far up- and downstream are assumed to be equal to the freestream pressure p_∞. A (total) pressure step change is seen at the propeller disk, which results in the thrust force. On the other hand, the velocity remains continuous across the propeller disk. An axial induction factor a is introduced to describe the propeller induced axial velocity. At the propeller disk the propeller induced velocity is aU_∞ and it increases to $2aU_\infty$ in the wake, leading to the expressions in Equation 2.9. This analysis also gives an expression of the thrust coefficient as a function of the axial induction factor, as shown in Equation 2.10. Lastly, it can be seen that by applying conservation of mass, the slipstream area must decrease due to the increasing velocity.

$$\begin{aligned} U_D &= (1+a)U_\infty \\ U_w &= (1+2a)U_\infty \end{aligned} \tag{2.9}$$

$$C_T = 4a(1+a)\left(\frac{\pi}{8}J^2\right) \tag{2.10}$$

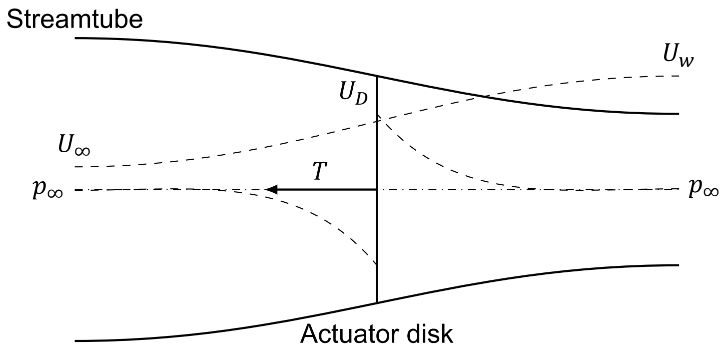

Figure 2.6: Schematic of the actuator disk model

2.2.2. Blade element momentum theory

The actuator disk model gives a good indication the overall performance of a propeller, but it is unsuitable to analyse propeller geometries. To perform a low-cost analysis on a propeller geometry, the actuator disk can be split into independent annular streamtubes, shown in Figure 2.7. These streamtubes can again be analyzed using equations for conservation of mass and conservation of momentum, like in the actuator disk model. This is the basis of the Blade Element Momentum (BEM) theory. This model takes into account axial and tangential velocities, but initially neglects 3D effects.

In each streamtube a 2D airfoil analysis can be done. This is shown in Figure 2.7. The blade element sees two velocity components, one axial and one tangential. The axial velocity can again be described using an induction factor, which gives: $U_a = U_\infty(1 + a)$. The same can be done for the tangential velocity. Over the width of the propeller disk swirl is added to the flow. This swirl velocity is $a'\Omega r$ at the propeller disk, where a' is the tangential induction factor. The swirl velocity increases and becomes $2a'\Omega r$ in the wake. Thus, at the blade element the tangential velocity given by $U_t = \Omega r(1 - a')$. The local velocity U, created by U_a and U_t has a certain angle, which is referred to as the advance angle ϕ. With the blade pitch and advance angle known, the angle of attack can be determined. Using a 2D airfoil analysis, the forces on the blade element can be calculated, which can be resolved in an axial and tangential force, as shown in Equation 2.11. By integrating over all streamtubes, the total thrust and torque for the propeller can be determined.

$$\begin{aligned} dF_x &= dL\cos(\phi) - dD\sin(\phi) \\ dF_z &= dL\sin(\phi) + dD\cos(\phi) \end{aligned} \tag{2.11}$$

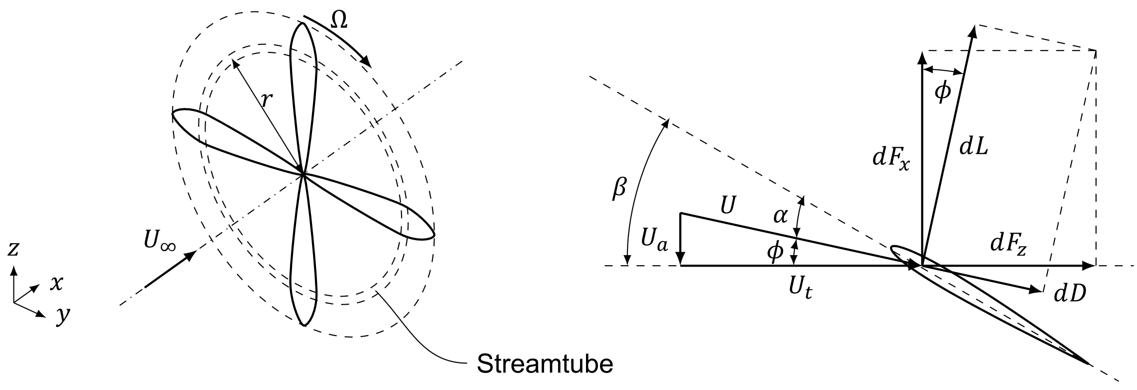

Figure 2.7: Schematic of the BEM theory

Since in each streamtube only a 2D analysis is performed, 3D effects are initially neglected. However, at the tip and root of the propeller blade trailing vortices are present, similar to tip vortices on a wing. Due to the rotation of the propeller, the shape of these vortices is helicoidal and this vortex structure has a large effect on the propeller induction factor [51]. This results in a tip and root loss.

While tip losses have a significant impact on the propeller performance, root losses can often be neglected, since the forces on the blade root are much lower compared to the tip. This is because at the root, where the radius is small, tangential velocity is much lower. This gives low dynamic pressure and leads to relatively small forces at the root, thus the circulation gradient at the root is also relatively small, which gives trailing vortices with little strength and does not lead to significant losses.

To calculate the tip loss, the induced velocity by the wake must be known. One could assume a rigid wake and calculate the induced velocities using the Biot-Savart law for each vortex filament [51]. This is computationally expensive and extra steps must be taken to obtain the solution for steady flow, as this way of modelling is time-depedent, while the BEM model is steady. Using an infinite number of blades could lead to acceptable results [52], but this is computationally expensive. A less computationally expensive method would be using exact solutions for a helicoidal wake. XROTOR[1] uses an extension of Goldstein's solutions [53]. Such a solution also models a rigid helicoidal wake, but for steady flow and at a much lower computational cost.

A widely used way to account for tip losses is by using the Prandtl tip factor [54]. Prandtl's solution replaces the helicoidal vortex sheet with disks, moving with the wake velocity $U_\infty(1+a)$. The resulting tip loss factor $F(r)$ is given by Equation 2.12, where R_w is the radius of the wake and d the distance between successive vortex sheets. These two variables are hard to define, so the exponent f is usually rewritten to an expression that is easier to evaluate. Glauert [52] introduced the expression shown in Equation 2.13, where ϕ_R is the flow angle at the tip. By replacing ϕ_R with the local flow angle, the exponent can be further simplified to Equation 2.14.

$$\begin{aligned} F(r) &= \frac{2}{\pi}\arccos\left(e^{-f}\right) \\ f &= \pi\left(\frac{R_w - r}{d}\right) \end{aligned} \tag{2.12}$$

$$f = \frac{B}{2}\left(\frac{R-r}{R}\right)\frac{1}{\sin(\phi_R)} \tag{2.13}$$

$$f = \frac{B}{2}\left(\frac{R-r}{r}\right)\frac{W_a}{W_t} \tag{2.14}$$

This tip loss factor can be easily implemented in a BEM code. Using an iterative scheme the equations can be solved. Prandtl's tip loss factor shows good agreement with Goldstein's solution. However, at high advance ratios the difference increases [55].

2.2.3. Propeller slipstream modelling

To calculate induced velocities from the propeller on a wing, a propeller slipstream model is needed. The slipstream contains the vortex sheet shed by the propeller, which propagates downstream. The strength of the vorticity in the wake is determined by the strength of the bound vortex on the propeller blade. Helmholtz's theorem says that a vortex can not end in a fluid. Since the bound vortex strength of the blade is not constant, trailing vortices must emerge. The strength of these trailing vortices is equal to the difference in the adjacent bound vortices.

Due to the rotation of the blades, this vortex sheet has a helicoidal shape. Furthermore, the vortex sheet must follow the fluid. Thus, the surface of the sheet is force free, without pressure discontinuity or normal velocity discontinuity [56]. When the propeller slipstream is modelled as a force free surface, it is referred to as a free wake model. The induced velocities of the wake are calculated using the Biot-Savart law, shown in Equation 2.15, where $\overline{dl}$ is an infinitesimal small vortex length and $\bar{r}$ is the radius from the vortex to a point. Using an algorithm, the system can be solved iteratively with the boundary conditions imposed. However, calculations for a free wake model are costly. A simpler model is the frozen wake model, which uses a prescribed axial and rotational velocity to propagate the vortices downstream. In this model, the vortex surface is not force free anymore. However, in the region close to the propeller, the shape of the slipstream is very similar for these two models [56]. Only in regions farther away of the propeller, the vortex sheet will roll up and the frozen wake model loses accuracy here.

[1] `http://web.mit.edu/drela/Public/web/xrotor/`

$$\overline{du} = \frac{\Gamma}{4\pi} \frac{\overline{dl} \times \overline{r}}{|\overline{r}^3|} \tag{2.15}$$

The free wake and frozen wake model, however, are time-dependent models, so extra steps are needed to calculate the time-averaged solution. One way to get a time-averaged solution directly is by using the slipstream tube model [12][28]. This model identifies two sources of vorticity in the wake. There is axial vorticity γ_a, parallel to the axis of rotation. Tangential vorticity γ_t is located on circles concentric with the axis of rotation, perpendicular to the axial vorticity. Lastly, on the propeller plane there is the bound vorticity from the blades, γ_p. A representation of the slipstream tube model is shown in Figure 2.8, where γ_a is located on the horizontal lines and γ_t on the circles. The vorticity coming from the propeller must be averaged, which is shown in Equation 2.16.

$$\begin{aligned} \gamma_a &= \frac{B}{2\pi r} \frac{d\Gamma}{dr} \\ \gamma_t &= \frac{nB}{U_\infty} \frac{d\Gamma}{dr} \\ \gamma_p &= \frac{B}{2\pi r} \Gamma \end{aligned} \tag{2.16}$$

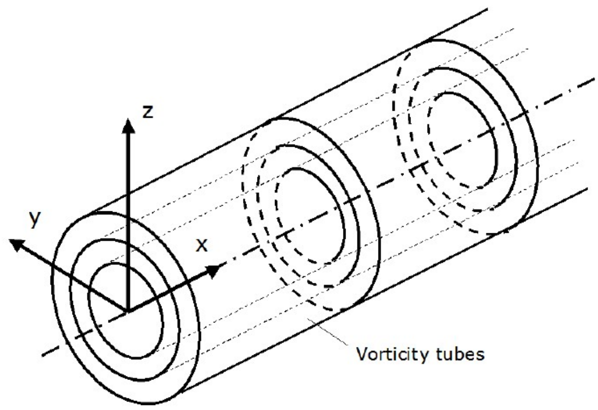

Figure 2.8: Slipstream tube model [28]

Together these two vorticity elements create rings of vorticity in the wake. By exploiting the geometric properties of these rings the integral in x direction can be evaluated analytically. This gives a solution for streamtubes going from the propeller disk at $x = 0$ to infinite. By integrating the solution over the radius, the induced velocity can be found at some point with coordinates $[x_p, y_p, z_p]$ using Equations 2.17 and 2.18 for the axial and tangential vorticity respectively. Here ϕ is the azimuth angle of the streamtube.

$$
\begin{aligned}
u_x &= 0 \\
u_y &= \int_{r_{hub}}^{R} a \int_0^{2\pi} \frac{c}{b^2+c^2}\left(1+\frac{x_p}{\sqrt{x_p^2+b^2+c^2}}\right) d\phi dr \\
u_z &= \int_{r_{hub}}^{R} a \int_0^{2\pi} \frac{-b}{b^2+c^2}\left(1+\frac{x_p}{\sqrt{x_p^2+b^2+c^2}}\right) d\phi dr
\end{aligned}
\tag{2.17}
$$

with :

$$
\begin{aligned}
a &= \frac{\gamma_a r}{4\pi} \\
b &= r\sin(\phi) - y_p \\
c &= -r\cos(\phi) - z_p
\end{aligned}
$$

$$
\begin{aligned}
u_x &= \int_{r_{hub}}^{R} a \int_0^{2\pi} \frac{b\sin(\phi) - c\cos(\phi)}{b^2+c^2}\left(1-\frac{-x_p}{\sqrt{x_p^2+b^2+c^2}}\right) d\phi dr \\
u_y &= \int_{r_{hub}}^{R} a \int_0^{2\pi} \frac{-\sin(\phi)}{\sqrt{x_p^2+b^2+c^2}} d\phi dr \\
u_z &= \int_{r_{hub}}^{R} a \int_0^{2\pi} \frac{\cos(\phi)}{\sqrt{x_p^2+b^2+c^2}} d\phi dr
\end{aligned}
\tag{2.18}
$$

with :

$$
\begin{aligned}
a &= \frac{\gamma_t r}{4\pi} \\
b &= r\sin(\phi) - y_p \\
c &= -r\cos(\phi) - z_p
\end{aligned}
$$

Conway [57] created a similar model using axial and tangential vorticity. For certain radial velocity distributions, exact expressions were derived for the induced axial and radial velocity components. In this analysis the velocity will be constant along the azimuth direction, so velocity will be a function of r and x. In Equation 2.19 the radial velocity distribution for an even polynomial function can be seen. Here $U_a(r,0)$ is the axial velocity at the propeller disk, U_{a0} is a scaling factor and μ is an integer. For this distribution of axial velocity, the induced radial and axial velocity can be written as Equation 2.20 and 2.21 respectively. The solution uses the gamma function $\Gamma(x)$ and the Bessel function of the first kind $J_n(x)$.

$$
U_a(r,0) = U_{a0}\left(1-(r/R)^2\right)^{\mu}
\tag{2.19}
$$

$$
U_r(r,x) = -\frac{2^{\mu}\Gamma(\mu+1)U_{a0}}{R^{\mu-1}} \int_0^{\infty} \frac{e^{-s|x|}J_{\mu+1}(sR)J_1(sr)}{s^{\mu}} ds
\tag{2.20}
$$

$$
\begin{aligned}
U_a(r,x) &= 2U_a(r,0) - \frac{2^{\mu}\Gamma(\mu+1)U_{a0}}{R^{\mu-1}} \int_0^{\infty} \frac{e^{-s|x|}J_{\mu+1}(sR)J_0(sr)}{s^{\mu}} ds \quad \text{for } x \geq 0 \\
U_a(r,x) &= \frac{2^{\mu}\Gamma(\mu+1)U_{a0}}{R^{\mu-1}} \int_0^{\infty} \frac{e^{-s|x|}J_{\mu+1}(sR)J_0(sr)}{s^{\mu}} ds \quad \text{for } x < 0
\end{aligned}
\tag{2.21}
$$

Furthermore, Conway found that by superposition of axial velocity distributions a solution could be found for a general distribution. This principle is shown in Equation 2.22.

$$U_a(r,0) = \sum_{\mu=1}^{N} U_{a0,\mu}\left(1-(r/R)^2\right)^{\mu} \tag{2.22}$$

2.2.4. Propeller in non-uniform flow

Until now the inflow field has been assumed to be uniform and aligned with the propeller rotation axis. When this is not the case, the steady propeller performance will change. Next to this there are some unsteady effects that will occur.

A useful case to examine is when the propeller is placed under and angle with respect to the inflow velocity. This will introduce both time-average and unsteady effects. The time-average effects will be discussed first. When the propeller is placed under angle of attack, the propeller will generate a vertical force and yawing moment [58][59]. The angle of attack will lead to a tangential velocity component (U_t) on the propeller blades, as shown in Figure 2.9. On the advancing blade side this tangential velocity acts in the same direction as the blade rotational velocity, while these velocities are in opposite direction on the retreating blade side. This difference causes an increase in angle of attack and dynamics pressure on the advancing blade and a decrease of angle of attack and dynamic pressure on the retreating blade, illustrated in Figure 2.9. The projection of the difference in thrust and drag on the advancing and retreating side leads to a force in the direction of the tangential velocity [60], or an upward velocity in Figure 2.9. Furthermore, the net effect in thrust of the difference on the advancing and retreating side is positive, thus thrust increases with increasing inflow angle [60][61][62].

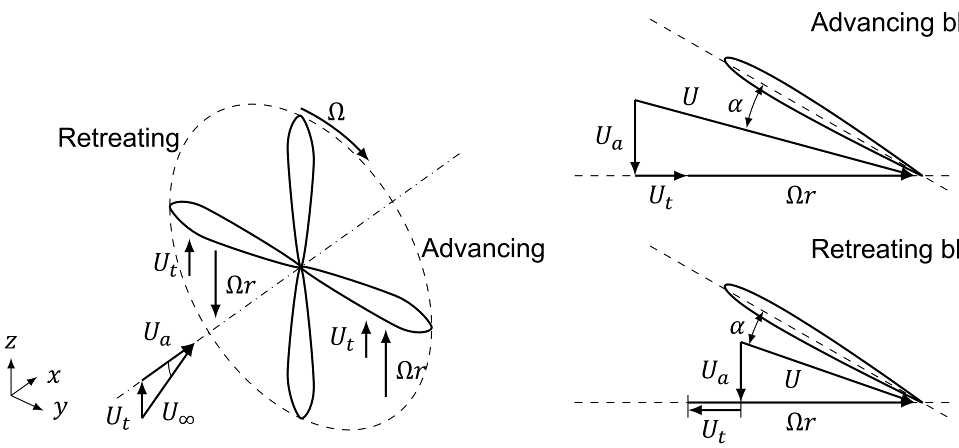

Figure 2.9: Change in angle of attack and dynamic pressure on blade elements due to an inflow angle

Another phenomenon that occurs when the propeller is placed under an angle is the skewing of the wake axis. Due to the freestream velocity not being aligned with the propeller thrust, the direction of the wake will not be on the propeller rotation axis [51]. This leads to a skew angle for the wake, which is smaller than the inflow angle, since axial velocity is added by the propeller. Because of this the induced velocities will vary at different azimuthal blade positions [63]. This then leads to a second force, perpendicular to the previously described force. The advancing side provides more thrust, thus the circulation is higher. So the induced velocity by the wake on the advancing side is also higher compared to the retreating side. This phenomenon is shown in Figures 2.10 and 2.11 obtained using CFD and using a lifting line method respectively. In these figures axial induced velocities are shown for a propeller under angle of attack. While CFD provides high fidelity results, the lifting line provides data on the aerodynamic principles at play. The region at azimuthal position $\Psi = 0°$ is closer to the wake of the advancing side and shows a higher induced velocity, while the region at $\Psi = 180°$ is farther away from the wake of the advancing side and shows a lower induced velocity. This difference in induced velocity causes a similar difference in lift and drag as previously shown in Figure 2.9. This will lead to a force in horizontal direction for a propeller under angle of attack, or to the right in Figures 2.10 and 2.11.

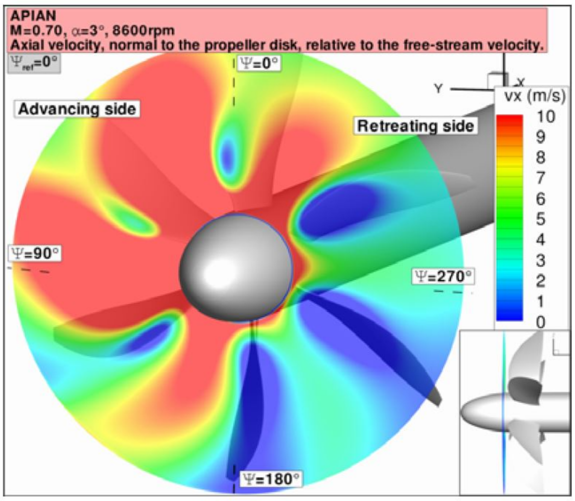

Figure 2.10: Axial velocities relative to the freestream velocity for a propeller at an angle of attack obtained using CFD [60]

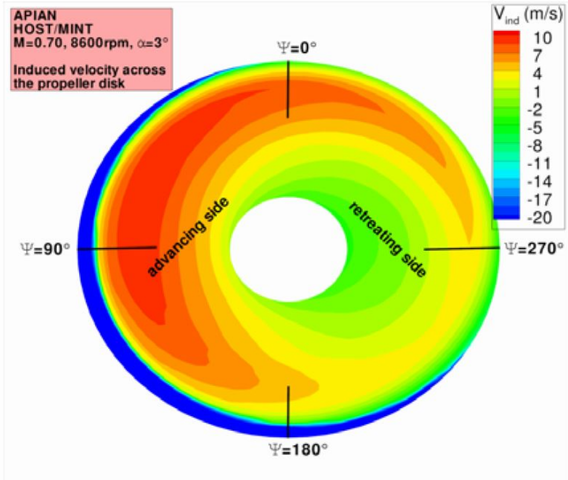

Figure 2.11: Induced velocities for a propeller at an angle of attack obtained using a lifting line method [60]

Next to time-averaged effects, there are also unsteady effects when a propeller is placed under an angle. While the blade is rotating, it will see a changing angle of attack and dynamic pressure. The result of this are fluctuating forces on the blades, which cause cyclic in-plane forces which are called 1P loads or first-order propeller loads. These forces are important for structural sizing, mainly for static sizing and for fatigue sizing [60].

The in-plane forces for a propeller under angle of attack can be calculated with the solutions derived by De Young [61]. However, a propeller that faces an arbitrary inflow can usually not be reduced to a simple angle of attack problem. This is usually the case when looking at propeller interaction with the wing or fuselage. Several models exist to calculate the propeller performance and in-plane forces for any inflow field. Methods that are relatively expensive are unsteady RANS CFD [40] and panel methods with a full representation of the propeller blade [64]. A more computationally efficient method has been developed by Van Arnhem, et al. [65] by determining a local advance ratio for each location on the propeller plane. Using a sensitivity map for a propeller in uniform conditions, the forces on each location can be calculated, resulting in an estimation of the propeller forces. When this model is compared to validation data, errors are shown to be ranging from 0.5% to 12%.

2.3. Propeller-wing interaction effects

This section will describe the propeller-wing interaction effects for a tractor configuration. First, the effects of the wing on the propeller are discussed in Section 2.3.1, followed by the effects of the propeller on the wing in Section 2.3.2. Finally, the influence of design variables on the propeller-wing interaction are discussed in Section 2.3.3.

2.3.1. Effects of the wing on the propeller

The main effects of the wing on the propeller in a tractor configuration are due to the circulation and vortices present from the wing. These will induce velocities upstream on the propeller. The direction of the induced velocities is determined by the position of the propeller with respect to the wing. Before the wing the propeller experiences mainly upwash from the bound vortex, and if the propeller is located inside the span, downwash from the tip vortices. Ribner [66] found that the induced velocities lead to a non-axisymmetric inflow for the propeller, causing 1P loads. However, from experiments conducted by Heidelberg and Woodward [67] it was concluded that the wing induced velocities on the propeller are practically uniform and it can be seen as an increase in angle of attack of the propeller. This is shown in Figure 2.12. Here the induced velocities for an isolated propeller at $\alpha = 1.5°$ are plotted on the left. On the right the induced velocities are shown for the installed propeller. It can be seen that the differences are very small.

Next to the vortex induced velocities there is blockage. This will lead to a decrease in axial velocity

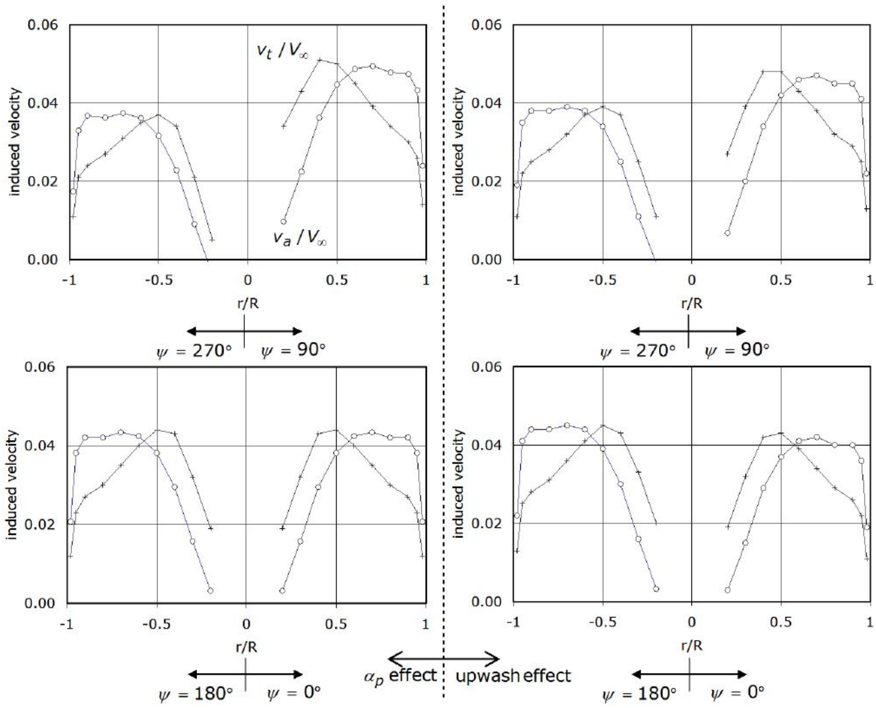

Figure 2.12: Comparison between an uninstalled propeller under an angle and an installed propeller in the upwash of a wing [67]

on the propeller, leading to a decreased advance ratio and increased thrust [39]. Finally, in Figure 2.13 all the sources of induced velocities on the propeller are shown. The blockage effect induces axial velocities, while the tip vortex induces in-plane velocities. The bound vortex induces a combination of axial and in-plane velocities. Here it can be seen that the tip vortex effectively decreases the advance ratio for a wingtip-mounted propeller. However, blockage seems to be the main source of the thrust increase [39].

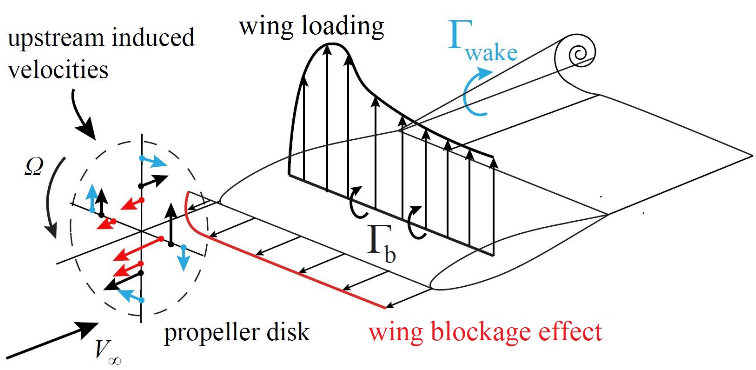

Figure 2.13: An overview of all the induced velocities from the wing on a tractor propeller [39]

2.3.2. Effects of the propeller on the wing

In this section the most important effects of tractor propellers on the wing will be discussed. It starts with describing the main effects of the propeller wake on the wing lift distribution, followed by a description of swirl recovery. This is followed by some notes on the modelling of swirl recovery in low-order methods, such as lifting line and VLM models. Finally, some interaction effects specific for wingtip-mounted propellers are discussed.

Next to these effects on the large scale flow on the wing, there are also effects on the boundary layer.

The turbulent wake of a tractor propeller could move transition of the wing more towards the leading edge [68]. The propeller slipstream could also lead to a boundary layer cycling between laminar and turbulent flow [69]. These boundary layer effects are not further discussed, since they are not relevant for this research.

Main effects on the lift distribution
In a tractor configuration a part of the wing will be immersed in the propeller slipstream. This leads to two main effects on the immersed part of the wing: an increase in dynamic pressure due to increased axial velocity and a change in angle of attack due to in-plane velocities.

In Figure 2.14 it is shown how these two effects affect the wing lift distribution. Firstly, the increase in axial velocity increases the dynamic pressure. This leads to an increase in lift for the same angle of attack. Furthermore, the increase in axial velocity is not the same along the span, since it is not uniform along the propeller blade. At different radial positions, the axial induction factor and thus the axial velocity is different. In Section 2.1.2 it was already discussed how the wing aerodynamics change when dynamic pressure increased in a circular jet. The in-plane velocities cause an angle of attack change. In the case of Figure 2.14, where the propeller center is aligned with the wing, this is due to tangential velocities only. It can be seen that this causes upwash on the upgoing blade and downwash on the downgoing blade. The amount of up- or downwash is dependent on the radius and tangential induction factor. Thus, the highest magnitude of up- or downwash is expected close to the blade tip, but not at the blade tip. Finally, the result of these two effects combined is also shown in Figure 2.14.

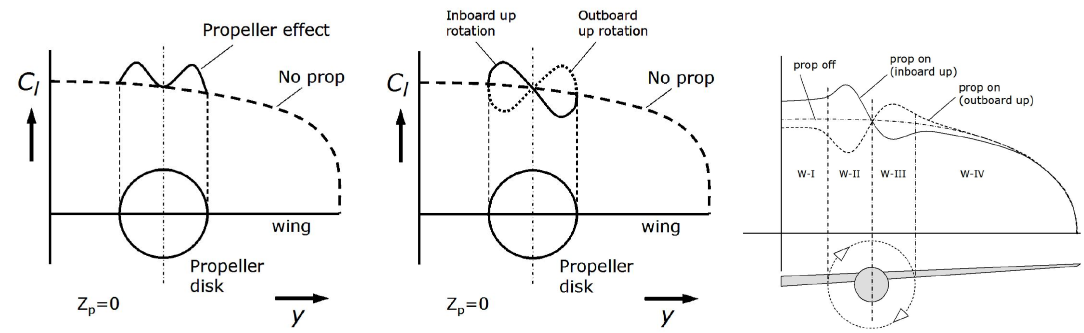

(a) Axial (b) Tangential (c) Combined

Figure 2.14: The effects of dynamic pressure and angle of attack on the wing lift distribution due to a propeller [28]

Swirl recovery
The change in angle of attack on the different wing section also leads to a phenomenon called *swirl recovery*. Due to swirl recovery the angular momentum in the propeller wake, which is considered a loss, can be used to generate forward drag. This principle is illustrated in Figure 2.15. Here a wing at $\alpha = 0°$ is shown. It can be seen that the down going blade produces downwash and the up going blade upwash. This leads to a change in the direction of the resultant force. However, the lift is always perpendicular to the inflow velocity, so this resultant force can be decomposed in a lift and drag component. Depending on the magnitude of the change in lift and the magnitude of the original lift vector, this may lead to negative induced drag on one or both sides of the propeller. Still, it can be seen that even when both positive and negative drag are produced, the net result is negative drag, leading to a better wing performance.

Modelling of swirl recovery
Due to swirl recovery, there will be less swirl in the wake. Since swirl recovery happens gradually over the wing, it can be assumed that the swirl will be overestimated when using low-order models. This would lead to an overestimated lift, which has been observed by several studies [28][71][72][73]. To counteract this problem a Swirl Recovery Factor (SRF) was introduced. However, this SRF has no physical meaning and even with the SRF included, the analysis tools were still overestimating lift [71][72]. Using a lifting line method, Nederlof [48] showed that the overestimation of lift, that the SRF tried to account for, was actually caused by improper modelling of the finite height of the increase axial

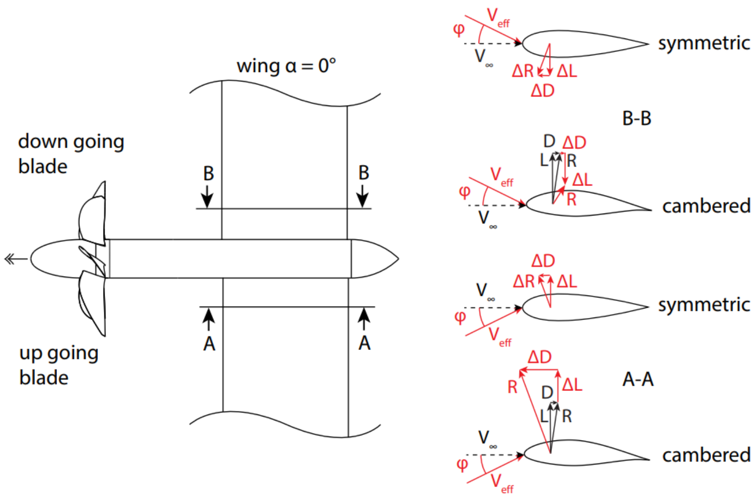

Figure 2.15: Schematic for swirl recovery for a symmetric and cambered wing at zero angle of attack [70]

velocity jet. This has been described in Section 2.1.2. With proper modelling of the finite jet height it was shown that the lift predicted with a lifting line model agrees with CFD data as shown in Figure 2.16. Although it can be seen that the lift is still somewhat overestimated. It is thought this can be improved by also taking into account the finite slipstream height of the swirl velocities, while the effect of swirl recovery does not seem to play a big role here.

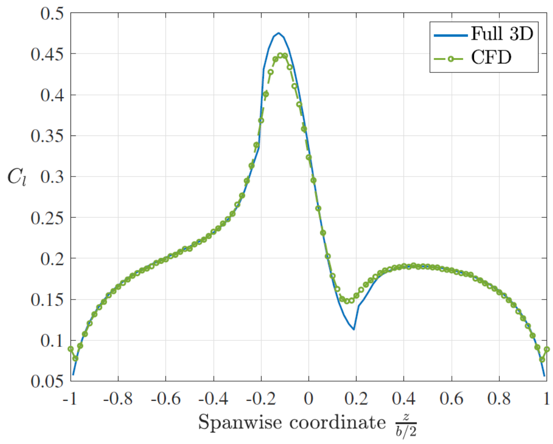

Figure 2.16: Comparison of the lift distribution for a wing in a jet with axial and tangential velocity between a lifting line model and CFD [48]

Interaction effects for wingtip-mounted propellers

In Section 1.1 it was already mentioned that inboard-up rotating wingtip-mounted propellers have a beneficial interaction effect with the wingtip vortex. For a tractor propeller, the wingtip vortex will be moved outboard, leading to an increase in effective aspect ratio and reducing drag [12][13][19][20]. On the other hand an outboard-up rotating propeller moves the wingtip vortex inboard, leading to a decrease of effective aspect ratio. In Figure 2.17 it can be seen that the inboard-up rotating propeller gives a more efficient wing. This interaction effect has also been investigated on a Fokker F27 scale model using windtunnel experiments [29]. The results can be found in Figure 2.18. Here again the benefit of inboard-up rotating propeller is shown.

One of the driving factors of the interaction is the amount of swirl in the propeller wake. Snyder and Zumwalt [20] used two different propeller designs to investigate the effect of swirl. They found that a

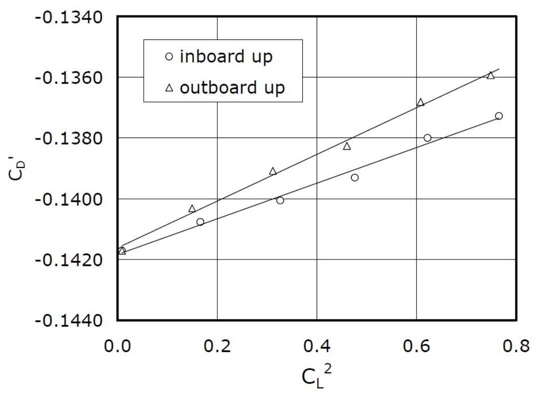

Figure 2.17: Lift and drag for a propeller-wing combination for inboard-up and outboard-up rotating propellers [29]

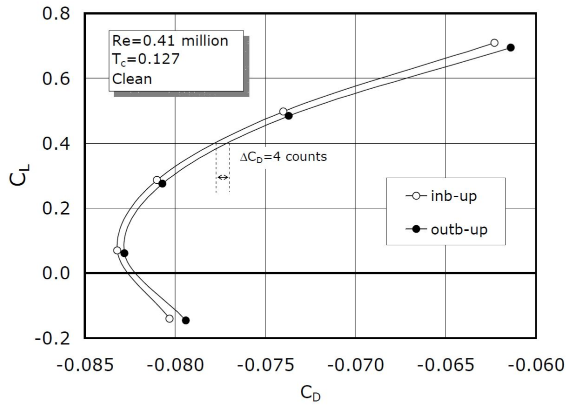

Figure 2.18: Lift and drag for a Fokker F27 scale model with inboard-up and outboard-up rotating propellers [29]

higher swirl gives a decrease in drag, which was validated by experimental data. Miranda and Brennan [12] investigated this effect by using the disk loading. The disk loading is defined as the ratio of thrust to disk area, which gives an equivalent pressure of the propeller disk. With increasing disk loading, the swirl in the wake also increases. They found that with increasing disk loading the drag also decreases. However, Della Vecchia, et al. [74] found that when the propeller diameter becomes too small, drag will increase with increasing disk loading. This is observed at a low lift coefficient where the strength of the wingtip vortex is small and will be shed from the edge of the nacelle. Furthermore, the small propeller vortex is also dissipated by the nacelle. This leads to a scenario where there is basically no interaction between the propeller wake and wingtip vortex, so no drag reduction is achieved here.

2.3.3. Propeller location

In this section some of the key variables for propeller-wing interaction for a tractor configuration are discussed.

Propeller streamwise position

Due to slipstream contraction, a wing in the propeller slipstream can experience an induced angle of attack and dynamic pressure increase due to the relative position with respect to the propeller. This is shown in Figure 2.19. When the streamwise position between propeller and wing is increased, the induced angle of attack (due to radial velocity) decreases and the dynamic pressure increases. Veldhuis [75] found that the net result of these effects is very small. In a more recent study by Veldhuis [29] an increase in propeller efficiency was found when the streamwise distance between propeller and wing was increased. Due to the upwash from the wing, the propeller experiences a non-uniform inflow when near to the wing. This causes velocity distortions in the wake, which affect wing performance. Furthermore, the dynamic pressure further downstream from the propeller is higher, further improving wing efficiency.

Propeller vertical position

A change in vertical position of the propeller also affects the wing by a change in angle of attack. This is due to slipstream contraction as shown in Figure 2.19. A second effect of the propeller vertical position is the change in wing area affected by the propeller slipstream. The cross section of the high dynamic pressure region of the propeller slipstream takes the form of a doughnut, due to the presence of the propeller hub. This is shown in Figure 2.20. When moving the propeller up or down with respect to the wing, a smaller or larger part of the wing experiences a high dynamic pressure. In an experimental study by Veldhuis [29] it was found that at high thrust settings, lift can be enhanced by putting the propeller at an offset in vertical direction. Furthermore, for a high propeller position, the lift can be increased more than for a low propeller position. This is due to the angle of attack effect. For low thrust settings, these effects are much less noticeable.

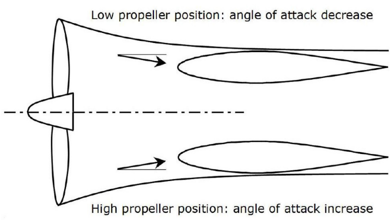

Figure 2.19: The effect of contraction on the local angle of attack in the propeller slipstream [28]

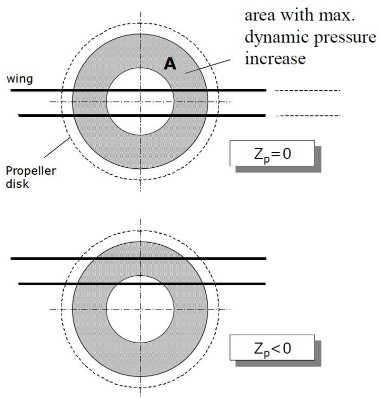

Figure 2.20: Schematic of the high dynamic pressure region of the propeller slipstream for a propeller with hub [29]

Propeller spanwise position

The spanwise position of the propeller determines the spanwise lift distribution of the wing due to increased dynamic pressure and angle of attack change as discussed in Section 2.3.2. Furthermore, when moving a inboard-up rotating propeller outboard, there is beneficial interaction between the swirl in the propeller slipstream and the wing tip vortex. This is shown in Figure 2.21. It can be seen that this effect is the strongest for wingtip-mounted propellers. When propellers are placed inboard, the effects are barely noticeable.

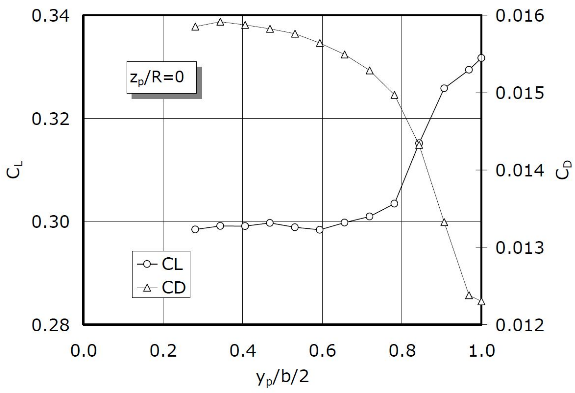

Figure 2.21: The effect of the propeller spanwise position on lift and drag [29]

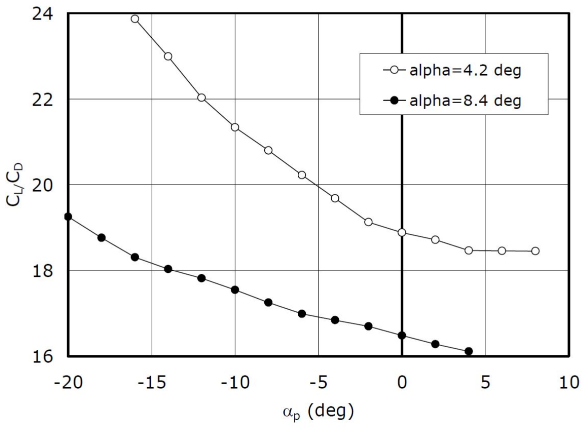

Figure 2.22: The effect of the propeller installation angle on the lift to drag ratio [29]

Propeller installation angle

When a tractor propeller is installed on the wing, it will see induced velocities from the wing. These induced velocities are almost equivalent to a negative angle of attack for the propeller. By changing the propeller installation angle, the propeller inflow can be better aligned, leading to an perpendicular inflow to the propeller plane [29]. This is beneficial for the propeller, as it reduces unsteady forces. Since the propeller will be installed at a negative angle, the wing will see increased upwash, increasing the lift. However, this effect is lower for lower thrust settings. Furthermore, this upwash acts mostly on the wing leading edge, resulting in more suction on the front of the wing, decreasing drag. The thrust vector will be directed downwards, decreasing the lift, but this is offset by the gain in wing lift [29]. In Figure 2.22 experimental results are presented for the wing lift to drag ratio at different propeller installation angles. A more negative installation angle increases the lift, leading to a higher lift to drag ratio.

3
Propeller model

In this chapter the setup of the numerical propeller model will be discussed. In Figure 3.1 a flowchart can be found for this model. It takes the propeller geometry, the lift and drag polars of airfoils at different radial stations and an externally induced velocity field as input. The external induced velocity field will eventually be the induced velocities by the wing. The outputs of the model are the propeller performance and propeller induced velocities from the slipstream tube model. The propeller induced velocities will be used as an input for the wing model. The propeller model itself consists of three main parts. The BEM model will be discussed in Section 3.1. The non-uniform inflow propeller analysis is described in Section 3.2. Finally, in Section 3.3 a description of the slipstream model is given.

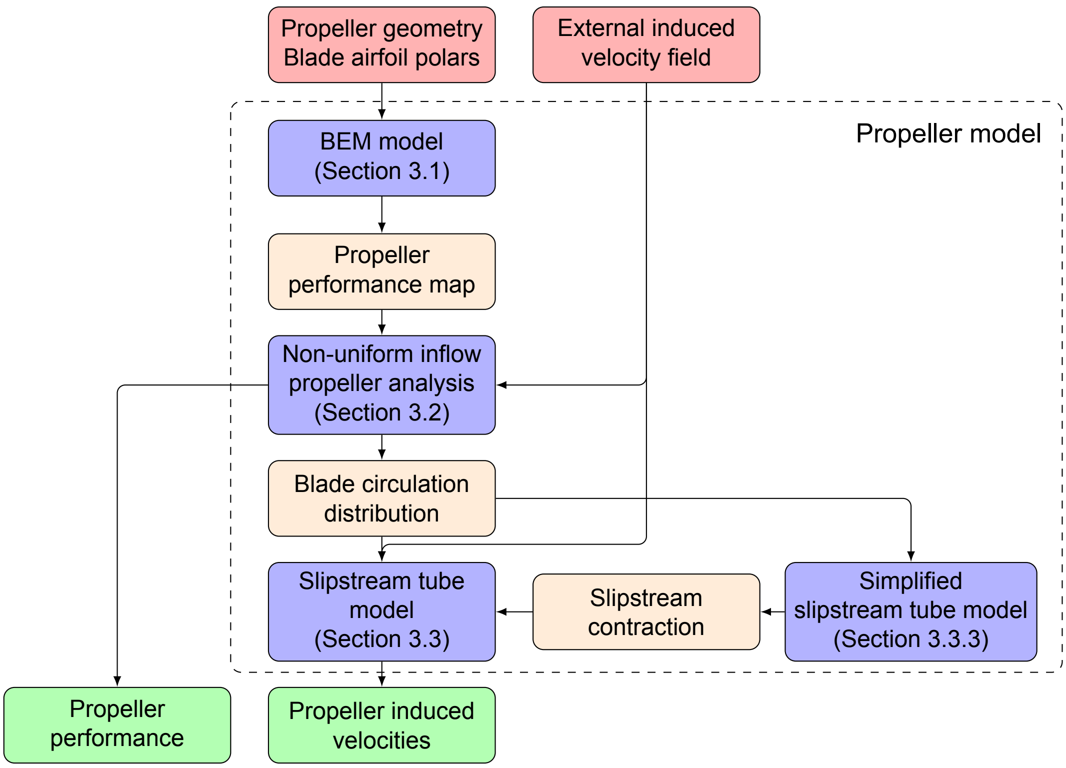

Figure 3.1: Flowchart for the numerical propeller model

3.1. BEM model

To analyze the isolated propeller without any disturbances in the inflow velocity field, a BEM model is used. The BEM model used, is based on the *graded momentum* formulation used in existing codes by Mark Drela, which includes XROTOR, QPROP and QMIL [76]. The graded momentum formulation uses the Prandtl tip loss factor. This means that the formulation is somewhat limited in its use, since this tip loss factor is not valid at higher advance ratios [55].

XROTOR has already been widely used at the TU Delft and the results usually show good agreement with CFD analysis [44][77][78]. However, XROTOR does not take direct airfoil polars as input. This was seen as a potential source of large errors for a parameterized propeller model. Thus, the decision was made to develop a BEM model, based on the XROTOR model, which could directly read airfoil polars.

3.1.1. BEM formulation

The solution for the BEM analysis must be obtained iteratively. To make the iteration faster and more stable, a dummy variable Ψ is introduced. This is the angle of the total velocity vector from the center of the total inflow velocity. Furthermore, the assumption is made that the induced velocity is perpendicular to the total velocity. This is only valid for lightly loaded propellers with Goldstein's circulation distribution, but this assumption also holds up for most cases [53][76]. Using the velocities presented in Figure 3.2 the velocities can be written as a function of Ψ, as presented in Equation 3.1.

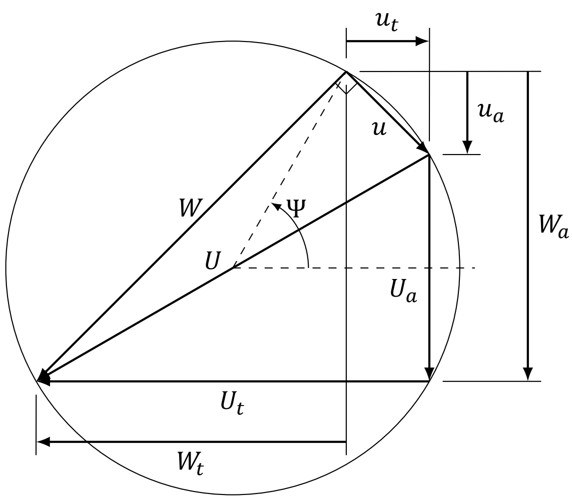

Figure 3.2: Definition of the velocities used by the BEM solver

$$
\begin{aligned}
W_a &= \frac{1}{2}U_\infty + \frac{1}{2}U\sin(\Psi) \\
W_t &= \frac{1}{2}\Omega r + \frac{1}{2}U\cos(\Psi) \\
u_a &= W_a - U_\infty \\
u_t &= \Omega r - W_t
\end{aligned}
\tag{3.1}
$$

The bound circulation on the blade can be related to the circumferential averaged tangential velocity $\overline{u_t}$, using Equation 3.2 [79]. Equation 3.3 gives the relation between the averaged and tangential velocity at the blade. This is also where the tip loss factor is applied. No root loss factor is applied, since it is also absent in XROTOR. By combining Equations 3.2 and 3.3, an expression for the circulation is obtained, as shown in Equation 3.4.

$$\frac{1}{2}B\Gamma = 2\pi r\overline{u_t} \tag{3.2}$$

$$\overline{u_t} = u_t F\sqrt{1+\left(\frac{4W_a}{\pi B W_t}\right)^2} \tag{3.3}$$

$$\Gamma = u_t \frac{4\pi r}{B} F \sqrt{1 + \left(\frac{4W_a}{\pi B W_t}\right)^2} \tag{3.4}$$

From the calculated velocities in Equation 3.1, the velocity and angle of attack seen by the blade can be calculated. Furthermore, Mach number and Reynolds number can be determined. From a 2D airfoil analysis the lift and drag coefficient can be obtained. For this 2D analysis XFOIL[1] was used, a panel code with boundary layer formulation that allows for 2D subsonic viscous airfoil analysis. Using XFOIL, the propeller airfoils were analyzed for different Reynolds numbers. During the analysis the boundary layer was turbulent, by forcing transition at the leading edge. Furthermore, the analysis is performed at a Mach number of zero. More information on this analysis will be given in Section 3.1.3. The lift and drag coefficient obtained with XFOIL are a function of angle of attack and Reynolds number. Mach number is taken into account by applying the Prandtl-Glauert correction. With the lift known, a second expression for the circulation is found using the Kutta–Joukowski theorem, shown in Equation 3.5.

$$\Gamma = \frac{1}{2} W c C_l(\alpha, Re) \frac{1}{\sqrt{1 - M^2}} \tag{3.5}$$

With the two expressions for Γ from Equations 3.4 and 3.5, the residual $\Delta\Gamma$ can be determined. Equation 3.6 shows the iterative scheme used to reduce the residual to some small number. In this case a residual of 10^{-12} was used, which can typically be reached in a few iterations. It also assures that the influence of floating point error on the convergence is negligible, since for a 64 bits floating point number in Python, the machine epsilon is about 10^{-16}. Using the dummy variable Ψ, the iteration is usually quite stable, however sometimes Ψ could become very large in magnitude. The code detects these values and returns Ψ to an acceptable value based on interpolation between radial stations.

$$\Psi_{new} = \Psi_{old} - \frac{\Delta\Gamma}{d(\Delta\Gamma)/d\Psi} \tag{3.6}$$

3.1.2. Induced velocity calculation

In the BEM model it is assumed that the induced velocity u is perpendicular to the total velocity vector W. This is true if the propeller follows Goldstein's optimal circulation distribution [76]. To investigate this assumption a propeller with Goldstein's optimal circulation distribution is investigated using the BEM code to see if the assumption holds. In Figure 3.3 the circulation distribution can be seen for a propeller that closely follows Goldstein's optimal circulation distribution [53]. Here w is defined as the velocity of the screw surface. However, no good definition for this velocity could be found in the literature and no velocity value was found that was in the right order of magnitude, so here $w = 2$ m/s is used, as a scaling factor. This is acceptable, since it clearly shows that the shape of the circulation distribution matches.

The induced axial and tangential velocities can be found using the BEM code, which uses the assumption that induced velocity is perpendicular to the total velocity. The induced velocities can also be calculated using a slipstream tube model, which physically models the circulation of the propeller in the wake. The results of this comparison can be found in Figures 3.4 and 3.5. It can be seen that both axial and tangential velocity follow the results of the slipstream tube model closely. Near the root some differences can be found in mainly the tangential velocity, this could be because no root correction is applied in the BEM code. When looking at the axial velocity, there is some difference around the maximum, while there is no difference here for the tangential velocity. This is because in the BEM code the circulation is highly dependent on the tangential velocity, while the axial velocity plays a much smaller role. This can be seen in Equation 3.4, where circulation is directly related to u_t, while u_a has only an indirect influence through the ratio of W_a/W_t. Thus, for the solution to converge for circulation Γ, the tangential velocity needs to be estimated more accurately, while errors in axial velocity have less influence on the solution.

Next, a propeller with an arbitrary circulation distribution is presented, which does not follow Goldstein's circulation distribution. This is done to see how the assumption of u perpendicular to W holds

[1] `https://web.mit.edu/drela/Public/web/xfoil/`

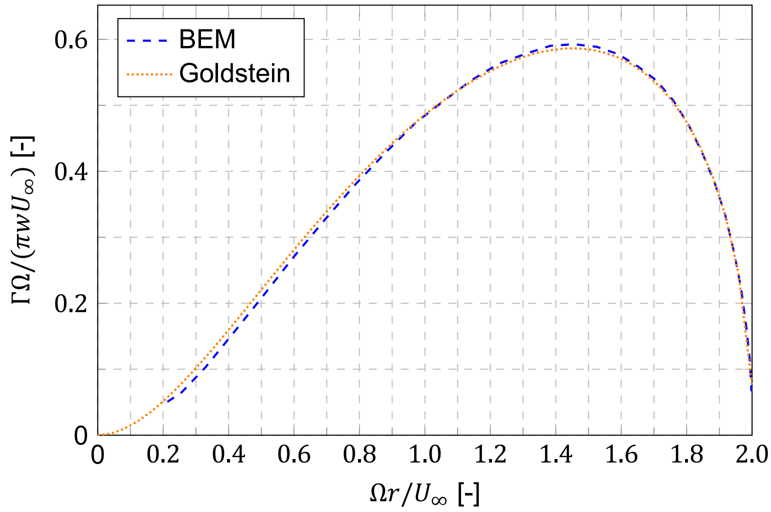

Figure 3.3: Goldstein's optimal circulation distribution

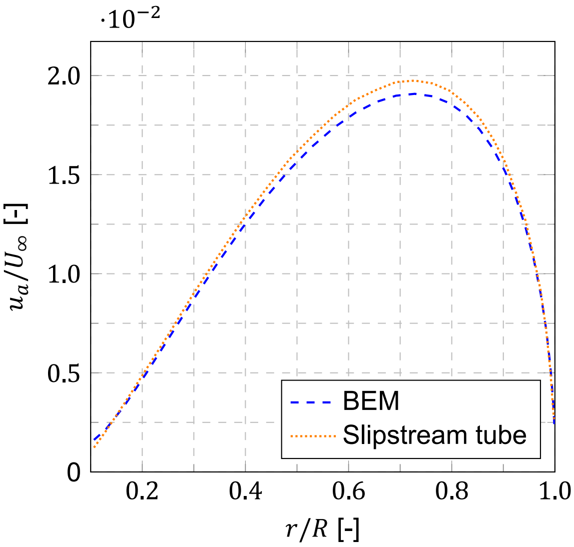

Figure 3.4: Comparison of the axial induced velocity by a propeller wake for a propeller with Goldstein's optimal circulation distribution

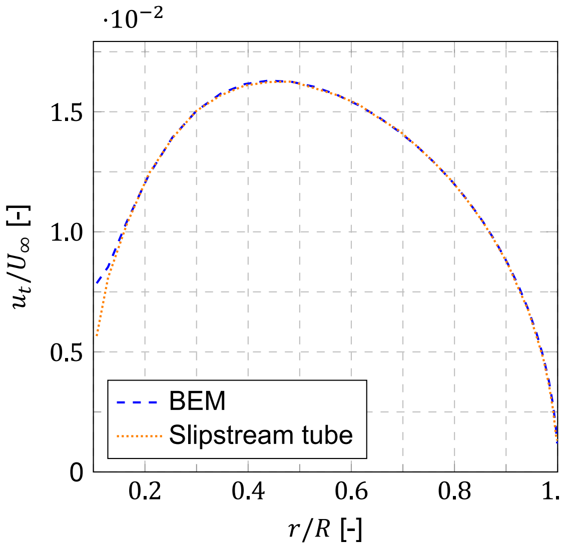

Figure 3.5: Comparison of the tangential induced velocity by a propeller wake for a propeller with Goldstein's optimal circulation distribution

up for an arbitrary propeller. The circulation distribution of the propeller blade is shown in Figure 3.6. Here again the value of w is used for scaling. It can be seen that the circulation distribution does not follow the Goldstein's distribution. Next, in Figures 3.7 and 3.8 the axial and tangential induced velocity distributions are presented. Here the results from the BEM code are compared to the induced velocities obtained using a slipstream tube model. It can be seen that the two tangential velocity distributions are very close, with only some deviation near the root. This is again due to the absence of a root correction, but it is expected to have minimal effect on the propeller performance.

When looking at the axial velocity distribution, it can be seen that the difference here is relatively large, especially around the maximum. This means that the assumption of perpendicular induced velocity to the total velocity does not hold anymore when the circulation distribution of the propeller deviates from Goldstein's optimal circulation distribution. However, the solution depends mainly on u_t as can be seen in Equation 3.4. Thus, the solution is relatively insensitive to errors in u_a. It is approximated that an error of 10% in u_a for all radial stations, leads to an error of around 2% for C_T and C_P. Furthermore, the differences in u_a are larger for higher loaded propellers and larger differences u_t are found for blades with higher loading near the blade root. Thus, it is concluded that the assumption of the induced velocity u being perpendicular to the total velocity vector W is still usable for propellers that do not follow Goldstein's optimal circulation distribution. This means that the BEM solver definition, as described in Section 3.1.1, can be used to model arbitrary propellers.

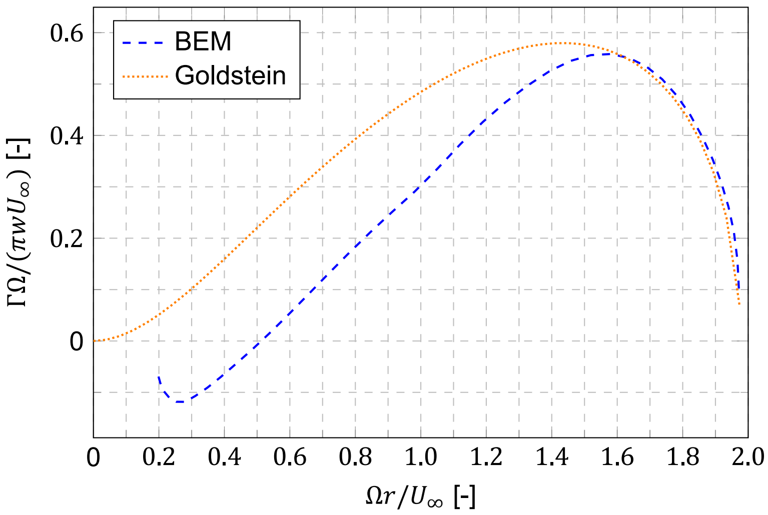

Figure 3.6: Comparison of the circulation distribution of an arbitrary propeller with Goldstein's optimal circulation distribution

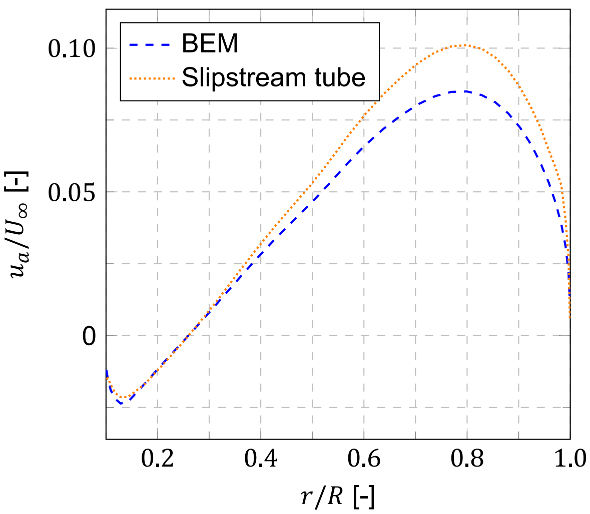

Figure 3.7: Comparison of the axial inducted velocity calculated with a BEM code and slipstream tube model for a propeller with the circulation distribution shown in Figure 3.6

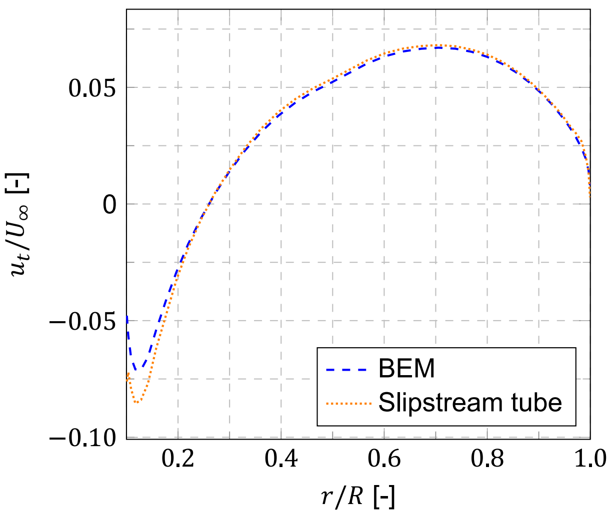

Figure 3.8: Comparison of the tangential inducted velocity calculated with a BEM code and slipstream tube model for a propeller with the circulation distribution shown in Figure 3.6

3.1.3. 2D airfoil analysis

The BEM model needs 2D airfoils polars to calculate the circulation and forces, as shown in Equation 3.5. These polars can come from any source, like CFD analysis, windtunnel experiments or a 2D panel method. Since the BEM model is already a lower order model, it makes sense to use a relatively inexpensive analysis for the airfoils. Thus, XFOIL was chosen to perform the 2D analysis.

XFOIL uses the e^N method [80] to predict the boundary layer transition. The point of transition influences the polar and thus the propeller performance. Transition is already hard to predict for the 2D case and transition models for 3D flow on a propeller blade are not well-established [81]. Experiments show that transition position is dependent on rotational speed [82] or even suggest that 2D effects still dominate the transition mechanism [83]. However, incorporating an advanced transition model is outside the scope of this research and a fixed transition point was chosen. The transition point was set as close to the leading edge as possible, so the whole airfoil would be subjected to turbulent flow. For this purpose $N_{crit} = 1$ and $x/c_{trip} = 0.05$ for the upper and lower surface were chosen. Finally, a Mach number of zero was chosen, since a Prandtl-Glauert correction is applied in the BEM solver, as shown before in Equation 3.5.

3.1.4. Comparison with XROTOR

The goal of the BEM code was to have a propeller analysis tool that would resemble the XROTOR code. The main difference is that the BEM code can directly read the airfoil polars, while XROTOR uses parameterized polars. These parameterized polars are described by nine variables, such as maximum lift coefficient and lift curve slope. Using these parameters, the lift and drag polars can be approximated at each radial station for a certain Reynolds number. Thus, in the case of XROTOR the Reynolds number must be assumed a priori, since the induced velocities on the radial stations are unknown. By running multiple analyses with XROTOR, the Reynolds number can be converged. Furthermore, XROTOR interpolates between different radial stations. So if the polar parameters are not smoothly distributed over the blade, XROTOR could find strange polars by interpolating between the stations. This could be fixed by defining a polynomial function along the blade for each parameter, which works as a smoothing function.

In Figure 3.9 and 3.10 a comparison can be seen for the polars at a radial station at $r/R = 0.3$ for the previously described ways to define the lift and drag polar. When the parameterized polar is used, it describes the lift in the linear region accurately, but it fails to describe the polar behaviour in the non-linear regions. When the smoothing function is applied, it introduces a shift in the lift curve. This makes sense, since in order to make the distribution of parameters along the blade smooth, the fit at a specific radial station will deviate from the best fit. When looking at the $C_l - C_d$ curve it can be seen that the parameterized model can not describe the shape properly, even without the smoothing applied. This is not a big problem, since the drag force is much lower in magnitude than the lift force.

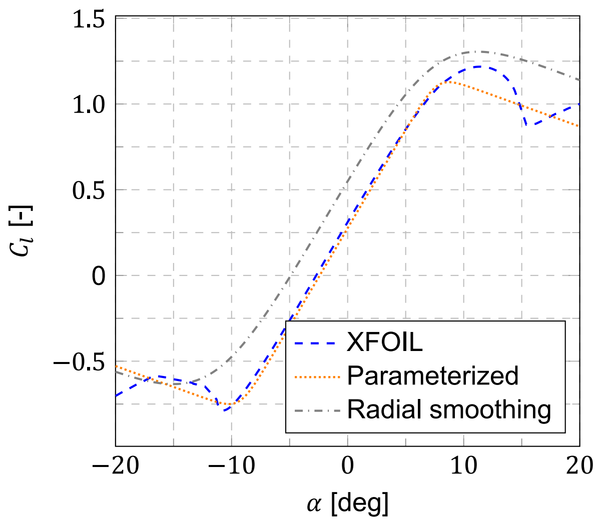

Figure 3.9: Comparison of lift polars for a propeller radial station at $r/R = 0.3$ for $Re = 82,500$

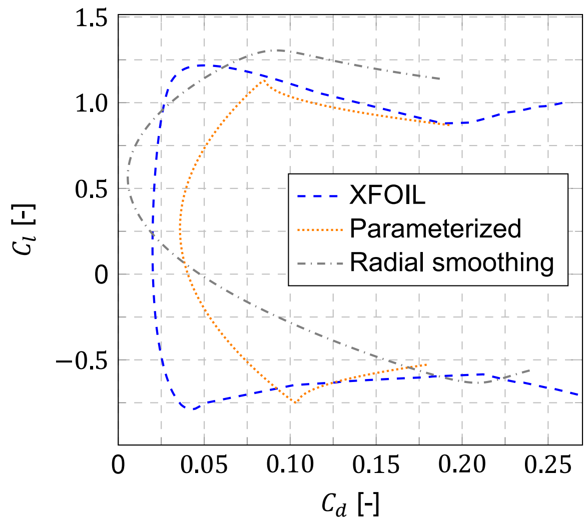

Figure 3.10: Comparison of drag polars for a propeller radial station at $r/R = 0.3$ for $Re = 82,500$

The difference in propeller performance for these different polar modelling methods can be found in Figures 3.11 and 3.12. At higher advance ratios the blades are largely operating in the linear regime of the lift polar, thus there is little difference here between the results of the BEM code and the XROTOR results without smoothing applied. The smoothing causes quite a shift in the lift polar, thus the results do not match here. At higher advance ratios larger parts of the blade will be operating in the non-linear regime of the lift polar. Large differences can be found between the results of the BEM code and XROTOR. Since the parameterized polar used by XROTOR does not capture the non-linear effects properly, it is expected that the BEM results should be better. However, it must be noted that predicting non-linear effects with low-order codes is very hard and the results should not be taken for granted.

Lastly, a comparison is made between the BEM formulation, the *graded momentum* (GRAD) for-

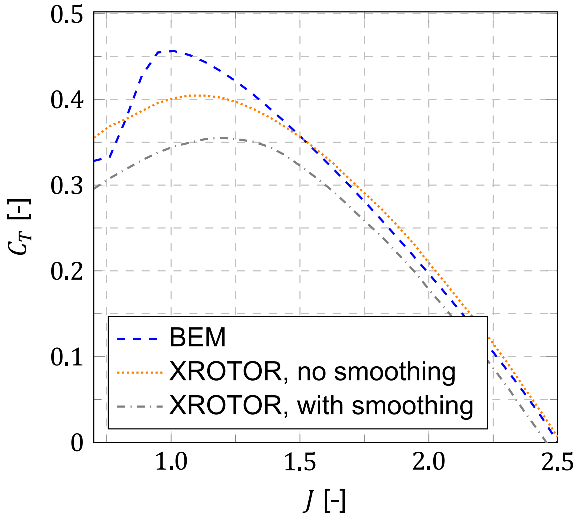

Figure 3.11: Comparison of propeller thrust for different ways of modelling the airfoil polars

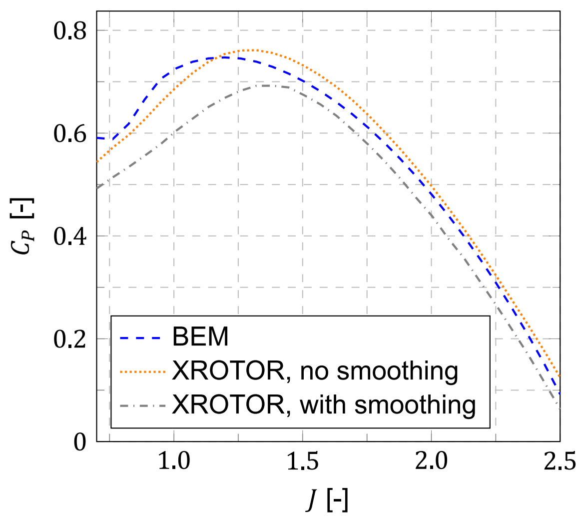

Figure 3.12: Comparison of propeller power for different ways of modelling the airfoil polars

mulation of XROTOR and the *potential* (POT) formulation of XROTOR. The BEM formulation must be similar to the GRAD formulation. The POT formulation calculates induced velocities using a fixed helicoidal wake model based using an extension of Goldstein's propeller solutions [53]. This more complex formulation should be more accurate than the GRAD formulation at higher advance ratios. Since the wake model used in the BEM code is based on the GRAD formulation, the results are compared to the POT formulation, to get a better understanding of the accuracy and limitations of the simpler wake model.

In Figures 3.13 and 3.14 the performance of the propeller for different formulations is shown. For fair comparison the BEM code now uses the same polars as XROTOR. It can be seen that there is little difference between the GRAD and POT formulation, even at high advance ratios. At low advance ratios there are some spikes in the results of the POT formulation. This is most likely due to bad solver convergence. It can also be seen that the results from the BEM code match the XROTOR results. Only at lower advance ratios there is some difference.

To investigate the differences at lower advance ratios, the radial distribution of circulation and blade angle of attack are plotted in Figures 3.15 and 3.16 for $J = 0.9$. Here again some spikes are found in the distribution from the POT formulation, again confirming that the differences are caused by bad solver convergence. When comparing the results of the BEM code and the GRAD formulation of XROTOR, it can be seen that the results are very close to each other. The small differences can be caused by some extra correction in the non-linear regime of the polars in XROTOR, however this has not been confirmed. Since the radial differences are so small, the difference in performance at lower advance ratios is accepted.

To conclude the comparison of the BEM code with XROTOR, the direct input of airfoil polars in the BEM code gives presumably more accurate results at low advance ratios, while avoiding the loss of accuracy when radial smoothing is applied. Furthermore, the *graded momentum* formulation of XROTOR is correctly implemented in the BEM code and there seems to be no significant difference with the *potential* formulation, making the BEM code suitable for the whole range of usable advance ratios.

3.2. Non-uniform inflow propeller analysis

To deal with an arbitrary non-uniform velocity inflow field for the propeller, the engineering method developed by Van Arnhem et al. [65] was used. This method was validated using CFD data. One of the validation cases was for a propeller under angle of attack, which closely resembles a propeller in the upwash in front of a wing. For this case the blade loading shows some phase lag, but the integral thrust and torque nearly coincide with the CFD data. However, for the in-plane forces larger differences were found, with the error increasing with increasing angle of attack. It is assumed however, that the

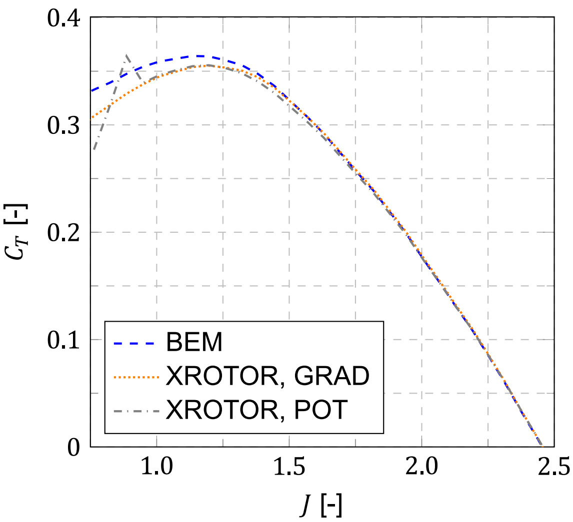

Figure 3.13: Comparison of propeller thrust for different BEM formulations

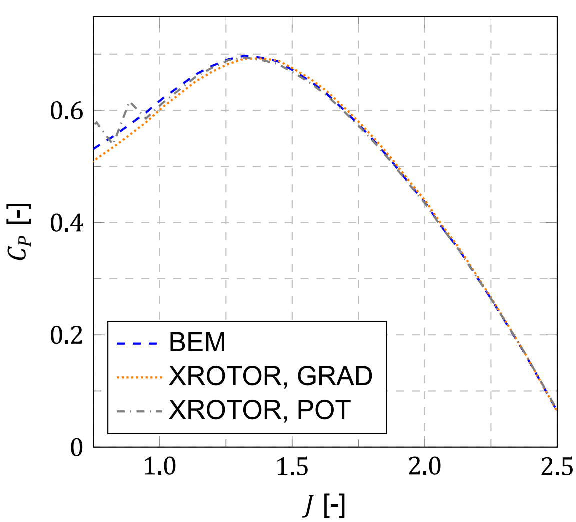

Figure 3.14: Comparison of propeller power for different BEM formulations

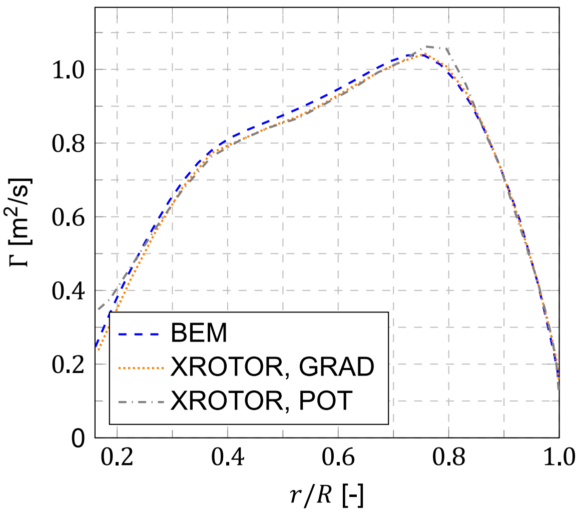

Figure 3.15: Comparison of blade circulation for different BEM formulations for $J = 0.9$

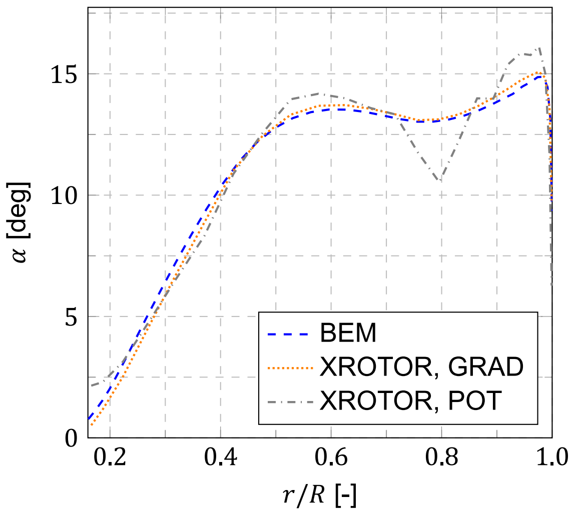

Figure 3.16: Comparison of local angle of attack for different BEM formulations for $J = 0.9$

contribution of the in-plane forces to the overall forces of the propeller-wing system is small, thus this error has only a minor influence.

The method starts out with a quasi-steady analysis. The freestream advance ratio J_∞ is assumed for the whole propeller. At a certain radial and azimuth position there is a velocity disturbance, which leads to a change in local advance ratio, denoted as ΔJ. At this position a local change in load must be calculated. This is done by assuming that $J_{eff} = J_\infty + \Delta J$ is applied to the full propeller. By comparing the loads at J_∞ and J_{eff}, a difference in loads can be found. This leads to local loading coefficients dC_T and dC_Q at some local point. This whole concept is shown in Figure 3.17; note that ΔJ in this figure is negative. By integrating the loads over the propeller disk, the performance for an arbitrary velocity inflow field can be obtained.

This analysis is applied twice. The local change in velocity disturbance with respect to the freestream can be resolved in an axial and tangential component. This leads to a ΔJ in axial and tangential direction. The corresponding changes in local loading can be found by using a so-called propeller performance map. These describe the loads on the propeller plane for changing axial or rotational velocity. In this case these performance maps are obtained using the BEM code. Finally, by superposition of the axial and tangential changes in load, the total change in load is obtained.

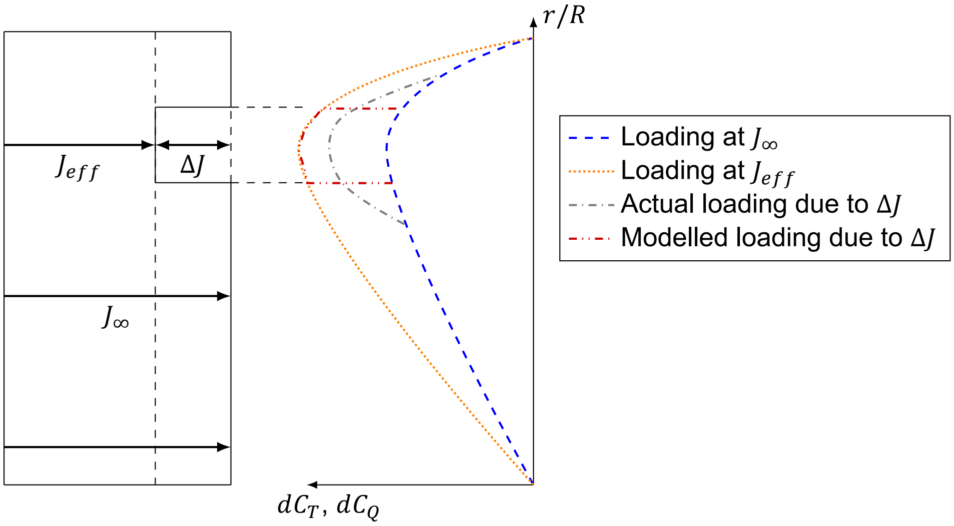

Figure 3.17: Schematic of the engineering method to analyse propellers in a non-uniform inflow [65]

However, unsteady effects also need to be taken into account. When an airfoil sees a change in inflow, the change in lift is not instantaneous due to the vorticity that will be shed into the wake due to a change in bound circulation. This leads to a change in phase and magnitude of the blade loads. The Sears function is applied to the quasi-steady results to obtain a solution that takes into account unsteady effects. For a more detailed description of this method the reader is referred to the corresponding paper by Van Arnhem et al. [65]. Furthermore, a verification case was provided with vertically varying axial and vertical perturbation velocities, as shown in Figures 3.18 and 3.19 respectively. No velocity perturbations in y direction were present. For this verification case the thrust and efficiency are compared in Figures 3.20 and 3.21 for the results found by Van Arnhem et al. and the Python code that will be used in the propeller model. These match almost perfectly, so this code is also verified.

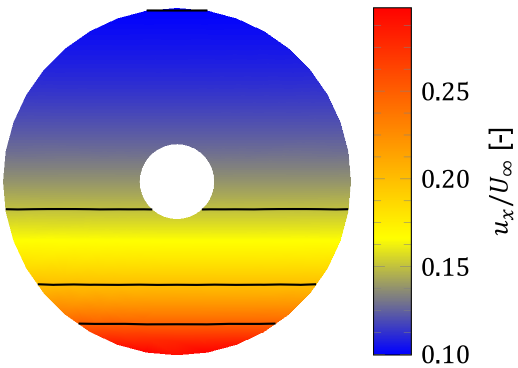

Figure 3.18: Axial velocity inflow perturbation used for verification [65]

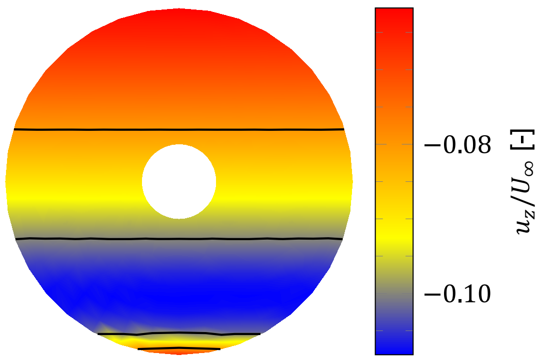

Figure 3.19: Vertical velocity inflow perturbation used for verification [65]

To calculate the influence of the propeller on the wing, the bound vorticity on the propeller disk must be known. To do this, the induced velocity of the wake on the propeller is needed, which is again a function of the bound circulation. Thus, to calculate the circulation it is assumed that the propeller induced velocity is given by the propeller at J_∞. With the induced velocities known, the local velocities at the propeller blade are known, so the advance angle can be calculated. Now the blade loads can be resolved into lift and drag, as shown in Equation 3.7. Furthermore, by summing the forces over the disk, in-plane forces are calculated if there is any force imbalance. Finally, the circulation is calculated by applying the Kutta–Joukowski theorem with the local velocity.

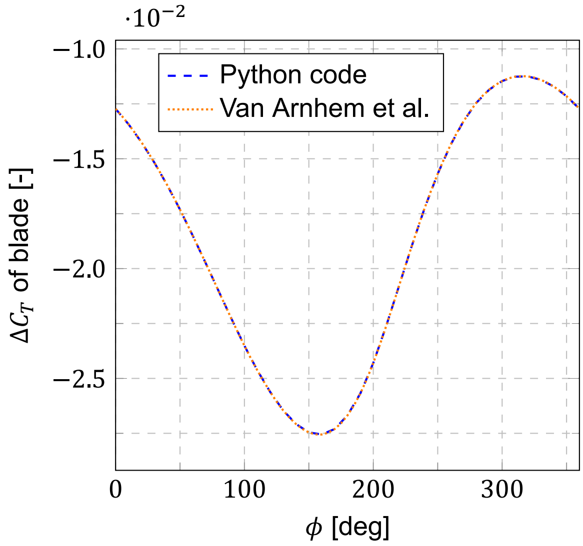

Figure 3.20: Comparison of the change in blade thrust for a propeller in non-uniform inflow

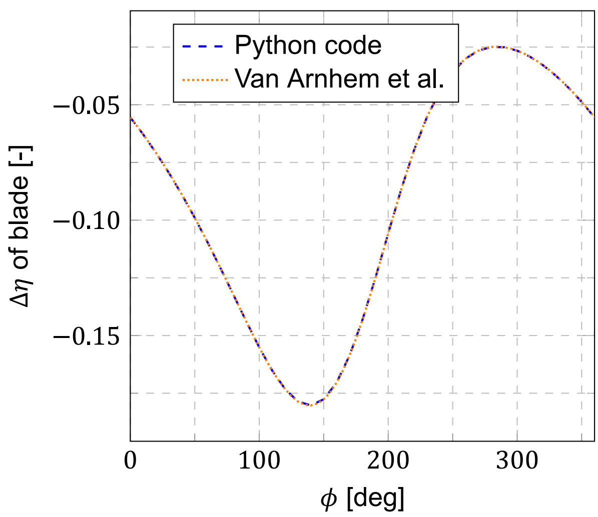

Figure 3.21: Comparison of the change in blade efficiency for a propeller in non-uniform inflow

$$
\begin{aligned}
dL &= dT\cos(\phi) + dQ\sin(\phi)\frac{1}{r} \\
dD &= -dT\sin(\phi) + dQ\cos(\phi)\frac{1}{r}
\end{aligned}
\tag{3.7}
$$

This method of calculating the propeller performance has some limitations. The most important one is the limited range of J in the data sets used. This is a problem when the propeller is under an angle of attack. In Figure 3.22, the ΔJ_t is plotted for a propeller under $5°$ angle of attack. It can be seen that near the hub the largest values are found. Due to the low radius, the original tangential velocity is low, thus any added tangential velocity causes a large ΔJ_t here. When the angle of attack is increased further, the ΔJ_t increases further, as shown in Figure 3.23. Very close to the hub, the ΔJ_t exceeds 1. At some point it will not be possible anymore to estimate the performance at such high or low advance ratios with the BEM code. Thus, if the ΔJ exceeds the range of available advance ratios, either the results for the minimum or maximum advance ratio are used. So here the estimated dL and dD are inconsistent with the ΔJ. However, it is expected that this only affects a small area of the propeller and thus has limited influence on the total propeller performance for a propeller in non-uniform inflow.

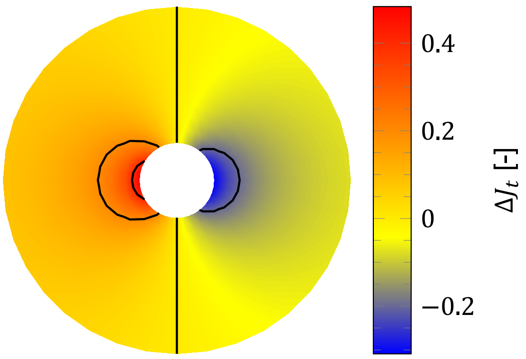

Figure 3.22: The change in tangential advance ratio for a propeller at $\alpha = 5°$

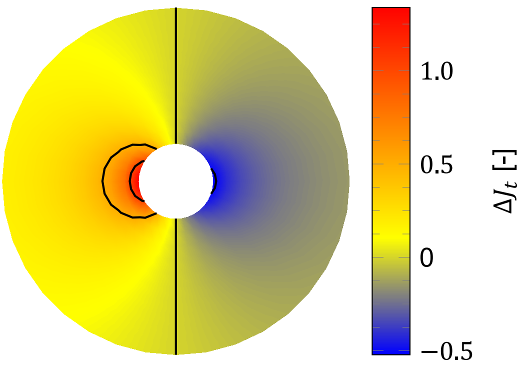

Figure 3.23: The change in tangential advance ratio for a propeller at $\alpha = 10°$

3.3. Propeller slipstream modelling

In this section a description of the slipstream model will be given. In Section 3.3.1 a general description of the slipstream tube model is given. This slipstream tube model is then enhanced by including an azimuthal circulation distribution (Section 3.3.2), slipstream contraction (Section 3.3.3) and slipstream deflection (Section 3.3.4). In Figure 3.24 it is shown how these enhancements are implemented. The slipstream tube is discretized with respect to x, r and ϕ and thus gives elements with dx, dr and $d\phi$. Each element has a corresponding vorticity γ. Furthermore, each element has some coordinates. There is a horizontal position x and vertical position z of the slipstream center. At the slipstream center a disk is placed, where the coordinates can be expressed with polar coordinates r and ϕ. This gives a total of four coordinates: x, r, ϕ and z for each element. The enhancements affect these properties of the discretized slipstream tube elements. The azimuthal circulation distribution changes the vorticity for x, r and ϕ. Contraction is based on conservation of mass and it changes the radius r which varies with the initial radius r_0 and x. It also can be seen that to apply this conservation of momentum, axial velocities are needed, which come from an intermediate model, namely Conway's model. Slipstream deflection changes the vertical position of the slipstream centerline, which varies with x. Finally, induced velocities are calculated by integrating over all the slipstream tube elements.

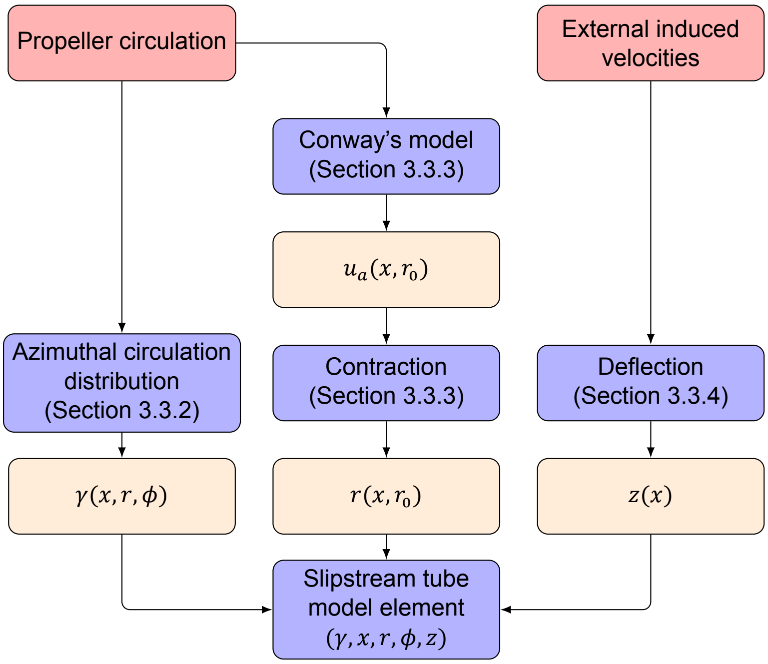

Figure 3.24: Flowchart for enhanced slipstream tube model

3.3.1. Slipstream tube model

For the propeller slipstream model a modified version of the slipstream tube model [12][28] was used. While in the original slipstream tube model the properties stay constant in axial and azimuth direction, for the modified model it was chosen to vary some parameters to better model the propeller slipstream and increase the fidelity of modelling of propeller-wing interaction. The radius changes in axial direction to model slipstream contraction, the slipstream centerline vertical position varies in axial direction to account for wake deflection and the circulation strength varies in azimuth direction to account for non-uniform inflow.

The traditional way of calculating the induced velocities with the slipstream tube model were given in Section 2.2.3 in Equations 2.17 and 2.18. For these equations the integral in x has been solved analytically. However, to vary parameters in axial direction, the full equations are needed. The form of these equations is shown in Equation 3.8. To calculate the induced velocity components at a point P, there are three sources of vorticity: the axial vorticity γ_a, tangential vorticity γ_t and the vorticity on the propeller disk γ_p. Functions f_a', f_t' and f_p are derived from the Biot-Savart law and describe the relation between this small part of the slipstream and point $P = [x_p, y_p, z_p]$. By multiplying these with the vorticity, the induced velocity is found and when this is integrated over the entire slipstream, the total induced velocity by the slipstream is found.

$$
\begin{aligned}
u_x(x,\phi,r) &= \int_{r_{hub}}^{R}\int_{0}^{2\pi}\int_{0}^{\infty}\gamma_t f'_{t,x}(P)dxd\phi dr + \int_{r_{hub}}^{R}\int_{0}^{2\pi}\gamma_p f_{p,x}(P)d\phi dr \\
u_y(x,\phi,r) &= \int_{r_{hub}}^{R}\int_{0}^{2\pi}\int_{0}^{\infty}\gamma_a f'_{a,y}(P)dxd\phi dr + \int_{r_{hub}}^{R}\int_{0}^{2\pi}\int_{0}^{\infty}\gamma_t f'_{t,y}(P)dxd\phi dr + \int_{r_{hub}}^{R}\int_{0}^{2\pi}\gamma_p f_{p,y}(P)d\phi dr \\
u_z(x,\phi,r) &= \int_{r_{hub}}^{R}\int_{0}^{2\pi}\int_{0}^{\infty}\gamma_a f'_{a,z}(P)dxd\phi dr + \int_{r_{hub}}^{R}\int_{0}^{2\pi}\int_{0}^{\infty}\gamma_t f'_{t,z}(P)dxd\phi dr + \int_{r_{hub}}^{R}\int_{0}^{2\pi}\gamma_p f_{p,z}(P)d\phi dr
\end{aligned}
\tag{3.8}
$$

The integrals in x with the form $\int_0^\infty \gamma f'(P)dx$ in Equation 3.8 are stepwise evaluated by using the exact integral solution $\gamma[f(P)]_x^{x+dx}$. The corresponding functions f can be found in Equation 3.9. The averaged circulation values of γ_a, γ_t and γ_p can be found in Section 2.2.3 in Equation 2.16. Subsequently, the integrals in ϕ and r are numerically evaluated using the rectangle rule. Thus, these integrals become a sum for elements with dx, dr and $d\phi$. By realizing this, properties can be varied for each element individually, this leads eventually to the enhanced slipstream tube model as shown in Figure 3.24. Note that the vertical position z, introduced by the slipstream deflection, is taken into account in the term c, similarly to z_p in Equation 3.9.

$$
\begin{aligned}
& & f_{t,x} &= \frac{r}{4\pi}\frac{(b\sin(\phi)-c\cos(\phi))(x-x_p)}{a\left((x-x_p)^2+a\right)^{1/2}} & f_{p,x} &= \frac{1}{4\pi}\frac{y_p\cos(\phi)+z_p\sin(\phi)}{\left({x_p}^2+a\right)^{3/2}} \\
f_{a,y} &= \frac{r}{4\pi}\frac{c(x-x_p)}{a\left((x-x_p)^2+a\right)^{1/2}} & f_{t,y} &= \frac{r}{4\pi}\frac{\sin(\phi)}{a\left((x-x_p)^2+a\right)^{1/2}} & f_{p,y} &= \frac{1}{4\pi}\frac{(-x_p\cos(\phi))}{\left({x_p}^2+a\right)^{3/2}} \\
f_{a,z} &= \frac{r}{4\pi}\frac{(-b)(x-x_p)}{a\left((x-x_p)^2+a\right)^{1/2}} & f_{t,z} &= \frac{r}{4\pi}\frac{(-\cos(\phi)}{a\left((x-x_p)^2+a\right)^{1/2}} & f_{p,z} &= \frac{1}{4\pi}\frac{(-x_p\sin(\phi))}{\left({x_p}^2+a\right)^{3/2}}
\end{aligned}
\tag{3.9}
$$

$$
\begin{aligned}
&\text{with}: \\
&\quad a = b^2 + c^2 \\
&\quad b = r\sin(\phi) - y_p \\
&\quad c = -r\cos(\phi) - z_p
\end{aligned}
$$

In order to verify the slipstream tube model, it is compared to the frozen wake model in Figures 3.25, 3.26 and 3.27. The frozen wake model consists of bound vorticity at the propeller plane and vorticity in the wake, which has a helicoidal shape, since the vorticity from the propeller is propagated downstream with the rotational speed and free stream velocity. By calculating the induced velocity over different time steps an average velocity is found. The frozen wake model is considered to model the propeller wake closer to reality, while the slipstream tube model gives a more simplified representation. However, calculating the induced velocity using the slipstream tube model is much faster, so it is preferred to use the slipstream tube model. This comparison will investigate if the frozen wake model can be replaced by a slipstream tube model and where discrepancies occur, if any.

In Figure 3.25 the axial induced velocity at $x = 0$ is shown. It can be seen that the frozen wake model shows a much higher axial velocity. This is caused by the influence of the bound vorticity on the propeller plane, which should be zero according to the slipstream tube model. The non-zero axial velocity from the vorticity on the propeller plane can be caused by numerical error. The distances at $x = 0$ are very small, thus small errors can cause large differences in induced velocity when using the Biot-Savart law. Also, small errors are introduced by having a finite timestep, so when the blade passes the evaluation point, it does so in an asymmetric manner, leaving a non-zero axial induced velocity when time-averaging. With an infinitesimal timestep this axial velocity will be zero. But, even without using the vorticity on the propeller plane, there is still some difference towards the tip between the frozen wake and slipstream tube model. This could be because towards the tip the vortex elements will be more and more curved, while near the root vortex elements will be more straight. It seems that the slipstream tube model does not capture this behaviour completely. Something similar can be seen for the tangential velocity in Figure 3.26. Furthermore, it can be seen that the difference in radial velocity

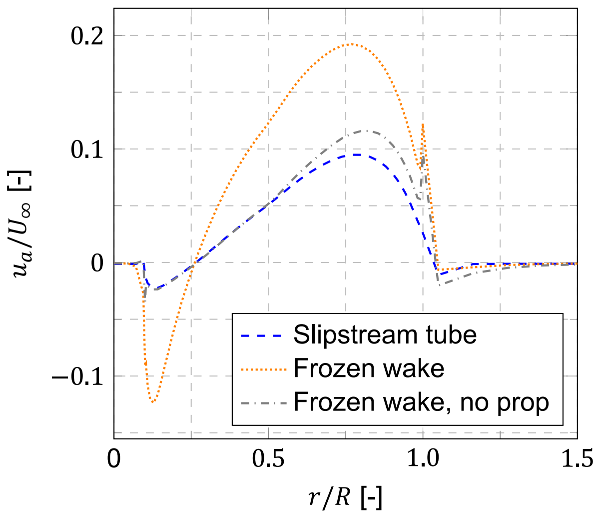

Figure 3.25: Comparison of axial induced velocity by the propeller slipstream at $x = 0$ for the slipstream and frozen wake model

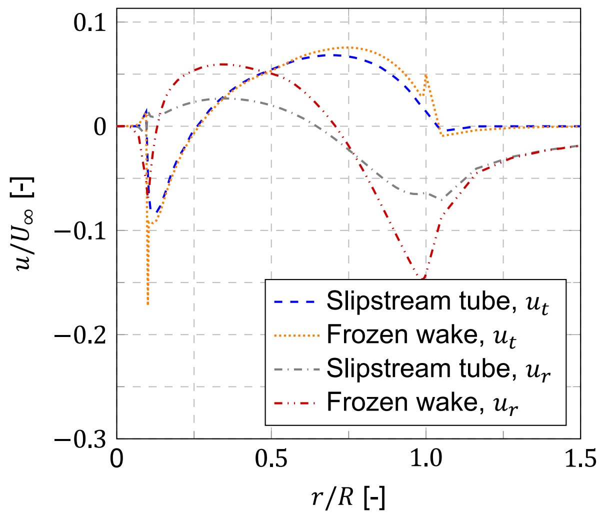

Figure 3.26: Comparison of tangential and radial induced velocity by the propeller slipstream at $x = 0$ for the slipstream and frozen wake model

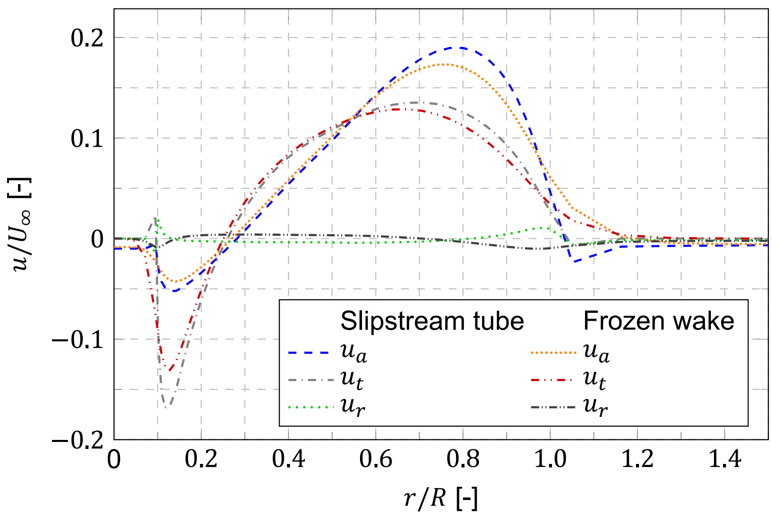

Figure 3.27: Comparison of the induced velocities by the propeller slipstream at $x = 2.5R$ for the slipstream and frozen wake model

is quite large. The cause of this is unknown, but the effect of this error is small, since the propeller will be more or less aligned with the wing in vertical direction. This means that the radial velocity will mainly act along the span of the wing, not causing any change in angle of attack or dynamic pressure. Thus, this difference is deemed acceptable.

In Figure 3.27 the induced velocities at $x = 2.5R$ can be found. The results at this distance from the propeller disk can be regarded as results for far downstream. Thus, it is expected that the axial and tangential velocities are doubled compared to $x = 0$. This seems to be the case for the slipstream tube model, while the frozen wake model underestimates the velocity increase a little. Furthermore, radial velocity is almost zero for both models, which is expected. Again, the largest differences are found towards the tip of the propeller. These differences are not too large ($\sim 2\%$ of U_∞), thus the slipstream tube model is an acceptable model to calculate propeller induced velocities.

3.3.2. Azimuthal circulation distribution

From the non-uniform inflow propeller analysis, an azimuthal distribution of circulation is obtained. This azimuthal distribution can be propagated downstream, but rotation must be taken into account. Using the rotation speed and freestream velocity, at each x-coordinate the angle of rotation is determined by $x_i\omega/U_\infty$, as shown in Figure 3.28. Here the freestream velocity U_∞ is chosen, rather than U_∞ plus the axial wake velocity, to give the same rotation to all radial stations. Also, ω was used, without taking into account the tangential velocity. With the tangential velocity included, the rotational velocity is increased. This gives a different azimuthal position for a certain x-coordinate. However, for the relatively short distance from propeller to wing, it is believed that not including tangential velocity has negligible effect on the azimuthal position and thus the velocities induced by the slipstream tube model.

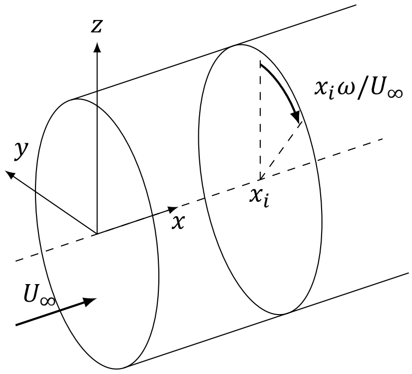

Figure 3.28: Propagation of the azimuthal circulation downstream

In Figures 3.29 and 3.30 the axial and tangential velocity are compared for a slipstream with an azimuthally uniform circulation distribution and one with an azimuthal non-uniform circulation distribution. The azimuthal non-uniform distribution is given by the uniform circulation distribution, with the circulation on one side reduced with 10%, which is representative for a propeller under an angle of attack. It can be seen that the development of both the axial and tangential velocity changes due to the azimuthal circulation distribution. Furthermore, the shape of the velocity development seems similar when comparing the slipstream tube model and frozen wake model. However, there seems to be a shift in x direction between the two models, where the frozen wake model predicts increases at lower x values than the slipstream tube model. It is thought that this is due to the absence of a helicoidal shape in the slipstream tube model. While the frozen wake uses continuous helicoidal trailing vortices, the slipstream tube model can only model this using discrete steps. It is suspected that this limitation becomes more visible when an azimuthal circulation distribution is applied, while it is less noticeable for an azimuthally uniform circulation distribution.

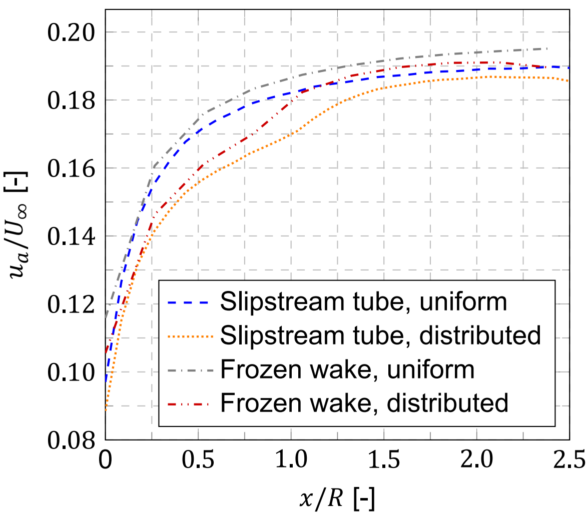

Figure 3.29: The effect of azimuthal circulation distribution on the axial induced velocity at radial station $r/R = 0.83$

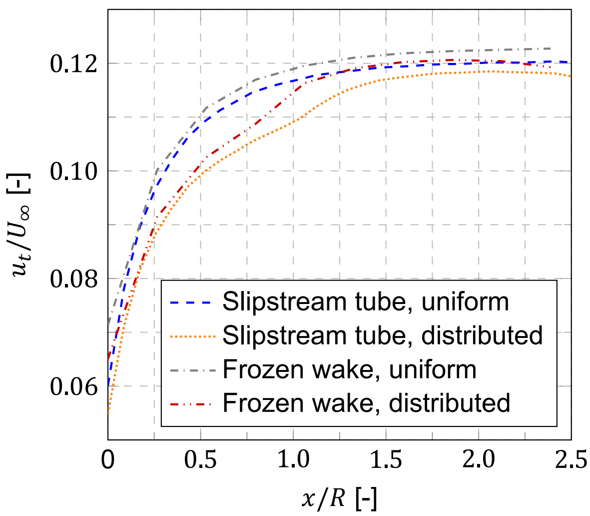

Figure 3.30: The effect of azimuthal circulation distribution on the tangential induced velocity at radial station $r/R = 0.83$

3.3.3. Slipstream contraction

The slipstream contraction is calculated by applying the conservation of mass to the slipstream. By assuming constant density Equation 3.10 is obtained, where r_0 and $u_{a,0}$ are evaluated at the propeller plane at $x = 0$. Now the induced axial velocities need to be calculated, which can be done using a slipstream tube model.

$$\frac{r}{r_0} = \sqrt{\frac{U_\infty + u_{a,0}}{U_\infty + u_a}} \tag{3.10}$$

However, to evaluate the axial velocity at all the positions in the wake is computationally expensive. Thus, the analytical solution by Conway [57] is used. By using superposition of analytical solutions, an analytical expression for the induced velocities can be found for an arbitrary radial distribution. In Equation 3.11 it can be seen that the axial velocity at the propeller disk needs to be represented using a number of even polynomial functions. By using a least squares method, the coefficients $U_{a0,\mu}$ are found for an arbitrary axial velocity distribution for a propeller. In Figure 3.31 it can be seen that by using eight polynomials, the shape of the axial velocity distribution can be approximated. By increasing the number of polynomials, the distribution can be better approximated, but high exponents can lead to large numerical error, or even overflow, when calculating induced velocity.

$$U_a(r,0) = \sum_{\mu=1}^{N} U_{a0,\mu} \left(1 - (r/R)^2\right)^{\mu} \tag{3.11}$$

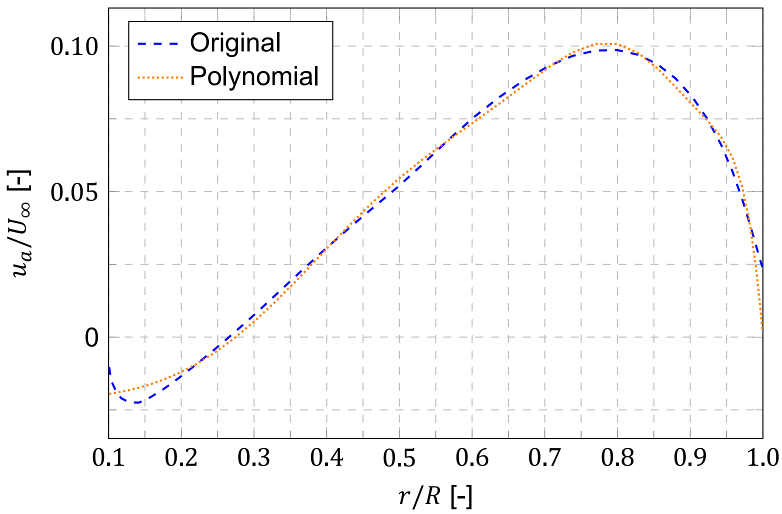

Figure 3.31: The representation of a axial velocity distribution at $x = 0$ by even polynomials

In Figure 3.32 a comparison can be seen between the axial induced velocity calculated with the slipstream tube model and with Conway's model by using superposition of the solution of eight even polynomials. It can be seen that the results match, except for the part near the propeller plane at $x = 0$. Around $x = 0$ a jump can be seen, which is due to the bound vorticity in the slipstream tube model. Conway's solution only calculates the induced velocity of the propeller wake, without the bound vorticity on the propeller blade. When the bound vorticity is discarded in the slipstream tube model, it can be seen that the results also match near the propeller plane.

With the axial velocity calculated by Conway's model, Equation 3.10 can be applied. The axial velocity behaves differently for different radial stations, so the contraction will be different for different radial stations. This is shown in Figure 3.33. It can be seen that near the root, there is some backflow, so here there is actually slipstream expansion. Furthermore, towards the tip there is more contraction. The contraction found by using the axial velocity obtained from Conway's model can be compared to the contraction found by Veldhuis [28]. Here a solution is found by applying the conservation of mass to a uniform actuator disk and by writing a potential function for the slipstream. This solution is shown

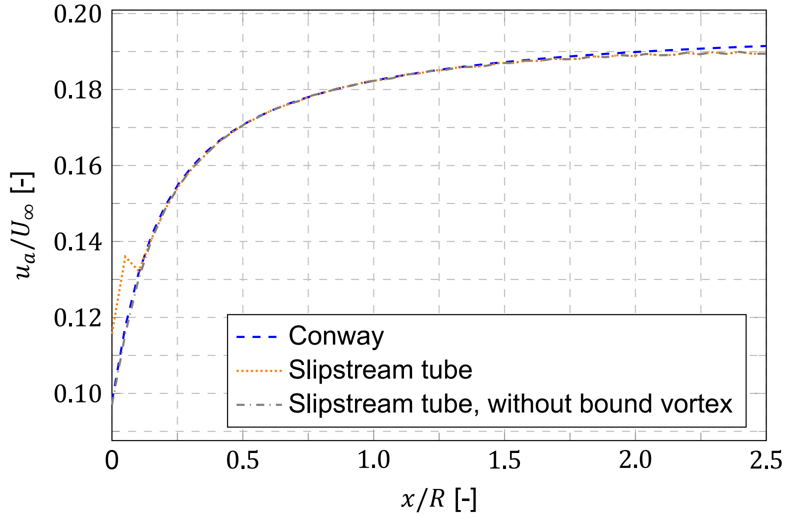

Figure 3.32: Comparison of the axial velocity calculated by the slipstream tube model and Conway's exact solution at $r/R = 0.83$

in Equation 3.12. The 'mean' contraction calculated with Conway's model seems to follow Veldhuis' solution, they have the same shape and magnitude. Thus, this way of calculating contraction seems to be usable to calculate the contraction for different radial stations.

$$\begin{aligned} \frac{R}{R_0} &= \sqrt{\frac{1+a}{1+a\left(1+\frac{x}{\sqrt{R^2+x^2}}\right)}} \\ \text{with :} & \\ a &= \frac{1}{2}\left(-1+\sqrt{1+\frac{2}{\pi}\frac{T}{\rho U_\infty^2 R^2}}\right) \end{aligned} \tag{3.12}$$

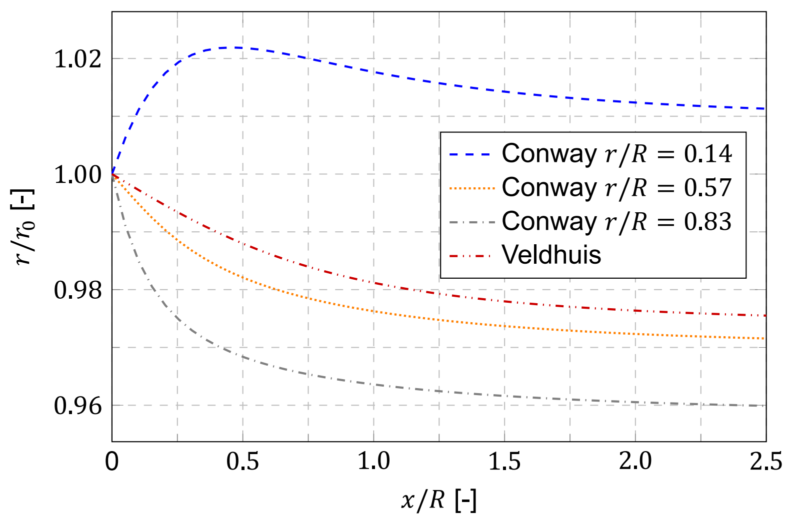

Figure 3.33: Comparison of the slipstream contraction for different radial stations compared to the contraction calculated using the method of Veldhuis [28]

In Figures 3.34 and 3.35 the axial and tangential slipstream induced velocities are shown at $r/R = 0.83$ for a slipstream with and without contraction. The results are compared to a frozen wake model with the same slipstream contraction. It can be seen that at this specific radial station the contraction decreases both the axial and tangential velocities slightly. Although there is an offset between the results of the slipstream tube and of the frozen wake model, the amount of change due to contraction is about the same for both models. This gives confidence that the effects of contraction are well modelled by the slipstream tube model.

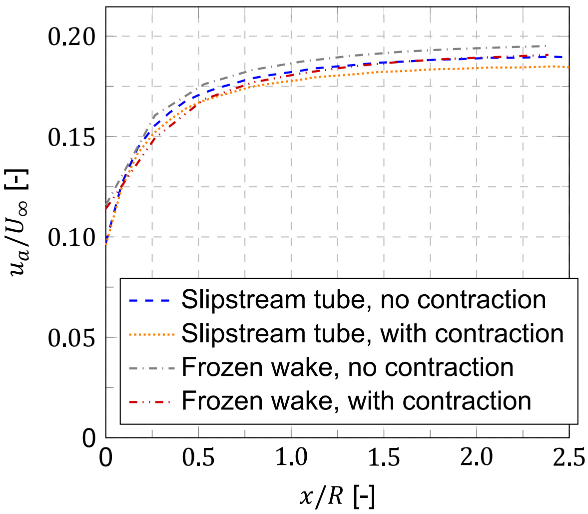

Figure 3.34: The effect of slipstream contraction on the axial induced velocity at radial station $r/R = 0.83$

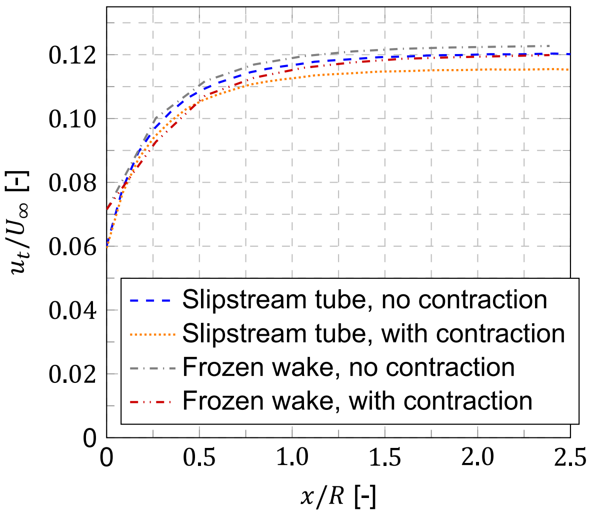

Figure 3.35: The effect of slipstream contraction on the tangential induced velocity at radial station $r/R = 0.83$

Lastly, the propeller will have a circulation distribution in both radial and azimuthal direction. However, Conway's model is only equipped to deal with radial distributions. To assess the effect of an azimuthal distribution of circulation, the propeller inflow is placed at an angle of attack of five degrees from the propeller centerline, while the propeller slipstream geometry remains fixed. This non-axial inflow causes a maximum difference in circulation in azimuthal direction of 33% (for the same radial station). The influence of this azimuthal circulation distribution on the induced axial velocity can be assessed with the slipstream tube model, as shown in Figure 3.36. The induced velocities are compared to a model where there is only radial distribution of circulation, by averaging azimuthally. Here it can be seen that near the root there are differences of about $0.01r/r_0$. The same kind of differences are found at the blade tip, although not shown here. However, since the circulation at these positions is usually low, the impact will be low. At the other radial stations the difference is practically negligible.

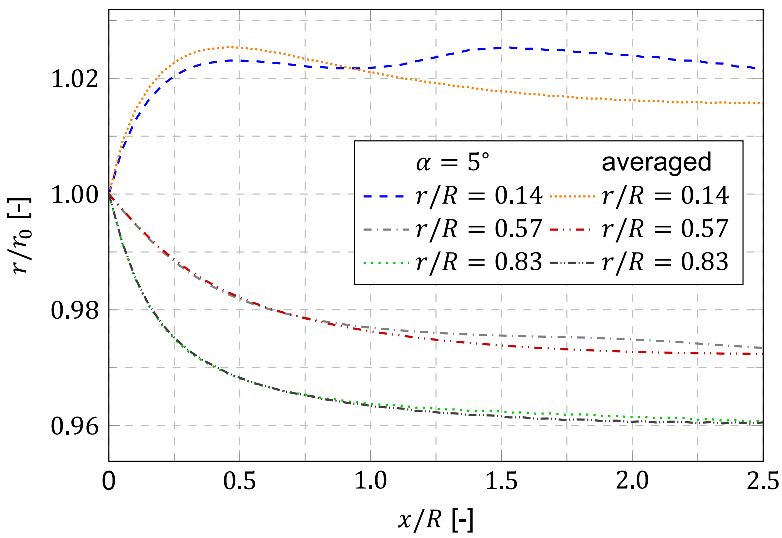

Figure 3.36: Comparison of the slipstream contraction for a propeller with an azimuthal circulation distribution with $\alpha = 5°$ and a propeller with the same circulation, but azimuthally averaged

To conclude, the slipstream contraction is being modelled by applying conservation of mass. To do this, axial velocities are needed throughout the propeller slipstream. These axial velocities are calculated using a superposition of analytical solutions for even polynomials. Using eight even polynomials the axial velocity distribution at the propeller plane can be approximated. When comparing this to the slipstream tube model, differences are negligible, except close to the propeller plane. Here bound vorticity is not modelled by Conway's solution, so the contribution of this axial velocity is not taken into account when calculating the contraction. Furthermore, even when the propeller has azimuthal variations in circulation, the contraction can be calculated by averaging azimuthally for each radial station. This will not lead to major differences in contraction, except at the root and tip, but the influence of this is very small.

3.3.4. Slipstream deflection

Slipstream deflection is expected to occur due to vertical external induced velocities $u_{z,i}$. By calculating the angle between U_∞ and $u_{z,i}$ a deflection Δz can be found over a horizontal distance Δx. This is shown in Figure 3.37. It was chosen to use U_∞ to calculate the deflection angle, instead of U_∞ plus the axial velocity in the propeller wake. This choice was made because the axial velocity is different for different radial stations. This would lead to different deflection angles for different radial stations. By using U_∞ there is a single deflection angle at each x-coordinate. This way the geometry does not become too complex. Since the velocity in x direction is underestimated using U_∞ instead of $U_\infty + u_{x,i}$, the deflection angle is overestimated. The effect of this is expected to be small for the relatively small distances from propeller to wing. Furthermore, a larger deflection for the part beyond the wing does not have a significant impact on the induced velocities on the wing, as the influence of vorticity decreases with increasing distance, according to the Biot-Savart law.

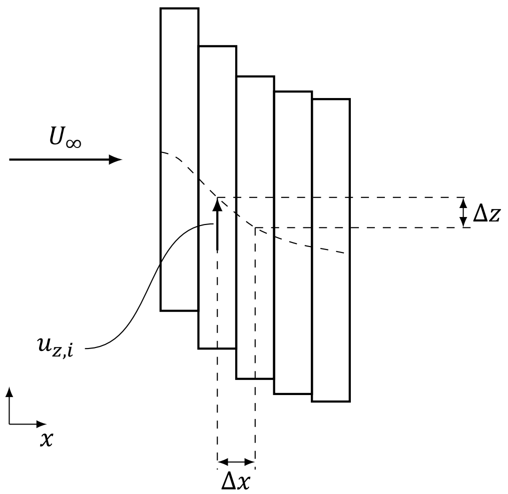

Figure 3.37: Schematic of the calculation of the slipstream deflection

In Figures 3.38 and 3.39 the axial and tangential velocities for a straight and deflected wake can be seen. These velocities are calculated at $r/R = 0.83$. The results are compared to a frozen wake model with the same deflection. It can be seen that the deflected wake produces slightly higher axial and tangential velocities when using the slipstream tube model. However, when deflection is applied to the frozen wake model, oscillations are observed. This is because at different x positions, the trailing vortex lines are just slightly differently oriented with respect to the evaluation point, leading to numerical errors. However, when looking at the average of this oscillation, still an increase in both axial and tangential velocity is observed when using the frozen wake model, giving confidence that the deflection is well represented using the slipstream tube model.

3.3.5. Slipstream numerical interpolation

The slipstream tube model is a numerically discretized model based on vorticity. Furthermore, the induced velocities are calculated by applying the Biot-Savart law. According to the Biot-Savart law, the induced velocity is inversely proportional to the circulation value. So in this dicretized model, the

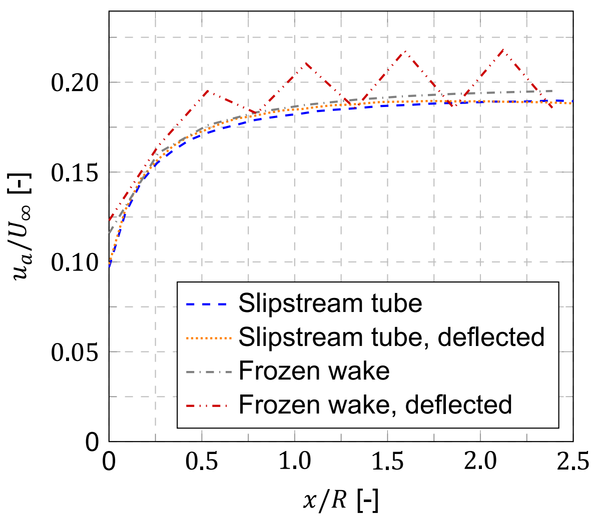

Figure 3.38: The effect of slipstream deflection on the axial induced velocity at radial station $r/R = 0.83$

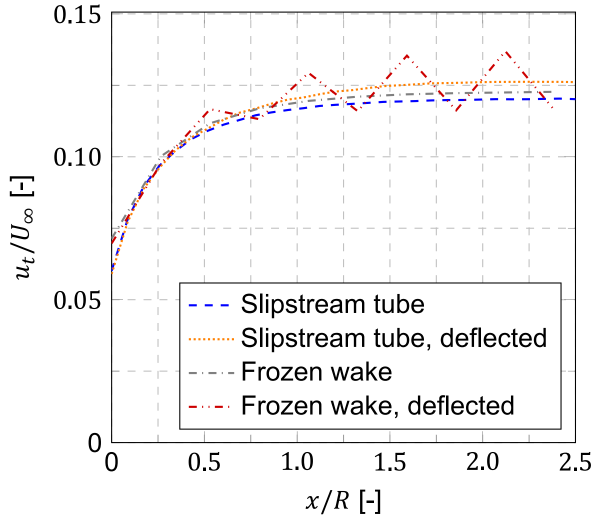

Figure 3.39: The effect of slipstream deflection on the tangential induced velocity at radial station $r/R = 0.83$

induced velocity will go to infinity when approaching one of the vortices, leading to unreliable results. To get reliable results from the slipstream tube model, the induced velocity could only be calculated on control points. These control points are located in the middle of the points where the vorticity is located. By interpolation the induced velocity can be estimated also on points in between these control points. This is shown in Figure 3.40. Here the induced axial velocity is shown for different azimuth positions. The black vertical lines indicate the azimuthal positions of the points where the vorticity is located. It can be seen that large peaks in induced velocity are found without the interpolation scheme and that these peaks are caused by the proximity to a vortex. When the interpolation scheme is applied no peaks are visible and the induced velocity is a smooth line, as expected.

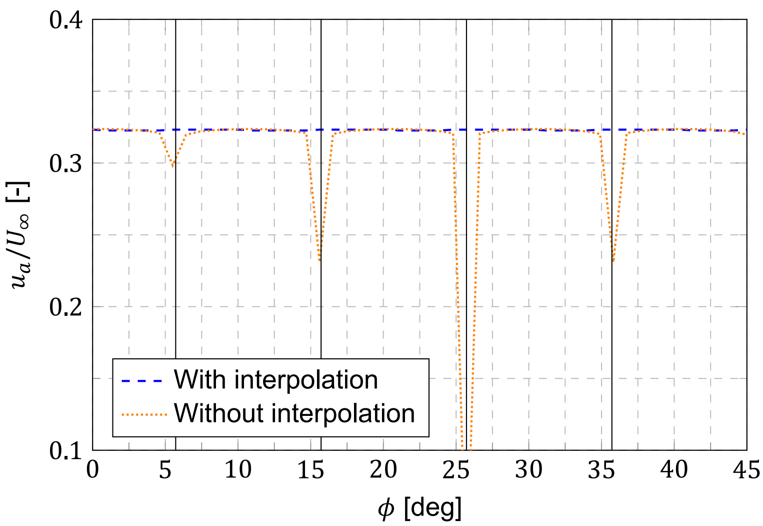

Figure 3.40: The reduction of numerical error by means of grid interpolation for the slipstream tube induced velocity calculation

4 Wing model

This chapter describes the numerical wing model used. The model is largely based on a VLM model, which was chosen based on a comparison of different potential flow models by Epema [71], as it provided a more prediction accurate of the spanwise lift distribution compared to a lifting line code, without the increased complexity of a panel method. Furthermore, a VLM code has been previously used by Koomen [84] to investigate the effect of tip-mounted propellers. Figure 4.1 shows a flowchart for the model. It takes as input the wing geometry, wing airfoil polars and external induced velocities. The external induced velocities will be due to the propeller. The output will be the wing performance and wing induced velocities. The wing induced velocities will be an input again for the propeller model. The VLM solver is discussed in Section 4.1. This is followed by the Trefftz plane analysis in Section 4.2. Since the wing will be dealing with a propeller slipstream, a jet correction is needed, which will be discussed in Section 4.3. While the VLM model is based on inviscid flow, viscous corrections are added, as described in Section 4.4. The correction for viscosity is seen in two places in the model: as a correction for lift and as a correction for drag.

4.1. VLM formulation

In order to take into account the influence of a propeller on the wing, the VLM formulation is changed from the standard formulation to include external induced velocities. These velocities, u_x and u_z, in this case are defined in the wing axis system, where x is in chordwise direction, y in spanwise and z is the height.

In the VLM code the wing is modelled by a number of panels, both chordwise and spanwise distributed. The panels are placed in a flat plane at $z = 0$, so they follow the 2D planform shape. This is also applicable for cambered airfoils, as the camber is taken into account by the boundary conditions by means of the camberline slope [85]. The implementation of this will be discussed later on. Each panel has an associated horseshoe vortex, with the bound vortex on the quarter-chord line of the panel (following the local sweep). Furthermore, each panel has a control point, located on the centerline of the panel at 3/4-chord. Horseshoe vortices extend from the bound vortex and go to infinity, also on the same 2D plane as the wing. This geometry is shown in Figure 4.2. With all the vortices and geometry located in one plane, the calculations are greatly simplified. However, it introduces slight errors when calculating the induced velocities at the control points when the angle of attack is high and when cambered airfoils are used [45]. Also the assumption of a straight wake, leads to a wake that is not completely force free. This, however, does not affect the far-field analysis done on the wake, as the wake is still drag free, since only forces in a direction perpendicular to the vortices can be generated [86].

The velocity perpendicular to the wing surface must be zero on every panel. In Equation 4.1 the expression for the normal velocity at panel i is given. Small angles are assumed for the angle of attack α and the airfoil camberline slope $\frac{\partial g}{\partial x}$. The normal velocity has a contribution from the freestream velocity U_∞, the external induced velocities in x and z direction u_x and u_z. Finally, the wing induced velocities of all the horseshoe vortices are present in the last term, where the strengths of the vortices Γ_j are unknown. Using the Biot-Savart law, the influence of horseshoe vortex j can be determined for control

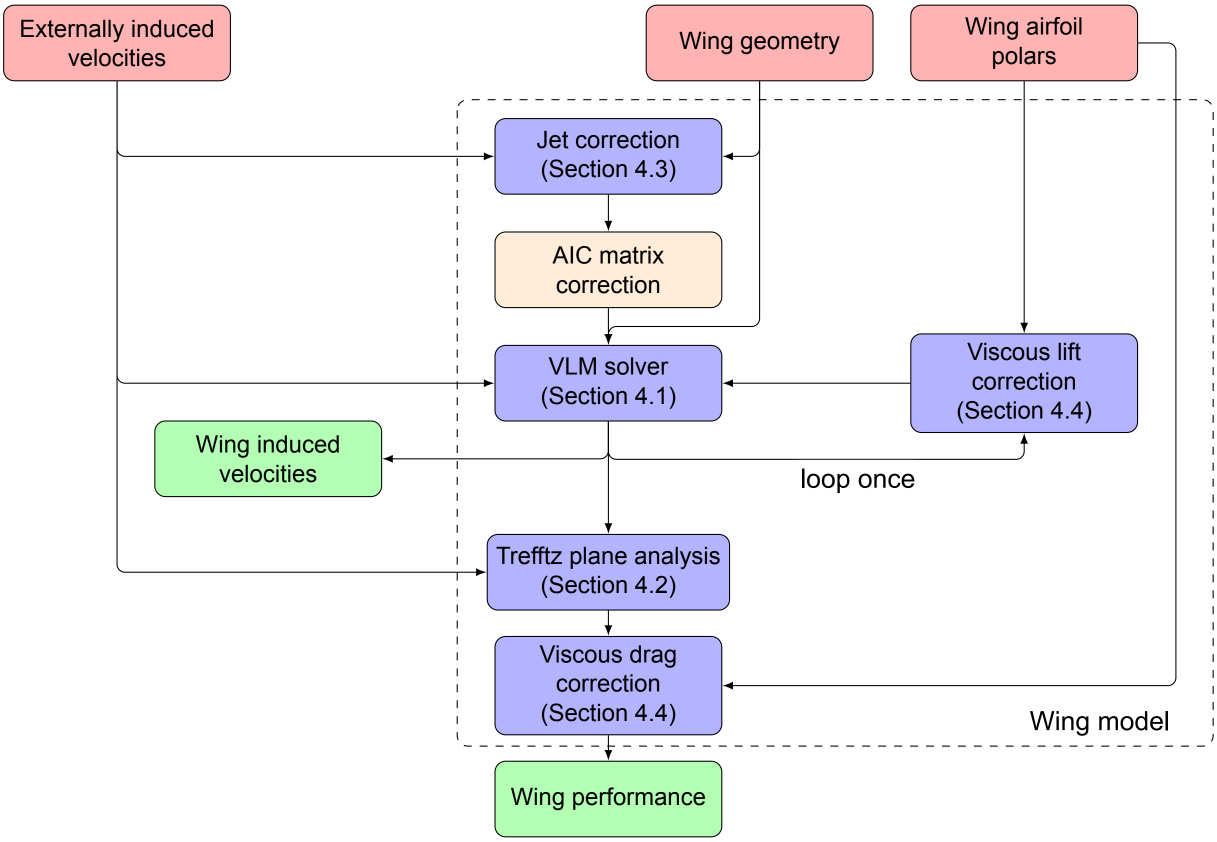

Figure 4.1: Flowchart for the numerical wing model

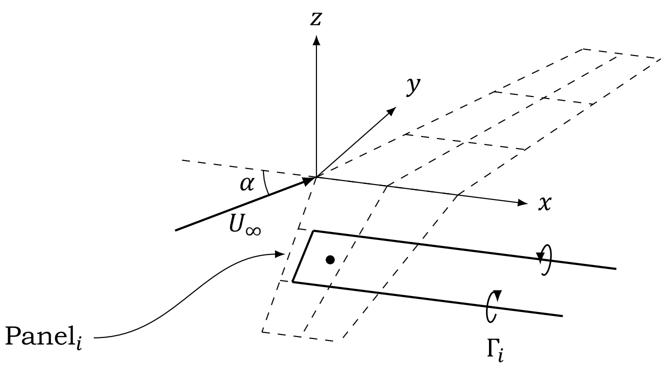

Figure 4.2: Schematic of the VLM formulation

point i. This gives $C_{j,i}\Gamma_j$ as induced velocity. By putting the coefficients C in an Aerodynamic Influence Coefficient matrix ($\overline{\overline{AIC}}$), a system can be set up, which can be solved for the circulation strength vector $\overline{\Gamma}$. This is shown in Equation 4.2, where $\overline{U_n}$ consists of the first three terms presented in Equation 4.1.

$$U_{n,i} = U_\infty\left(\frac{\partial g}{\partial x} - \alpha\right) + u_x\frac{\partial g}{\partial x} - u_z - \sum_j C_{j,i}\Gamma_j \tag{4.1}$$

$$\overline{\overline{AIC}} \times \overline{\Gamma} = \overline{U_n} \tag{4.2}$$

With the circulation known, the lift can be calculated using the Kutta–Joukowski theorem. In order to calculate the final velocity vector, a value is needed for the wing induced velocity. Here the induced velocity is calculated in the Trefftz plane, where the induced velocity can be calculated using infinite trailing vortices [45]. The final velocity vector is given by Equation 4.3, where u_i is the wing induced velocity. The lift must be perpendicular to the freestream velocity, which gives Equation 4.4 to calculate the lift. By integrating the lift on all the panels, the total lift can be obtained. Note that without the external induced velocities and by neglecting the contribution of u_i, the expression for lift simplifies to the standard formulation $dL = \rho\Gamma U_\infty dy$.

$$\overline{U} = \begin{bmatrix} U_x \\ U_z \end{bmatrix} = \begin{bmatrix} U_\infty \cos(\alpha) \\ U_\infty \sin(\alpha) \end{bmatrix} + \begin{bmatrix} u_x \\ u_z \end{bmatrix} + \begin{bmatrix} 0 \\ u_i \end{bmatrix} \tag{4.3}$$

$$dL = \rho\Gamma \left(U_x \cos(\alpha) + U_z \sin(\alpha)\right) dy \tag{4.4}$$

VLM verification

To check the validity of the VLM formulation, verification is done using two different wing planforms. The first planform used for verification is an elliptical wing. For an elliptical wing there exists an exact solution for the circulation and induced velocity [1]. These are given in Equations 4.5 and 4.6 respectively. In these equations Γ_0 is the circulation at the center of the wing. Furthermore, the induced velocity has a constant value along the wingspan. In Figures 4.3 and 4.4 it can be seen that the results of the VLM code are in accordance with the exact solution. The induced velocity calculated by the VLM code differs from the exact solution only near the wingtips. This is probably caused by the finite number of vortices used in the VLM code, which leads to a less accurate prediction of the induced velocity towards the tip. Furthermore, rounding error might also play a role at the tip. The induced drag is calculated at the wing quarter chord, but the chord goes to zero at the tip. This makes the calculation prone to rounding errors.

$$\Gamma(y) = \Gamma_0 \sqrt{1 - \left(\frac{2y}{b}\right)^2} \tag{4.5}$$

$$u_i = -\frac{\Gamma_0}{2b} \tag{4.6}$$

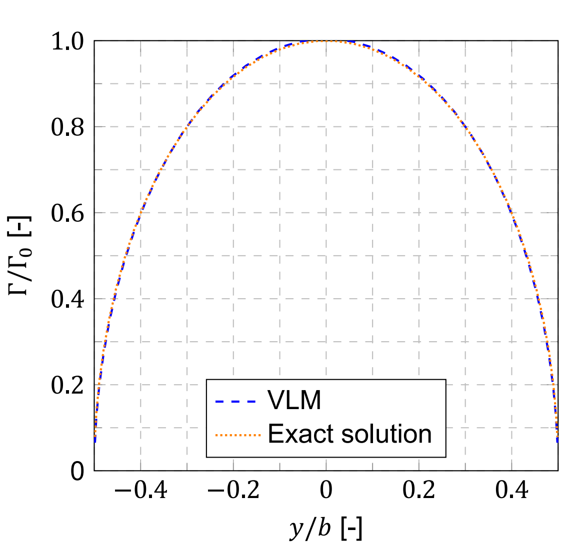

Figure 4.3: Comparison of the circulation distribution of an elliptic wing

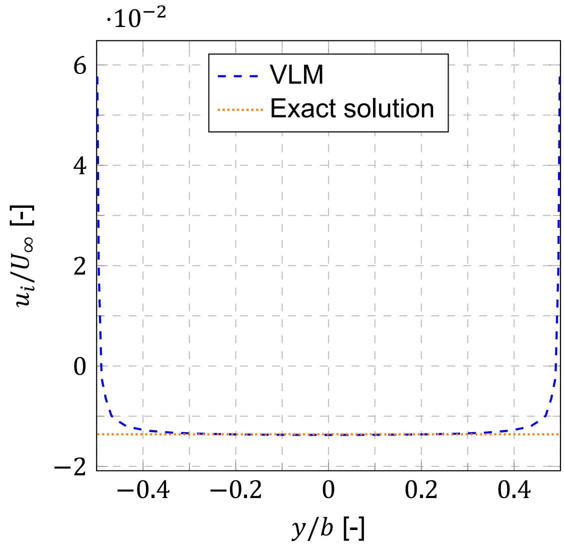

Figure 4.4: Comparison of the wing induced velocity distribution of an elliptic wing

The VLM code is also compared to existing VLM codes: XFLR5[1] and AVL[2]. All codes were given the same geometry and same panel layout to compare the results fairly. The results are produced for a tapered swept wing with aspect ratio 10 with a cambered NACA2412 airfoil. In Figure 4.5 the lift curve

[1] http://www.xflr5.tech/xflr5.htm
[2] http://web.mit.edu/drela/Public/web/avl/

is plotted for the different codes. It can be seen that the results are very close to each other. The AVL results seem to produce slightly higher values for C_L, but this is well within the margin of error expected for such a low-cost method. Next, the spanwise distribution of the lift is compared in Figure 4.6 for a wing at $\alpha = 5°$. The VLM code shows a good match with the XFLR5 data. AVL gives higher sectional lift coefficients, this is expected since total forces are also higher. This is most likely caused by a slight difference in velocity vector definition. Thus, the VLM code seems to be working correctly.

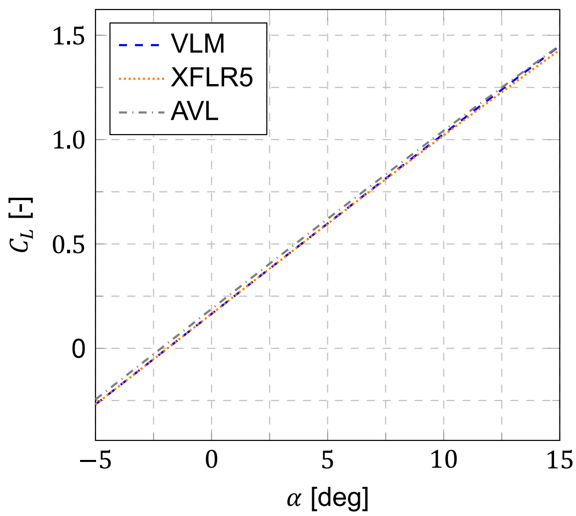

Figure 4.5: Comparison of the lift polar for different VLM solvers

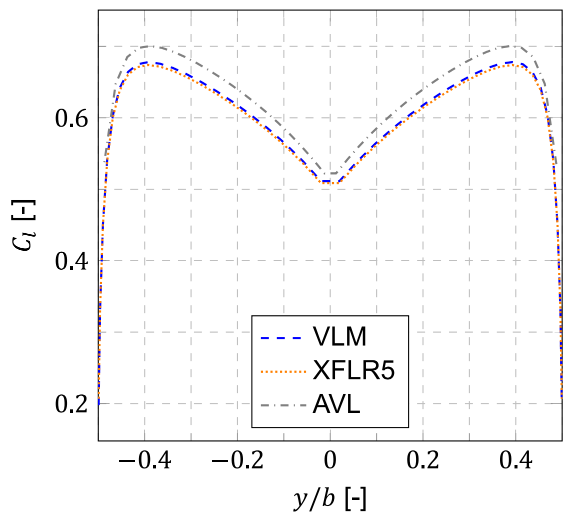

Figure 4.6: Comparison of the lift distribution at $\alpha = 5°$ for different VLM solvers

4.2. Trefftz plane analysis

The drag is calculate using a Trefftz plane analysis. This analysis is based on the derivations by Katz and Plotkin [45] and Veldhuis and Heyma [87]. For the analysis a control volume is used, which encloses our object of interest, as shown in Figure 4.7. S_u is far upstream, while S_d is far downstream. S_b follows a streamline. To this control volume, conservation of momentum is applied, as shown in Equation 4.7. Furthermore, a potential is introduced: $\Phi = U_\infty x + \phi$, where ϕ describes the disturbance velocities. This gives the following boundary conditions:

- at S_u: $\phi = 0$ and $p = p_\infty$
- at S_b: $\overline{U} \cdot \overline{n} = 0$ and p is continuous

$$\iint_S \rho \overline{U}(\overline{U} \cdot \overline{n}) dS = -\iint_S (p\overline{n}) dS + \overline{F} \tag{4.7}$$

Now Equation 4.7 can be applied to the control volume. This is shown in Equation 4.8. In the final step the integral is written as an integral of surface S, which is S_d, since the properties are written as differences at S_d compared to the upstream values.

$$\begin{aligned} D &= \iint_{S_u} p n_x dS - \iint_{S_d} p n_x dS + \iint_{S_u} \rho \frac{d\Phi}{dx}(\nabla\Phi \cdot \overline{n}) dS - \iint_{S_d} \rho \frac{d\overline{\Phi}}{dx}(\nabla\Phi \cdot \overline{n}) dS + T \\ &= \iint_{S_u} p_\infty dS - \iint_{S_d} p dS + \iint_{S_u} \rho U_\infty (\nabla\Phi \cdot \overline{n}) dS - \iint_{S_d} \rho (U_\infty + \phi_x)(\nabla\Phi \cdot \overline{n}) dS + T \\ &= \iint_S p_\infty - p dS + \iint_S \rho \phi_x (U_\infty + \phi_x) dS + T \end{aligned} \tag{4.8}$$

In Equation 4.9 an expression for the difference in pressure is derived. Here Δp_t is a total pressure jump. This equation can be substituted into Equation 4.8, which gives Equation 4.10.

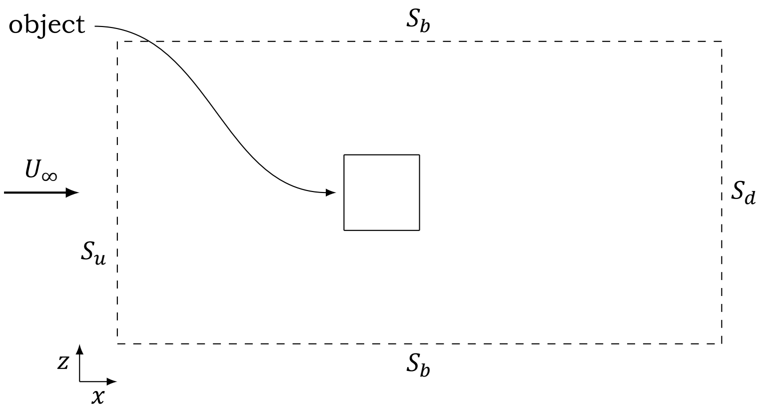

Figure 4.7: Schematic of a general Trefftz plane analysis

$$
\begin{aligned}
p_\infty - p &= \frac{1}{2}\rho\left(\nabla\phi^2 - \frac{1}{2}\rho U_\infty^2\right) - \Delta p_t \\
&= \frac{1}{2}\rho\left((U_\infty + \phi_x)^2 + \phi_y^2 + \phi_z^2\right) - \frac{1}{2}\rho U_\infty^2 - \Delta p_t \\
&= \frac{1}{2}\rho\left(\phi_x^2 + \phi_y^2 + \phi_z^2\right) + \rho U_\infty \phi_x - \Delta p_t
\end{aligned}
\tag{4.9}
$$

$$
\begin{aligned}
D &= \iint_S p_\infty - p dS + \iint_S \rho\phi_x(U_\infty + \phi_x) dS + T \\
&= \iint_S \frac{1}{2}\rho\left(\phi_x^2 + \phi_y^2 + \phi_z^2\right) + \rho U_\infty\phi_x - \Delta p_t + \rho\phi_x(U_\infty + \phi_x) dS + T \\
&= \iint_S \frac{1}{2}\rho\left(-\phi_x^2 + \phi_y^2 + \phi_z^2\right) - \Delta p_t dS + T
\end{aligned}
\tag{4.10}
$$

Equation 4.10 is the final equation for a generic Trefftz plane analysis. Now the propeller and wing can be added to the control volume, as shown in Figure 4.8. Two areas can now be defined, one outside the flow captured by the propeller, S_o, and one that is captured by the propeller, S_i. For the area outside the captured area, there is no total pressure jump and $\phi_x = 0$. This gives Equation 4.11, which corresponds with the expression that is used for a Trefftz plane analysis of a wing only [45].

$$
D = \frac{1}{2}\rho \iint_{S_o} \phi_y^2 + \phi_z^2 dS \tag{4.11}
$$

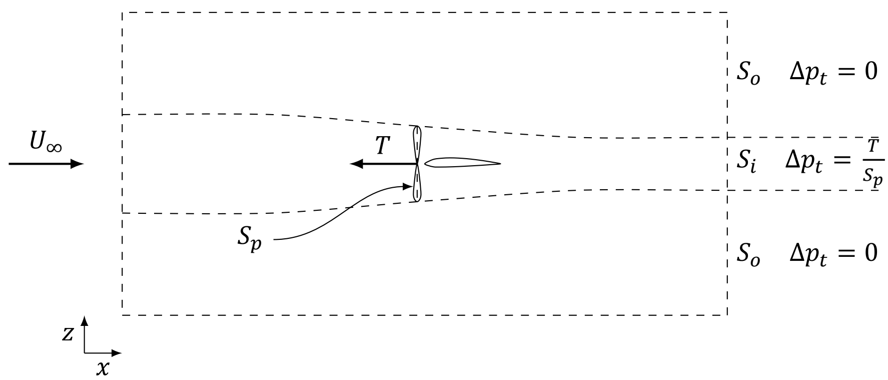

Figure 4.8: Schematic of a Trefftz plane analysis with a propeller-wing system

In the area captured by the propeller, the total pressure jump Δp_t equals $\frac{T}{S_p}$, where S_p is the propeller disk area. This leads to Equation 4.12. Now the equation is split into two parts, one for drag and one for thrust. It can be seen that the conventional expression for drag is found. Furthermore, the expression for thrust is consistent with the equations derived by actuator disk theory. This can be quickly verified when the equations $\phi_x = 2U_\infty a$ and $S_p U_\infty(1+a) = S_i U_\infty(1+2a)$ are applied.

$$\begin{aligned}
D &= \iint_{S_i} \frac{1}{2}\rho\left(-\phi_x^2 + \phi_y^2 + \phi_z^2\right) - \frac{T}{S_p} dS + T \\
D &= \frac{1}{2}\rho \iint_{S_i} \phi_y^2 + \phi_z^2 dS \\
T &= \iint_{S_i} \frac{1}{2}\rho\phi_x^2 + \frac{T}{S_p} dS
\end{aligned} \tag{4.12}$$

In Equations 4.11 and 4.12 the same expressions were found to calculate the drag for both the area captured and not captured by the propeller. Thus, this expression can be applied to the entire Trefftz plane. This is shown in Equation 4.13. The potential is written as the sum of the wing and propeller: $\phi = \phi_w + \phi_p$. After this, the identity in Equation 4.14 is used to rewrite the surface integrals as line integrals. Then this relation is used for the normal velocity: $\frac{\partial \phi}{\partial n} = u_n$. Furthermore, second derivatives in disturbance velocities are zero far downstream: $\nabla^2\phi = 0$. Finally, the difference in velocity over the wake is equal to the circulation: $\Delta\phi = \Gamma$. Equation 4.13 shows three contributions to drag: the wing induced drag, the propeller-wing interaction effect and the propeller drag. The propeller drag is ignored, since it is inconsistent with the BEM model that will be used. Thus, the final expression shown in Equation 4.13 has only two contributions to the drag.

$$\begin{aligned}
D &= \frac{1}{2}\rho \iint_{S_i} \phi_y^2 + \phi_z^2 dS \\
&= \frac{1}{2}\rho \iint_S \phi_{w_y}^2 + \phi_{w_z}^2 dS + \rho \iint_S \phi_{w_y}\phi_{p_y} + \phi_{w_z}\phi_{p_z} dS + \frac{1}{2}\rho \iint_S \phi_{p_y}^2 + \phi_{p_z}^2 dS \\
&= \frac{1}{2}\rho \int_C \Delta\phi_w u_{n_w} dC + \rho \int_C \Delta\phi_w u_{n_p} dC + \frac{1}{2}\rho \iint_S \phi_{p_y}^2 + \phi_{p_z}^2 dS \\
&= \frac{1}{2}\rho \int_{-b/2}^{b/2} \Gamma_w u_{n_w} dy + \rho \int_{-b/2}^{b/2} \Gamma_w u_{n_p} dy + \frac{1}{2}\rho \iint_S \phi_{p_y}^2 + \phi_{p_z}^2 dS \\
&= \frac{1}{2}\rho \int_{-b/2}^{b/2} \Gamma_w \left(u_{n_w} + u_{n_p}\right) dy
\end{aligned} \tag{4.13}$$

$$\iint_S \phi_y^2 + \phi_z^2 + \phi(\nabla^2\phi) dS = \int_C \frac{\partial \phi}{\partial n}\phi dC \tag{4.14}$$

This Trefftz plane analysis is compared to the drag calculation done by XFLR5 and AVL for a wing-only case. In Figure 4.9 the total wing drag is compared for these different codes. The three methods almost exactly agree with each other, except at very high lift coefficients. Here XFLR5 predicts a lower drag than the VLM code and AVL. This could be because XFLR5 most likely uses a small angle approximation, while full trigonometric functions are used in the VLM code. Furthermore, at these high lift coefficients, it is expected that a VLM code gives a poor prediction, so any numerical errors here are irrelevant. Next, in Figure 4.10 the spanwise distribution of drag is plotted for a wing at $\alpha = 5°$. Results from the VLM code match with the XFLR5 data. Only AVL shows a completely different distribution, this is because AVL does not calculate drag using a Trefftz plane analysis, so the results presented here are most likely calculated on the wing. Thus, this is not a fair comparison, since drag forces in different locations are compared. To conclude, the Trefftz plane analysis implemented in the VLM code is in agreement with existing codes.

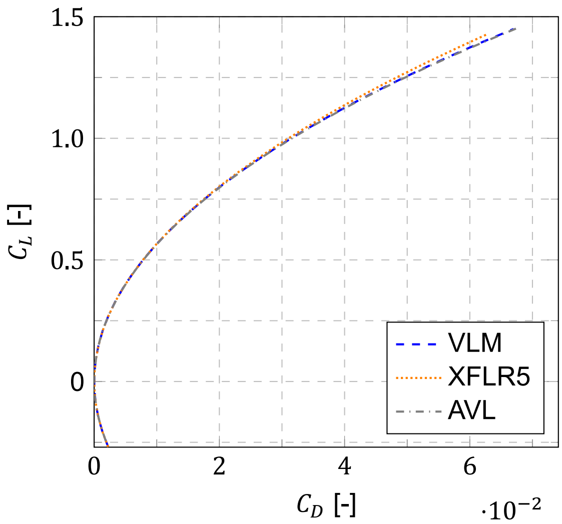

Figure 4.9: Comparison of the drag polar for different VLM solvers

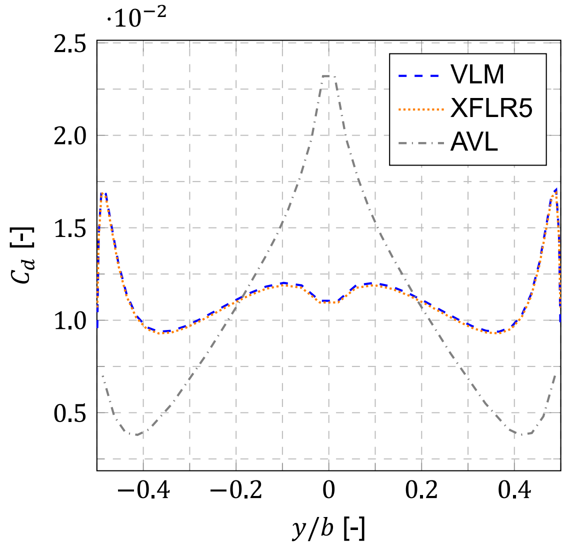

Figure 4.10: Comparison of the drag distribution at $\alpha = 5°$ for different VLM solvers

4.3. Jet correction

In the VLM code, when the external induced velocity is applied as a boundary condition, it actually represents a velocity disturbance uniform in z direction. However, a propeller slipstream is finite in height and this affects the influence of this induced velocity. This phenomenon is mainly visible in effects of the axial velocity and can be neglected for the tangential velocity [48]. There are 2D methods that take the effect of a finite slipstream with axial velocity on the lift of an airfoil into account. These methods are relatively easy to compute and apply, but unfortunately they can not be extended into a 3D method [48]. A method that can be applied to a 3D wing and jet has been developed by Rethorst [50][49]. This method was developed for a completely symmetrical case, where the jet is located in the center of the wing.

The solution is based on the geometry shown in Figure 4.11. A circular jet is located in the center of the wing. Outside the jet there is U_∞ and inside the jet U_j. Furthermore, it is known that on the jet boundary there must be pressure continuity and slipstream continuity, where slipstream continuity makes sure that velocities on both sides of the jet are in the same direction. To find the influence of a vortex somewhere in the domain, two potential functions are created, one that describes the influence inside the jet and one that describes the influence outside the jet. This gives a solution that consists of three parts. One part is the regular relation between circulation and position calculated using the Biot-Savart law. The other two parts are the corrections for the finite jet. To create this correction the horseshoe vortex is split into a part consisting of two infinite parallel lines, called the even part, and a part consisting of two semi-infinite opposite horseshoe vortices, called the odd part. This is shown in Figure 4.12.

The corrections are denoted with G. If the conventional way to calculate the induced velocity due to a vortex would be: $u_i = \frac{1}{4\pi}C\Gamma$, then the correction is applied as follows: $u_i = \frac{1}{4\pi}(C + G)\Gamma$. In the case of the horseshoe vortex the correction consists of two parts, the odd and even part: $G = G_o + G_e$. The odd and even correction are derived in a similar manner. There must be a potential for inside the jet boundary and one for outside the jet boundary. These two must match according to the boundary conditions. This gives two solutions for the correction, one for when the point being evaluated is inside the boundary and one for when it is outside the jet. However, the vortex can also be located either within or outside the jet and this again gives a different solution. Thus, there are four possible cases, depending on the location of the vortex and the point where the induced velocity is being evaluated.

The four different possible cases for the correction are given in Equation 4.15 and 4.16 for the even and odd part respectively. Here the first letter of the subscript denotes the position of the point and the second the position of the vortex. So G_{oj_e} is the correction of the even part for a point outside the jet and the vortex inside the jet. Furthermore, some non-dimensional values are used here. The

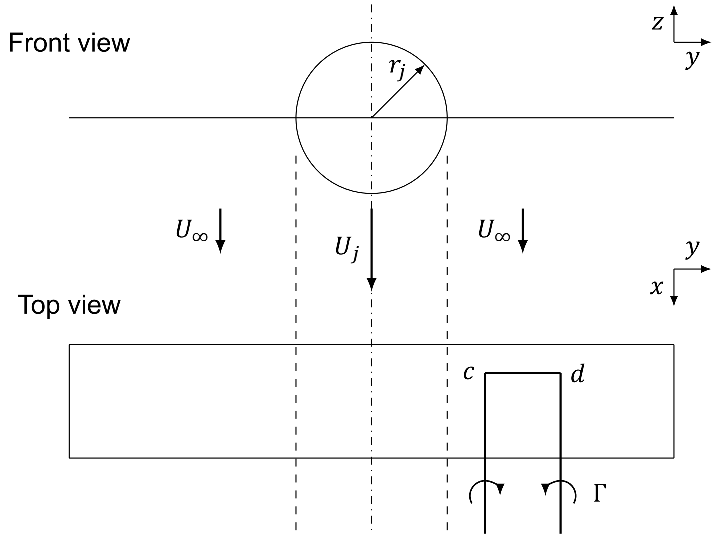

Figure 4.11: Geometry used by Rethorst [49][50] to calculate a jet correction

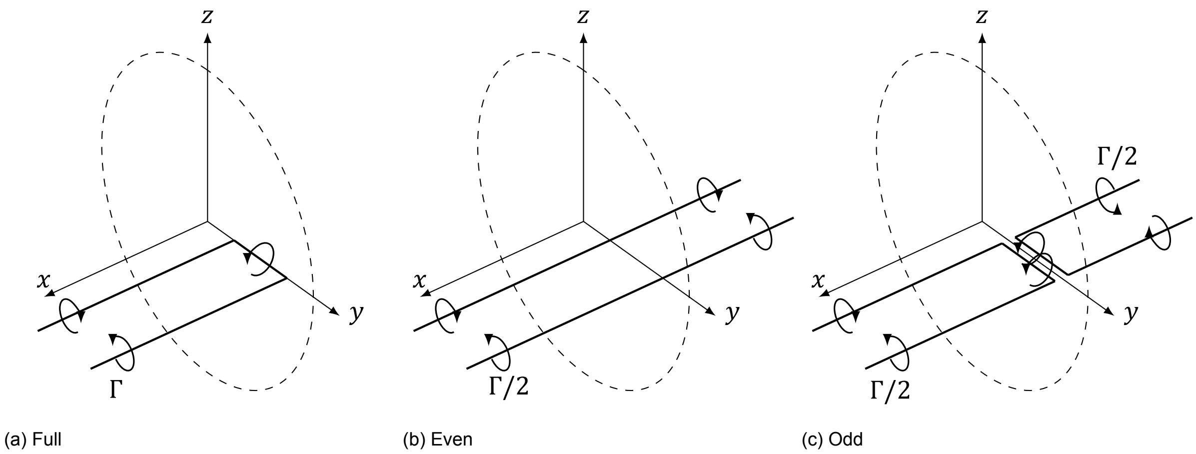

Figure 4.12: Definition of the even and odd part of a horseshoe vortex

coordinates are $\xi = x/r_j$ and $\eta = y/r_j$. $\mu = U_\infty/U_j$ is the ratio between the freestream and jet velocity. The spanwise locations of the horseshoe vortex are given by c and d, which are non-dimesionalized with the jet radius. The jet radius is given by r_j, which is the only dimensional number used here. Furthermore, modified Bessel functions of the first and second kind are used, I and K respectively. Also, the derivatives I' and K' are used. The functions are all of order $2p+1$. And unless specified, the functions take the argument λ.

$$
\begin{aligned}
G_{jj_e}(\eta) &= \frac{1}{r_j}\frac{1-\mu^2}{1+\mu^2}\left(\frac{1}{1/d-\eta} - \frac{1}{1/c-\eta} + \frac{1}{1/d+\eta} - \frac{1}{1/c+\eta}\right) \\
G_{oj_e}(\eta) &= -\frac{1}{r_j}\frac{(1-\mu)^2}{1+\mu^2}\left(\frac{1}{\eta-c} - \frac{1}{\eta-d} + \frac{1}{\eta+d} - \frac{1}{\eta+c}\right) \\
G_{jo_e}(\eta) &= G_{oj_e}(\eta) \\
G_{oo_e}(\eta) &= -G_{jj_e}(\eta)
\end{aligned}
\tag{4.15}
$$

$$
\begin{aligned}
G_{jj_o}(\xi,\eta) &= \frac{1}{r_j}\frac{8}{\pi\eta}\sum_{p=0}^{\infty}(2p+1)^2\int_0^{\infty}\frac{KK'I(\eta\lambda)\sin(\xi\lambda)}{\frac{1}{1/\mu^2-1}-\lambda IK'}\int_{c\lambda}^{d\lambda}\frac{I(\lambda\beta)}{\lambda\beta}d(\lambda\beta)d\lambda \\
G_{oj_o}(\xi,\eta) &= \frac{1}{r_j}\frac{8}{\pi\eta}\sum_{p=0}^{\infty}(2p+1)^2\int_0^{\infty}\left(\frac{1}{\mu-\lambda(1/\mu-\mu)IK'}-1\right)\frac{K(\eta\lambda)\sin(\xi\lambda)}{\lambda}\int_{c\lambda}^{d\lambda}\frac{I(\lambda\beta)}{\lambda\beta}d(\lambda\beta)d\lambda \\
G_{jo_o}(\xi,\eta) &= \frac{1}{r_j}\frac{8}{\pi\eta}\sum_{p=0}^{\infty}(2p+1)^2\int_0^{\infty}\left(\frac{1}{\mu-\lambda(1/\mu-\mu)IK'}-1\right)\frac{I(\eta\lambda)\sin(\xi\lambda)}{\lambda}\int_{c\lambda}^{d\lambda}\frac{K(\lambda\beta)}{\lambda\beta}d(\lambda\beta)d\lambda \\
G_{oo_o}(\xi,\eta) &= \frac{1}{r_j}\frac{8}{\pi\eta}\sum_{p=0}^{\infty}(2p+1)^2\int_0^{\infty}\frac{II'K(\eta\lambda)\sin(\xi\lambda)}{\frac{1}{1/\mu^2-1}-\lambda IK'}\int_{c\lambda}^{d\lambda}\frac{K(\lambda\beta)}{\lambda\beta}d(\lambda\beta)d\lambda
\end{aligned}
\tag{4.16}
$$

Now the correction can be applied to a symmetrical wing. To demonstrate the way the correction is applied, a wing with five panels is assumed, as shown in Figure 4.13, with a jet present in the center, the radius is not relevant at this time. Note that for the correction to work, the jet centerline must be in the center of one the horseshoe vortices and the jet boundary must coincide with one of the horseshoe boundaries (or trailing vortices). Since $\Gamma_1 = \Gamma_4$ and $\Gamma_2 = \Gamma_5$, a system of equations can be written that solves for a vector containing Γ_1, Γ_2 and Γ_3. This is shown in Equation 4.17. It can be seen here that the correction is applied by utilizing the symmetric condition of the system of equations that must be solved.

$$
\left(\begin{bmatrix} C_{11}+C_{15} & C_{12}+C_{14} & C_{13} \\ C_{21}+C_{25} & C_{22}+C_{24} & C_{23} \\ C_{31}+C_{35} & C_{32}+C_{34} & C_{33} \end{bmatrix} + \begin{bmatrix} G_{11} & G_{12} & G_{13} \\ G_{21} & G_{22} & G_{23} \\ G_{31} & G_{32} & G_{33} \end{bmatrix}\right)\begin{bmatrix}\Gamma_1 \\ \Gamma_2 \\ \Gamma_3\end{bmatrix} = \begin{bmatrix} U_{n,1} \\ U_{n,2} \\ U_{n,3}\end{bmatrix} \tag{4.17}
$$

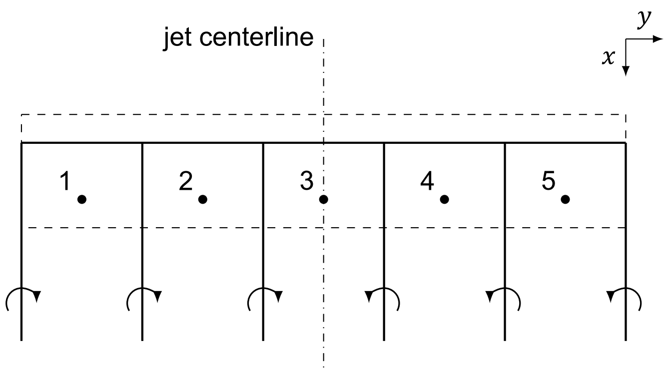

Figure 4.13: Simple geometry used to calculate a jet correction for a jet located at the wing center

To get to a correction that works on a wing where the jet is not located in the center of the wing, Equation 4.17 must be rewritten to better understand how the correction is applied. In Equation 4.18 the full system is shown, which also includes Γ_4 and Γ_5. Here it can be seen that the correction has to be divided over the two symmetric vortex pairs. For example, the correction factor G_{11} is applied to Γ_1 and Γ_5. When $G_{11}/2$ is applied to both Γ_1 and Γ_5, the same equations are obtained in both Equation 4.17 and 4.18. However, it is somewhat arbitrary to divide G_{11} equally over both vortices. If G_{11} would be applied to Γ_1 only, the same equations, as shown in Equation 4.17, would still be obtained. Note that there always must be a horseshoe vortex located on the jet centerline, which does not form a symmetry pair.

$$\left(\begin{bmatrix} C_{11} & C_{12} & C_{13} & C_{14} & C_{15} \\ C_{21} & C_{22} & C_{23} & C_{24} & C_{25} \\ C_{31} & C_{32} & C_{33} & C_{34} & C_{35} \\ C_{41} & C_{42} & C_{43} & C_{44} & C_{45} \\ C_{51} & C_{52} & C_{53} & C_{54} & C_{55} \end{bmatrix} + \begin{bmatrix} G_{11}/2 & G_{12}/2 & G_{13} & G_{12}/2 & G_{11}/2 \\ G_{21}/2 & G_{22}/2 & G_{23} & G_{22}/2 & G_{21}/2 \\ G_{31}/2 & G_{32}/2 & G_{33} & G_{32}/2 & G_{31}/2 \\ G_{21}/2 & G_{22}/2 & G_{23} & G_{22}/2 & G_{21}/2 \\ G_{11}/2 & G_{12}/2 & G_{13} & G_{12}/2 & G_{11}/2 \end{bmatrix}\right) \begin{bmatrix} \Gamma_1 \\ \Gamma_2 \\ \Gamma_3 \\ \Gamma_4 \\ \Gamma_5 \end{bmatrix} = \begin{bmatrix} U_{n,1} \\ U_{n,2} \\ U_{n,3} \\ U_{n,4} \\ U_{n,5} \end{bmatrix} \tag{4.18}$$

This leads to a method to apply this jet correction to a wing with a jet which is not located at the centerline of the wing. Firstly, the correction for a jet with the centerline at the wing center must be calculated. This is done by extending the wing to create a symmetric one, as shown in Figure 4.14, creating a virtual wing extension. By dividing the correction factor by two, the correction can be applied to each individual horseshoe vortex. The underlying assumption is that the vortex pairs (horseshoe vortex pairs that have equal distance from the jet centerline) have approximately the same strength. Furthermore, the correction of the vortex pairs that have one vortex in the virtual wing extension is still divided by two, although there is no second vortex that uses the other part of the correction. For these vortices it is assumed that these vortices are far away from the jet and the correction here has little effect. For the case shown in Figure 4.14, this means that Equation 4.18 is reduced to Equation 4.19. The results of this method show a good match with CFD data, as shown in Figure 4.15, which has also been shown by Nederlof [48]. Here the correction is applied to a single chordwise panel VLM code. The correction that has been discussed here is called the *equally divided correction*.

$$\left(\begin{bmatrix} C_{11} & C_{12} & C_{13} & C_{14} \\ C_{21} & C_{22} & C_{23} & C_{24} \\ C_{31} & C_{32} & C_{33} & C_{34} \\ C_{41} & C_{42} & C_{43} & C_{44} \end{bmatrix} + \begin{bmatrix} G_{11}/2 & G_{12}/2 & G_{13} & G_{12}/2 \\ G_{21}/2 & G_{22}/2 & G_{23} & G_{22}/2 \\ G_{31}/2 & G_{32}/2 & G_{33} & G_{32}/2 \\ G_{21}/2 & G_{22}/2 & G_{23} & G_{22}/2 \end{bmatrix}\right) \begin{bmatrix} \Gamma_1 \\ \Gamma_2 \\ \Gamma_3 \\ \Gamma_4 \end{bmatrix} = \begin{bmatrix} U_{n,1} \\ U_{n,2} \\ U_{n,3} \\ U_{n,4} \end{bmatrix} \tag{4.19}$$

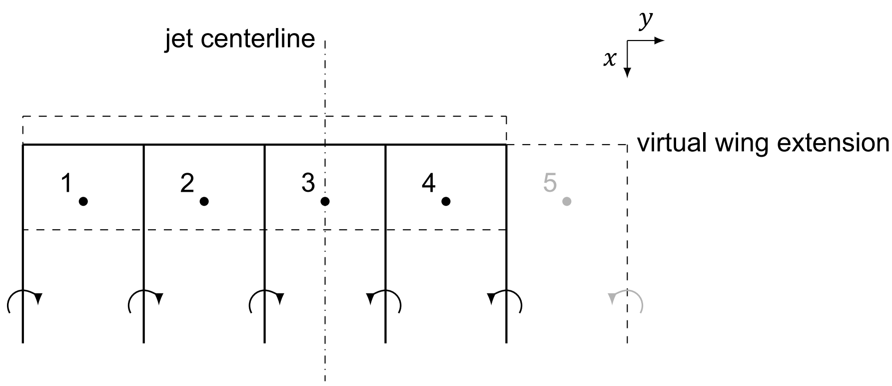

Figure 4.14: Simple geometry used to calculate a jet correction for a jet not located at the wing center

The method of dividing the jet correction equally is relatively straight forward. However, other methods of dividing the correction are possible. When evaluating the normal velocity at the control point of horseshoe vortex 1, it can be seen that vortex 1 has more influence than vortex 3. This reasoning can also be extrapolated to the correction factor. So actually G_{11} in the first line of Equation 4.18 should be applied more to Γ_1. When the points and vortices are even farther away from the jet centerline, this effect becomes even stronger. Thus, it can be assumed that the correction factor is only applied to the vortex that is closest. This leads to Equation 4.20, where the correction is basically applied to each symmetry side of the jet centerline. For the control point of the center vortex it is arbitrary to which symmetry side the correction is applied, as long as the vortex strengths are similar. For the case shown in Figure 4.14, this method results in Equation 4.21. This method also yields good results, as shown in Figure 4.15, where this method is called the *symmetry correction*.

$$\left(\begin{bmatrix} C_{11} & C_{12} & C_{13} & C_{14} & C_{15} \\ C_{21} & C_{22} & C_{23} & C_{24} & C_{25} \\ C_{31} & C_{32} & C_{33} & C_{34} & C_{35} \\ C_{41} & C_{42} & C_{43} & C_{44} & C_{45} \\ C_{51} & C_{52} & C_{53} & C_{54} & C_{55} \end{bmatrix} + \begin{bmatrix} G_{11} & G_{12} & G_{13} & 0 & 0 \\ G_{21} & G_{22} & G_{23} & 0 & 0 \\ G_{31} & G_{32} & G_{33} & 0 & 0 \\ 0 & 0 & G_{23} & G_{22} & G_{21} \\ 0 & 0 & G_{13} & G_{12} & G_{11} \end{bmatrix}\right) \begin{bmatrix} \Gamma_1 \\ \Gamma_2 \\ \Gamma_3 \\ \Gamma_4 \\ \Gamma_5 \end{bmatrix} = \begin{bmatrix} U_{n,1} \\ U_{n,2} \\ U_{n,3} \\ U_{n,4} \\ U_{n,5} \end{bmatrix} \tag{4.20}$$

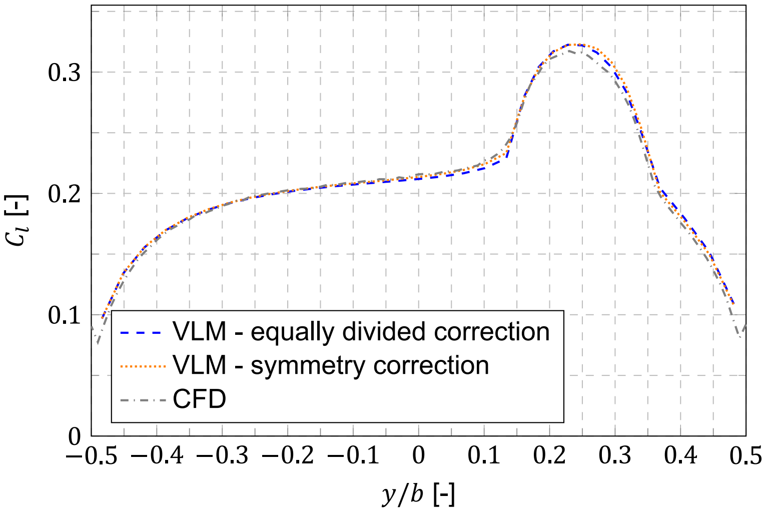

Figure 4.15: Comparison of the lift distribution for a wing with jet with $R/b = 0.1$ at $y/b = 0.25$ [48]

$$\left(\begin{bmatrix} C_{11} & C_{12} & C_{13} & C_{14} \\ C_{21} & C_{22} & C_{23} & C_{24} \\ C_{31} & C_{32} & C_{33} & C_{34} \\ C_{41} & C_{42} & C_{43} & C_{44} \end{bmatrix} + \begin{bmatrix} G_{11} & G_{12} & G_{13} & 0 \\ G_{21} & G_{22} & G_{23} & 0 \\ G_{31} & G_{32} & G_{33} & 0 \\ 0 & 0 & G_{23} & G_{22} \end{bmatrix}\right) \begin{bmatrix} \Gamma_1 \\ \Gamma_2 \\ \Gamma_3 \\ \Gamma_4 \end{bmatrix} = \begin{bmatrix} U_{n,1} \\ U_{n,2} \\ U_{n,3} \\ U_{n,4} \end{bmatrix} \tag{4.21}$$

Now the jet can be placed at the wingtip. When this is done, the wing must be extended again to calculate the correction for a completely symmetrical case. However, in this case, there is no vortex on the other side of the jet symmetry line. So in this case it makes sense to use the method where the jet correction is applied to only one side of the jet centerline. This is basically an extreme case of the previously described *symmetry correction*. Again this results in a good match with CFD data, as shown in Figure 4.16.

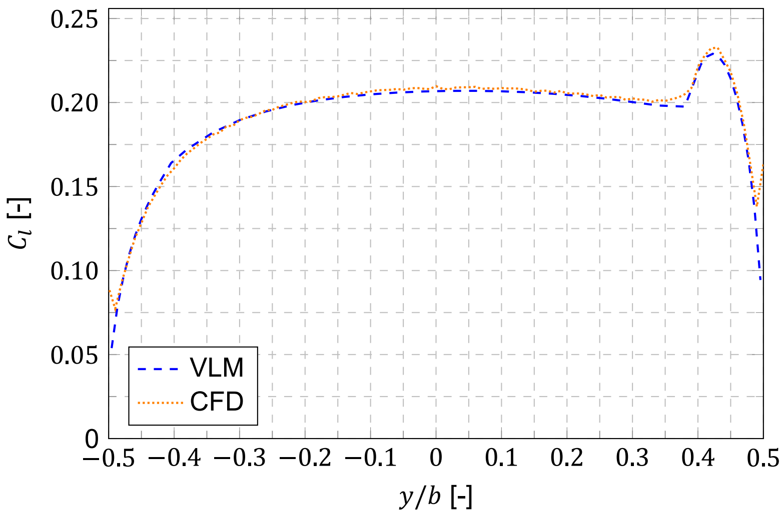

Figure 4.16: Comparison of the lift distribution for a wing with jet with $R/b = 0.1$ at the tip of the wing [48]

For the correction to work, the jet centerline must be in the center of one of the panels and the jet boundary must coincide with the boundary of one of the panels. As this is not always the case, some small changes must be made to the jet geometry to calculate the velocity. For the tip-mounted case, the real jet centerline will coincide with the outer boundary of the tip panel and the jet has a radius r. But in the correction the jet centerline is offset by s_0, as shown in Figure 4.17. Furthermore, the radius is changed so the boundary coincides with a panel boundary, which gives a new radius r_j. With a high enough panel density, these changes have little effect on the correction and an even smaller effect on the wing circulation calculation.

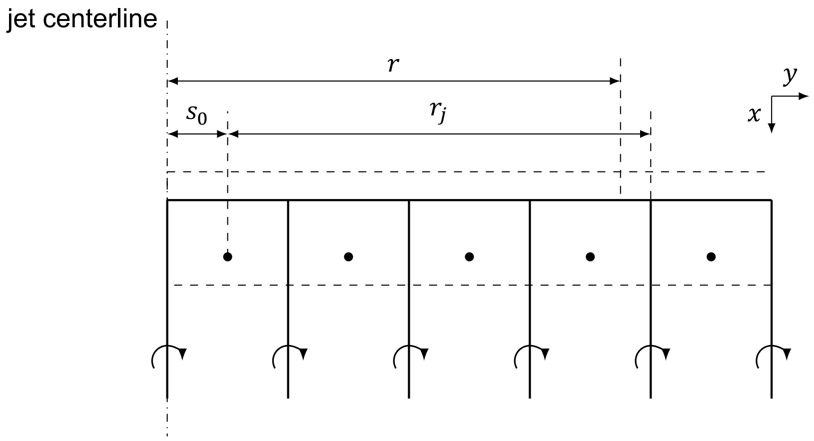

Figure 4.17: The difference in jet radius and position due to panel density

Furthermore, the propeller will not always be exactly at the same height (z-coordinate) as the wing. Here the correction is not valid anymore. To still calculate a correction in this case, it is assumed that the induced velocities seen at the wing are due to a propeller located at the same height as the wing. This gives a difference in the real geometry and the geometry used for the correction calculation, as shown in Figure 4.18. Here the propeller is located at height dz above the wing plane, while the jet correction assumed that the propeller is located at the same z-coordinate as the wing. It is assumed that for a relatively low dz/r, that this difference in geometry will have a minor influence on the correction, which will again translate in a very minor influence on the calculated forces on the wing.

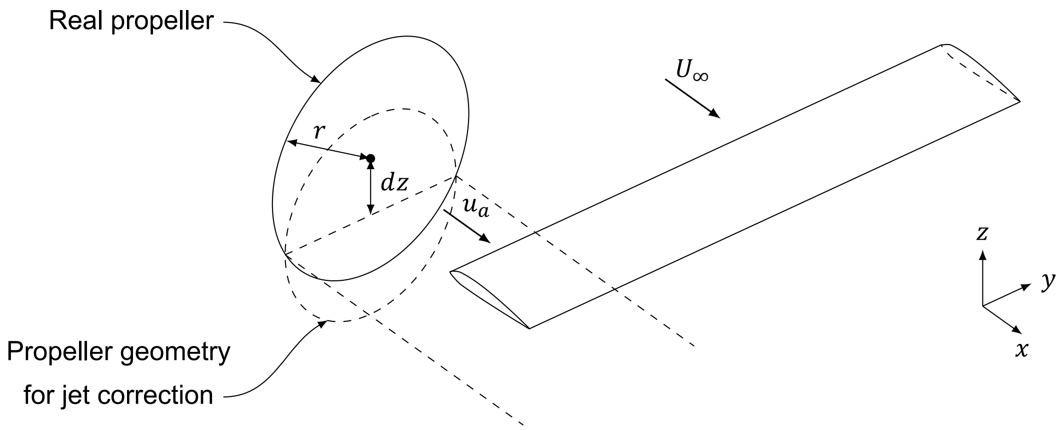

Figure 4.18: The difference in jet geometry and modelled geometry due to vertical location of the jet

Finally, a real propeller has a distribution of axial velocity, while the correction is written for a uniform jet. Prabhu [88] showed that for the even part of the correction, superposition could be used to describe a correction for a jet with an arbitrary (radial symmetrical) velocity distribution. This principle is shown in Figure 4.19. For each step, a jet can be defined with radius r_i. The correction for this step G_i, can then be calculated using the velocity difference with the jet at r_{i-1}, which gives $\mu_i = (U_\infty + u_{i-1})/(U_\infty + u_i)$. Here r_{i-1} is one step closer to the wing root than r_i. Then the total jet correction G is given by the sum of all G_i. While this superposition was only applied for a case with infinite vortices, here it is applied to full horseshoe vortices. Since the odd and even part of the jet correction are based on the same physical principles, it was assumed that it can also be applied to a case with horseshoe vortices.

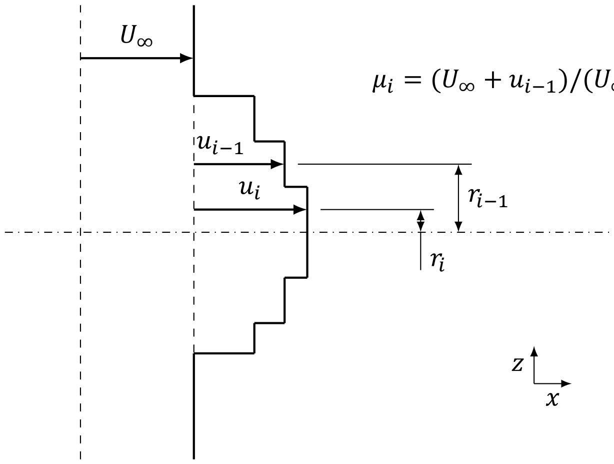

Figure 4.19: Discretization of a jet velocity profile for the calculation of the jet correction

4.4. Viscous correction

The VLM method is an inviscid method, so the lift curve will be completely linear and the viscous drag is not included. To still model these effects for a relatively low computational cost, two corrections are added to the VLM code: a viscous correction on the lift and the inclusion of profile drag.

The viscous correction on the lift has been developed by Horsten and Veldhuis [89]. In this method the inviscid results of the VLM code are corrected by adding a local angle of attack correction based on the difference between the inviscid and viscous lift. This is shown in Equation 4.22. The effective angle of attack α_{eff} for a wing section is calculated as usual, it is the geometric angle of attack α minus the induced drag α_{ind}. On top of this some extra correction is added to account for the difference between the viscous and invisicid lift, which is called $d\alpha_{corr}$.

$$\alpha_{eff} = \alpha - \alpha_i + d\alpha_{corr} \tag{4.22}$$

This correction $d\alpha_{corr}$ is calculated using Equation 4.23. By calculating the lift without any corrections using the VLM code the effective angle of attack at each wing section is obtained. With the effective angle of attack known, $C_{l,visc}$ and $C_{l,inv}$ can be obtained at this angle of attack using 2D analysis. The inviscid lift coefficient $C_{l,inv}$ is obtained using thin airfoil theory, as this is the 2D equivalent analysis for the VLM code, which also is inviscid without taking the airfoil thickness into account. The viscous lift coefficient $C_{l,visc}$ is obtained using XFOIL[3]. $C_{l,visc}$ is also dependent on Mach and Reynolds number, which are obtained from the VLM results. Since XFOIL takes into account thickness while thin airfoil theory does not, this correction also corrects for the fact that VLM does not take into account wing thickness. Furthermore, the viscous lift coefficient is dependent on Mach number, thus this also results in a rudimentary correction for compressibility. Now the change in lift must be translated into a change in angle of attack, this is done by dividing by the inviscid lift curve slope $\frac{dC_{l,inv}}{d\alpha}$, which equals 2π in thin airfoil theory.

$$d\alpha_{corr} = \frac{C_{l,visc}(\alpha, Re, M) - C_{l,inv}(\alpha)}{\frac{dC_{l,inv}}{d\alpha}} = \frac{C_{l,visc} - C_{l,inv}}{2\pi} \tag{4.23}$$

Finally, $d\alpha_{corr}$ can be used as input for the VLM code and by solving the system of equations again, the corrected lift is found. In Figure 4.20 the lift curve is plotted when the VLM code is used with and without this viscous correction on the lift for a wing with aspect ratio 10. It can be seen that in the linear part slightly higher lift values are obtained when using the correction, this is mainly due to the effect of thickness. Furthermore, the lift curve remains linear here. Above around $10°$ angle of attack a decrease in lift is seen due to viscous effects. It can be seen that the lift curve slope decreases with increasing angle of attack, as expected. In Figure 4.21 the effective angle of attack is shown for the

[3]`https://web.mit.edu/drela/Public/web/xfoil/`

wing at $\alpha = 18°$. The viscous correction decreases the effective angle of attack. It can also be seen that for the lower angle of attack values, this decrease is less in magnitude, since here the viscous effects are less present.

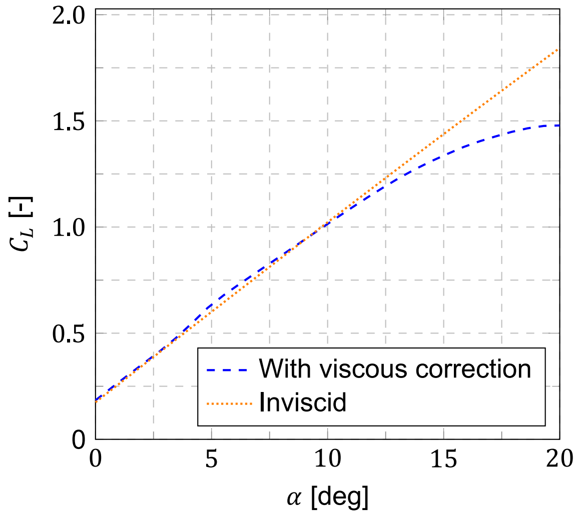

Figure 4.20: Comparison between inviscid and viscous lift polar

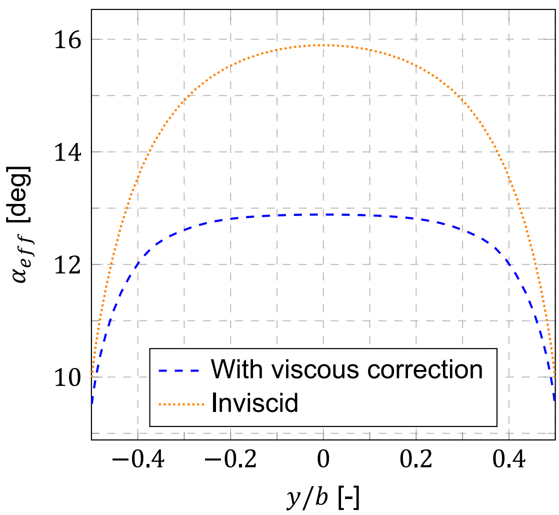

Figure 4.21: Comparison between inviscid and viscous lift distribution at $\alpha = 18°$

Next to the viscous correction on the lift, viscous drag was added to the VLM code. The VLM code conventionally only calculated the induced drag, as profile drag is not modelled here. Using a 2D drag polar obtained using XFOIL, the profile drag can be estimated by finding the corresponding profile drag for the sectional lift coefficient per wing section. If for a certain lift coefficient multiple drag values are found, then the drag value that best matches the angle of attack is chosen. This is the case for lift coefficients near and in the non-linear regime. The profile drag is simply added to the inviscid drag, giving the total drag, as shown in Equation 4.24. The results of this correction are shown in Figure 4.22. It can be seen that at $C_L = 0$, the inviscid drag is also zero, as expected. With the viscous case, profile drag is added and the drag at $C_L = 0$ is non-zero. For the other lift coefficients, it can be seen that the drag with profile drag included, is always higher than the induced drag.

$$C_{D,t} = C_{D,i} + C_{D,p} \tag{4.24}$$

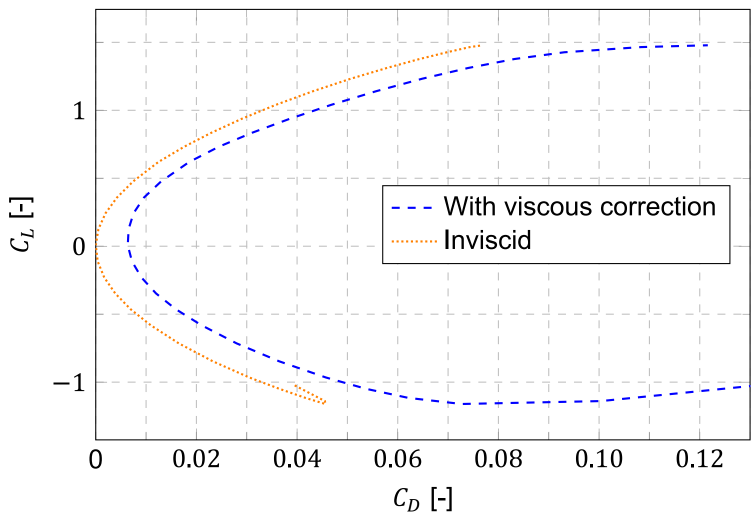

Figure 4.22: Comparison between inviscid and viscous drag polar

For propeller-wing interaction, the wing can be split in to two distinct parts: the part that is inside the propeller slipstream and the part that is outside the propeller slipstream. The part outside the propeller slipstream sees the undisturbed freestream velocity. The part inside the propeller slipstream encounters the propeller wake. This changes the boundary layer behaviour of this part of the wing. Some experiments have shown that the wing boundary layer in the propeller slipstream sees cyclic behaviour that goes from laminar to turbulent and back again for two or three bladed propellers [90][91]. A more recent experimental study showed that when the wing is inside the propeller slipstream the transition point is moved forwards compared to a clean wing [92]. Furthermore, when the number of blades is increased, the cyclic laminar-turbulent behaviour in the boundary layer is destroyed. Based on this, it was decided to use fully turbulent airfoil polars for the wing sections inside the propeller slipstream, since the propellers that will be used have four or six blades. It was also decided to use fully turbulent polars on the wing sections outside the propeller slipstream, this would be helpful for a Computational Fluid Dynamics (CFD) study, as the CFD model could also force transition, making the results comparable. In the end, this CFD study could not be accomplished within the time frame of this project. Finally, the XFOIL settings used for the fully turbulent airfoil sections were: $N_{crit} = 1$ and $x/c_{trip} = 0.05$ for both the upper and lower surface.

5 Integration and convergence of numerical tools

This chapter deals with the integration of the tools described in Chapters 3 and 4. In Section 5.1 it is described how the different numerical models are integrated to calculate the performance of a propeller-wing model. Section 5.2 discusses the convergence of the different numerical models. Finally, in Section 5.3 an indication of the computational time for these numerical models is given.

5.1. Propeller-wing interaction

By integrating the numerical propeller model, described in Chapter 3, and the wing model, described in Chapter 4, a propeller-wing system can be analyzed. Since the propeller and wing require the output of one another as input, the system is analyzed using a convergence loop, as shown in Figure 5.1. First the propeller is analyzed, as it is less dependent on the wing, than the other way around. This will give a good first estimate of the propeller inputs, which consist of the velocities on the wing and the velocities in the farfield, needed for the drag calculation. Then the wing is analyzed and using the wing induced velocities, the propeller inflow is defined and the propeller slipstream deflection is calculated. Then it is checked if the propeller and wing forces are unchanged (within margin) with respect to the previous iteration. If not, the loop will be repeated.

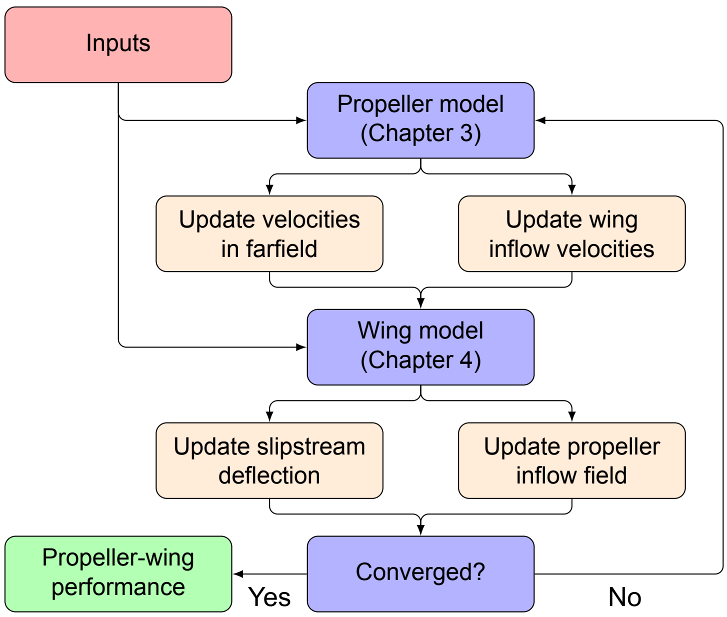

Figure 5.1: Flowchart for integration of the numerical propeller and wing model

To have the propeller and wing interact with each other, some coordinate transformations need to be carried out. The propeller and wing coordinate system both have the same general orientation. The x direction is backwards in the horizontal plane, the z direction is upwards and the y direction is to the left (when looking from the front) to complete the right-handed system. However, the coordinate systems are both oriented with respect to their respective angles of attack. Furthermore, the origin of the wing coordinate system is located at the wing center leading edge, and the origin of the propeller coordinate system at the propeller midpoint on the propeller plane. This is shown in Figure 5.2. Using a simple coordinate transformation, vectors and coordinates can be transformed from one to the other coordinate system. Finally, the forces that are relevant must be defined in a coordinate system aligned with the freestream velocity. Wing forces are always calculated in this coordinate system, but propeller forces must still be rotated if the propeller is under an installation angle.

By summing the forces a thrust, lift, drag and power are found for the propeller-wing system. This is shown in Equation 5.1, with a definition for the thrust and power coefficients in Equation 5.2.

$$
\begin{aligned}
L_{prop-wing} &= L_{wing} + T_{prop}\sin(\alpha_{prop}) + F_{z,prop}\cos(\alpha_{prop}) \\
D_{prop-wing} &= D_{wing} + F_{z,prop}\sin(\alpha_{prop}) \\
T_{prop-wing} &= T_{prop}\cos(\alpha_{prop}) \\
P_{prop-wing} &= P_{prop}
\end{aligned}
\tag{5.1}
$$

$$
\begin{aligned}
T_C &= \frac{T}{\frac{1}{2}\rho U_\infty^2 S} \\
P_C &= \frac{T}{\frac{1}{2}\rho U_\infty^3 S}
\end{aligned}
\tag{5.2}
$$

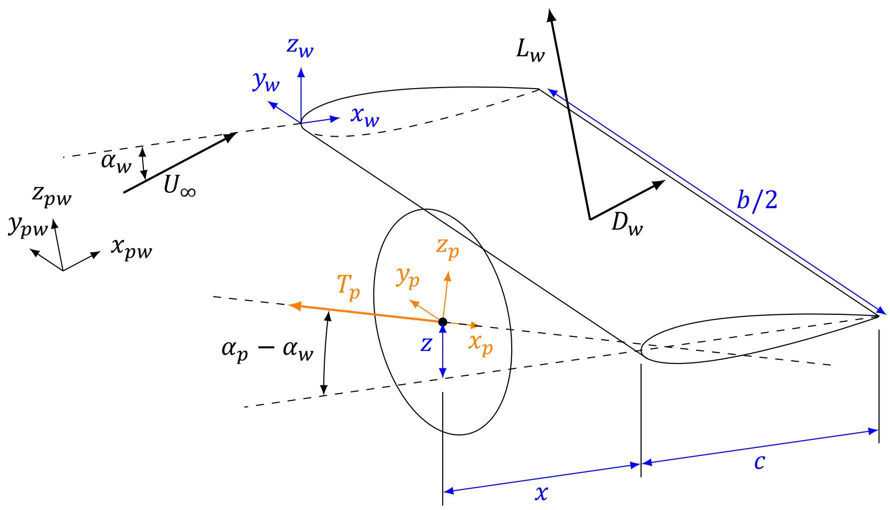

Figure 5.2: Schematic of the different coordinate systems used in the propeller-wing numerical model

5.2. Convergence

In this section the convergence study will be discussed. All the different modules that make up the propeller-wing analysis model will be tested individually first. The goal is to get the results of the entire system within approximately 1% of the asymptotic value. However, since the lift, drag, thrust and power coefficient can all have values around zero, it was chosen to translate this requirement to absolute values. This gives a maximum deviation of 0.001 for C_L, 0.0001 for C_D, 0.001 for C_T and 0.001 for C_P, based on typical values. For the intermediate results a conservative value of maximum 0.5% deviation from the asymptotic value is chosen, or half of the absolute requirements. At the end it is checked if this is sufficient for the full integrated model.

The presented results show a deviation from the results with the most refined point. So if there is a tool that produces result F, this F can be obtained using different levels of refinement. In this example, the number of panels determines the refinement. If F was evaluated with a maximum of 100 panels, then this F is equal to F_0. For a result with 10 panels $F_{p=10}$ is obtained and a deviation of $\Delta F = |F_{p=10} - F_0|$ can be calculated. This ΔF could again be divided by F_0 to normalize the result.

5.2.1. Convergence of the propeller model

The BEM code, as described in Section 3.1, uses a number of annular streamtubes along the blade span. This number is given by $N_{r/R}$. In Figure 5.3 it can be seen how C_T and C_P converge with $N_{r/R}$. It can be seen that the requirement for C_T and C_P is satisfied for $N_{r/R}$ above 30, where the deviation is lower than 0.0005. To have some margin, a radial discretization of $N_{r/R} = 40$ was chosen. This number will also be used in the subsequent non-uniform inflow model and slipstream model.

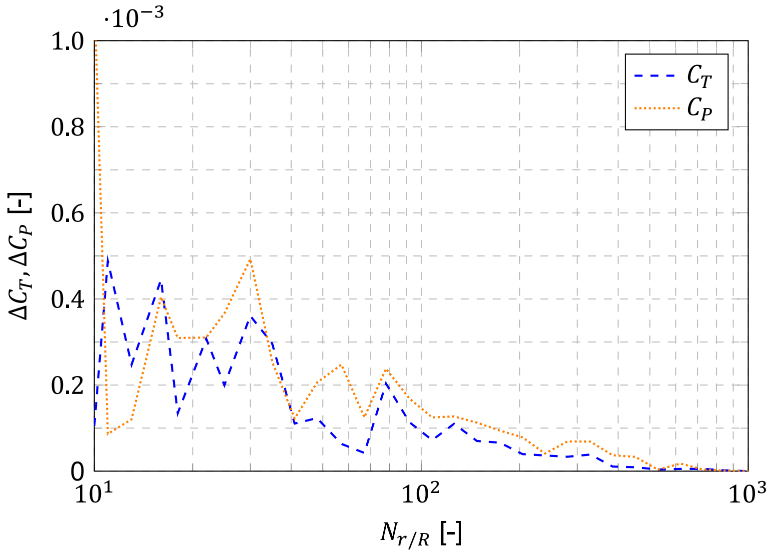

Figure 5.3: Convergence of the propeller performance for the number of radial stations

The non-uniform inflow model was described in Section 3.2. Here it was also shown that for high propeller angles of attack, the local advance ratio can become very large in magnitude. To eliminate errors from these large values of ΔJ, the non-uniform inflow model convergence was evaluated for a propeller at $\alpha = 5°$. The non-uniform inflow model requires a propeller performance map. This gives the performance of the propeller for a certain range of advance ratios. Between these available advance ratios, the propeller performance will be interpolated. Since C_T and C_P are practically linear in the parts of the performance map where non-linear effects are not dominating, a low number of points in this performance map can be used. This is shown in Figure 5.4. Here N_{points} is the number of points in the propeller map. It can be seen that with only a few points, the force and power coefficients show little deviation. Since computational cost is relatively low, $N_{points} = 7$ was chosen.

The non-uniform inflow model also uses a discretization in azimuth direction, which corresponds to timesteps per rotation. This number of azimuthal steps, N_ϕ, is shown to have little effect on the error, as shown in Figure 5.5. Even with $N_\phi = 10$, the model gives results within the requirements.

Finally, the circulation of the non-uniform inflow model is given to the slipstreamtube model. Thus, the radial and azimuthal discretization are the same as for the non-uniform inflow model. The convergence for these are given in Figures 5.6 and 5.7. It can be seen that the chosen $N_{r/R} = 40$ leads to a deviation of less than 0.05% U_∞, well below the requirement. For the azimuthal discretization $N_\phi = 30$ is found to be sufficient, although afterwards a small spike can be seen with a maximum deviation of 0.75% U_∞ for the axial velocity, it is expected that this has minor influence on the overall results and $N_\phi = 30$ should suffice.

Next the discretization in x direction is examined in Figure 5.8. Here N_x shows the number of steps in x direction per rotation. It can be seen that for $N_x = 12$ the error is below 0.5%. Since N_x is the number of steps per rotation, the total number of steps in x direction depends on the freestream

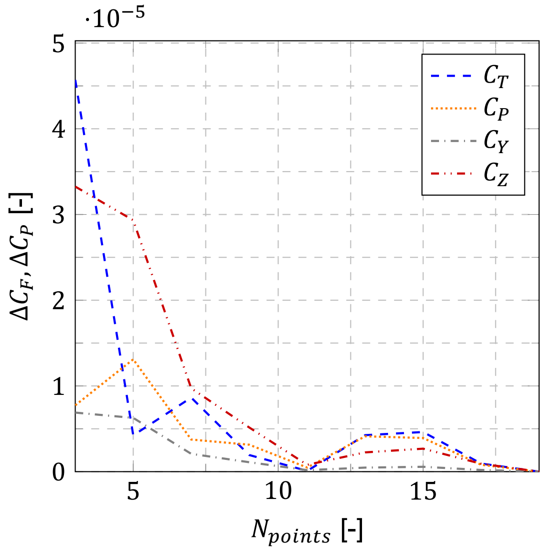

Figure 5.4: Convergence of the propeller performance for the number of points in the propeller performance map

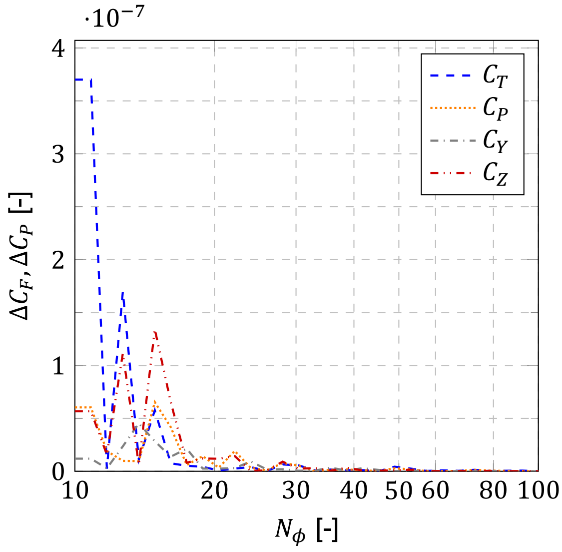

Figure 5.5: Convergence of the propeller performance for the number of azimuthal stations

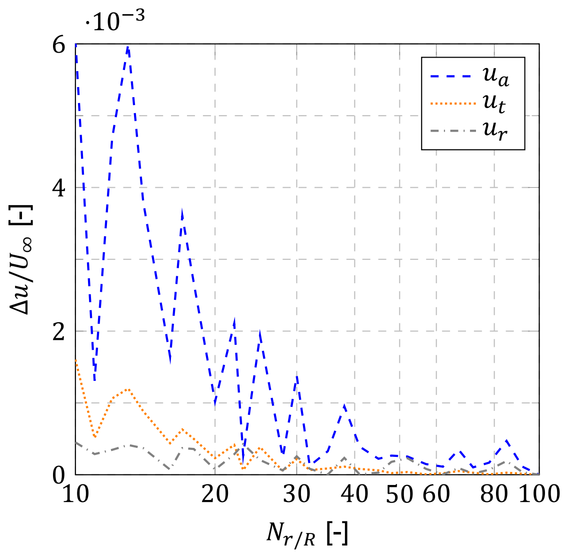

Figure 5.6: Convergence of the propeller induced velocities for the number of radial stations

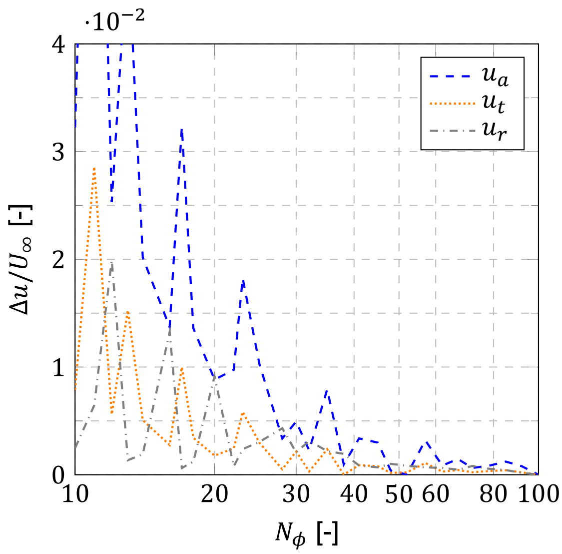

Figure 5.7: Convergence of the propeller induced velocities for the number of azimuthal stations

velocity, rotational speed and modelled length of the slipstream. This must be kept in mind, since certain combinations of these variables can lead to an excessively large number of steps in x direction, increasing computational time.

5.2.2. Convergence of the wing model

For the wing model the number of chordwise and spanwise panels is investigated. The results of this are shown in Figures 5.9 and 5.10. It can be seen that for the C_L the number of chordwise and spanwise panels must be about the same. For C_D the deviation is mainly dependent on the number of chordwise panels. Here a number of 30 satisfies the requirement of a maximum ΔC_D of 0.0001. This gives a number of spanwise panels of 26.

Next the convergence of the jet correction is discussed. The jet correction has been discussed in Section 4.3. The jet correction gives a correction on the Aerodynamic Influence Coefficient (AIC) matrix, this correction is denoted as G. Since G is a correction on the system to be solved, the influence is not one-to-one, as shown in Figure 5.11. It seems that a 10% deviation in G only leads to about

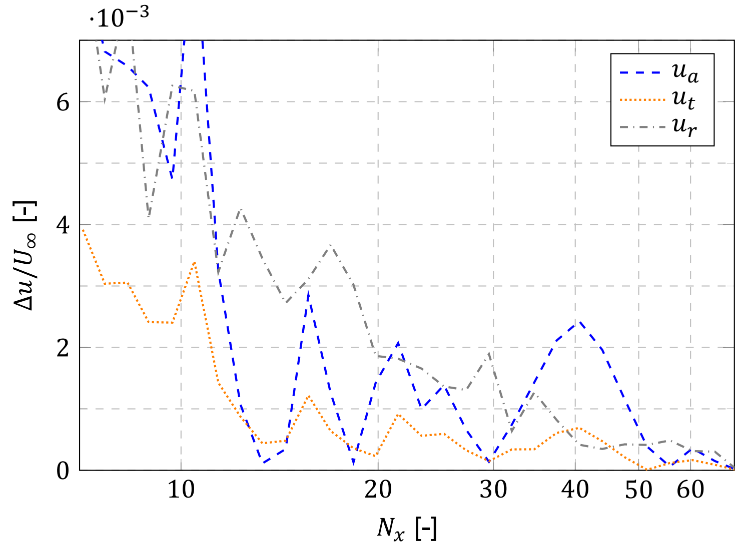

Figure 5.8: Convergence of the propeller induced velocities for the number of streamwise steps per rotation in the propeller slipstream

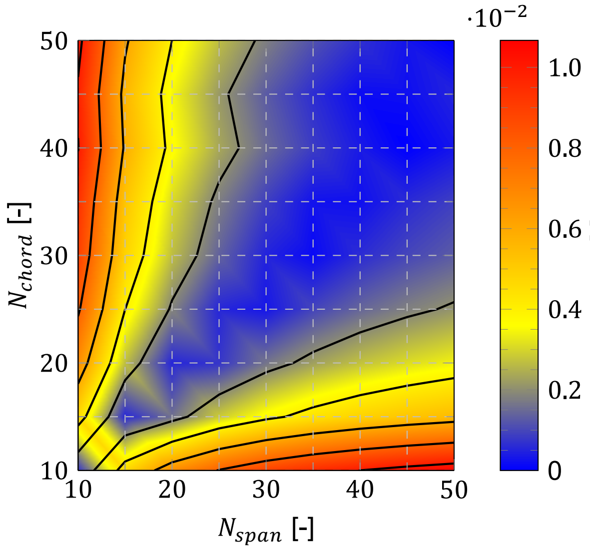

Figure 5.9: Convergence of the wing lift coefficient for the number of chordwise and spanwise panels

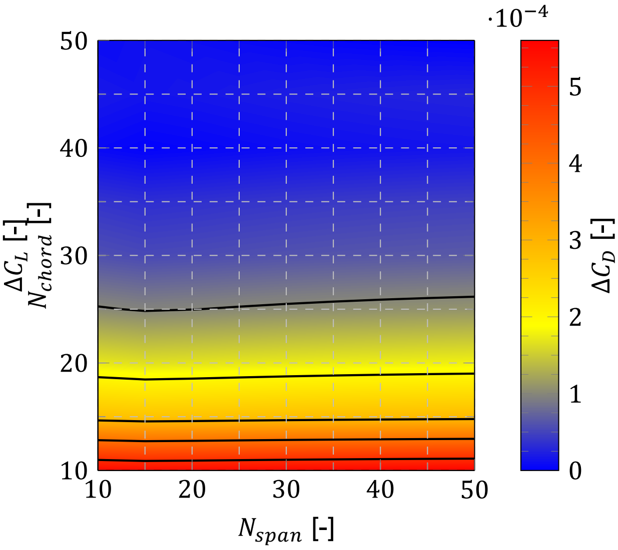

Figure 5.10: Convergence of the wing drag coefficient for the number of chordwise and spanwise panels

0.7% deviation in circulation. Thus, the convergence of the jet correction has been studied in terms of influence on the circulation. As the requirement for circulation, a maximum relative error of 0.01 or 1% was set.

In Equation 4.15 and 4.16 in Section 4.3 the expressions to calculate the jet correction were given. In Equation 5.3 one of these equations is repeated. It can be seen that there are two sum/integrals to infinity. And there are two integrals which need to be calculated numerically. Firstly, the upper limit of the sum determines the number and order of Bessel functions used. The convergence for this is shown in Figure 5.12. It can be seen that a sum of about 10 functions is enough. Next, there is the integral over variable λ with upper limit infinity. In Figure 5.13 it can be seen how the deviation decreases with increasing upper limit, λ_{up}. Here an upper limit of around 4 seems sufficient.

$$G_{jj_o}(\xi,\eta) = \frac{1}{r_j}\frac{8}{\pi\eta}\sum_{p=0}^{\infty}(2p+1)^2\int_0^{\infty}\frac{KK'I(\eta\lambda)\sin(\xi\lambda)}{\frac{1}{1/\mu^2-1}-\lambda IK'}\int_{c\lambda}^{d\lambda}\frac{I(\lambda\beta)}{\lambda\beta}d(\lambda\beta)d\lambda \tag{5.3}$$

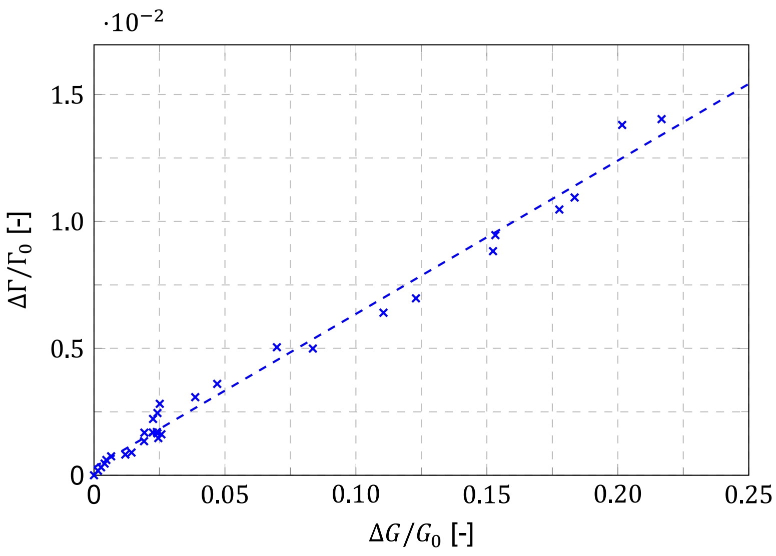

Figure 5.11: Relation between the error in jet correction and the error in circulation

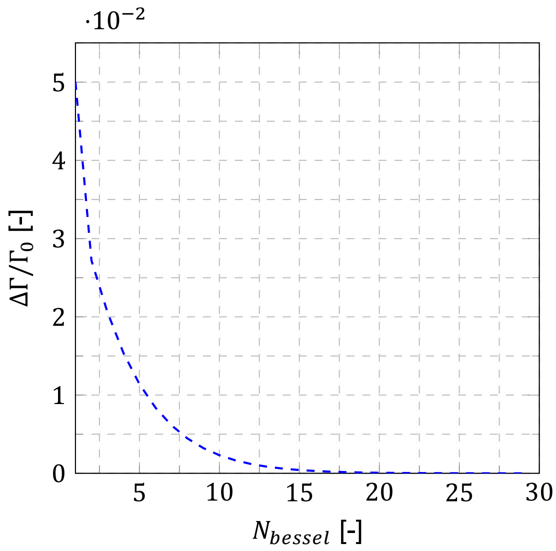

Figure 5.12: Convergence of the wing circulation for the number of Bessel functions

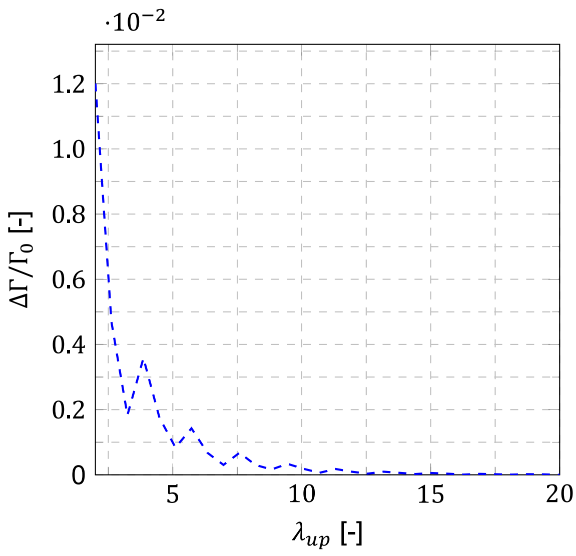

Figure 5.13: Convergence of the wing circulation for the upper limit of the integral of λ

The integrals from Equation 5.3 were calculated using a midpoint rule scheme. Thus, a step for λ and $\lambda\beta$ needs to be chosen. The convergence for these parameters is shown in Figures 5.14 and 5.15. In Figure 5.15 $d\lambda\beta$ has been normalized with the interval $[c\lambda, d\lambda]$, which gives $d\lambda\beta'$. To satisfy the requirements of a maximum deviation of 0.5%, $d\lambda = 0.1$ was chosen. For larger values of $d\lambda\beta'$ some diverging behaviour was found, where the sums and integrals would give values of infinity. Thus, $d\lambda\beta' = 0.005$ was chosen, which gives results well within the requirements.

5.2.3. Convergence of the propeller-wing model

The values of the numerical settings present in the model have been determined by looking at the deviation of the intermediate results from the respective asymptotical value. These values can be found in Table 5.1 in the column *Initial value*. To determine the convergence of the whole model all the settings were scaled by a scaling factor SF. By multiplying or dividing the initial settings by SF the convergence for the whole system is determined. With a higher SF, the model is more refined. So, for example, $N_{r/R}$ would be multiplied with SF, while $d\lambda$ would be divided by SF. The results of this investigation can be found in Figures 5.16 and 5.17, where the settings have been applied to a typical

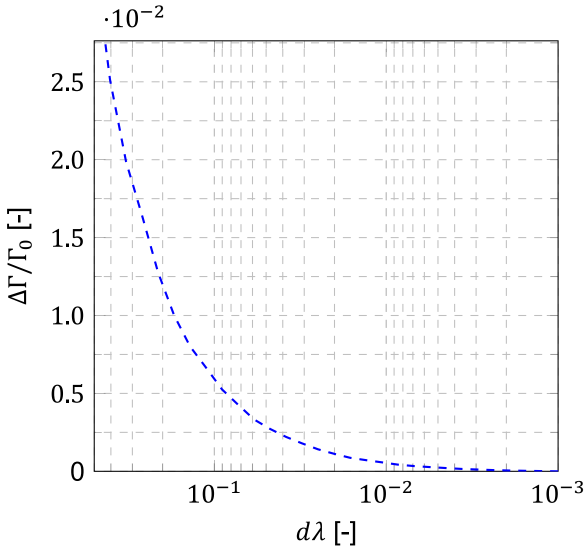

Figure 5.14: Convergence of the wing circulation for the numerical integration step λ

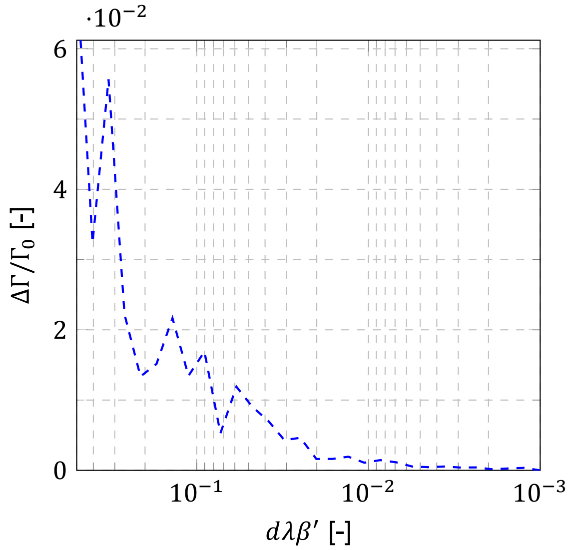

Figure 5.15: Convergence of the wing circulation for the numerical integration step $\lambda\beta'$

wingtip-mounted propeller case. It can be seen that at the initial settings or $SF = 1$, the deviations from the asymptote are below the defined requirements. Thus, the final settings were chosen at $SF = 0.8$, which decreases computational time. These final values can be found in Table 5.1.

Table 5.1: Results of the convergence study

	Initial value	Final value
$N_{r/R}$	40	32
N_{points}	7	7
N_{ϕ}	30	24
N_x	12	9
N_{chord}	30	24
N_{span}	26	20
N_{bessel}	10	8
λ_{up}	5	4
$d\lambda$	0.1	0.125
$d\lambda\beta'$	0.005	0.005

5.2.4. Convergence of the iterative loop

As shown in Figure 5.1, the propeller-wing interaction must be solved iteratively. The iterative loop is started by a propeller analysis, as the propeller performance is the least affected by the interaction. When updating the input for the propeller and wing model, a residual can be calculated, which is the difference between the parameters of the current iteration and the previous iteration. This residual is will be referred to as the convergence residual. The solution has converged when this residual is below the constraints of 0.001 for C_L, 0.0001 for C_D, 0.001 for C_T and 0.001 for C_P. In Figure 5.18 the development of the residual for a typical case can be seen. All parameters show nice converging behaviour and seem to converge with the same rate. C_T and C_P show lower residuals of about an order of magnitude smaller than C_D, since C_T and C_P are less affected by the interaction effects. Thus, C_L and C_D are the critical parameters for convergence. It can be seen that convergence is typically reached within two iterations, which corresponds to three evaluations of the propeller-wing model.

While the iterative loop usually shows converging behaviour, there are some cases where this does not occur. This typically happens for cases with high thrust. In Figure 5.19 an example is shown of the behaviour for such a case. While C_T and C_P converge, C_L and C_D do not show strong converging behaviour. C_D shows a great reduction in residual for up to iteration three, but after that no large residual

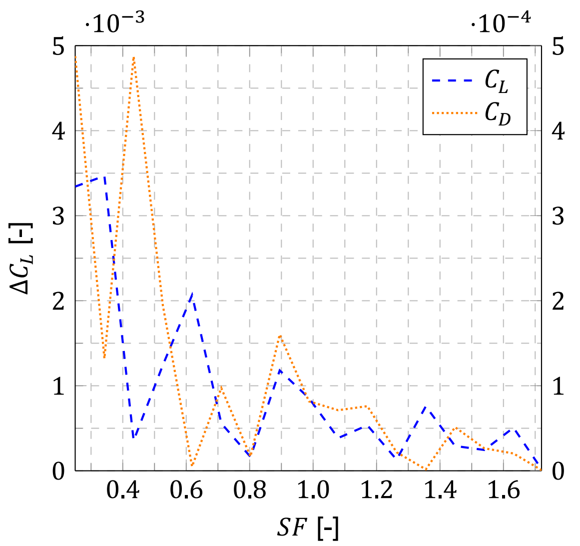

Figure 5.16: Convergence of the wing lift and drag by applying a scaling factor to the numerical settings

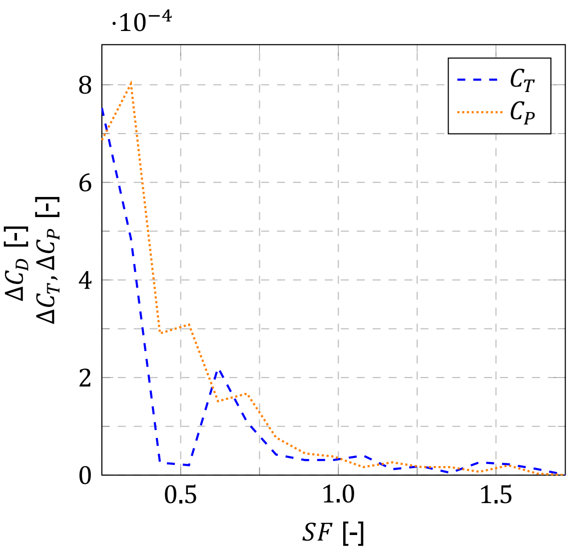

Figure 5.17: Convergence of the propeller thrust and power by applying a scaling factor to the numerical settings

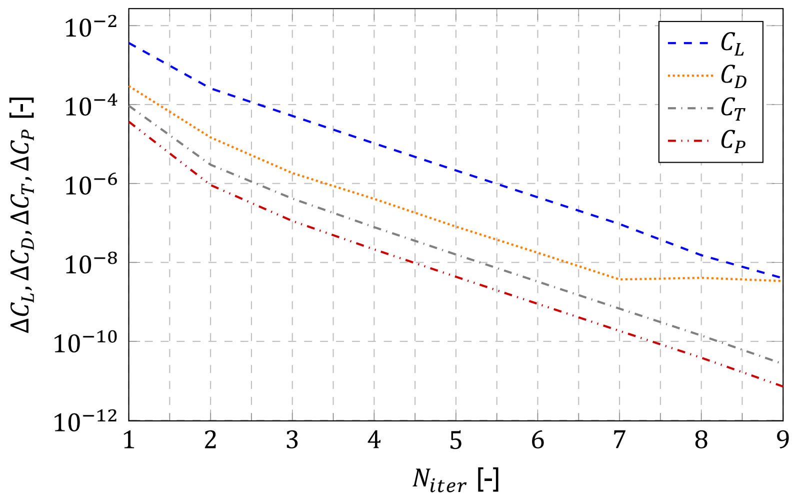

Figure 5.18: Typical iterative convergence for the propeller-wing model

decrease is observed. The residual of C_L even seems to be somewhat constant, with little change from the first iteration. To avoid that the model will try to converge such a non-converging case, the maximum number of iterations was set to three. This way the cases that show converging behaviour will converge, while it prevents these non-converging cases to iterate infinitely.

5.3. Computational time

In Figure 5.20 a breakdown is given for the computational time. This analysis was done on a system with a 2.2 GHz Intel Core i7-8750H processor with 16.0 GB installed RAM. It can be seen that the computational time needed for the propeller model is almost constant for different numerical settings. The time needed to calculate the induced velocities and analyze the wing model scale almost quadratically with the scaling factor. With more refined numerical settings, the arrays used become very large, thus the amount of RAM becomes limiting, which could potentially lead to higher computational times if not enough RAM is available.

Each evaluation of the propeller-wing model for the chosen scaling factor of 0.8 takes about 40 seconds. In order to converge typically three to four evaluations are needed. Furthermore, some extra time is needed to read polar files, resulting in a total analysis time of between 150 to 210 seconds.

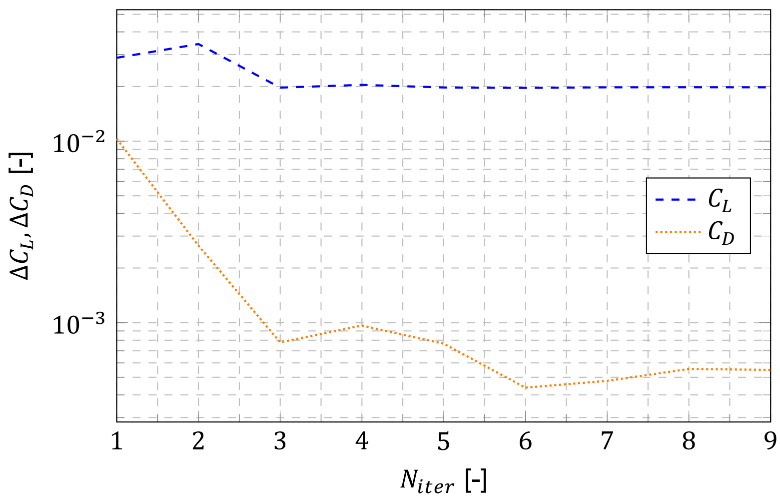

Figure 5.19: Non-converging behaviour found for the propeller-wing model at high thrust settings

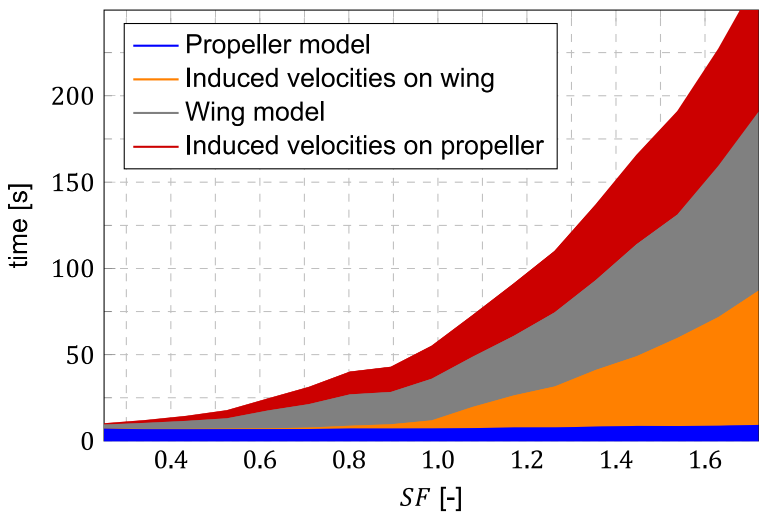

Figure 5.20: Breakdown of the computational time of a single evaluation of the propeller-wing model for different numerical settings based on the average of 25 runs

6

Validation

In this chapter the numerical tools are validated using experimental data. First the isolated propeller model and isolated wing model will be validated in Section 6.1 and 6.2 respectively. Finally, in Section 6.3 the integrated propeller-wing model is validated.

6.1. Isolated propeller

The first set of validation data is from a series of windtunnel measurements by Sinnige et al. [41]. The experiments were carried out in the Low-Turbulence Tunnel at Delft University of Technology, with a turbulence level of around 0.1%. The propeller model is a four-bladed propeller with a diameter of 0.237 m. This propeller is called the PROWIM propeller. The blade pitch is defined at 75% radius and is set at $23.9°$. The radial distribution of the chord and twist can be found in Figure 6.1. For this isolated propeller case the propeller was sting mounted, as shown in Figure 6.2. The measurements were done using an external balance. To not measure the forces acting on the sting, a separately supported sleeve was put around the sting. Furthermore, the leading edge of the sleeve was 1.5 times the propeller diameter away from the propeller, practically eliminating upstream effects on the propeller. The propeller is also attached to a nacelle with a diameter of 0.070 m. To exclude the nacelle effects in the data, measurements were done with a dummy hub and spinner, which gives a blades-off model. By subtracting the blades-off forces from the measurements, the isolated propeller forces are obtained, neglecting the interference components.

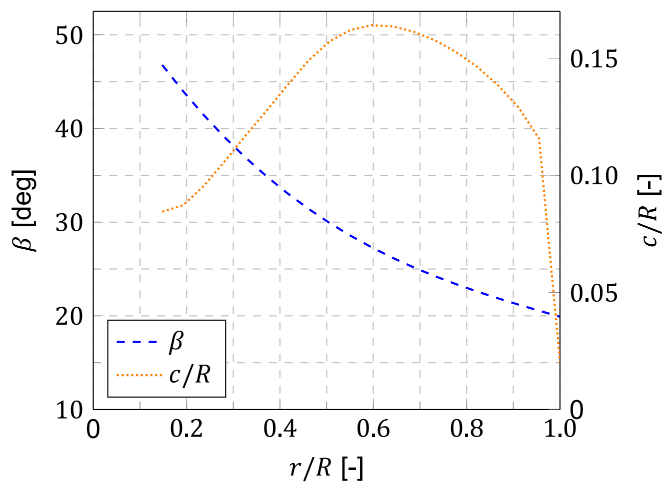

Figure 6.1: Twist and chord distribution of the PROWIM propeller

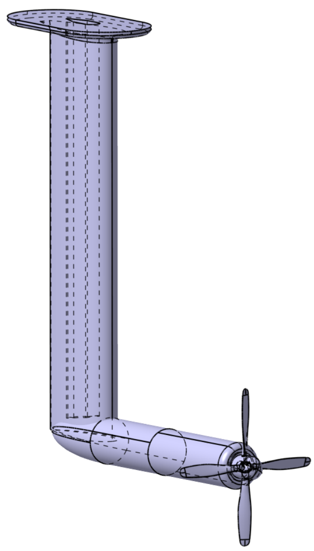

Figure 6.2: CAD model of the windtunnel setup for the PROWIM propeller [41]

In Figures 6.3, 6.4 and 6.5 the propeller performance with changing advance ratio can be found. It can be seen that the numerical results follow the same trend as the experimental results, but an offset is seen. By changing the pitch angle in the numerical model by $-1.2°$, a much better match is found. This offset could be caused by a simple geometry modelling error. However, the twist distribution is known from technical drawings and CAD models, thus a geometry modelling error seems unlikely. The offset can also be caused by the presence of the nacelle, which is not taken into account in the numerical model. Although the data is corrected for nacelle forces, the interaction effects are not accounted for. However, at such a low angle of attack no significant forces are produced on the nacelle [93]. Thus, it is assumed that there are no vorticity induced velocities of the nacelle on the propeller. There is also blockage from the nacelle, which is not modelled in the numerical model. However, this will mainly affect the part of the propeller near the hub, where forces are relatively low, thus it is expected that this has little influence on the performance of the propeller.

Thus, the offset is most likely caused by errors in the 2D airfoil polars. For the analyzed range of operating conditions, the Reynolds number on the blade sections are relatively low. Typically, the maximum Reynolds number of the blade would be between $1 \cdot 10^5$ and $1.5 \cdot 10^5$, while the lowest Reynolds numbers are around $3 \cdot 10^4$. For lower Reynolds numbers, the importance of viscous effects increases. This makes it harder for numerical methods to make accurate predictions at lower Reynolds numbers [94]. This could cause an offset in propeller performance with respect to the windtunnel data. In the subsequent results of this propeller, this offset of $-1.2°$ will be applied to the propeller pitch for easier comparison of the results.

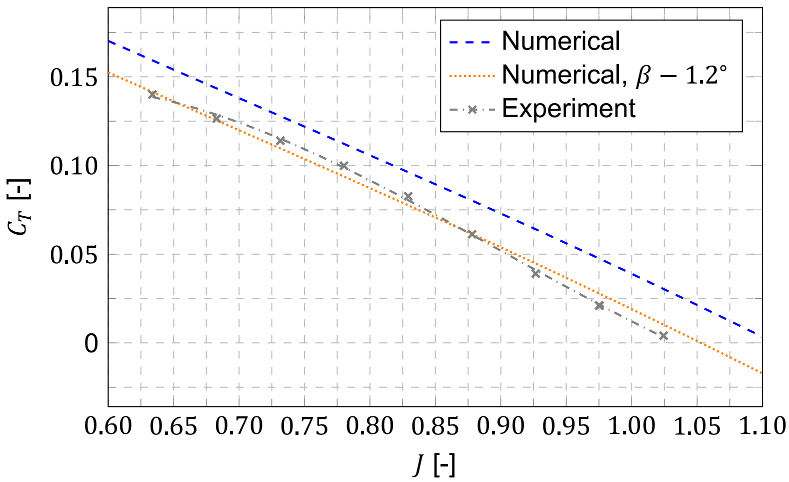

Figure 6.3: Propeller thrust coefficient with varying advance ratio for the PROWIM propeller at $\alpha = -0.2°$ and $Re_D = 620,000$

Next to the offset, some differences in behaviour can be seen. For the thrust, as shown in Figure 6.3, the numerical results seem almost linear, while the experimental data has a wave-like shape. It is suspected that this is caused by the fact that the non-linear regime of the blade airfoils can not be modelled accurately by the numerical model. The numerical model relies on 2D airfoil lift and drag curves to calculate the propeller forces. However, at very low or high advance ratios large parts of the propeller blade will operate in the non-linear regime. For the parts of the propeller in the non-linear regime, the propeller forces cannot be accurately calculated by simple 2D panel methods. Furthermore, 3D effects can change the stall behaviour at a radial station [95]. So in these areas the numerical model will produce inaccurate results. While the differences are quite small for C_T, in Figure 6.4 it can be seen that the difference in C_P between numerical and experimental data increases for decreasing advance ratio.

In Figure 6.6 the effect of Reynolds number can be seen. For the experimental data it is observed that the thrust coefficient is slightly higher for higher Reynolds numbers. This increase in C_T is also seen in the numerical data. However, at higher advance ratios this increase is underestimated. This could again be caused by inaccuracies of the blade section polar data. At higher advance ratios, the rotational speed is lower, thus the Reynolds numbers on the propeller blades are also lower. This would make it more likely that the effect of Reynolds number could not be modelled accurately. Thus, the effect of Reynolds number on propeller performance is underestimated at higher advance ratios.

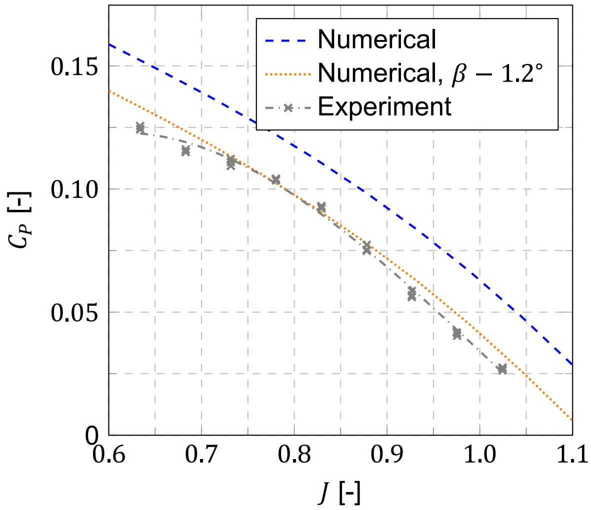

Figure 6.4: Propeller power coefficient with varying advance ratio for the PROWIM propeller at $\alpha = -0.2°$ and $Re_D = 620,000$

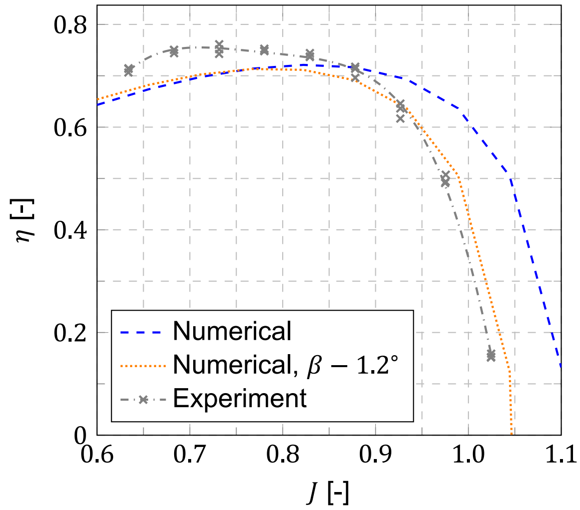

Figure 6.5: Propeller efficiency with varying advance ratio for the PROWIM propeller at $\alpha = -0.2°$ and $Re_D = 620,000$

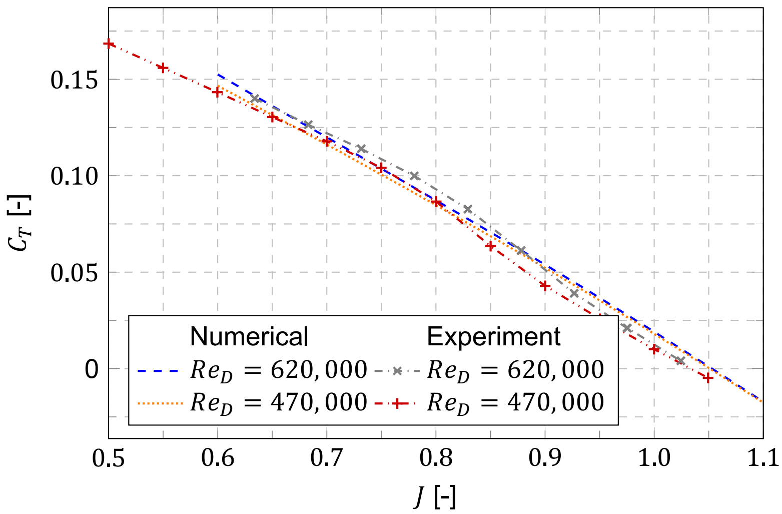

Figure 6.6: The effect of Reynolds number on propeller thrust coefficient for the PROWIM propeller at $\alpha = -0.2°$

The effect of angle of attack is shown in Figure 6.7. Here the thrust coefficient is shown for two advance ratios. In the experimental data it can be seen that thrust coefficient increases for increasing angle of attack. But, when the advance ratio is decreased, the magnitude of this effect decreases. It can be seen that the numerical model also shows an increase of thrust for increasing angle of attack. This effect does not seem to be captured by the numerical model. This means that the increase in C_T with increasing α is overestimated for low advance ratios and underestimated for higher advance ratios. This can possibly be explained by the presence of the nacelle, which is not modelled in the numerical model. Due to the differences in thrust on the propeller blades, a non-axisymmetric pressure field is created on an axisymmetric nacelle [93]. This pressure field differs from the nacelle pressure field without propeller and is thus not accounted for in the measurement data. For a propeller under angle of attack it was found that this pressure distribution generated mainly a side force on the nacelle due to the difference in thrust on the advancing and retreating (left/right) side of the propeller. This gives a different dynamic pressure on both sides, which leads to a difference in pressure and a resulting force. The skewing of the wake axis also creates a thrust difference in top and bottom side of the propeller [60]. This changes the dynamic pressure and thus pressure distribution on the top and bottom side of the nacelle with respect to the nacelle without propeller. This increases circulation around the nacelle, resulting in an added force. This process is shown in Figure 6.8, where a + denotes an increase and

– a decrease. The resulting force F can be decomposed in a thrust/drag and lift component. It is expected that this creates the difference in C_T between the numerical and experimental data, as shown in Figure 6.7.

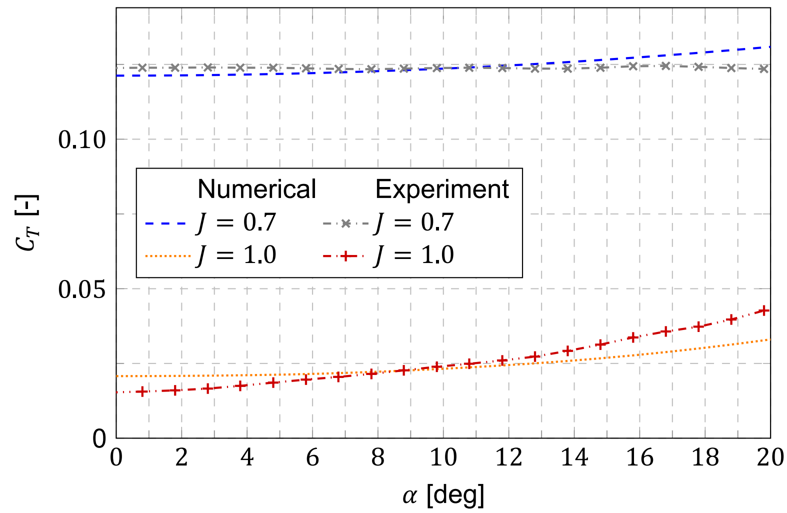

Figure 6.7: The effect of angle of attack on propeller thrust coefficient for the PROWIM propeller at $Re_D = 620,000$

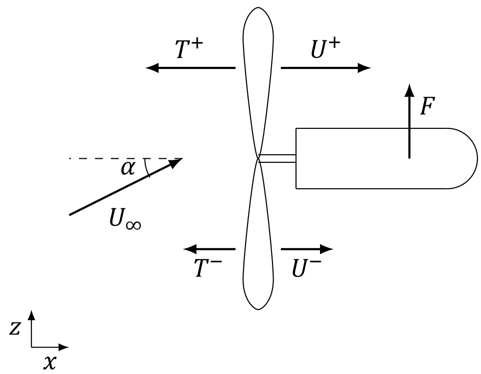

Figure 6.8: Creation of nacelle forces due to the difference in thrust on the propeller

The second set of validation data for the isolated propeller is from a series of windtunnel measurements done at the Open-Jet Facility at Delft University of Technology [96][97][98]. This windtunnel provides a turbulence level of about 0.5%. The model used, was a TUD-XPROP propeller model with six blades and a diameter of 0.4046 m. The data used here is for a pitch angle of $20°$ at $r/R = 0.7$. The corresponding radial distribution of twist and chord are shown in Figure 6.9 and a picture of the propeller is given in Figure 6.10.

In Figure 6.11 the results can be found for the TUD-XPROP propeller. There are two effects that can be investigated here. The first one is the change in thrust due to advance ratio. It can be seen that the numerical model predicts the right trend, but there is an offset with respect to the validation data. This offset seems to be around the same magnitude as the offset found in the first data set and could be corrected for by a small change in pitch setting. It can be seen that for high advance ratios, the difference between experimental and numerical data is increasing. This suggests an effect of Reynolds number on the propeller blades. At higher advance ratio, the rotational decreases, giving lower Reynolds numbers on the blades. For these Reynolds numbers it is harder to predict the lift and drag curves using numerical models. Thus, larger errors are expected at higher advance ratios. The second effect that is shown in Figure 6.11 is the effect of propeller Reynolds number Re_D. For the experimental data an increase in C_T is seen for an increasing propeller Reynolds number. The same is seen in the numerical data. However, it can also be seen that at the same advance ratio, the difference between the experimental data and numerical data is lower for higher Re_D. This can mainly be seen

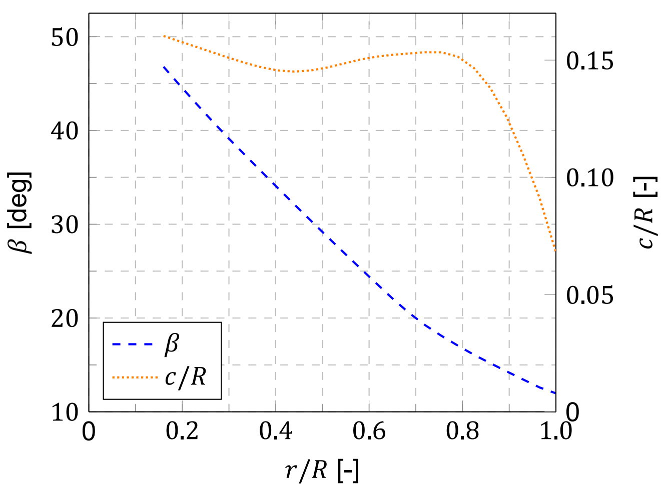

Figure 6.9: Twist and chord distribution of the TUD-XPROP propeller

Figure 6.10: Windtunnel model of the TUD-XPROP propeller [96][97][98]

when comparing the data for $Re_D = 317,000$ and $Re_D = 475,000$ for $0.35 < J < 0.5$. The smaller difference at higher Re_D suggests that the difference between the experimental and numerical data is caused by modelling errors due to low Reynolds numbers on the propeller blade.

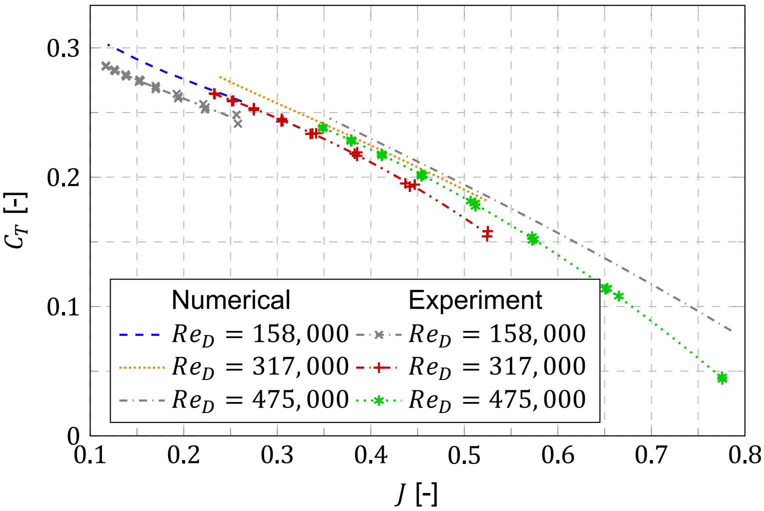

Figure 6.11: The effect of Reynolds number on propeller thrust coefficient for varying advance ratio for the TUD-XPROP propeller at $\alpha = 0°$

To conclude, the propeller model predicts the main trends found with varying advance ratio, Reynolds number and angle of attack. In both the PROWIM and TUD-XPROP analysis an almost constant offset in C_T and C_P was found between the numerical and experimental data. This seems to be caused by inaccurate modelling of the airfoils polars, since the propellers operate in conditions that give relatively low Reynolds numbers on the propeller blades. Lower Reynolds numbers increase the importance of viscous effects, which are hard to model accurately by numerical tools. This gives an offset in the propeller performance when comparing the numerical model to the windtunnel data. In the case of the PROWIM propeller a much better match was found by changing the pitch with $-1.2°$. Despite the offset, the numerical model seems to predict most trends accurately, but not for cases where non-linear effects are significant. This is for high (positive or negative) angles of attack on the blades and for low propeller Reynolds numbers.

6.2. Isolated wing

The isolated wing is validated using experimental data from Koomen [84]. The experiments were conducted in the Low-Turbulence Tunnel at Delft University of Technology with a half model. A *ground board* is used as a reflection plane at the root of the half wing. The airfoil used by this wing is the NACA64$_2$A015 airfoil, a symmetrical NACA 6-series airfoil with modified trailing edge. Two configurations are available: one with a smooth wingtip fairing and one with a nacelle. It is expected that the data with the smooth wingtip will provide the best match with the numerical results. However, also the data with the nacelle are plotted, to get an idea of the influence of the nacelle, since the nacelle is not modelled by the numerical model. In Figure 6.12 the geometry for the two configurations can be seen.

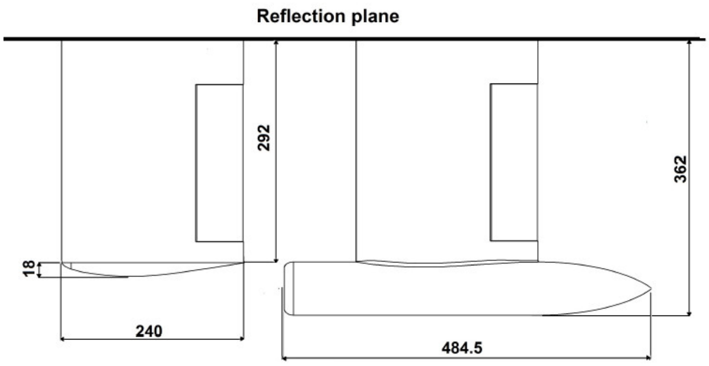

Figure 6.12: Geometry of the validation wing [84]

Total forces

In Figures 6.13 and 6.14 the results can be found. Here the validation data is obtained using an external balance. Using the numerical model the wing geometry with and without nacelle is approximated. For the wing without nacelle, a halfspan $b/2$=0.292 m was chosen. Extending the wing to account for the fairing of 18 mm did not lead to significant change in the results, thus this value was kept. For the configuration with nacelle, the wing was extended to $b/2$=0.362 m. So in the numerical model, the wing is extended with the span of the nacelle, with the same NACA64$_2$A015 airfoil as on the rest of the wing. The results presented are normalized with the clean wing area, so S=0.14 m^2.

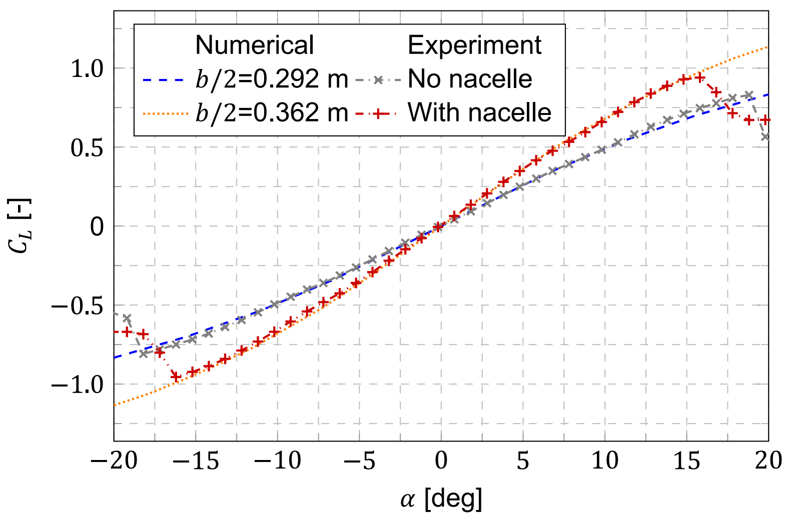

Figure 6.13: Lift for the validation wing

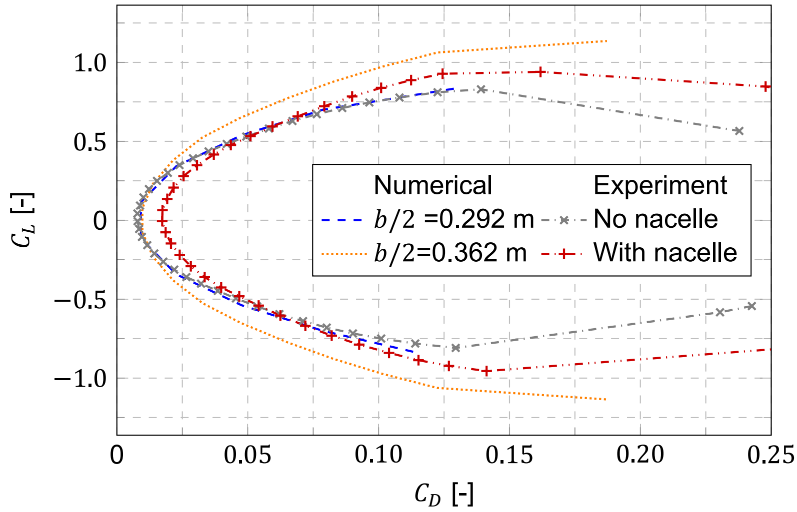

Figure 6.14: Drag for the validation wing

First the data for the wing without nacelle is compared. This case is expected to show the best match with the numerical results. As can be seen in Figure 6.13 the lift matches very well in the linear part of the lift curve. When approaching $C_{L,max}$ the lift curve slope decreases a little, which is also well modelled due to the viscous correction of the numerical model. Finally, after $C_{L,max}$ the wing stalls and lift decreases suddenly. This is not captured by the viscous correction, since the flow is fully separated here, which is not captured well by low-order models. In Figure 6.14 it can be seen that the predicted drag shows good agreement with the validation data up to $C_{L,max}$. When the wing stalls, the drag increases rapidly due to increasing pressure drag. Pressure drag is not modelled by the numerical model. Furthermore, at $C_L = 0$, induced drag $C_{D,i} = 0$. So all the drag in this case is from the viscous correction. It can be seen that the drag coefficient at $C_L = 0$ matches with the experimental data, so the viscous drag is calculated correctly.

Now the case with nacelle is examined. In Figure 6.13 it can be seen that the lift is very well approximated by the numerical model. For the case with nacelle some differences were expected, since the nacelle has a larger chord and a different shape from the airfoil. The lift calculated by the numerical model shows the same behaviour as for the case without nacelle, so the nacelle can effectively be seen as an increase of aspect ratio. Again, the same discrepancies are found when the wing enters stall. When looking at the drag coefficient in Figure 6.14, large errors can be found for the case with nacelle. However, the error seems to be a somewhat constant offset in C_D. This constant offset is most likely due to the difference in the estimated profile drag. The cross-sectional shape of the nacelle has less influence on the induced drag, but profile drag is highly dependent on the cross-sectional shape. The nacelle in the numerical model has the same cross section as the rest of the wing, while in reality the chord is longer and the shape is less aerodynamic. This would increase friction drag, thus the drag predicted by the numerical model is underestimated. So, the numerical model still gives the right behaviour for lift and drag for a wing with nacelle, but the drag is underestimated. This must be taken into account when modelling a wing with nacelle.

Spanwise distribution

Next to the external balance data, also pressure data was available, so the spanwise lift distribution can be compared. This is shown in Figure 6.15. The data is normalized using $b/2$=0.292 m for the case without nacelle and $b/2$=0.362 m for the case with nacelle. In Figure 6.15 it can be seen that the lift is over predicted by the numerical model for the case without nacelle. This is peculiar, since the external balance data shows a good match with the numerical results. The same holds for the case with nacelle. There are slight differences in lift distribution, while the external balance measurements are in accordance with the numerical results. Furthermore, the data for the case with nacelle also seems to show some noise.

For these pressure measurements it was suspected that the flap present in the wing might not exactly at zero deflection, which could explain the slight difference in sectional wing lift. The flap is located at spanwise position $0.10 < y/b < 0.45$ for the case without nacelle and $0.08 < y/b < 0.36$ for the case with nacelle. This could lead to slightly higher or lower lift in this area simply due to the difference in aerodynamic shape. Furthermore, trailing vortices that originate at the ends of the flap can influence the lift distribution near the ends of the flap. It is hard to say if this small flap deflection had a significant influence on the lift distribution, since no datapoints outside this area are available. This makes the data hard to compare, but it can be seen that the predicted change in lift due to the wing extension by nacelle has the right magnitude. Since the total forces are predicted correctly, this builds confidence that the numerical model produces accurate results.

A comparison for the drag could not be made. In the experiment, the spanwise drag distribution consists of pressure drag. In the numerical model drag can only be split into induced drag and profile drag, thus no useful comparison could be made here.

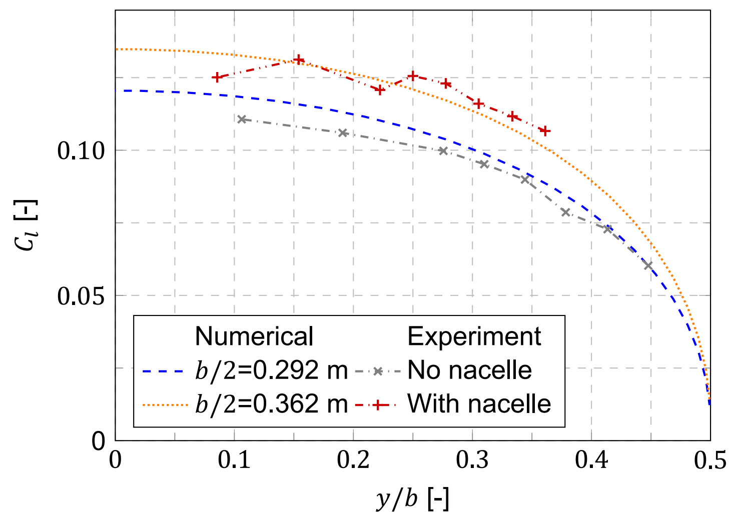

Figure 6.15: Spanwise lift distribution of the validation wing at $\alpha = 2°$

To conclude the wing validation, the lift and drag are predicted accurately by the numerical model up to $C_{L,max}$. Beyond $C_{L,max}$, the decrease in lift and increase in drag are not captured by the numerical model. The nacelle is modelled in the numerical model by an extension of the wing, using the same airfoil profile as the rest of the wing. This gives accurate results for lift, but drag is underestimated by the numerical model. This is likely because profile drag is underestimated, since the nacelle cross sectional shape will give a higher profile drag than the airfoil section used in the numerical model. Lastly, spanwise lift distribution given by the numerical model is close to the one given by experimental data, but some differences are found in magnitude and shape. These differences seem to result from errors in the test setup.

6.3. Propeller-wing

With the validation of the propeller model and wing model described in the previous sections, the propeller-wing system can be validated. This is done using experimental data from Sinnige et al. [41]. The model used, consists of a wing with the NACA 64_2A615 cambered airfoil of which the dimensions can be found in Figure 6.16. At the wing tip a nacelle is located with a four-bladed propeller. This model is the PROWIM propeller as described in Section 6.1. Here again the propeller pitch of the windtunnel model was set to $23.9°$ at $r/R = 0.75$. The x-distance from the wing leading edge to the propeller centerpoint is $0.853R$, and the z-distance is $0.042R$. The forces of the propeller-wing system were obtained using an external balance.

The wing modelled by the numerical model has a span of $2 \cdot 0.952 \cdot 0.730$=1.39 m. This slightly lowers the aspect ratio of the wing, but it ensures that the propeller is located in the right place, since the propeller in the numerical model has to be aligned with the wingtip in order for the jet correction to be applied. Furthermore, a transition strip was applied to the wing at $x/c = 0.12$, so most of the wing would see turbulent flow. Thus, it was chosen to use fully turbulent polars for the viscous corrections of the wing. Since a modelling offset was found in the validation of the propeller, it was chosen to correct for this offset, so the validation can focus on the interaction effects. This means the pitch of the propeller was changed to $22.7°$.

Results are presented for three cases. Firstly, the wing data is presented for the propeller-off (prop-off) case, where no propeller is installed. Next to this, two cases with an installed wingtip-mounted propeller are presented: one with $J = 0.9$ and one with $J = 0.7$.

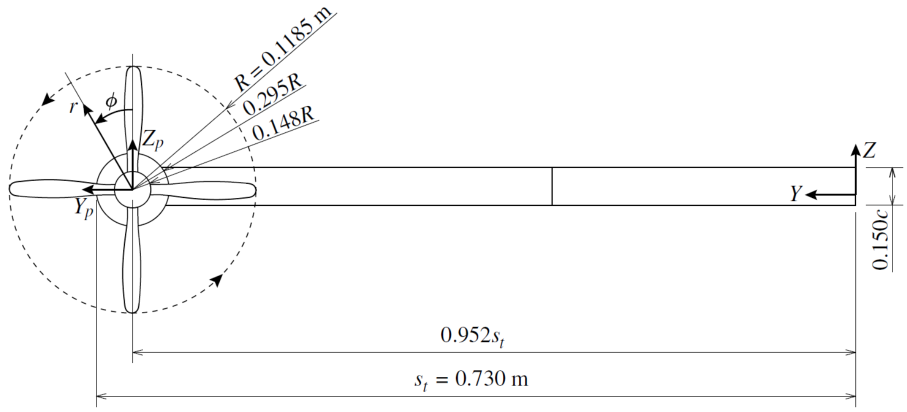

Figure 6.16: Geometry of the propeller-wing system used for validation

In Figure 6.17 the lift polar can be found for the propeller-wing system. It can be seen that in the prop-off case the numerical model underestimates the lift curve slope. This is probably caused by the difference in aspect ratio of the two wings. However, these differences are relatively small and expected for a slight change in aspect ratio. With decreasing advance ratio, or increasing thrust, the lift increases. This is the case in both the numerical data and validation data. The increase in lift for the linear part of the lift curve is similar for both the numerical and validation data. It can be seen that the difference between the prop-off and $J = 0.9$ conditions is very small. For the case with $J = 0.7$ the change is more pronounced.

For the validation data, the lift curve slope increases from the prop-off to $J = 0.7$. The numerical model still predicts a curve slope increase, but this increase is underestimated. At higher angle of attacks this leads to a big difference in performance. This difference in lift curve slope could be cause by a modelling error of the propeller slipstream. When the propeller is at an angle of attack, the slipstream will bend downwards, due to added axial velocity, but eventually becomes more aligned with the freestream velocity. This phenomenon has a great effect on the induced angle of attack on the wing. Thus, improper modelling here could lead to a difference in lift curve slope. Another influence on the lift curve slope is the nacelle. There are two ways the nacelle forces change due to propeller interaction [39]. A propeller under an angle produces different amounts of thrust at different azimuthal positions. This gives different amounts of dynamic pressure in the propeller wake for different azimuthal positions. In the case of a propeller under angle of attack, this increases the normal force. The second phenomenon is the roll up of the propeller hub vortices along the suction side of the nacelle, which results in a low pressure on the suction side, further increasing the normal force on the nacelle. While the first effect is captured by the propeller slipstream model, the second is not. Since this effect is both dependent on angle of attack and thrust, this could explain the discrepancy in lift curve slope.

In Figure 6.18 the system drag is shown for the propeller-wing system, consisting of propeller thrust and wing drag, as well as smaller contributions from propeller in-plane forces. In the prop-off condition the drag is underestimated by the numerical model, due to the presence of the nacelle. The part of the nacelle modelled in the numerical model has an airfoil cross section. In reality the nacelle has a larger chord than the airfoil and a less aerodynamic shape which increases the friction drag. This has also been explained in Section 6.2. This difference in friction drag between the experimental and numerical results would increase with increasing dynamic pressure. When the thrust increases with decreasing advance ratio, the dynamic pressure over the nacelle is increased, thus the difference in drag is larger. Furthermore, the modelling of the propeller slipstream deflection, as mentioned before, could also affect the drag by modelling a slightly different induced angle of attack.

For the spanwise lift distribution experimental data from Koomen [84] was used. The propeller-wing

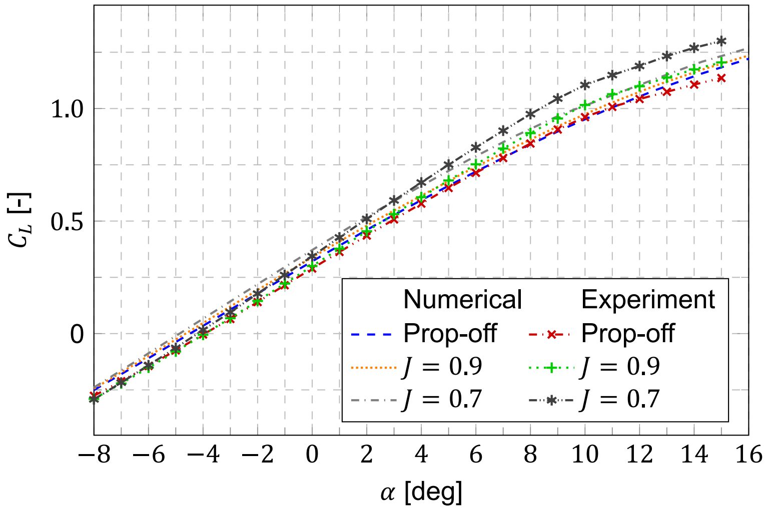

Figure 6.17: Lift for the validation propeller-wing system

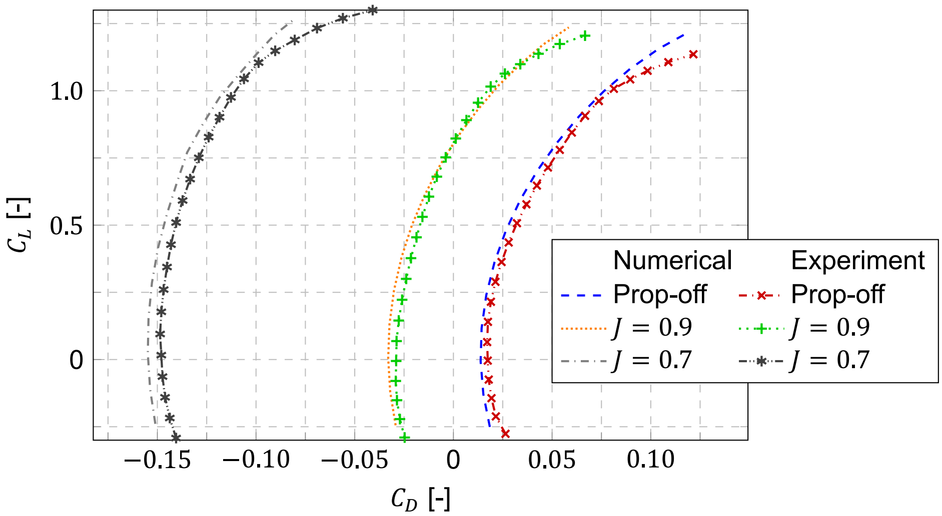

Figure 6.18: Drag for the validation propeller-wing system

model uses the same wing as shown in Figure 6.12 and it uses the same PROWIM propeller as the model used by Sinnige et al. [41]. To model the wing a half span of $b/2 = 0.327$ m was used, so the propeller would be in the right position, since the jet correction in the numerical model only works for a propeller mounted exactly at the wingtip. The results of this comparison can be found in Figure 6.19, where the results are normalized with $b/2 = 0.327$ m. With a propeller diameter of 0.237 m the wing area directly in the propeller slipstream is bound by $0.31 < y/b < 0.5$.

When comparing the propeller-off condition, it can be seen that the lift is underestimated due to a smaller span. The small change in span creates a relatively large error in the lift distribution for such a low aspect ratio wing. For the cases with propeller-on it can be seen that the magnitude of the lift directly behind the propeller is predicted closely by the numerical model. Only for $J = 0.7$ a dip in lift force is seen at the propeller tip ($y/b = 0.31$). This could be caused by negative loading near the propeller tip, which gives negative induced velocities (opposite the freestream velocity) or backflow. This backflow is also captured by the numerical propeller model, but since the part affected by backflow is rather small, approximately 5% of the radius, the effect of this on the wing is not fully captured in the numerical model. It is concluded that the effect of this is rather small and that this effect is over-represented in the validation data due to the location of the pressure taps.

Finally, the inboard wing section can be compared. Both the experimental and numerical data show an increase in lift in the propeller-on condition compared to propeller-off. In the numerical model the

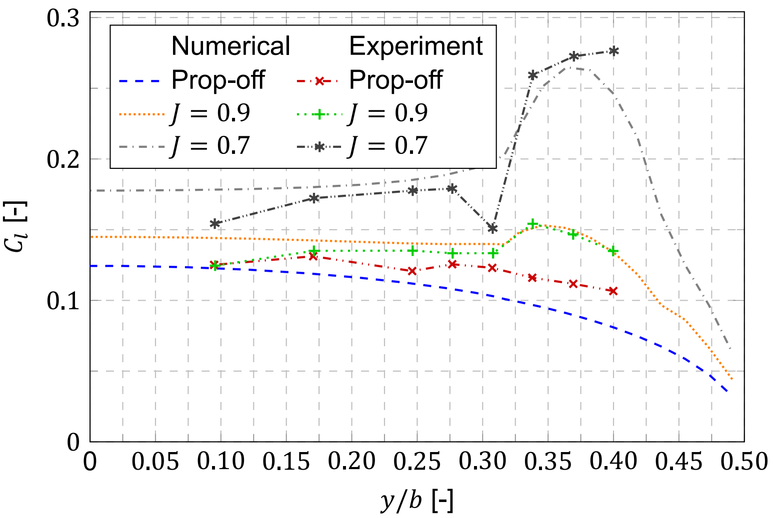

Figure 6.19: Spanwise lift distribution for the validation propeller-wing system

propeller induces still a small velocity on the inboard regions of the wing. This vertical velocity has a magnitude of about $0.005U_\infty$, but it still increases the angle of attack, which leads to a higher lift. Due to the presence of the propeller, the strength of the wingtip vortices are reduced and the wing also sees lower self induced velocities, which further increases angle of attack. The combination of these effects leads to a substantial increase in inboard lift. In the experimental data the magnitude of this increase in lift is less than what is predicted by the numerical model. Especially the difference between propeller-off and $J = 0.9$ is much lower. This can again be explained by a possible small flap deflection, which has been noticed by Koomen [84]. The flap would start at $y/b = 0.09$, which could explain the low C_l here. At the edge of the flap a trailing vortex would form, which induces some velocity on the nearby wing section. This could lead to a lower C_l.

To conclude, the numerical model can model most major trends for propeller-wing interaction. However, there are still some differences found when comparing to numerical data. These are expected to come from modelling errors of the propeller slipstream, which dictates the propeller-wing interaction in a tractor configuration. Furthermore, at high angles of attack and at very low or very high advance ratios non-linear effects will have a large effect on the performance. These include viscous effects in 3D, which are not captured by the numerical model.

7 Metamodelling

Metamodelling describes the steps and models used to create an approximate statistical model to represent the response of a detailed, deterministic computer code. Metamodelling is often also referred to as Design of Experiments (DOE), modern DOE or Response Surface Methodology (RSM). These terms however, strictly only refer to a part of the metamodelling process. Firstly, experimental design is done to sample the design space, this is described by DOE. Furthermore, a choice must be made for the model used to describe the response surface and then the model must be fitted to the data. This part is described by RSM. Lastly an optimization or evaluation of the response surface can be performed.

Now, some basic concepts are introduced. The true data is denoted as y_i, with $\overline{y}$ being the mean. y_i is the true response for some point in the design space, x_i, which is usually a vector for a multi-dimensional design space. The response surface f can be evaluated at x_i, which gives $f(x_i)$, which is shortened to f_i. $y_i - f_i$ gives the residual. Using the relations in Equation 7.1, the R^2 value can be calculated. Here three sum of squares (SS) are defined, due to the model (regression, SS_R), due to residual (error, SS_E) and the total (SS_T). In Equation 7.1 it can also be seen that R^2 is a ratio. Thus, $R^2 = 0.9$ would mean that 90% of the variability of the data is explained by the model. Thus, a higher R^2 means it explains or matches the data better. However, this does not mean that a higher R^2 gives a more accurate response surface [99]. R^2 will always increase when new degrees of freedom are introduced to the response surface, but it could lead to poor predictions for new points. While R^2 is the leading single measure for verifying the accuracy for a model of a deterministic experiment [100], it will be shown in Section 7.3, that examining R^2 only is often not enough.

$$
\begin{aligned}
R^2 &= SS_R/SS_T \\
SS_E &= \sum_i (y_i - f_i)^2 \\
SS_T &= \sum_i (y_i - \overline{y})^2 \\
SS_R &= SS_T - SS_E
\end{aligned}
\tag{7.1}
$$

Finally, in order to investigate the propeller-wing interaction using metamodelling, the design parameters must be defined. The number of design parameters determines the dimension of the response surface, which will determine the number of points that need to be evaluated. Thus, the number of design parameters must be kept to a minimum, while still providing enough information to answer the research questions, defined in Chapter 1. The choice of design parameters will be described in Chapter 8.

This chapter will give an overview of the theory of metamodelling and of the choices made regarding metamodelling. Firstly, in Section 7.1 information is given on Design of Experiments, concluded by a choice of sampling method to be used. Next, in Section 7.2 Response Surface Methodology is described, concluded with a choice of response surface to be used. Finally, with the chosen sampling method and response surface, it is investigated how the quality of the response surface can be assessed in Section 7.3.

7.1. Design of Experiments (DOE)

One of the main steps of the metamodelling process is Design of Experiments (DOE) or the sampling of the design space. DOE aims to get the most information out of a limited set of data points. Classical DOE is used to collect information from physical experiments, where a random error is present in the data points. In conventional experiments a *one factor at a time* approach is usually applied. However, such a way of conducting experiments does not give inside on interaction effects with other factors, and it is very costly when the effects of many factors need to be investigated. With classical DOE many factors can be varied at the same time. It optimizes the use of each data point and it minimizes the effects of random errors.

The principles of classical DOE can be applied to deterministic computer experiments to optimize the use of each data point and thus minimize the number of experiments that needs to be run, which is often referred to as modern DOE. A major difference is that no random errors are present in computer experiments. Thus, experimental designs that have space-filling properties are mostly applied in modern DOE. This space-filling is needed to minimize bias error [99], or the error between the true response and the modelled response.

Overview of sampling methods

There are many ways to approach experimental design, which are also described as sampling methods. Factorial designs start out with a number of levels on each design variable. For each combination of levels a sample is taken, leading to a full factorial design. This means that the number of samples scales exponentially with the number of dimensions. So for a design space of dimension n with k levels, the number of points scales with k^n. Thus, usually a factorial design is used for an initial understanding of interaction effects. With two levels linear effects can be investigated and with three levels quadratic effects [100]. To reduce the number of sampling points the fractional factorial design can be used, which uses a fraction of the points used by the full factorial design, but it still scales exponentially. A two-level full factorial design can be enhanced by adding center points and star points to each level, which leads to a central composite design. With this method quadratic effects can be investigated for less computational cost, since the number of points scales with 2^n. The full factorial, fractional factorial and central composite design for $n = 3$ and $k = 2$ are shown in Figure 7.1.

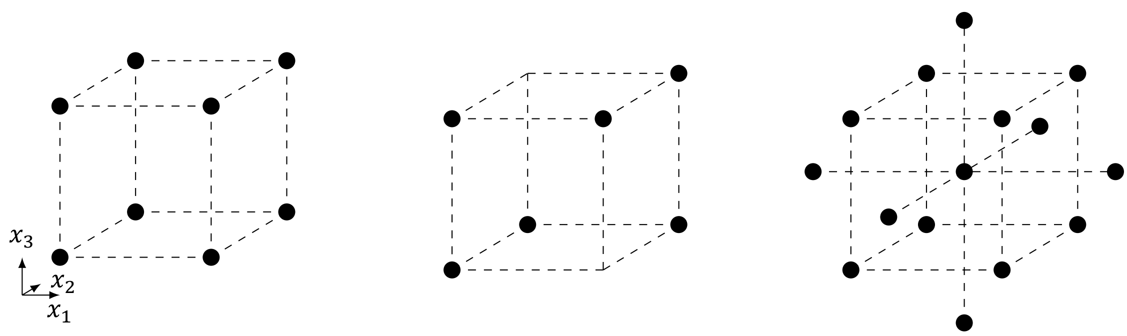

(a) Full factorial (b) Fractional factorial (c) Central composite design

Figure 7.1: Examples of different sampling methods for $n = 3$ and $k = 2$

While the methods based on factorial designs are useful in some cases, they usually sample mostly near the boundaries of the design space. To get a good response model for a number of samples, bias error needs to be minimized by filling the design space. One widely used sampling method is Monte Carlo sampling. Monte Carlo sampling simply generates a number of random sampling points in the design space. Implementation of Monte Carlo sampling is relatively easy, but it could leave large parts of the design space empty. To solve this problem extensions of Monte Carlo sampling have been developed, such as Stratified Monte Carlo sampling, where the design space is subdivided into bins and in each bin a random point is chosen. However, this method again scales exponentially with the number of dimensions. A Monte Carlo and Stratified Monte Carlo sampling example for $n = 2$ are shown in Figure 7.2.

Another sampling method that is popular for computational experiments is Latin Hypercube Sampling (LHS), which was developed as an alternative to Monte Carlo sampling [101]. LHS starts out by specifying a number of levels k. Using these levels, bins are created throughout the design space, which leads to k^n bins, for n dimensions. Then bins are chosen for sampling, such that for each one-dimensional projection of each level only one bin contains a sampling point. This is illustrated in Figure 7.2. It can be seen that in this case $k = 9$, which leads to nine samples. Thus, LHS is very easily scaleable. Finally, in each chosen bin a point will be placed. This is commonly done at random, but the point can also simply be placed at the center of the bin. Due to the random nature of the sampling, there is still a chance that the sampling provides bad coverage of the design space or that points are highly spatially correlated. There are extensions of LHS that address these problems.

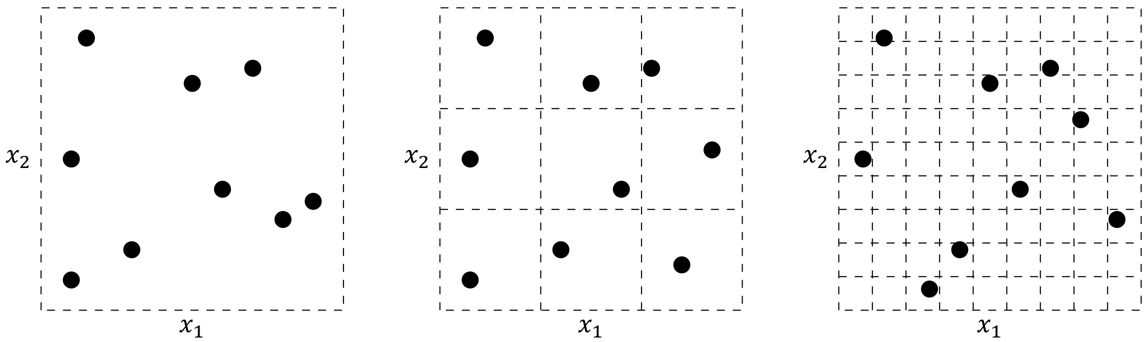

(a) Monte Carlo Sampling (b) Stratified Monte Carlo (c) Latin Hypercube Sampling

Figure 7.2: Examples of sampling methods for $n = 2$ [102]

Choice of sampling method

The LHS method was chosen to sample data points, since it provides adequate space-filling and sampling can be generated for any number of points. Since the bins would probably have a small size, it was chosen to keep the sampling points in the center of the bins, as randomization would not lead to significant differences and only complicate the sampling algorithm. The algorithm used is shown in Equation 7.2, where n is the number of dimensions, k the number of points. Π is a random permutation of the sequence of integers consisting of $0, 1, ..., k - 1$.

$$\begin{aligned} x_j^{(i)} &= \frac{\Pi_j^{(i)} + 0.5}{k} \\ \text{with :} &1 \leq j \leq n \\ &1 \leq i \leq k \end{aligned} \tag{7.2}$$

To determine the number of sampling points, some tests can be done. First a look can be taken at the R^2 value. When adding more points, R^2 will increase, but at some point, adding more points will lead only to a small increase in R^2. This is shown in Figures 7.3 and 7.4. This R^2 value is based on all the 100 data points that were available, from which a subset is used to create the response surface. The error bands give the standard deviation for the R^2 value, since it depends on the random samples generated using LHS. It can be seen clearly that the R^2 increases for the number of points. Furthermore, R^2 seems to increase asymptotically. Thus, a number of sampling points should be chosen for which a higher number of sampling points does not provide significantly more benefit. While using LHS, the areas near the corners can be empty. Thus, corner points were added to increase the accuracy of the response surface. Figure 7.3 shows regular LHS, while Figure 7.4 is enhanced by adding corner points. It can be seen that this increases the rate of convergence slightly, thus it was chosen to use LHS sampling with corner points. In this case, around fifteen points seem to be enough to create a response surface for this data set. After that only a slight increase in R^2 can be gained.

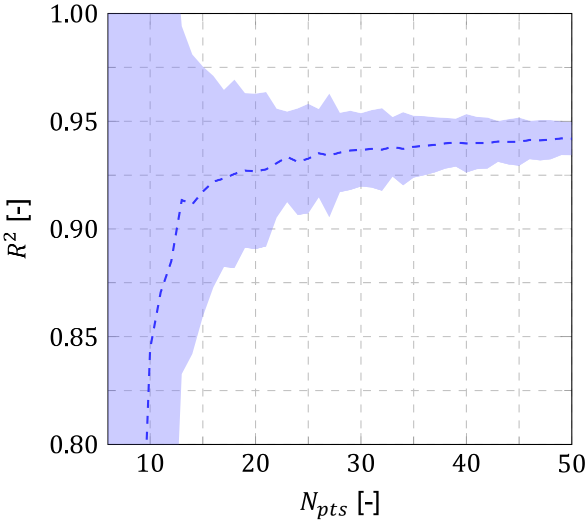

Figure 7.3: R^2 for LHS sampling without corner points with 1σ error bands

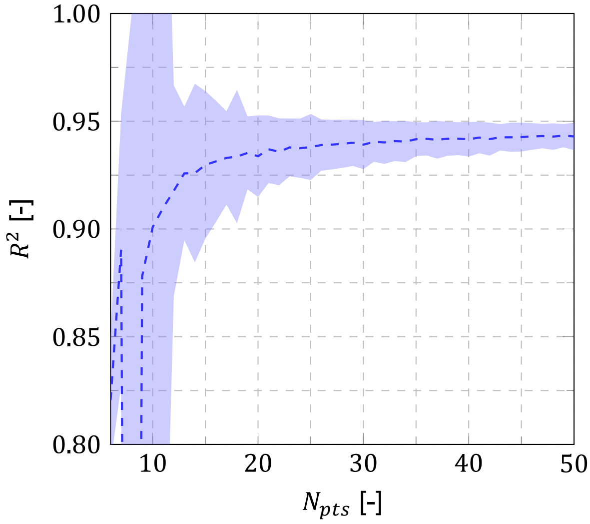

Figure 7.4: R^2 for LHS sampling with corner points with 1σ error bands

7.2. Response Surface Methodology (RSM)

Response Surface Methodology encompasses the process of choosing and fitting a response surface to data, with the goal to provide an accurate approximation of the real data.

Overview of types of response surfaces

There are many types of response surfaces. A very basic response surface is a polynomial function. A polynomial function can be fitted to the data, which gives a smooth, differentiable response surface. Most frequently linear polynomials are used to find relations between variables or quadratic polynomials for optimization problems. An alternative way to use polynomials is using splines. Here the design space is divided in parts, where each part has its own polynomial function. On the boundaries these polynomials must match. Compared to using a single polynomial function, splines offer more flexibility to adapt to complex data. A drawback of the use of polynomials is that high order polynomials are not very robust, due to the way they reduce residuals [103].

A more modern type of response surface comes in the form of neural networks. Neural networks are complex systems where inputs are converted to outputs by using neurons or nodes. To describe a response surface, the neural network must be trained by giving it data. Based on this training data, the neural network will adjust weights associated to the nodes, leading to a good fit. This training of neural networks can be computationally expensive and the behaviour of the neural network can be unpredictable [104]. The main benefit of the neural network is that it is highly adaptable.

When using deterministic computer models with no measurement error, the residuals computed from conventional response surface fitting have no obvious statistical meaning. [105]. Thus, Kriging was developed. Kriging utilizes a global function and a function for local deviation from the global function. For a more detailed description of the Kriging model, the reader is referred to the work of Cressie [106]. A key part of the Kriging model is the correlation function. This correlation function correlates the semi-variance to the distance between points. Since there are many correlation functions available, the Kriging model is highly flexible. Furthermore, Kriging provides a response surface that follows the data exactly and gives an estimation of the covariance throughout the design space. A downside of Kriging is that it does not produce an explicit function.

Choice of response surface

The Kriging model was the first choice for creating a response surface model for the data, since it provides an exact fit to a deterministic computer model and it gives an estimate of the covariance. Furthermore, the computational cost is relatively low. However, the data from the propeller-wing model does contain a convergence residual, as described in Section 5.2.4 of Chapter 5. When this convergence residual is big, it creates local peaks in the response surface, when using Kriging, since the response surface will exactly go through each point. For this reason it was chosen to use a polynomial response surface, to smooth out these local peaks due to convergence residual. Furthermore, it is believed that noise due to the convergence residual will be averaged out by using a polynomial response surface. Thus, the response surface would provide an average trend in the data. It is assumed that modelling errors of the numerical model are random, so averaging can be applied. However, this could not be verified.

The general form of a multivariate polynomial is given in Equation 7.3. Here n is the number of dimensions or number of variables and k is the order of the polynomial. The number of indices i is equal to the number of dimensions and can take any integer value from 0 to k. To fit the polynomials to the data points the least squares method is used, which minimizes the residual by solving a system of equations. With this method also weights can be given to the data points. Since the convergence residual for the data points is known, less weight can be given to data points with a large convergence residual. This means that these points are given less significance in determining the shape of the polynomial. It is expected that this will be enough to smooth out local peaks due to ill-converged points.

$$f(x_1, x_2, ..., x_n) = \sum_{i_1+i_2+...+i_n \leq k} a_{i_1,i_2,...,i_n} \prod_{j=1}^{n} x_j^{i_j} \tag{7.3}$$

The derivation for the least squares method starts with a definition of the sum of squares of residuals (ssr), as shown in Equation 7.4. Here the value of the data point is y_p at x_p and N is the number of available data points. w_p is the weight given to each data point. In this case, the weights are determined by the inverse of the convergence residual. Since the generalized equations are becoming hard to read the rest of the derivation is written for a polynomial with number of dimension $n = 2$ and degree $k = 1$. This leads to the derivatives in Equation 7.5. The derivatives are taken with respect to the unknown coefficients a_{00}, a_{01} and a_{10}. To get the minimum value of ssr, these derivatives must be zero. This leads to a system of equations, shown in Equation 7.6, which can be easily solved for the unknown coefficients.

$$\begin{aligned} ssr &= \sum_{p=1}^{N} w_p (y_p - \sum_{i_1+i_2+...+i_n \leq k} a_{i_1,i_2,...,i_n} \prod_{j=1}^{n} x_{j,p}^{i_j})^2 \\ ssr &= \sum_{p=1}^{N} w_p (y_p - a_{00} - a_{10}x_{1,p} - a_{01}x_{2,p})^2 \end{aligned} \tag{7.4}$$

$$\begin{aligned} \frac{\partial ssr}{\partial a_{00}} &= -2\sum_{p=1}^{N} w_p (y_p - a_{00} - a_{10}x_{1,p} - a_{01}x_{2,p}) = 0 \\ \frac{\partial ssr}{\partial a_{01}} &= -2\sum_{p=1}^{N} w_p x_{1,p} (y_p - a_{00} - a_{10}x_{1,p} - a_{01}x_{2,p}) = 0 \\ \frac{\partial ssr}{\partial a_{10}} &= -2\sum_{p=1}^{N} w_p x_{2,p} (y_p - a_{00} - a_{10}x_{1,p} - a_{01}x_{2,p}) = 0 \end{aligned} \tag{7.5}$$

$$\begin{bmatrix} \sum w_p & \sum w_p x_{1,p} & \sum w_p x_{2,p} \\ \sum w_p x_{1,p} & \sum w_p x_{1,p}^2 & \sum w_p x_{1,p} x_{2,p} \\ \sum w_p x_{2,p} & \sum w_p x_{1,p} x_{2,p} & \sum w_p x_{2,p}^2 \end{bmatrix} \begin{bmatrix} a_{00} \\ a_{10} \\ a_{01} \end{bmatrix} = \begin{bmatrix} \sum w_p y_p \\ \sum w_p x_{1,p} y_p \\ \sum w_p x_{2,p} y_p \end{bmatrix} \tag{7.6}$$

To choose the degree of polynomial that will be used for the response surface, it must be determined how well the data is approximated using different polynomials different degrees. An increase in the number of degrees of freedom will always increase the R^2. Furthermore, a polynomial with too many degrees of freedom, might result in a bad response surface, with large peaks between the data points

[103]. By plotting the R^2 against the degree of the polynomial, it can be visually determined which degree of polynomial suffices. An example of such a plot is shown in Figure 7.5. Here it can be seen that increasing the degree of polynomial from one to two gives a great benefit. However, with increasing degree, this gain becomes less and less. In this case a second or third degree polynomial seems to be a good fit.

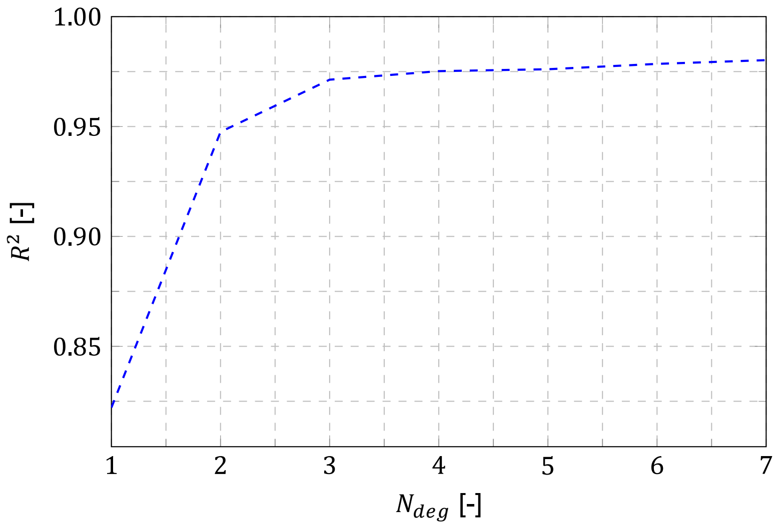

Figure 7.5: An example that shows R^2 increasing with the number of degrees of the polynomial response surface

7.3. Quality of the response surface

In the previous sections it has been discussed that the response surface will consist of a polynomial function and the data points will be sampled using LHS with corner points. To create a good response surface, the response surface must follow the data points and predict the values in the design space with certain accuracy. There are two main factors that determined the quality of the response surface: the degree of the polynomial and the number of sampled data points. In the introduction of this chapter the quality of the response surface has been linked to the R^2 value, but here this will be further examined by a 2D example.

The 2D example consists of the propeller-wing model described in Section 8.1 of Chapter 8, where $A = 11.5$, $\theta = 0°$, $D/b = 0.14$, $x/c = 0.2$ and $z/D = 0$. A detailed description of the model is not relevant at this point. The design variables are the design lift coefficient and design thrust coefficient. The design lift coefficient is obtained by changing the angle of attack of the wing. The design thrust coefficient is found by finding the point of maximum efficiency of the isolated propeller for the given thrust, by changing advance ratio and pitch angle. Note that the thrust coefficient here is non-dimensionalized using wing parameters, so T_C is used. $C_{L,des}$ ranges from 0 to 1.5 and $T_{C,des}$ from 0 to 0.05. For this experiment a grid of 10x10 points is evaluated to have knowledge over the whole design space. From these 100 points subsets can be sampled by using LHS.

7.3.1. Setting up the metamodel

This example case will examine the change in lift, ΔC_L, which is defined as: $C_{L,prop-on} - C_{L,prop-off}$. First, the degree of the response surface is determined. This is done by plotting the R^2 for the degree of the polynomial N_{deg}, as shown in Figure 7.6. It can be seen that increasing the response surface beyond $N_{deg} = 3$ yields little benefits in terms of R^2. Based on R^2 either $N_{deg} = 2$ or $N_{deg} = 3$ seem to be good options.

In Figures 7.7, 7.8, 7.9 and 7.10 the response surfaces for a N_{deg} of two, three, four and seven are plotted. It can be seen that even though the R^2 changes little for N_{deg} above three, there are still changes in the shape of the response surface. However, these changes in shape are not significant, as according to the R^2 value, they do not provide a better explanation for the data.

The previous results were obtained using all 100 points on the sampled grid. However, for the real

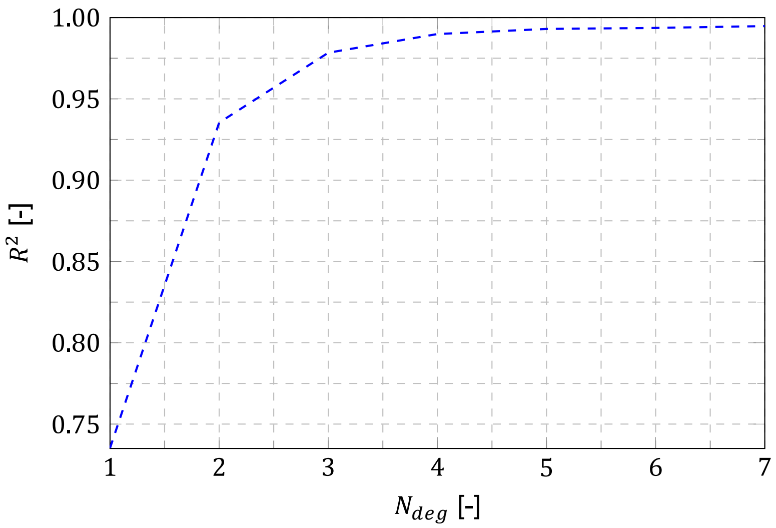

Figure 7.6: R^2 for different degrees of the polynomial used to describe ΔC_L

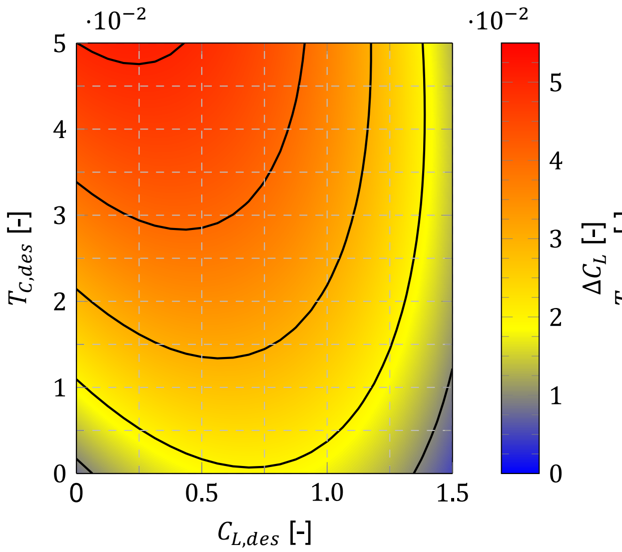

Figure 7.7: Response surface when using a polynomial of degree 2

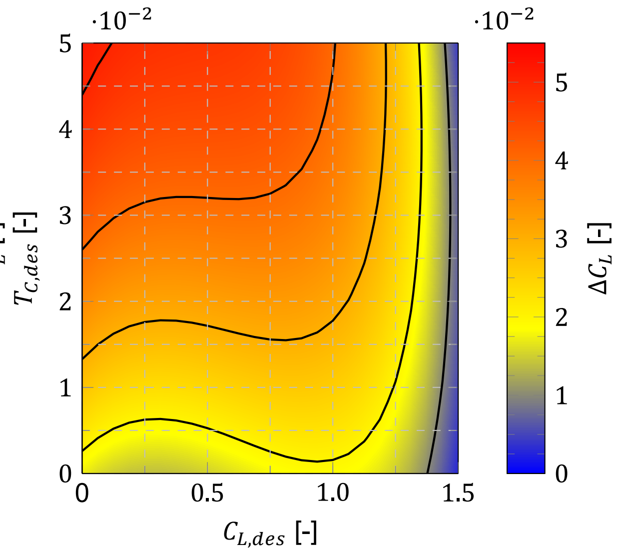

Figure 7.8: Response surface when using a polynomial of degree 3

experiment, LHS will be used to sample more efficient amount of points. This is investigated in Figures 7.11 and 7.12 for a response surface of degree two and three respectively. It can be seen that both response surfaces converge to a value of R^2 with increasing number of points. However, for a response surface of degree three, this converged R^2 value is higher, as expected from Figure 7.6. On the other hand, the polynomial with degree two needs less sampling points to reach convergence.

Assume that a polynomial of degree two has been chosen. In this case a number of sampling points of 20 should suffice, as increasing the number of points does not lead to major benefits. However, to illustrate the workings of the response surface, a number of 15 sampling points will be used in the subsequent examples. This leads to a low quality response surface and a high quality response surface. Both are sampled using 15 points, but the difference in quality is determined by the random difference in sampling point locations. In the next sections the characteristics of both will be described,

7.3.2. Example of a low quality response surface

The first example is one that results in a low quality response surface, shown in Figures 7.13 and 7.14. Firstly, the shape of the response surface does not match with Figure 7.7. The R^2 values obtained for

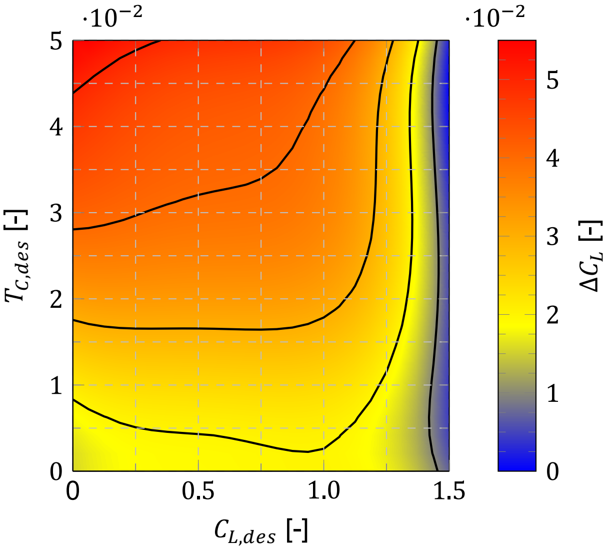

Figure 7.9: Response surface when using a polynomial of degree 4

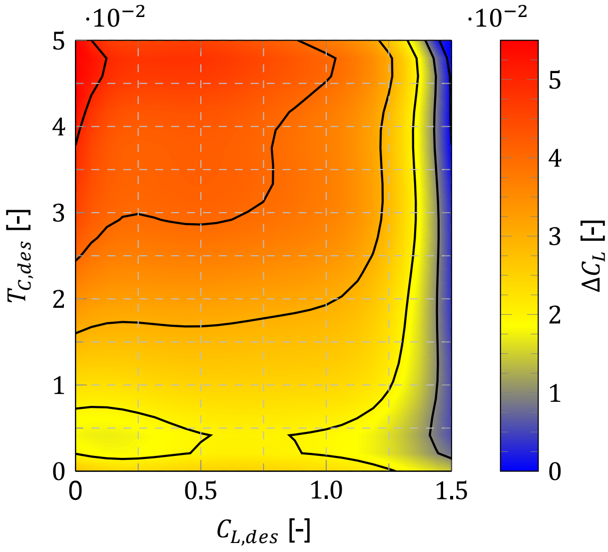

Figure 7.10: Response surface when using a polynomial of degree 7

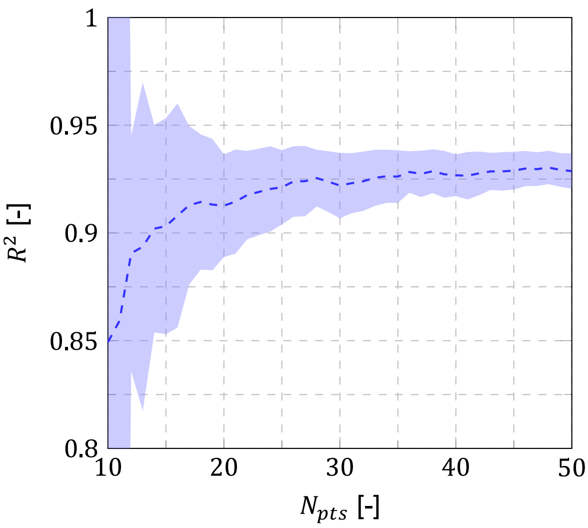

Figure 7.11: R^2 for different number of sampling points using LHS and a polynomial of degree 2

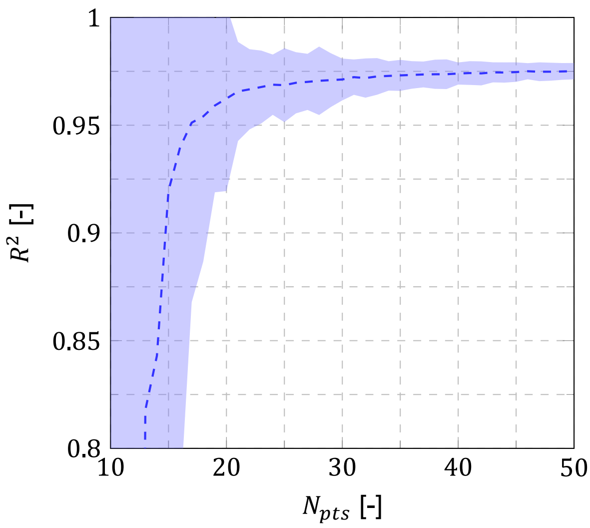

Figure 7.12: R^2 for different number of sampling points using LHS and a polynomial with degree 3

this response surface are also relatively low. $R^2 = 0.713$ was obtained using all 100 data points and $R^2 = 0.656$ with a standard deviation of 0.200 was obtained using ten random points for validation. Also points can be defined in low density areas, to get an idea of how well the response surface predicts the data. For ten points in low density areas $R^2 = 0.494$ was obtained. When examining Figure 7.14 it can be seen that the maximum residual for the sampled data points is about $0.6 \cdot 10^{-2}$ and about 95% of the points has a residual lower than $0.5 \cdot 10^{-2}$. This would indicate a good fit with the data, but when another set of data points is used to calculate the residuals, the response surface performs much worse. When taking the 100 available data points, only 70% has a residual lower than $0.5 \cdot 10^{-2}$ and this is about 40% for the points in low density areas. In short, the high residuals and low R^2 indicate a response surface that does not represent the data.

7.3.3. Example of a high quality response surface

Next, a better performing response surface is presented. The results for this response surface are shown in Figures 7.15 and 7.16. It can be seen that the shape of the response surface matches the

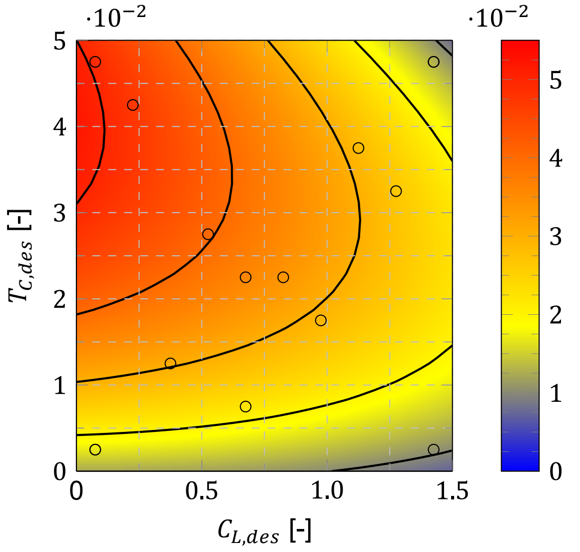

Figure 7.13: An example of a low quality response surface

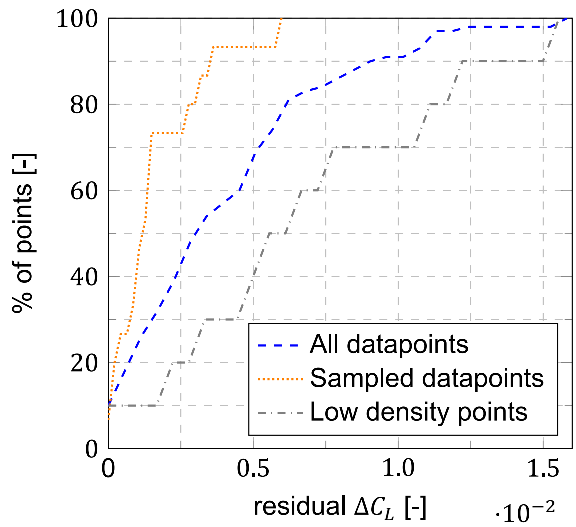

Figure 7.14: An example of cumulative residual plots for a low quality response surface

one in Figure 7.7 closely. This example has a $R^2 = 0.925$ for 100 data points. Using ten random validation points $R^2 = 0.907$ with standard deviation of 0.055 is obtained. Using ten points in low density regions $R^2 = 0.962$ is obtained. These are all relatively high values for R^2, so this already indicates that this response surface represents the data well. Next, the residuals are examined. In Figure 7.14 it can be seen that for the sampled data points the maximum residual is about $0.5 \cdot 10^{-2}$. Using any other subset of data points in the design space gives similar values of residuals, thus the response surface seems to represent all the data well, based on the residuals.

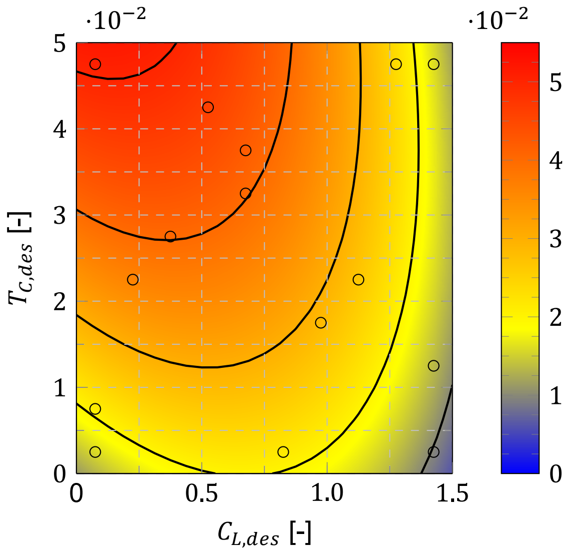

Figure 7.15: An example of a high quality response surface

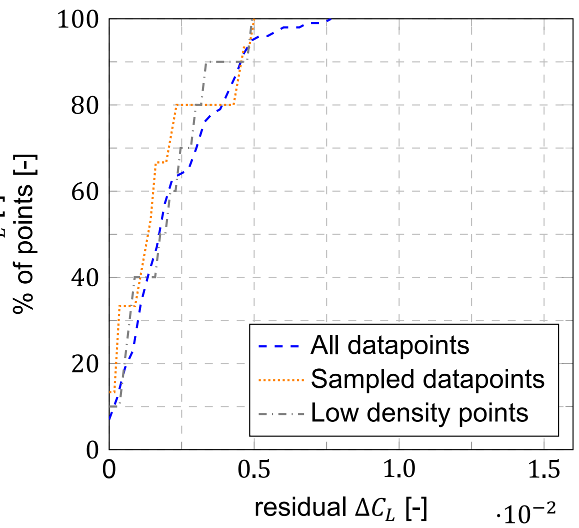

Figure 7.16: An example of cumulative residual plots for a high quality response surface

A final test can be done by looking at the correlation between the residual and the value, as shown in Figure 7.17. If the response surface would be represent all data equally well, then the correlation between the residual and data should be zero. This correlation is represented by the orange line, which shows a slight negative correlation. In the ideal case this line would be horizontal on the y-axis. This negative correlation is introduced by the fact that the polynomial function cannot follow the data well in some parts of the design space. This could be fixed by using a more complex function. But in this case the slope is very low, so the bias is not too strong. Furthermore, it can be seen that the residual is overall lower than the value it represents, giving confidence that a change in model response is a significant change.

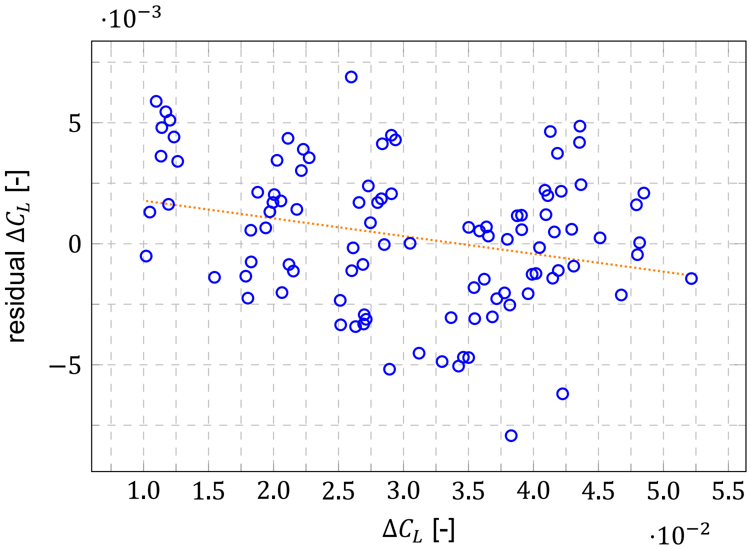

Figure 7.17: An example of a residual bias plot for a high quality response surface

7.3.4. Final remarks

It has been shown that R^2 provides some guidance in choosing the right number of sampling points and the right number of degrees for the response surface. In both cases a number as low as possible is chosen, where an increase does not provide significant benefit. By examining the cumulative residuals of different subsets of points, it can be checked if the response surface is accurate outside the sampling points. In the previous examples a grid of data points was available to validate the response surface, but this will not be the case for the final experiments. In this case next to the sampled data, which will be used to construct the response surface, other data sets will be sampled as well. It was decided to make one set of validation data using random sampling and another set which samples from low density areas. By comparing the residuals for these data sets the quality of the response surface can be assessed.

8 Results

In this chapter the results are presented. Three metamodels were made. The first metamodel investigates the effects of the wing lift distribution and propeller-wing relative position. The results for this metamodel are presented in Section 8.1. The second metamodel uses the same design parameters as metamodel 1, but it doubles the thrust, so the influence of thrust can be determined. The results for metamodel 2 are presented in Section 8.2. Lastly, a third metamodel is presented in Section 8.3. Metamodel 3 investigates the effects of propeller efficiency and the effect of the relative magnitude of thrust. Using these three metamodels the research objectives presented in Section 1.2 of Chapter 1 can be answered. Throughout this chapter, trend lines will be seen with shaded bands. Here, the trend line gives the average trend, while the shaded bands indicate the spread in the data by visualizing 1σ for the data represented on the vertical axis. This spread is caused by variation in variable parameters that are not included in the graph.

8.1. Metamodel 1: Wing geometry and propeller position

This section describes the results for the first metamodel. Firstly, the design parameters are introduced in Section 8.1.1. Then some information on the investigated performance parameters is given in Section 8.1.2. After this, data is sampled and a response surface is created. The quality of this response surface is assessed in Section 8.1.3. Finally, the results from the response surface are presented in Sections 8.1.4 and 8.1.5. Section 8.1.4 deals with the effect of the design parameters on the performance parameters. Lastly, in Section 8.1.5 it is investigated if there is any correlation between the performance parameters.

8.1.1. Parameterization

The first metamodel uses five design parameters or design variables. These are: the aspect ratio A, wing twist θ, propeller diameter D, propeller horizontal position x and propeller vertical position z. These are all shown in Figure 8.1. These five parameters change the wing lift distribution and the relative position of the propeller with respect to the wing. In order to generalize the results, the dimensional parameters are non-dimensionalized, except the wing twist θ, which is given in degrees. A summary of the design parameters and their limits can be found in Table 8.1.

- **Wing aspect ratio**
  The aspect ratio of the wing was chosen to be between 7 and 16. The lower limit is based on the windtunnel models used at Delft University of Technology to investigate propeller-wing interaction. The upper limit is based on the X-57 Maxwell design [26]. Wing area is kept constant, so aspect ratio is changed by changing both span and chord.
- **Wing twist**
  The twist added to the wingtip is between $0°$ and $10°$ to change the spanwise lift distribution. A positive twist was chosen, since it is expected that more outboard loading on the wing would enhance propeller-wing interaction.
- **Propeller diameter**
  The diameter is divided by the wing span, which gives D/b as non-dimensional parameter. D/b

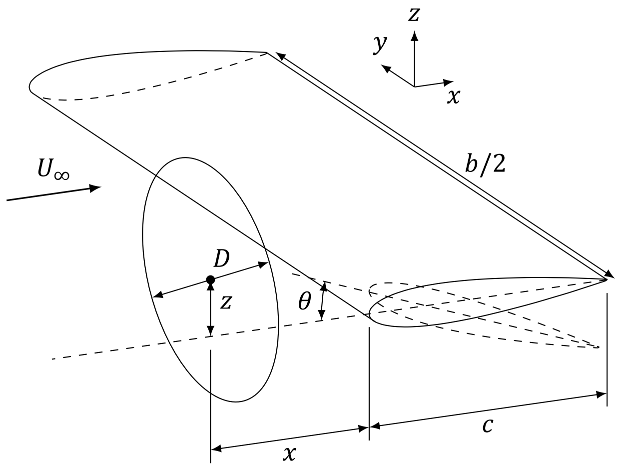

Figure 8.1: Definition of the variables used for parameterization for metamodel 1

measures the fraction of the wing surface that is located in the propeller slipstream. However, when the aspect ratio increases, the span increases, so D will be larger. But still the same wing area will be immersed in the propeller slipstream. The values of D/b will be between 0.08 and 0.2, based on the work by Della Vecchia [74]. Outside these values, a change in D/b seems to have little effect on the propeller-wing interaction.

- **Propeller horizontal position**
  The propeller x position is non-dimensionalized using the chord c, which gives x/c. The chord c was chosen here, since x and c both have the same orientation. Above $x/c = 1.5$ the x-position seems to have little influence on the propeller and values lower than $x/c = 0.5$ are hard to realise due to space needed for the nacelle [28][29]. It must be noted that the chord c changes with aspect ratio, so x/c is dependent on aspect ratio.
- **Propeller vertical position**
  The propeller z position is non-dimensionalized using the propeller diameter, leading to z/D. While z/D influences the performance significantly for a range of $-0.5 < z/D < 0.5$ [28][29], it was chosen to limit the range to $-0.2 < z/D < 0.2$. This was done because outside this range it is uncertain if the interaction would still be modelled properly.

Table 8.1: Design parameters and bounds for metamodel 1

	lower bound	upper bound
A	7	16
θ	0°	10°
D/b	0.08	0.20
x/c	0.1	1.5
z/D	-0.2	0.2

Next to these variable parameters, there are some other important design parameters that are kept constant. Firstly, the wing area is 6.5 m^2, which is roughly based on the wing area of the X-57 Maxwell [26]. Furthermore, sweep is set to zero, as it is yet unknown if the jet correction is applicable to swept wings. Although taper is a convenient way to change the shape of the spanwise lift distribution, the taper ratio is kept at 1. This is done because when the taper ratio is changed, it changes the area of the wing in the propeller slipstream, making it hard to compare the data. The number of blades equals six, based on the TUD-XPROP windtunnel model of a propeller used at Delft University of Technology. The propeller blade twist and chord distribution are also modelled after this propeller, which are shown in Figure 6.9 in Section 6.1 of Chapter 6. Furthermore, a freestream velocity of $U_\infty = 80$ m/s was chosen at atmospheric conditions at 8000 ft, based on the cruise conditions of the X-57 Maxwell [26]. This gives a freestream Mach number of 0.24, which lies well within the subsonic regime where the numerical model can make accurate predictions.

Moreover, C_L and T_C are kept constant. It was chosen to have C_L constant for the propeller-wing system, while T_C is constant for the isolated propeller, as little change in thrust is expected due to interaction effects. This is done to fairly compare the datapoints. Thus, the influence of the magnitude of the lift is eliminated and the effects of lift distribution can be investigated. A constant C_L also makes sense from a design perspective, since the C_L is a fixed design requirement. A constant C_L was obtained by evaluating each propeller-wing design at two wing angles of attack. Note that the propeller is always aligned with the freestream velocity or $\alpha_{prop} = 0$. By assuming a linear lift-curve slope, the wing angle of attack for the design lift coefficient, $C_{L,des}$ could be determined. At this interpolated wing angle of attack, the propeller-wing system is evaluated, which gives $C_{L,prop-on}$. Typically the error of $C_{L,prop-on}$ with respect to $C_{L,des}$ is lower than 4%. Furthermore, this error tends to be one-sided only, thus the spread of C_L values is relatively small, making the evaluated cases comparable to each other. Based on a realistic cruise lift coefficient, $C_{L,des} = 0.6$ was chosen. As mentioned before, the propeller is always aligned with the freestream velocity. This means that the lift value is affected by the propeller vertical in-plane force only and not by the thrust.

As mentioned, it is decided to keep the thrust constant at a $T_{C,des}$. This $T_{C,des}$ is the isolated propeller thrust coefficient $T_{C,iso}$, since it is hard to predict the installed thrust coefficient $T_{C,prop-on}$. This gives a typical difference of $T_{C,prop-on}$ of less than 2% compared to the $T_{C,des}$. When designing the propellers, a certain thrust requirement is given. This thrust depends on the drag of the wing and the drag of the rest of the aircraft. Since the drag of the rest of the aircraft is unknown, a value for thrust needs to be assumed. The C_D of the clean wing ranges from 0.013 to 0.022, thus it was chosen to operate at $T_C = 0.05$ to include drag from the rest of the aircraft, which translates to a $T_C = 0.025$ for each propeller. It was decided to analyze the system at a constant thrust and not to make the thrust equal to wing drag. This would also make it harder to compare data points. At a higher T_C, the wing is also exposed to higher axial and tangential momentum, which drive the interaction. At a constant T_C, the amount of axial momentum in the slipstream is approximately equal. The tangential momentum depends on the propeller efficiency η. For a realistic propeller at cruise, the propeller will operate at maximum efficiency η_{max}, thus it was chosen to operate the propeller at η_{max}, instead of constant η. η_{max} can be achieved by changing the propeller pitch angle and advance ratio. In Figure 8.2 it can be seen what the effect of different radii is on η_{max} for $T_C = 0.025$ for a single propeller. For the range of radii shown, there is a range of about 0.15 in η_{max}, and the difference is especially significant at smaller radii. This must be taken into account when looking at the data, since propellers with a smaller radius provide more tangential velocity.

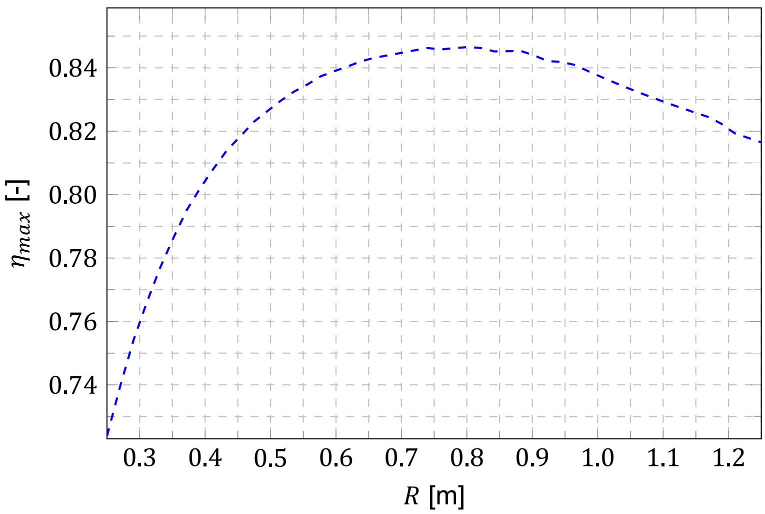

Figure 8.2: The change in maximum propeller efficiency with radius for a single propeller with $T_C = 0.025$

8.1.2. Metamodel set-up

In this section the set-up of the metamodel will be discussed. It was decided to create response surfaces for five performance parameters:

- **Change in drag**, ΔC_D
  The change in drag is defined as the difference between wing drag with propeller and wing drag without propeller, $C_{D,prop-on} - C_{D,clean}$. This means that a negative ΔC_D gives a reduction in drag. This gives an indication of the benefits or drawbacks of wingtip-mounted propeller-wing interaction.
- **Drag**, C_D
  To evaluate the drag, the value for wing drag with the propeller, or $C_{D,prop-on}$, is used. The change in drag does not indicate if a propeller-wing combination gives a low drag or not, only if the propeller-wing interaction effect is beneficial or not. Thus, C_D also needs to be evaluated.
- **Change in lift**, ΔC_L
  Since the model is created at a certain system lift coefficient $C_{L,des}$, only the change in lift is evaluated by ΔC_L, which is defined as $C_{L,prop-on} - C_{L,clean}$. Here $C_{L,prop-on}$ is the propeller-wing system evaluated at the estimated angle of attack that should result in $C_{L,des}$. However, since $C_{L,prop-on}$ and $C_{L,des}$ are usually not the same, it was chosen to use $C_{L,prop-on}$ to calculate ΔC_L. This is because $C_{L,prop-on}$ and $C_{L,clean}$ are both evaluated at the same angle of attack and thus give consistent results. In this case C_L is the wing lift plus any vertical propeller forces. However, the majority of the change in C_L is due to change in wing lift.
- **Change in lift-to-drag ratio**, $\Delta(L/D)$
  All evaluations are done at (approximately) the same C_L, thus the lift-to-drag ratio is determined by the drag. Since drag is already being evaluated, it would be redundant to also evaluate the lift-to-drag ratio. However, the $C_{L,clean}$ does change for different wing designs, thus the $\Delta(L/D)$ is dependent on both lift and drag and it gives an indication of the change in performance due to propeller-wing interaction. This parameter is defined as follows: $\Delta(L/D) = (L/D)_{prop-on} - (L/D)_{clean}$
- **Change in thrust**, ΔT_C
  The thrust of the isolated propeller is kept constant, but due to propeller-wing interaction there is still come change in thrust. This is being evaluated by ΔT_C. This is defined as $\Delta T_C = T_{C,prop-on} - T_{C,iso}$. It was found that the change in power ΔP_C is proportional to ΔT_C, thus it is not included as a performance parameter.

For the defined response surfaces the degree of the polynomial function and the number of sampling points need to be determined. This was done by evaluating 1500 points in the design space using Latin Hypercube Sampling (LHS). Next to this, 150 validation points were sampled, which are used to give an estimate of the accuracy by evaluating R^2. In Figure 8.3 the R^2 is shown for different degrees of polynomial. It can be seen that the different parameters show different behaviour. All parameters, except C_D show an initial increase in R^2 with increasing degree of polynomial, but after some point it decreases. It is believed that this is due to the high amount of degrees of freedom of a multi-dimensional polynomial function for higher degree of polynomial. For example, a polynomial of degree 5 has 252 degrees of freedom. When the data is fitted, the response surface approximates the data well at the evaluated points, but will show peaks elsewhere. This leads to a lower R^2. For a lower degree of polynomial, the response surface will give a smooth trend through the data, which gives a better R^2. Thus, a balance must be found for N_{deg}. For ΔC_D, ΔC_L, $\Delta(L/D)$ and ΔT_C polynomials of degree 3, 2, 3 and 3 were chosen. In Figure 8.3 it can be seen that these values give a high R^2, but do not risk lowering the response surface accuracy by having a high N_{deg}. For C_D is can be seen that the response is mostly linear. However, adding more degrees does not seem to harm the accuracy, so in the end $N_{deg} = 2$ was chosen.

Next, the number of sampling points needs to be determined. This is done using Figure 8.4. Here the R^2 for a certain number of sampling points is divided by the R^2 obtained using 1500 points. It can be seen that the R^2 initially rises sharply with increasing number of points, but after a certain number of points only small improvements of R^2 can be obtained. A number of 750 evaluation points was chosen to be sufficient. It falls well behind the sharp rise for lower number of points, thus this is a somewhat conservative number of sampling points.

8.1.3. Metamodel quality

The quality of the metamodel is assessed in several ways. In Table 8.2 a summary can be found of the quality evaluation. The first three columns show the minimum value, maximum value and the

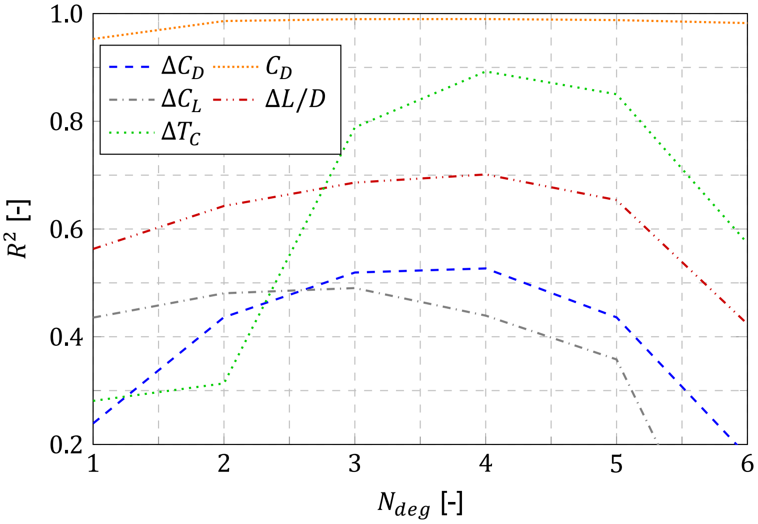

Figure 8.3: R^2 for different number of degrees of the polynomial response surface for metamodel 1

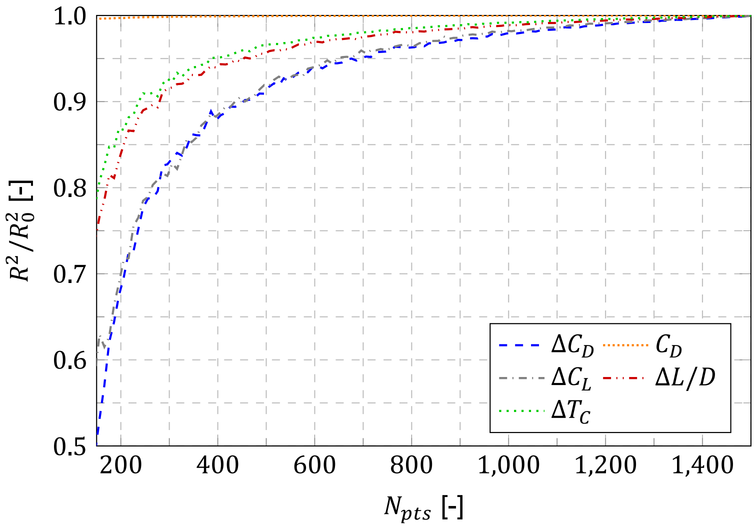

Figure 8.4: R^2 for different number of sampling points for metamodel 1

subsequent range of the data. This gives an idea of the differences between data points. Next, the sampled data points are used to create a response surface of degree N_{deg}. This leads to an R^2 value for the sampled data points. It can be seen that the R^2 for C_D is very high, meaning that the relation of C_D with the design parameters is represented well by the metamodel. The R^2 for ΔC_L and ΔC_D is relatively low. This is due to the fact that C_L and C_D are very sensitive to interaction effects. This gives uncertainty in the predictions of the numerical model, which manifests as some error in the results. It is assumed that these modelling errors are random and by fitting a surface through many datapoints, these errors will be averaged out. However, this means that there will always be a relatively large difference between the value of the datapoint and the predicted value by the response surface, leading to a relatively small R^2. To verify this hypothesis, the residual is given in the last column. 90% of the datapoints has a lower residual than the value shown in Table 8.2. When comparing the residuals to the range of the data, it can be seen that the residual is typically about 10% of the range, independent of the R^2 value. This gives confidence that the response surface for ΔC_L and ΔC_D is still useful, but small changes predicted by the response surface should be evaluated critically.

To further analyse the quality of the response surface, two sets of validation points are used. The first set is sampled randomly in the design space. The second set is sampled in areas with a low density of sampling points. In Figure 8.5 the results for ΔC_D can be seen. It can be seen that the

Table 8.2: Summary of the response surface results for metamodel 1

	min	max	range	N_{deg}	R^2	residual (90% of points)
ΔC_D	-0.00265	0.00059	0.00324	3	0.710	0.00039
C_D	0.0154	0.0297	0.0143	2	0.980	0.00052
ΔC_L	-0.0087	0.0449	0.053	2	0.561	0.0043
$\Delta(L/D)$	0.78	6.54	5.76	3	0.860	0.63
ΔT_C	-0.00068	0.00077	0.00145	3	0.863	0.00008

distribution of residuals for sampled points show the same behaviour as for the randomly selected validation points. This further builds confidence that the response surface is able to accurately predict the ΔC_D in the design space. The residual for the low density areas is overall higher, this is expected, as the response surface has less information here. These low density areas are mainly at the edges of the design space. Thus, when evaluating data from the edges, it must be taken into account that results can be inaccurate. Next, in Figure 8.6 the bias of the residuals is evaluated. It can be seen that there is a positive relation between the data value and the corresponding residual. This gives a strong indication that the real function of ΔC_D should be more complex and is not fully captured by the polynomial functions used. When evaluating the data, this means that larger (more negative) values of ΔC_D should be even larger (more negative), while smaller values should be even smaller (or positive). Similar results are obtained for the response surface of ΔC_L.

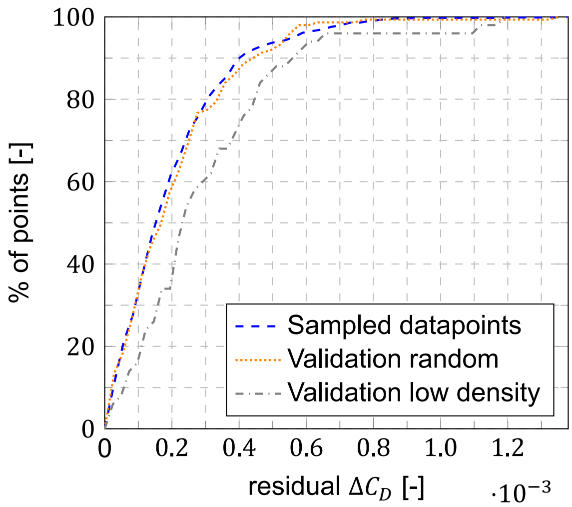

Figure 8.5: Comparison of residuals of ΔC_D for metamodel 1

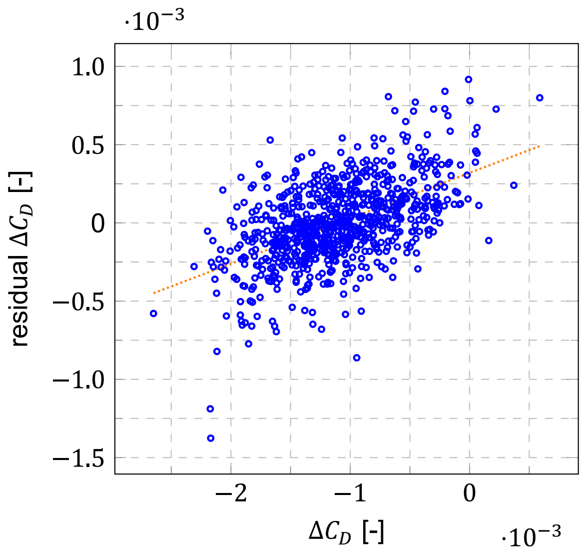

Figure 8.6: Bias of residuals of ΔC_D for metamodel 1

The same analysis was done for the other performance parameters. In Figures 8.7 and 8.8 the results for T_C are shown. Similar graphs were obtained for the parameters C_D and $\Delta(L/D)$. It can be seen that the sampled points give a similar residual distribution to the random validation points. While in the edges of the design space, with low sampling density, the residual tends to be higher. When examining the bias, there seems to be a slight negative or positive slope, however, the slope is usually relatively low and seems to be mainly motivated by outliers. This means that for most areas in the design space, there is little to no bias.

As a final check of the quality of the response surface, some cross sections were evaluated and plotted against 2D validation data of the same cross section. In this case the cross sections were taken for varying A and θ and at constant $D/b = 0.14$, $x/c = 0.8$ and $z/D = 0$. By varying only two parameters, a 2D slice of the data is created, which can be easily visualized. The 2D validation data is also obtained using 2D LHS and a response surface is constructed using polynomials. However, the 2D data can be sampled at a higher sampling point density, thus it is expected that the 2D response surface represents the data better. However, the 2D sampled response surface cannot average out

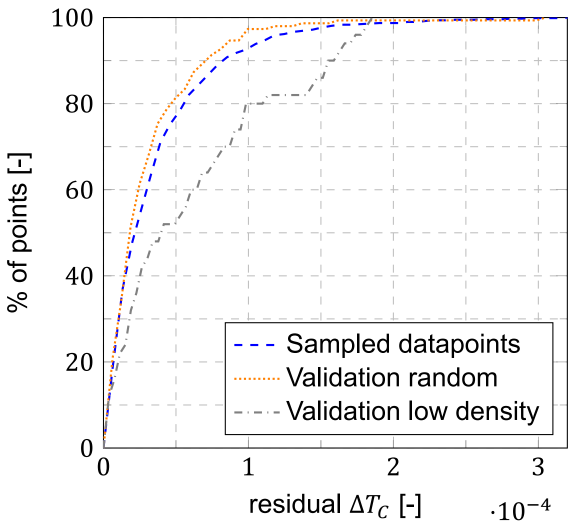

Figure 8.7: Comparison of residuals of ΔT_C for metamodel 1

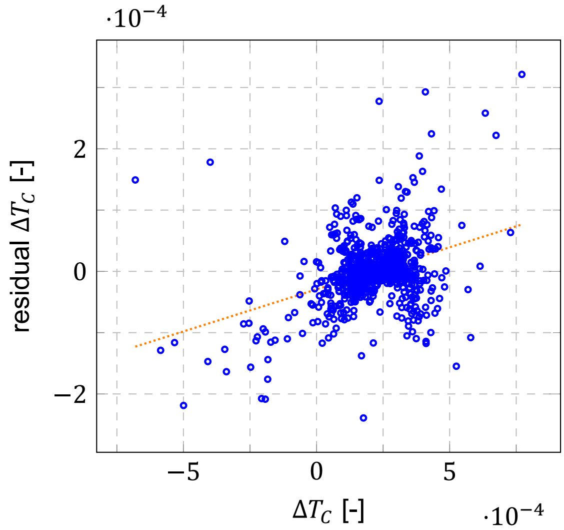

Figure 8.8: Bias of residuals of ΔT_C for metamodel 1

any numerical errors from the other design parameters. Thus, the 2D data should not be taken as an absolute truth. In Figures 8.9 and 8.10 results for ΔC_D are shown for metamodel 1 (the 5D response surface) and the 2D validation response surface respectively. It can be seen that the shapes match somewhat. In the upper left corner the highest values (less negative) of ΔC_D are found and it decreases generally with both θ and A. However, in the 2D response surface it can be seen that ΔC_D decreases with increasing A till it reaches a minimum and then increases again. This is not captured by the 5D response surface. However, the difference between the data is relatively small, about $2 \cdot 10^{-4}$, which is in the same range as the expected residual, as shown in Figure 8.5. Thus, this gives confidence that ΔC_D is modelled correctly.

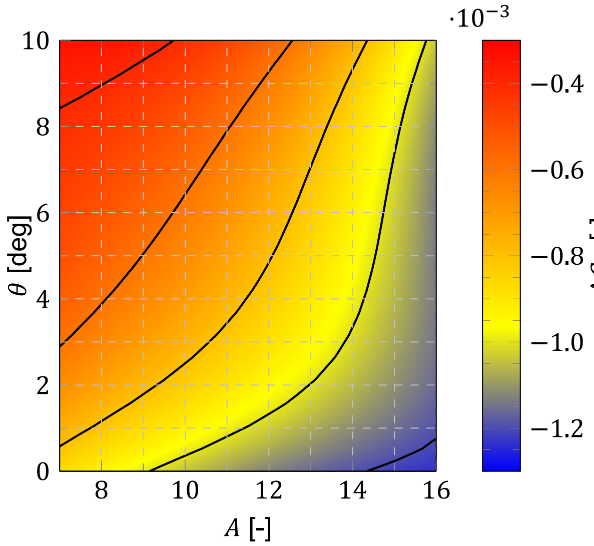

Figure 8.9: A cross section of the response surface for ΔC_D

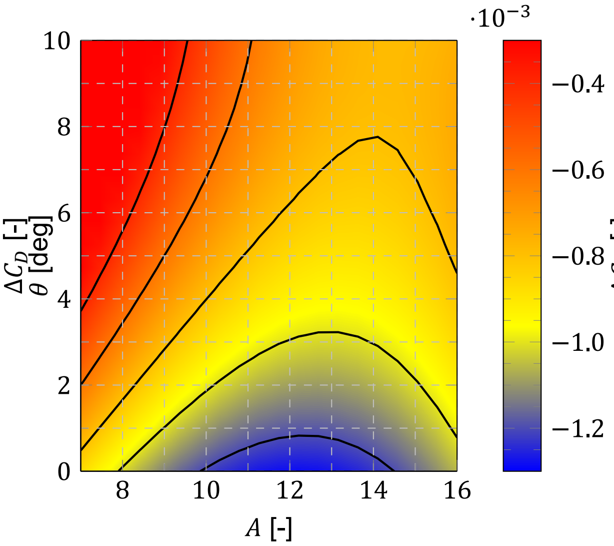

Figure 8.10: Validation data obtained by using a 2D response surface for ΔC_D

Also, a comparison is made for ΔT_C. The cross section from the 5D response surface and the 2D validation response surface are shown in Figures 8.11 and 8.12 respectively. The 5D response surface predicts the main trends, but the shape of the cross section is slightly different from the shape presented in the validation data. Especially in the lower left corner, the high ΔT_C area has a very different shape. However, again the errors are relatively small, about $1 \cdot 10^{-4}$, which is also in the order of the response surface residual. Thus, it seems that ΔT_C is modelled correctly.

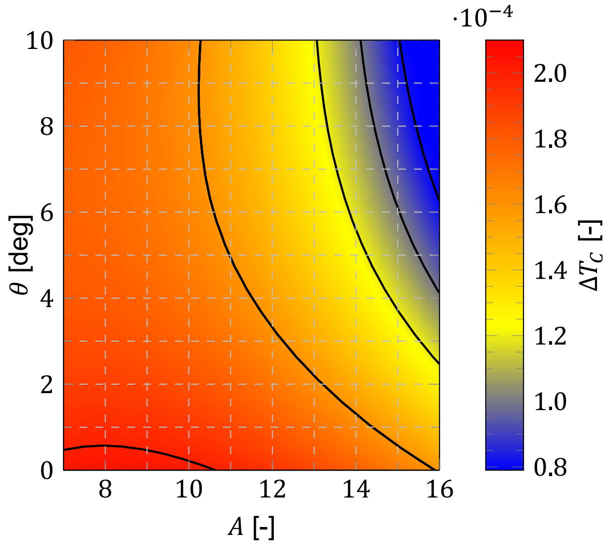

Figure 8.11: A cross section of the response surface for ΔT_C

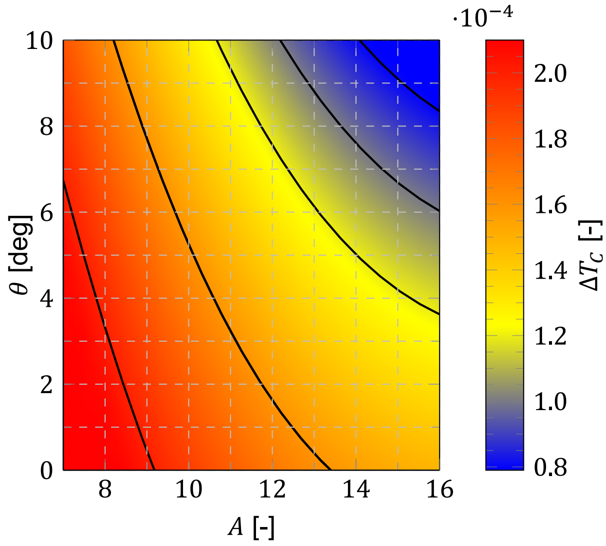

Figure 8.12: Validation data obtained by using a 2D response surface for ΔT_C

In this section only a small portion of the data is presented. ΔC_D and ΔT_C are presented, since they are representative of the other performance parameters. Furthermore, more cross sections of the data were investigated, also for other design parameter combinations. However, all results were very similar, thus only the two previously described cross sections were discussed. Thus, it is concluded that the create response surface can predict the main trends for the chosen performance parameters in the design space. However, the value of the expected residual must be considered when evaluating the significance of predicted differences.

8.1.4. Design parameter interaction

In this section interaction between design parameters is investigated. These design parameters are A, θ, D/b, x/c and z/D. Interaction is investigated by looking at how performance parameters are directly related to the design parameters.

Main interaction mechanism

Before analyzing the results, the main propeller-wing interaction mechanism is explained and how it is modelled by the numerical model. Firstly, two flow regions are defined on the wing. These are shown in Figure 8.13. Here the wing with propeller (solid lines) is seen. The dashed line shows the propeller slipstream boundary, which lies inside the propeller boundary, due to contraction. This slipstream boundary separates the two regions. Region I is outside the propeller slipstream and is thus not directly affected by the propeller slipstream. Region II lies within the propeller slipstream and is thus directly affected.

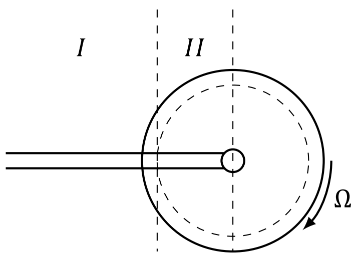

Figure 8.13: Definition of the flow regions on the wing

Next, the lift is affected by the change in dynamic pressure and the change in angle of attack. In Figure 8.14 an overview of the velocities on the wing can be found. It can be seen that the propeller induces both a horizontal ($u_{p,x}$) and vertical ($u_{p,z}$) velocity. The horizontal velocity is mostly dependent on the propeller axial velocity and thus the thrust, while the vertical velocity is mostly dependent on the propeller tangential velocity and thus the swirl. The wing also induces a vertical velocity ($u_{i,w}$) due to the trailing vortices in the wake. It can be seen that due to the geometry, dynamic pressure is mainly affected by $u_{p,x}$, while angle of attack is mostly dependent on $u_{p,z}$ and $u_{i,w}$. In region I only $u_{i,w}$ will be present. However, $u_{i,w}$ is also affected by the propeller, since $u_{i,w}$ depends on the wing circulation distribution.

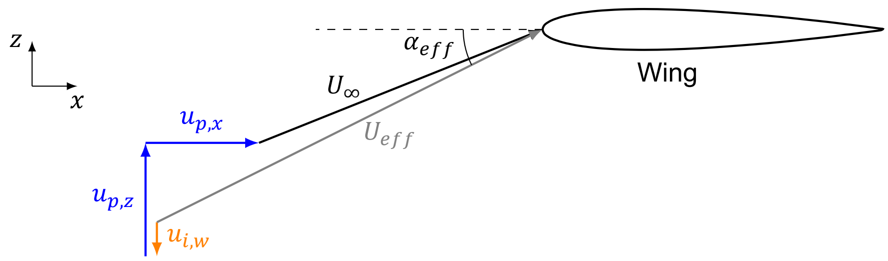

Figure 8.14: Schematic of the velocities acting on a wing section

The effect of propeller-wing interaction on drag is mostly dependent on vertical induced velocities in the numerical model. Thus, trailing vortices from the wing play an important role. This is schematically shown in Figure 8.15. Due to the propeller induced velocities on the wing, the lift increases for the part of the wing in the propeller slipstream. This increased lift actually leads to a larger wingtip vortex, since spanwise circulation gradients near the tip are higher. This creates more negative wing induced velocities, but due to the decrease in lift at the propeller slipstream boundary on the wing, a trailing vortex in opposite direction is created on the wing at the jet slipstream boundary. This further decreases induced velocities in the part of the wing inside the propeller slipstream, but it induces more positive velocities on the rest of the wing, region I. This leaves the part of the wing inside the slipstream, region II, with highly negative wing induced velocities. To this the propeller induced velocities are added, which are upwards (positive) for inboard-up rotating propellers with positive blade loading. This will counteract the increased negative induced velocities due to the trailing vortices. Figure 8.16 shows an example of how this looks in practice. Here the vertical induced velocity $u_{i,z} = u_{p,z} + u_{i,w}$ is plotted. The propeller slipstream boundary is located at $y/b = 0.45$. At this spanwise position the influence of the trailing vortex at the slipstream boundary is clearly seen. There is more positive induced velocity on the outside of the jet and more negative induced velocity on the inside. Within the jet, it can be seen that the wing induced velocities $u_{i,w}$ are more negative compared to the propeller-off case. This is counteracted by the propeller induced velocities, leaving a part with increased and a part with decreased induced velocity compared to the propeller off case. Lastly, for the section of the wing outside the slipstream it can be seen that the induced velocities are less negative, as expected.

Change in drag

The change in drag coefficient, ΔC_D is very sensitive to changes in induced velocities and it seems to be affected by all design parameters. In Figures 8.17 and 8.18 results are shown for ΔC_D for different values of x/c, D/b and A. Firstly, the main effects will be explained by investigating the effect of the design parameters on the wingtip vortex and propeller swirl interaction.

The magnitude of ΔC_D increases for higher values of x/c and it reaches an asymptote as x/c increases. This is expected, as the induced velocities change with x/c. From the propeller plane, induced velocities increase with increasing x, until they reach their final asymptotic value. This behaviour clearly has an influence on the ΔC_D. The change in drag is caused by an increase in lift on the part of the wing inside the slipstream (region II). With increasing x/c the dynamic pressure increases and tangential velocities increase. When discussing the change in lift, it will be seen that due to the relative change of these two, the increase in lift is less for increasing x/c. Using Figure 8.15, it can be seen that a smaller increase in lift leads to a smaller upwards induced velocity in the part of the wing outside the jet (region I). This increases induced drag. However, in the part of the wing inside the jet (region II), the induced velocity is more positive, decreasing induced drag here. Since the drag is calculated in the Trefftz plane, far downstream, x/c has no direct influence on the induced drag, as the vertical induced velocities are calculated downstream. This means that with increasing x/c, the propeller induced velocities stay constant, leading to more positive trailing vortex induced velocities on the part of the wing inside

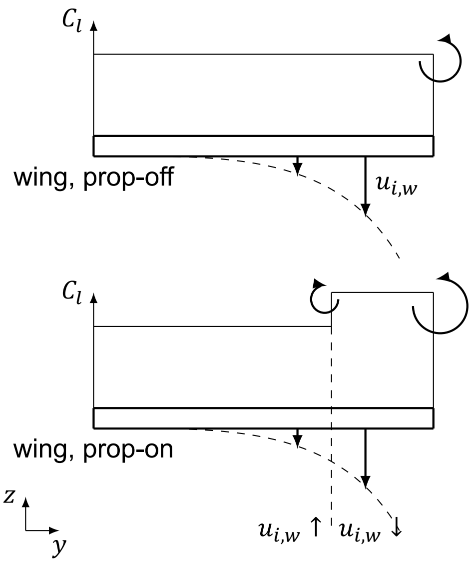

Figure 8.15: Effect of the lift distribution on the wing induced velocities

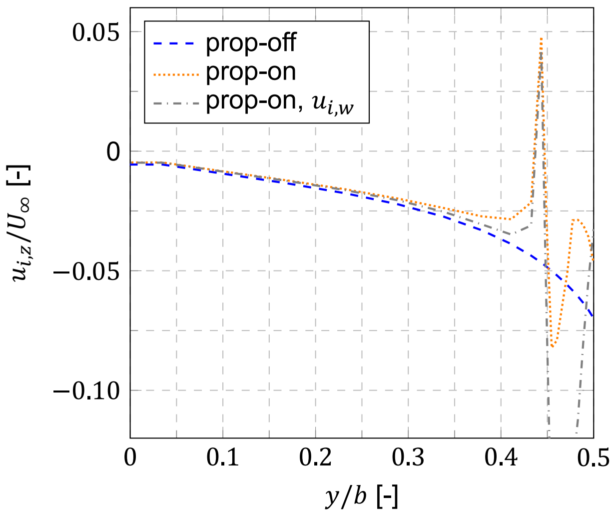

Figure 8.16: The effect of the propeller on the total vertical induced velocities on the wing

the propeller slipstream (region II). This decreases induced drag. It is concluded that ΔC_D increases (more negative) with increasing x/c, due to a decrease in lift on the part of the wing in the propeller slipstream, which reduces the induced velocities due to trailing vortices on the part of the wing inside the propeller slipstream. This interaction effect between ΔC_D and ΔC_L will be further explored in Section 8.1.5.

Next to x/c, D/b also has some influence on the ΔC_D. With increasing D/b a larger ΔC_D is expected. D/b is a measure of the relative surface area of the wing that is immersed in the propeller slipstream. It seems that with increasing affected surface area, the strength of the wingtip vortex can be further reduced, leading to a lower induced drag, compared to the prop-off condition. It is expected that this is mainly due to the effect of the induced tangential velocities of the propeller. With a larger part of the wing in the propeller slipstream, a larger part of the wing sees a lower (more positive) induced velocity, which decreases induced drag.

Figure 8.17 shows the results for $A = 8$, while Figure 8.18 shows results for $A = 15$. The influence of aspect ratio on the change in drag is expected to come from two contributions. Firstly, there is a hidden x/c effect. As aspect ratio increases for an equal surface area, the span increases and chord decreases. This decrease in chord, leads to a lower x for the same x/c. Thus, increasing the aspect ratio results basically in a shift in x/c. This should increase the magnitude of ΔC_D for higher aspect ratio. The second phenomenon is that an increase in aspect ratio decreases the wingtip vortex strength. It is expected that a small wingtip vortex would lead to less benefit from the propeller-wing interaction, this should lead to a decrease in the magnitude of ΔC_D with increasing aspect ratio. However, when comparing Figures 8.17 and 8.18, the magnitude of ΔC_D increases (more negative) with increasing aspect ratio, thus it is concluded that the main effect of aspect ratio on ΔC_D is due to the effect of horizontal position. However, it must be noted, that this effect is relatively small for most D/b values. For $D/b = 0.20$ the effect seems the largest. This could be because for a higher D/b a larger part of the wing is affected by the propeller slipstream. Thus, the same change in induced velocity by changing x/c, should lead to a larger difference in ΔC_D for higher D/b. However, in the graphs it is seen that for constant A, the change in ΔC_D is similar for all D/b Thus, it is believed that for $D/b = 0.20$ the change in ΔC_D due to aspect ratio is over estimated by the response surface. This is likely, since $D/b = 0.20$ is at the edge of the design space where the largest residuals are expected.

Next, some minor effects on ΔC_D will be discussed. As can be seen in Figures 8.17 and 8.18 there are still relatively large spread around the trend lines. These effects are mainly due to the vertical position of the propeller slipstream. In Figure 8.19 it is shown that the propeller horizontal position x, the propeller vertical position z and the slipstream deflection, determine the vertical position where the propeller slipstream crosses the wing z'. Furthermore, the slipstream deflection is dependent on the

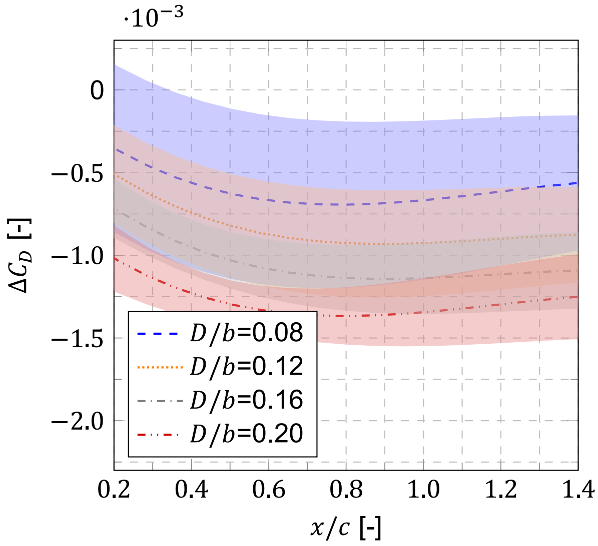

Figure 8.17: The effect of x/c and D/b on ΔC_D for $A = 8$ and $T_{C,des} = 0.05$

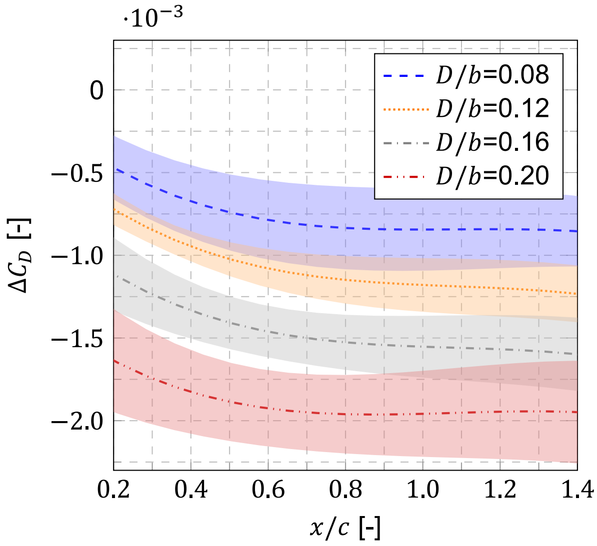

Figure 8.18: The effect of x/c and D/b on ΔC_D for $A = 15$ and $T_{C,des} = 0.05$

wing circulation. z' is the relative vertical position from the propeller slipstream center to the wing. It can be seen that this relative position z' determines the influence of the propeller induced radial velocity u_r. If z' is negative, with the wing below the mean propeller slipstream line, then u_r will increase angle of attack and reduce induced drag. If z' is positive, then u_r decreases angle of attack and increases induced drag. It must be noted that for the analyzed propeller-wing systems, z and z' are usually about the same. z/D ranges from -0.2 to 0.2, while the typical slipstream deflection is about $0.03D$ (upward) at the wing.

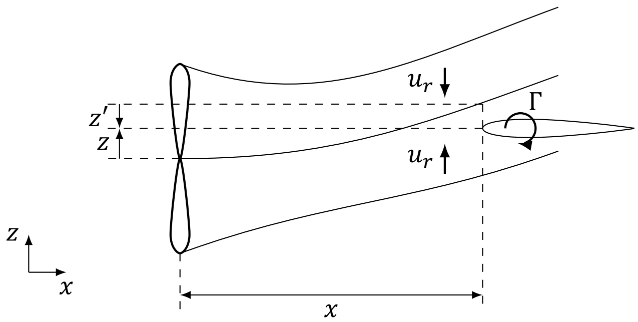

Figure 8.19: Schematic of the effect of slipstream deflection on propeller-wing interaction

Furthermore, the area of the wing affected by the slipstream changes with z', as shown in Figure 8.20. Due to the presence of the propeller hub, the propeller slipstream area has a doughnut shape. It can be seen that the marked area of the wing changes due to a change in z'. A higher or lower z' will give a larger affected wing area and thus leads to increased lift and decreased lift. A lower or higher z' also changes the way how the propeller induced tangential velocity u_t acts on the wing. It can be seen that for a low or high z', the effect of u_t on angle of attack will be decreased. This leads to less lift and more induced drag on the wing. Note that with a higher or lower z' also a larger part of the wing sees increased dynamic pressure, this changes the lift distribution thus also has some effect on drag.

Since ΔC_D is mainly dependent on vertical induced velocities on the wing, the numerical model is rather sensitive to change in z', since there are many ways this influences induced velocities. Thus, no clear relations are found in the data with respect to these phenomena. It mainly results in spread in the data, which can be seen in Figures 8.17 and 8.18.

Lastly, the influence of profile drag is discussed. Profile drag is somewhat dependent on angle of attack. But in the linear regime, the profile drag coefficient is almost constant. This leaves the influence of dynamic pressure. The propeller increases dynamic pressure on part of the wing. Here, the profile

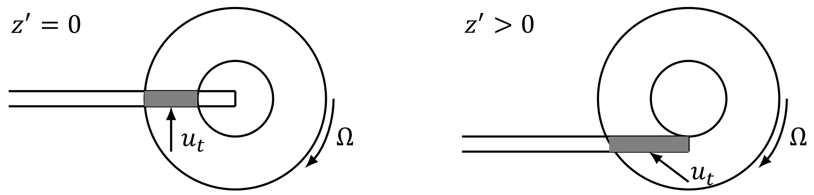

Figure 8.20: Change in propeller-wing interaction due to propeller vertical position

drag increases. This leads to an increase in profile drag for all designs. However, this increase is typically an order of magnitude lower than the decrease in induced drag. Thus, no clear influence of profile drag is present in the presented data.

Drag

As shown in Figure 8.21, the drag is mainly dependent on the wing parameters. The value of wing drag is about an order of magnitude larger than that of the change in drag due to propeller-wing interaction. This means that the drag for a propeller-wing system is mainly determined by the value of the clean wing drag, while the beneficial interaction can only provide some improvements. However, these improvements are relatively low compared to the improvements that can be obtained by changing the wing parameters. Increasing the aspect ratio decreases induced drag. Furthermore, increasing outboard twist increases induced drag as well, since the lift distribution will deviate more from the elliptical lift distribution, as shown in Figure 8.22. This will lead to more prominent wingtip vortices and thus more drag. So the value of C_D is mainly determined by the wing design, while propeller-wing interaction can only add some improvements in C_D on top of the initial value. This is consistent with data found by Koomen [84] and Sinnige et al. [41], where for similar C_L and T_C values similar changes in C_D were obtained.

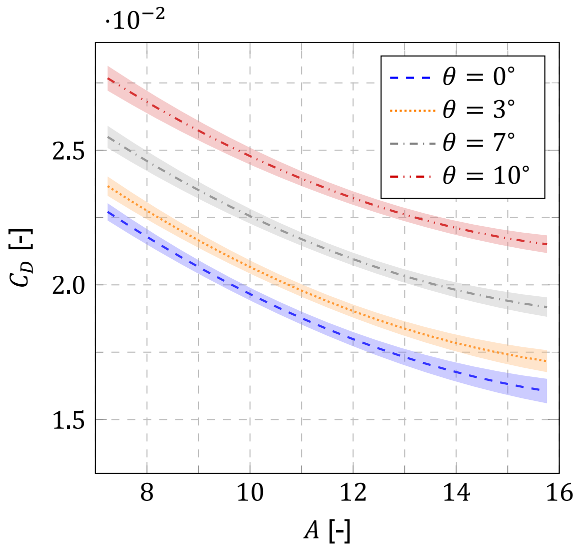

Figure 8.21: The effect of A and θ on C_D for $T_{C,des} = 0.05$

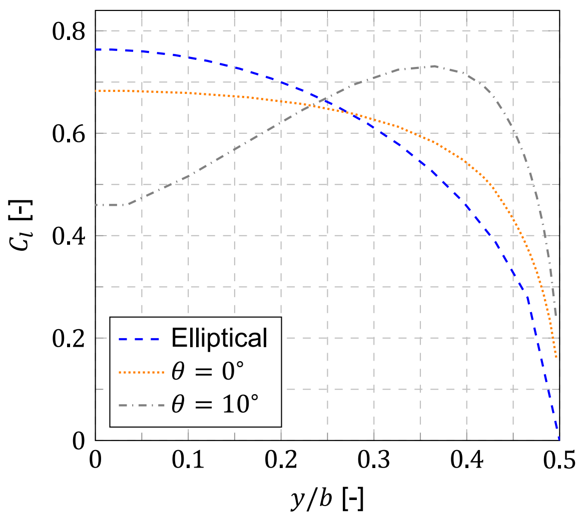

Figure 8.22: Clean wing lift distributions with different outboard twist for $C_L = 0.6$

Change in lift

The change in lift seems to be mostly dependent on z/D and x/c, as shown in Figure 8.23. If z/D increases from the lower z/D values, ΔC_L increases. Around $z/D = 0.08$, this increase stops. If z/D is increased further, ΔC_L will start to decrease. This relation seems for hold for all the data. Since the maximum ΔC_L only appears for a positive z/D and not a negative z/D with the same magnitude, it is believed that the change in ΔC_L with z/D is due to radial velocity in the propeller slipstream. In Figure 8.19 it was shown that for a high propeller position, radial velocity causes an increase in angle of attack, while for a low propeller position, the angle of attack is decreased. The propeller hub was defined at

$r_{hub}/D = 0.075$. By evaluating the numerical model, the slipstream deflection for different configurations can be found. From this, a typical (positive) slipstream deflection of $0.03z/D$ was obtained. This means that for a value of $z/D = 0.1$, the wing would typically cross the slipstream just below the low dynamic pressure center of the slipstream, left by the presence of the propeller hub. Thus, it seems that the maximum increase in ΔC_L is obtained when the wing is immersed in the part of the propeller slipstream just below the low dynamic pressure area of the propeller hub.

Changing z/D also changes the wing area affected by the propeller slipstream. This has been shown in Figure 8.20. From this it is expected that for a position just below or above the propeller hub, the maximum increase in dynamic pressure is obtained, which should increase lift and thus ΔC_L. However, changing the vertical propeller position also changes the influence of the propeller induced tangential velocity. If the wing is not in the center of the slipstream, the vertical component of the tangential velocity will decrease. This would lead to a decrease in ΔC_L. If one of the previous described phenomena would dominate, a peak would be expected for both positive and negative values of z/D. As seen in Figure 8.23, this is not the case. However, the response surface is of order two, so the response surface can not model such behaviour. However, when increasing the order of the response surface, no such behaviour was found. Thus, it is concluded that the effect of propeller radial velocity is the dominating effect of z/D on ΔC_L.

Next to z/D, x/c seems to have an influence on ΔC_L. When investigating ΔC_D it was seen that an increase in x/c increases the vertical induced propeller velocity and thus lowers C_D. An increase in the vertical induced velocity would mean a greater decrease in drag and a higher increase in lift. However, the opposite is observed. With a higher x/c, the ΔC_L decreases. It seems that an increase in horizontal induced propeller velocity results in a decrease of angle of attack. Figure 8.14 shows that for an increase in $u_{p,x}$ angle of attack will decrease. However, this is dependent on the relative values of the horizontal and vertical induced velocities. Note that the absolute effect of this is still an increase in angle of attack, while this gain in angle of attack decreases with increasing x/c. Figure 8.25 shows the typical development of the induced velocities with x. It can be seen that $u_{p,z}$ shows a vary rapid increase with increasing x, but it quickly reaches its asymptotic value. The rise of $u_{p,x}$ is much slower and it slowly converges to the asymptotic value. Thus, for most x, increasing x leads to a relatively small increase in $u_{p,z}$ and a relatively large increase in $u_{p,x}$. This leads to a decrease of angle of attack with increasing x.

In Figure 8.24 it can be seen that the spread in ΔC_L at constant x/c is mainly caused by D/b. Again, with increasing D/b, the surface area of the wing in the propeller slipstream increases. This results in a larger area where lift increases, thus a larger ΔC_L.

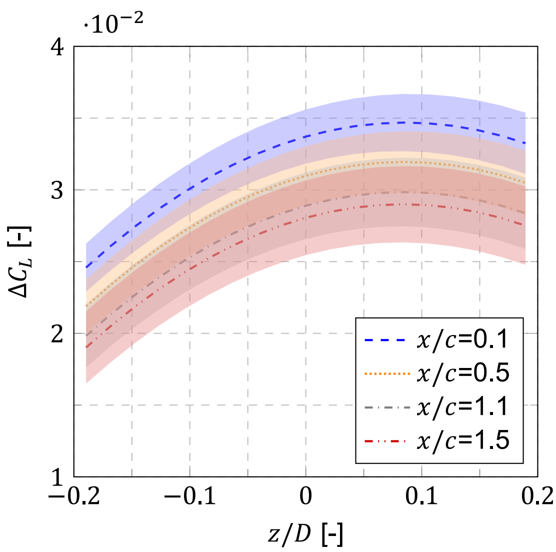

Figure 8.23: The effect of z/D and x/c on ΔC_L for $T_{C,des} = 0.05$

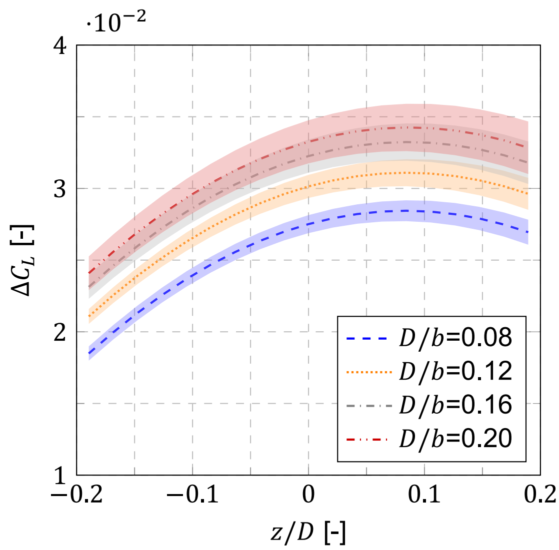

Figure 8.24: The effect of z/D and D/b on ΔC_L for $x/c = 0.5$ and $T_{C,des} = 0.05$

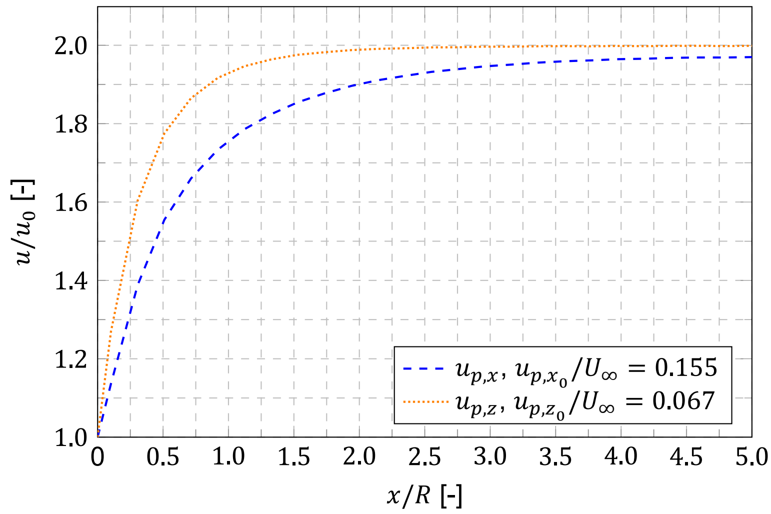

Figure 8.25: The development of horizontal and vertical propeller induced velocities with axial position

Change in lift-to-drag ratio

The change in lift-to-drag ratio $\Delta(L/D)$ is dependent on all previously discussed performance parameters: ΔC_D, C_D and ΔC_L. However, when analyzing the results, D/b, A and θ are found to be the main drivers of $\Delta(L/D)$, as shown in Figures 8.26 and 8.27. Thus, it seems that $\Delta(L/D)$ is mainly dependent on the absolute value of drag C_D and the change in drag ΔC_D. The same is found in the performance parameter interaction study, which will be discussed later. The value of C_D is important, since for a lower C_D, the same ΔC_D results in a larger $\Delta(L/D)$. In Figure 8.21 it can be seen that for an increasing aspect ratio A and decreasing outboard wing twist θ, C_D decreases and $\Delta(L/D)$ increases. In Figures 8.17 and 8.18 it was shown that ΔC_D increases with increasing D/b. Thus, $\Delta(L/D)$ also increases with D/b. Finally, the absolute values of L/D range from 22 for low A and high θ to 38 for high A and low θ. This gives a typical relative L/D increase of about 10%.

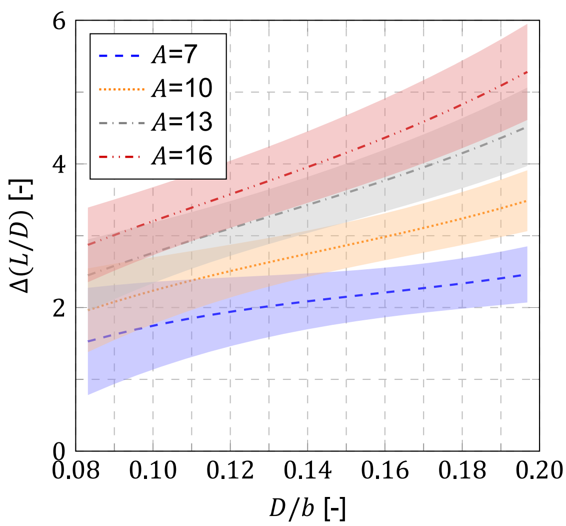

Figure 8.26: The effect of D/b and A on $\Delta L/D$ for $\theta = 3°$ and $T_{C,des} = 0.05$

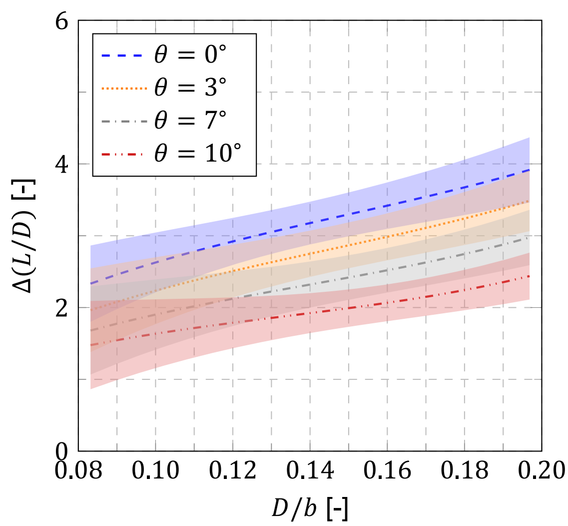

Figure 8.27: The effect of D/b and A on $\Delta L/D$ for $A = 9$ and $T_{C,des} = 0.05$

8.1.5. Performance parameter interaction

In this section the interaction between performance parameters is investigated. The performance parameters are: ΔC_D, C_D, ΔC_L, $\Delta(L/D)$ and ΔT_C. The relationships found between performance parameters will be explained using the knowledge obtained from the design parameter interaction study.

In Figures 8.28 and 8.29, the relation between ΔC_L and ΔC_D is shown. In Figure 8.28 it is shown that there is a negative correlation between ΔC_L and ΔC_D for constant x/c. This means an increase in ΔC_L gives a further decrease in ΔC_D. This makes sense, as both ΔC_L and ΔC_D are driven by the amount of propeller induced velocity. So for more propeller induced velocities, it makes sense that this will be beneficial for both ΔC_L and ΔC_D in most cases. The interaction effect has been shown in Figure 8.15, where an increase in lift on the part of the wing in the propeller slipstream leads to a trailing vortex which induces positive velocities on the part of the wing outside the slipstream. However, the influence of x/c is not mutually beneficial. It can be seen that for higher x/c, the achievable ΔC_D becomes more negative, while the achievable ΔC_L decreases. The effect of x/c on ΔC_L and ΔC_D has already been explained in the design parameter interaction study, Section 8.1.4. The interaction between ΔC_L and ΔC_D is different here, because when changing x/c, induced velocities change for the lift calculation, but not for the drag calculation, as a Trefftz plane analysis is used. The net result of this interaction is then a positive relation between ΔC_L and ΔC_D. Thus, for the design of x/c a trade-off needs to be made between gains in lift or drag.

Figure 8.28 has ΔC_D on the horizontal axis and ΔC_L on the vertical axis, while this is flipped for Figure 8.29. Due to the large spread of the data points it would be possible to find an accidental correlation. However, both graphs show the same behaviour, so the correlation between ΔC_L and ΔC_D seems to be significant. Only for the $x/c = 0.1$, the correlation found seems to have a different shape in the two graphs. This is attributed to the response surface error, as $x/c = 0.1$ lies at the edge of the design space and the same shapes are found for all other values of x/c.

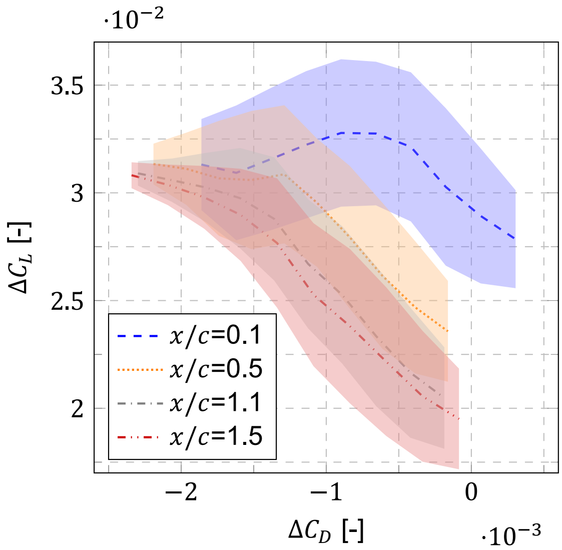

Figure 8.28: Correlation between ΔC_L and ΔC_D for constant x/c at $T_{C,des} = 0.05$

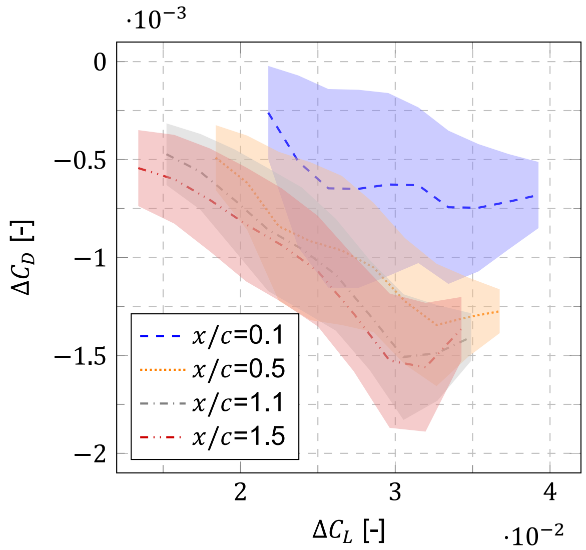

Figure 8.29: Correlation between ΔC_D and ΔC_L for constant x/c at $T_{C,des} = 0.05$

In Figures 8.28 and 8.29 it can be seen that for a constant x/c, there is still some spread in the data. This is the influence of the design parameters z/D and D/b, as shown in Figures 8.30 and 8.31 respectively. It can be seen that a constant z/D gives an almost constant ΔC_L. In order words, z/D has a much larger impact on ΔC_L than ΔC_D. Thus, z/D can be chosen to maximize ΔC_L as it does not affect ΔC_D in a significant way. The opposite is true for D/b. It can be seen that for a constant D/b, ΔC_D is almost constant, so the impact of D/b is larger on ΔC_D than ΔC_L. Thus, D/b should be chosen to minimize drag.

Figure 8.32 summarizes the findings for the relations between ΔC_L and ΔC_D. By varying x/c a design space is chosen. Then, by using z/D and D/b, the ΔC_L and ΔC_D can be maximized. The design point with maximum benefit from propeller-wing interaction would be in the upper left corner of the design space. However, this would not necessarily lead to the best system performance. Since lift coefficient and thrust are constant for the presented data, the best performance would actually be given by the points with lowest drag. However, it has been shown that the absolute value of drag is mainly dependent on the wing design parameters A and θ, but it would still be beneficial to get the largest (most negative) ΔC_D to further maximize aerodynamic performance.

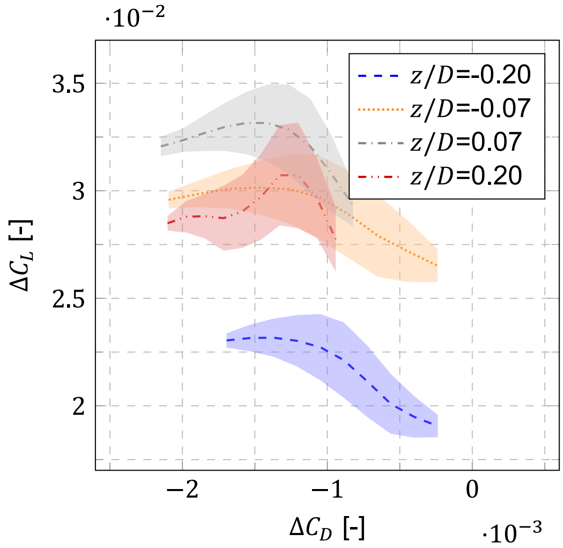

Figure 8.30: Correlation between ΔC_L and ΔC_D for constant z/D at $x/c = 0.5$ and $T_{C,des} = 0.05$

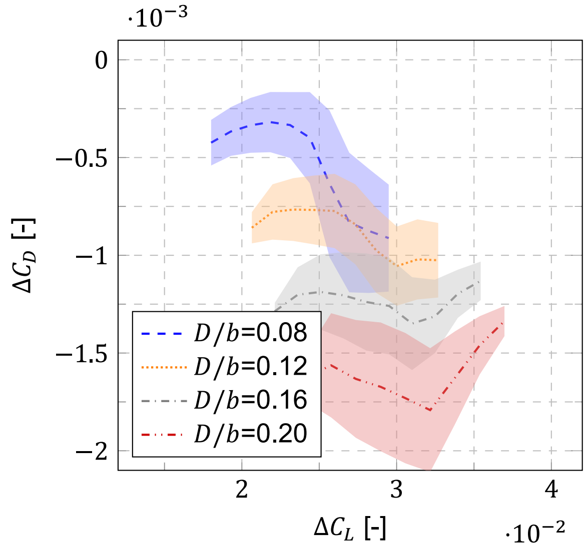

Figure 8.31: Correlation between ΔC_D and ΔC_L for constant D/b at $x/c = 0.5$ and $T_{C,des} = 0.05$

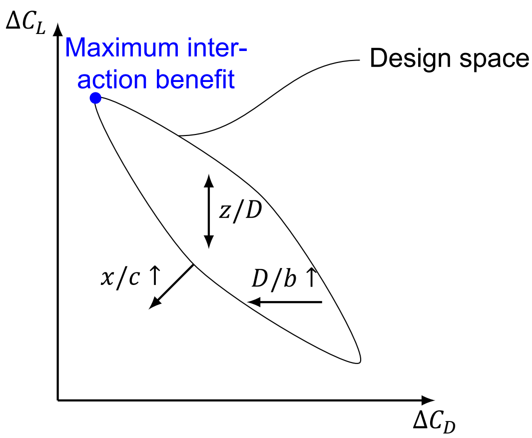

Figure 8.32: Schematic representation of the interaction between ΔC_L and ΔC_D and design parameters

In Figure 8.33 the relation between C_D and ΔC_D is shown. It can be seen that lines of constant A and θ give a linear relation. This is because for the same A and θ, the clean wing is the same and thus the clean C_D. The final value of C_D is determined by the ΔC_D, so this gives a linear relation. Furthermore, it can be seen that the magnitude of ΔC_D is typically an order of magnitude smaller than C_D, thus the final value of C_D mainly depends on the drag of the clean wing, while propeller-wing interaction can only provide some improvement to this initial C_D.

Next, in Figure 8.34 it can be seen that $\Delta(L/D)$ and ΔC_D are linearly dependent for constant A and θ. Constant A and θ represents the wing design. Thus, for a certain wing, the gain in wing efficiency is mainly determined by ΔC_D. Furthermore, the slope of the lines change for different A. It can be seen that for increasing A, the slope becomes more negative. This is due to the lower C_D expected at higher A, which gives more gain in $\Delta(L/D)$ for the same ΔC_D. These conclusions are consistent with the results found in the design parameter interaction study of the previous section.

Lastly, in both the design parameter interaction study and performance parameter interaction study, the change in thrust coefficient ΔT_C has not been discussed. This is because no correlations were found between ΔT_C and other design or performance parameters. Furthermore, ΔT_C is relatively small, with a maximum increase of 2% with respect to T_C.

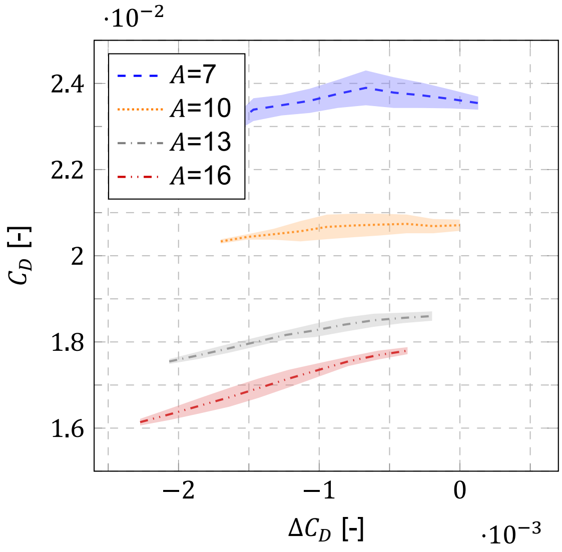

Figure 8.33: Correlation between C_D and ΔC_D for constant A at $\theta = 3°$ and $T_{C,des} = 0.05$

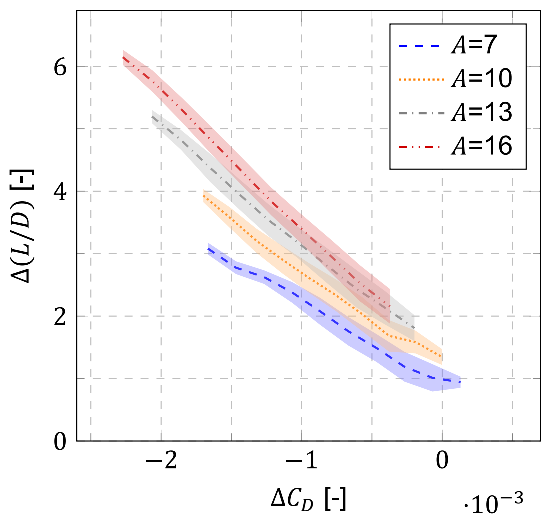

Figure 8.34: Correlation between $\Delta L/D$ and ΔC_D for constant A at $\theta = 3°$ and $T_{C,des} = 0.05$

8.2. Metamodel 2: Wing geometry and propeller position with increased thrust

The second metamodel uses the same parametrization as model 1. Design parameters are: A, θ, D/b, x/c and z/D, with their bounds given in Table 8.1. Performance parameters are defined as: ΔC_D, C_D, ΔC_L, $\Delta(L/D)$ and ΔT_C. Furthermore, all other settings are kept the same, except the design thrust $T_{C,des}$. While $T_{C,des} = 0.05$ for metamodel 1, it was increased to $T_{C,des} = 0.10$ for metamodel 2. This gives $T_C = 0.05$ for each propeller. By doing this the influence of the amount of thrust on the parameter interaction is investigated. With increased thrust there is more axial velocity and swirl in the propeller slipstream. It is expected that this will enhance wing performance, but it also costs more power to provide this thrust.

Since the set-up of metamodel 2 is practically the same as for metamodel 1, the set-up of metamodel 2 is not described in detail. For more information on the set-up of the metamodel, the reader is referred to Sections 8.1.4 and 8.1.2. Section 8.2.1 starts with an assessment of the quality of the produced response surfaces. This is followed by investigating the influence of design parameters on performance parameters in Section 8.2.2. Lastly, in Section 8.2.3 interaction between performance parameters is investigated.

8.2.1. Metamodel quality

The quality of the second metamodel has been checked in the same way as for the first metamodel. The number of sampled points was 750, based on the analysis of the first metamodel. The number of degrees of the polynomials has also been kept the same as for the first metamodel, as no major differences in behaviour were found. A summary of the values found with the second metamodel can be found in Table 8.3. It can be seen that a lot of the values are very similar to the first metamodel. The major difference is that the range of ΔC_D, ΔC_L and $\Delta(L/D)$ has increased. The values of R^2 and the residual are all approximately the same.

Table 8.3: Summary of the response surface results for metamodel 2

	min	max	range	N_{deg}	R^2	residual 90% limit
ΔC_D	-0.00590	0.00069	0.00659	3	0.691	0.00061
C_D	0.0147	0.0286	0.0139	2	0.940	0.00082
ΔC_L	-0.0083	0.0718	0.0801	2	0.487	0.0062
$\Delta(L/D)$	-0.29	11.97	12.27	3	0.799	1.07
ΔT_C	-0.00045	0.00116	0.00161	3	0.869	0.00011

In Figures 8.35 and 8.36 the residuals for ΔC_D are plotted. Again, two sets of validation data were used: one with randomly sampled points in the design space and one with points sampled in areas with a low sampling density. In Figure 8.35 it can again be seen that the behaviour of the residuals for the randomly sampled validation points is very similar to the residuals of the data. The residuals in the low density areas are again higher, meaning that the predictions by the response surface are more likely inaccurate. Again, the low density regions are mostly near the edges of the design space. In Figure 8.36 it can be seen that there is some bias in the residuals. This indicates that the real function of ΔC_D is likely to be much more complex and it can only be approximated with this polynomial function. Lastly, when compared to its counterpart of the first metamodel, Figure 8.6, it can be seen that for increased thrust more negative values of ΔC_D are possible. Similar results were obtained for ΔC_L and $\Delta(L/D)$, where more positive values could be obtained at the increased thrust level.

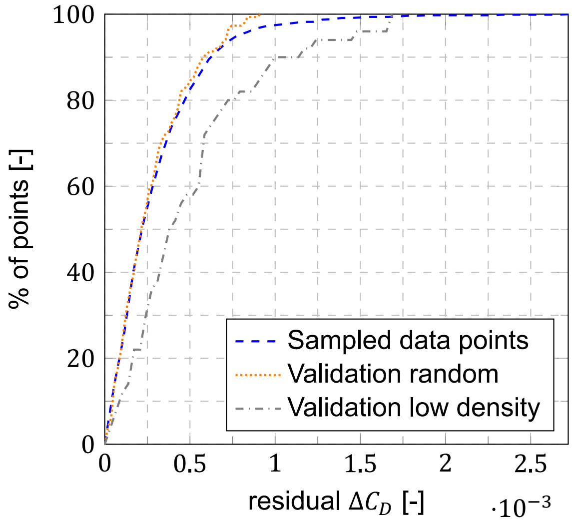

Figure 8.35: Comparison of residuals of ΔC_D for metamodel 2

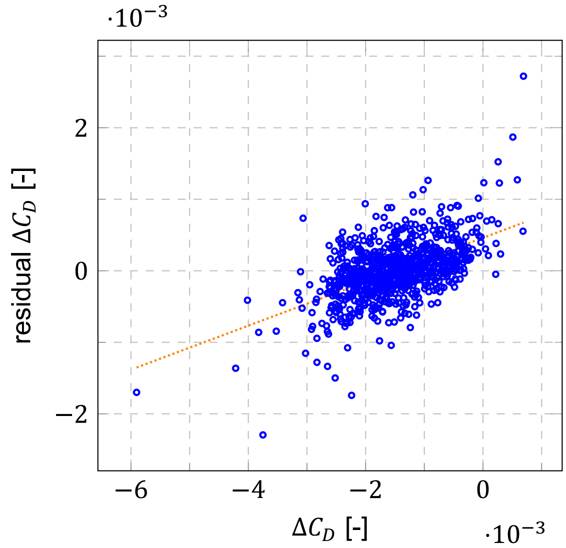

Figure 8.36: Bias of residuals of ΔC_D for metamodel 2

8.2.2. Design parameter interaction

In this section interaction between design parameters (A, θ, D/b, x/c, z/D) is investigated. Furthermore, comparisons with the data from metamodel 1 are made to investigate the influence of thrust on the propeller-wing interaction.

Change in drag

In Figures 8.37 and 8.38 it is shown how ΔC_D is dependent on D/b and x/c. Figure 8.38 shows results for $A = 15$. Here the same behaviour is found as when using the first metamodel, as shown in Figures 8.17 and 8.18. The mechanisms of this interaction are explained in Section 8.1.4. However, Figure 8.37 shows different behaviour for $A = 8$. It is expected that ΔC_D is more negative for increasing D/b, since this leads to a larger part of the wing affected by the propeller slipstream, but this behaviour is not found in Figure 8.37. This could be explained by the smaller span of the low aspect ratio wing. This gives also smaller propeller radii for the same range of D/b. If the radius of the propeller becomes smaller, the propeller induced axial velocity must increase to provide the same thrust. The axial velocity scales linearly with the propeller disk area and thus quadratically with the radius. This means that the increase in axial velocity due to a reduction in propeller radius is larger in magnitude for smaller propellers. This is shown in Figure 8.39. Here the average axial velocity on the propeller disk is plotted for different D/b. Because the surface area of the wing is constant, a smaller aspect ratio leads to a smaller span and thus smaller propellers. It can be seen that for $A = 8$ (smaller propellers) the graph is much steeper compared to the one for $A = 15$. Furthermore, the tangential velocity shows a similar behaviour, as it is dependent on the axial velocity. Thus, it is concluded that for increasing D/b, a larger part of the wing is in the propeller slipstream, leading to a more negative ΔC_D. However, when the diameter is small, an increase in D/b again gives a larger part of the wing in the propeller slipstream. However, this effect is counteracted by a relatively large reduction in propeller induced velocities, since the change in induced velocity scales quadratically with diameter. The net effect of this is a more positive ΔC_D for propellers with small diameter.

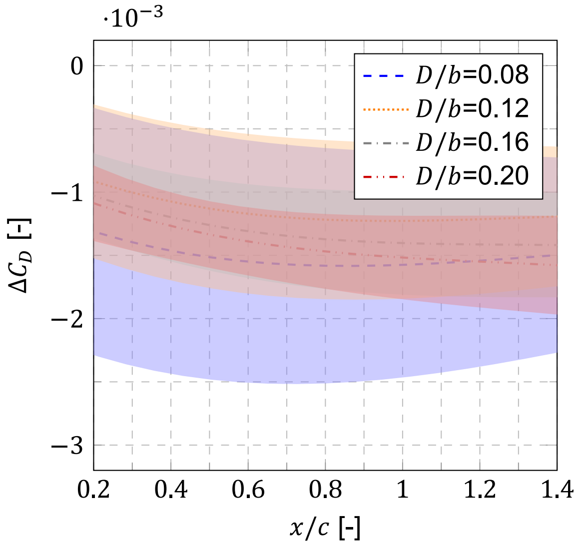

Figure 8.37: The effect of x/c and D/b on ΔC_D for $A = 8$ and $T_{C,des} = 0.10$

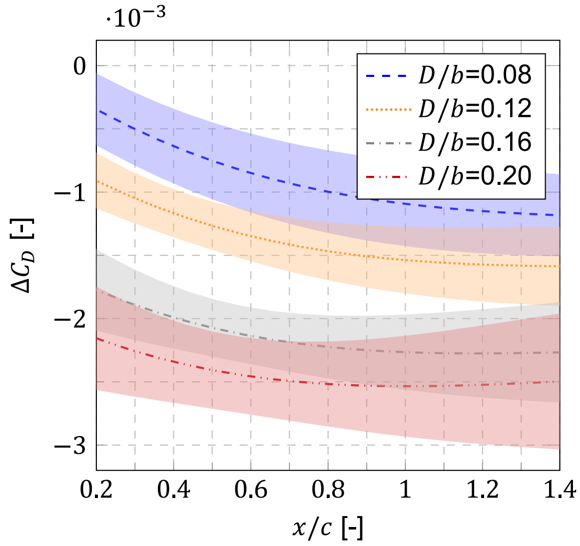

Figure 8.38: The effect of x/c and D/b on ΔC_D for $A = 15$ and $T_{C,des} = 0.10$

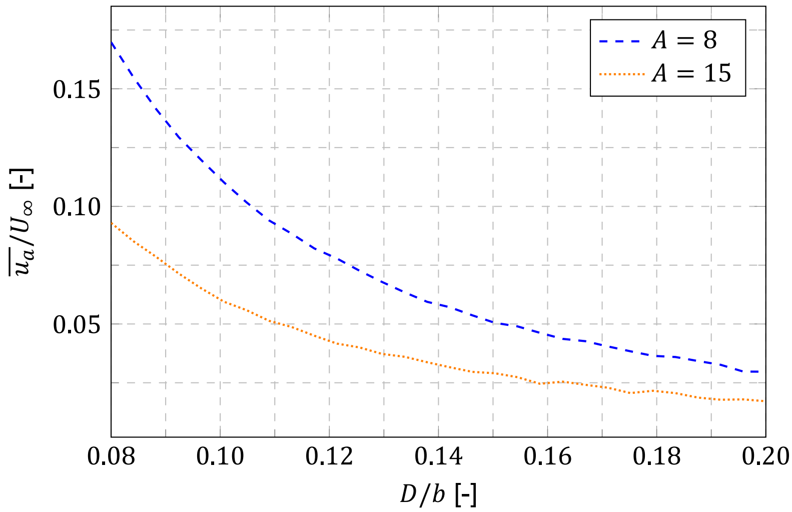

Figure 8.39: Comparison of the rates of change of propeller induced axial velocities with diameter

Drag

In Figure 8.40 the drag coefficient C_D is plotted for different A and θ. It can be seen that the drag is mainly dependent on the wing variables. Thus, the final drag value is mainly dependent on the clean wing drag, while the propeller-wing interaction only provides an additional drag reduction. When comparing this graph to Figure 8.21, it can be seen that the drag is overall lower for a higher thrust level. This is because with higher thrust, the increase in lift is also higher. This will be shown later. A higher lift increase means that, for the same design lift coefficient, the wing can operate at a lower angle of attack. This lowers the initial induced drag value of the wing, which is translated in a lower total drag when the propeller is installed. In other words, with increased thrust, the wing can achieve the same lift coefficient at a lower angle of attack, which decreases the drag. However, it is not yet sure if it is worth increasing thrust to lower the wing drag. This will be further discussed in Section 8.3, where the total system efficiency will be investigated.

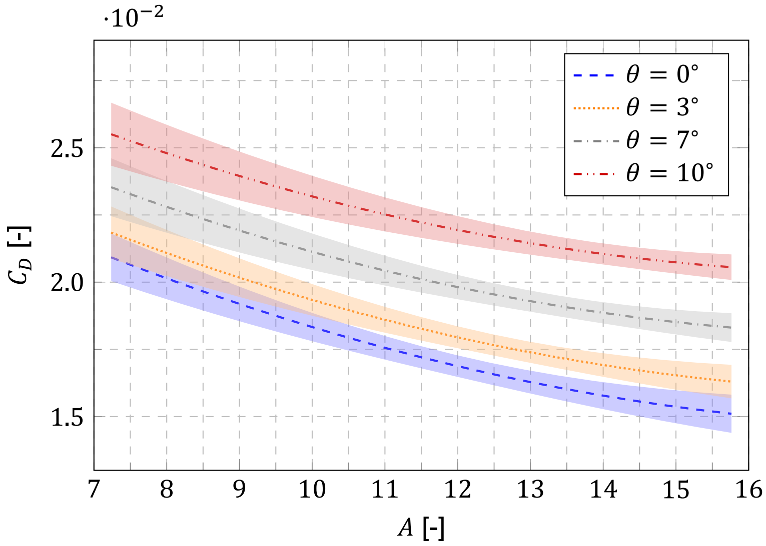

Figure 8.40: The effect of A and θ on C_D for $T_{C,des} = 0.10$

Change in lift
The results for the change in lift ΔC_L are shown in Figure 8.41 and 8.42. It can be seen that ΔC_L is dependent on z/D, x/c and D/b, as already discussed in Section 8.1.4. When comparing Figures 8.41 and 8.42 to Figures 8.26 and 8.27 obtained with metamodel 1, it can be seen that with increased thrust, ΔC_L increases as well. This is because the propeller induced velocities are larger in magnitude for higher thrust. Furthermore, for increased thrust, the maximum ΔC_L is obtained at a higher z/D. This shift in z/D is expected to come from a shift in radial velocity distribution in the slipstream. For higher thrust it seems that higher radial velocities are found at higher radial positions, shifting the optimal propeller vertical position for ΔC_L to a higher z/D. Furthermore, the increased lift on the part of the wing in the propeller slipstream has little influence on the propeller slipstream deflection. It is expected that when lift is increased on the part of the wing inside the slipstream, the local circulation increases. Since the circulation of the outboard part of the wing is the closest to the slipstream, the circulation here has the most effect on the slipstream deflection. Thus, when outboard circulation is increased at constant lift coefficient, it is expected that deflection increases, as shown in Figure 8.19. However, for metamodel 2 a typical deflection of $0.03D$ was obtained, similar to that of metamodel 1, indicating that the change in lift distribution has little influence on slipstream deflection.

Change in lift-to-drag ratio
In Figures 8.43 and 8.44 the influence of D/b, A and θ on the change in lift-to-drag ratio $\Delta(L/D)$ can be found. Again this shows that $\Delta(L/D)$ is mainly dependent on C_D and ΔC_D. $\Delta(L/D)$ increases with increasing A, with increasing D/b and decreasing θ. Furthermore, for low A and low D/b, these relations do no longer hold, because for propellers with a small area, the velocities change more rapidly. This has been explained when discussing the change in drag. When comparing the effect of thrust, using Figures 8.26 and 8.27 obtained with metamodel 1, it can be seen that increased thrust gives higher $\Delta(L/D)$ values, as expected from the drag and lift analysis.

Change in thrust
In metamodel 1, with low thrust, no correlation of the change in thrust ΔT_C was found with any design parameter or performance parameter. However, with increased thrust, a negative correlation of ΔT_C with z/D was found, as shown in Figure 8.45. This correlation with z/D seems to be the result of an angle of attack effect. The circulation on the wing induces upwash in front of the wing, resulting in an angle of attack at the propeller disk. However, the wing also induces a horizontal velocity component, as shown in Figure 8.46. It can be seen that above the wing this horizontal velocity component decreases the increase in angle of attack α, while it increases angle of attack below the wing. So, both above and below the wing there is an increase in angle of attack, but the increase below the wing is greater. At greater angle of attack, the propeller will produce more thrust, thus the negative correlation in Figure

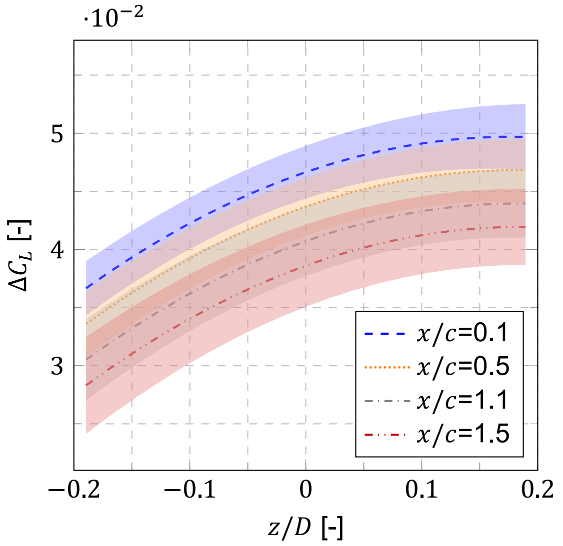

Figure 8.41: The effect of z/D and x/c on ΔC_L for $T_{C,des} = 0.10$

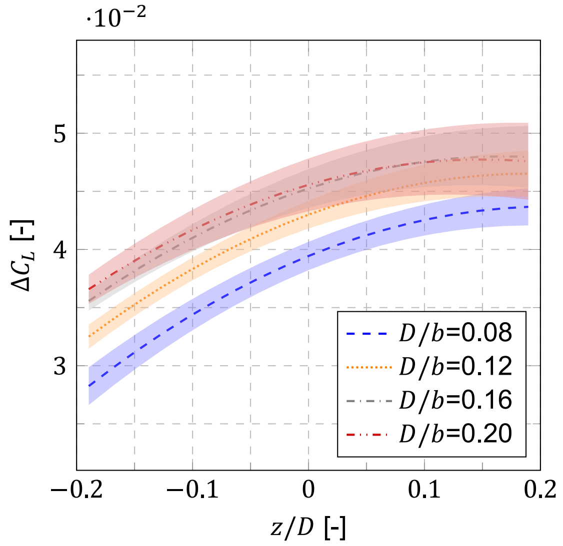

Figure 8.42: The effect of z/D and D/b on ΔC_L for $x/c = 0.5$ and $T_{C,des} = 0.10$

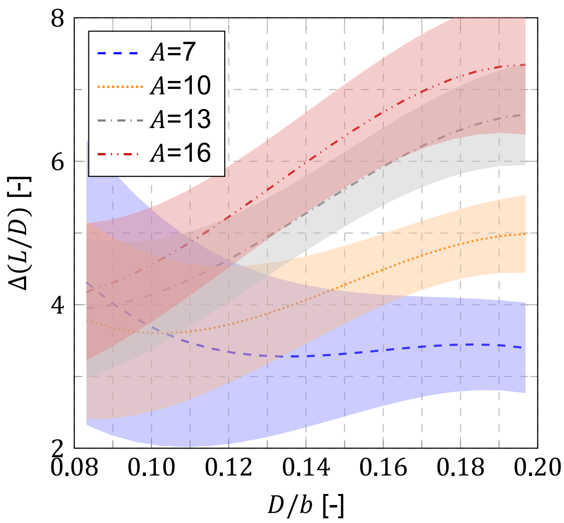

Figure 8.43: The effect of D/b and A on $\Delta L/D$ for $\theta = 3°$

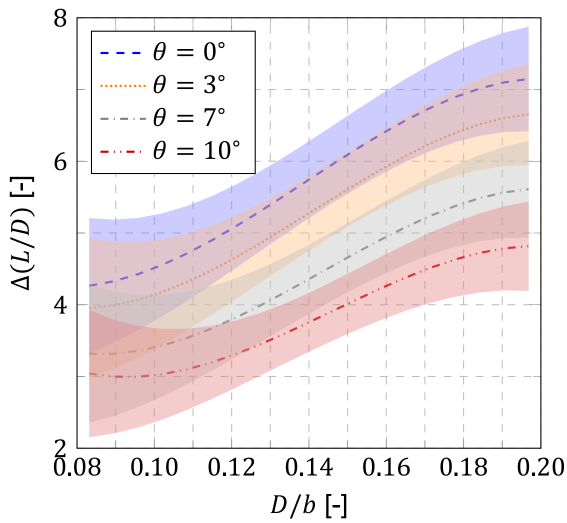

Figure 8.44: The effect of D/b and A on $\Delta L/D$ for $A = 13$

8.45 is found. It seems that because of the increased thrust, the circulation on the part of the wing inside the slipstream is increased. Only with increased circulation, the wing induced horizontal velocity component is significant enough to change angle of attack, while this was not the case for metamodel 1. The spread in the data in Figure 8.45 is suspected to be the cause of different x/c and different ΔC_L values at constant z/D. Note that in Figure 8.46, blockage effect from the wing is not shown, as this is not modelled by the numerical model.

8.2.3. Performance parameter interaction

In this section the interaction between performance parameters is investigated for metamodel 2. The performance parameters are: ΔC_D, C_D, ΔC_L, $\Delta(L/D)$ and ΔT_C, as described in Section 8.1.2.

In Figures 8.47 and 8.48 a correlation between ΔC_L and ΔC_D for constant x/c is investigated. There seems to be a slight negative correlation, similar to metamodel 1. However, it can be seen that the lines produced by Figures 8.47 and 8.48 have quite a different shape. This indicates that the correlation is not very strong. Furthermore, in Figures 8.49 and 8.50 results are plotted for constant z/D and D/b respectively. It can be seen that changes in z/D mainly result in a change in ΔC_L and it does not affect

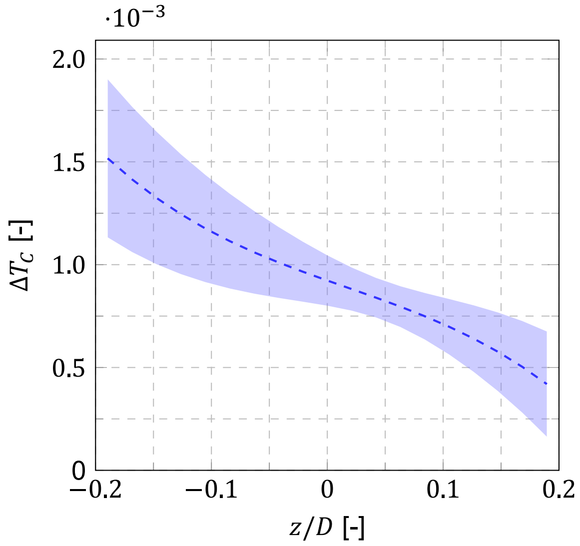

Figure 8.45: The effect of z/D on ΔT_C for $T_{C,des} = 0.10$

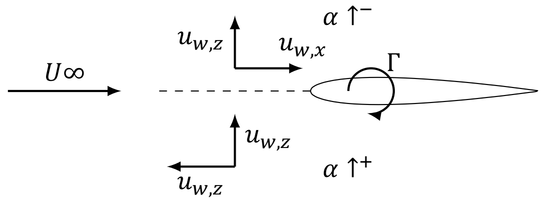

Figure 8.46: Schematic showing how the angle of attack in front of the wing is affected by circulation

ΔC_D significantly. A change in D/b mainly changes ΔC_D, as was found for metamodel 1. However, for smaller D/b values, also a significant change in ΔC_L is found when changing D/b. This means that when D/b is small, it can not be chosen independently of ΔC_L, while this is the case when thrust is lower. This is caused by a change in interaction mechanism when D/b is lower, which has been explained in Section 8.2.2. Lastly, when comparing Figures 8.47 and 8.48 to their counterparts for lower thrust, Figures 8.28 and 8.29, it can be seen that for increased thrust, ΔC_L is higher and ΔC_D is lower (more negative). This is due to the increased level of propeller-wing interaction with increased thrust. For drag this mainly influences the change in induced drag, since profile drag increases with increasing dynamic pressure. However, the change in profile drag is typically an order of magnitude lower than the change in induced drag, thus induced drag effects are dominant.

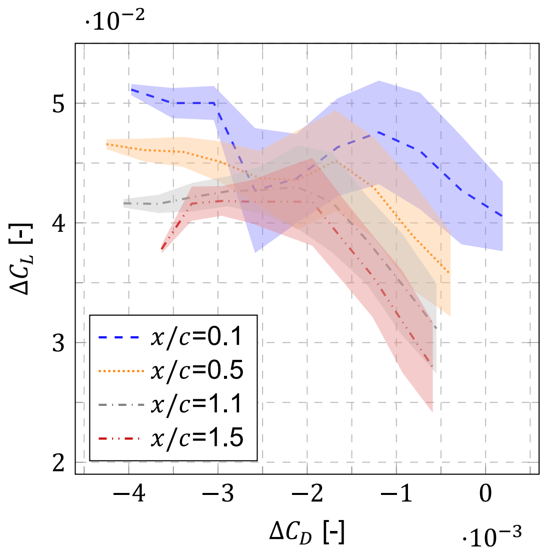

Figure 8.47: Correlation between ΔC_L and ΔC_D for constant x/c at $T_{C,des} = 0.10$

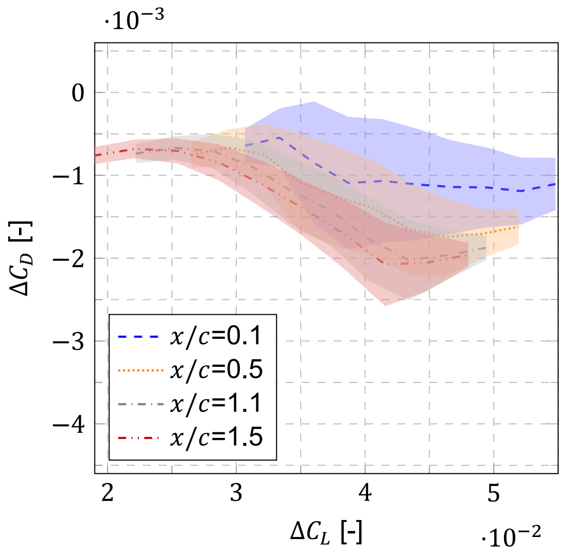

Figure 8.48: Correlation between ΔC_D and ΔC_L for constant x/c at $T_{C,des} = 0.10$

Now, the relations drawn for ΔC_L and ΔC_D in Figure 8.32 can be updated. This is shown in Figure 8.51. Again the design point that gives the maximum benefit from the propeller-wing interaction is indicated, but this point does not necessarily give the best system performance, as discussed in Section 8.1.5. In Figure 8.51 an arrow is added to indicate the influence of T_C. It can be seen that a higher T_C is

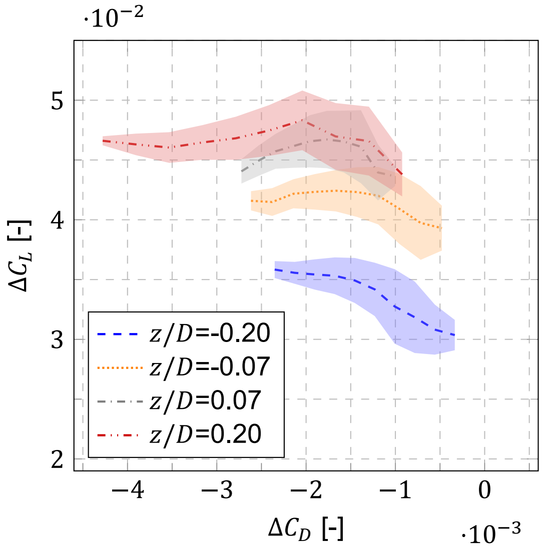

Figure 8.49: Correlation between ΔC_L and ΔC_D for constant z/D at $x/c = 0.5$ and $T_{C,des} = 0.10$

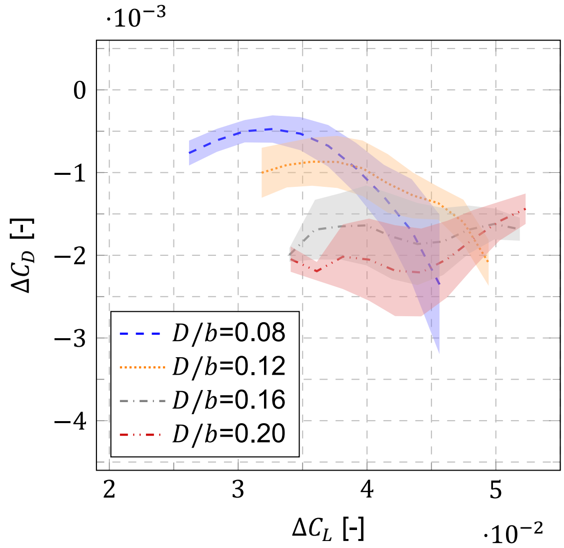

Figure 8.50: Correlation between ΔC_D and ΔC_L for constant D/b at $x/c = 0.5$ and $T_{C,des} = 0.10$

beneficial for both ΔC_L and ΔC_D. Of course, this is paired with an increase in power and the increase in thrust is limited, as the aircraft can only produce the amount of thrust needed to overcome drag. Other design aspects must also be considered when maximizing the thrust at the wingtips, such as structural design and one-engine out (OEI) condition. Lastly, in Figure 8.51 it can be seen that the influence of the design parameters remains the same as discussed in Section 8.1.5. Only at high T_C and relatively low values of D, the interaction effects change due to different behaviour of the propeller slipstream induced velocities. This phenomenon has been discussed in Section 8.2.2.

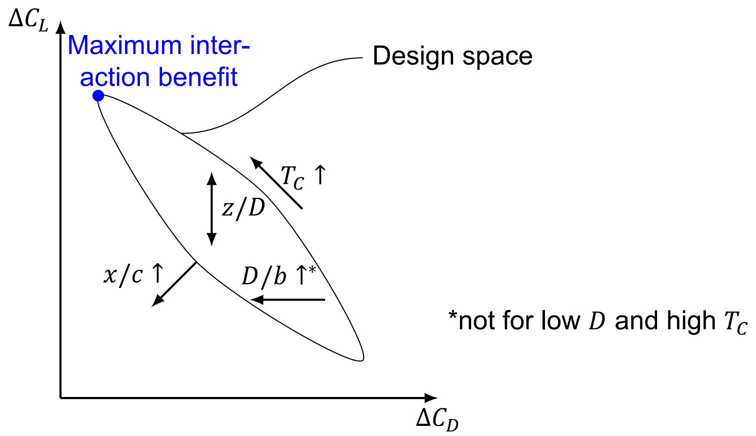

Figure 8.51: Schematic representation of the interaction between ΔC_L and ΔC_D and design parameters, revisited for metamodel 2

8.3. Metamodel 3: Lift, thrust and swirl

The third and final metamodel was made to investigate the relative influence of thrust and swirl. This was investigated to see which designs would lead to a high total system efficiency. By lowering propeller efficiency, a better wing aerodynamic efficiency could be obtained or vice versa. By evaluating the total system efficiency it can be quantified if such a trade-off would be beneficial or not. In Section 8.3.1 the design variables of this model are introduced. In Section 8.3.2 the performance parameters are described. Furthermore, the number of sampling points and degree of the response surfaces are determined. Subsequently, in Section 8.3.3 the quality of the created response surfaces is assessed.

Finally, in Section 8.3.4 the results obtained by this metamodel are discussed.

8.3.1. Parametrization

Metamodel 3 consists of four design parameters: the design thrust coefficient $T_{C,des}$, a swirl multiplication factor SMF, the design lift coefficient $C_{L,des}$ and wing aspect ratio A. These parameters are all non-dimensional. A summary of the design parameters is given in Table 8.4. Furthermore, the flight conditions were the same as in metamodel 1. The propeller-wing design parameters were as follows: $\theta = 0$, $D/b = 0.14$, $x/c = 0.2$ and $z/D = 0$, which gives a conventional and representative propeller-wing configuration.

- **Design thrust coefficient**
  The design thrust coefficient $T_{C,des}$ was included to see if absolute and or relative values of lift and thrust influence the propeller-wing interaction. The lower bound was set at zero, or negligible amount of thrust. This is to investigate for which amount of thrust the propeller-wing interaction would result in benefits in performance. Using distributed propulsion, it is always possible to design wingtip-mounted propellers for less thrust. For the upper bound, $T_{C,des} = 0.12$ was chosen, hence slightly above the $T_{C,des}$ used in metamodel 2. The operational settings for $T_{C,des}$ are given by advance ratio and pitch for the highest efficiency at the corresponding thrust level. Highest efficiency was chosen, since this would be a realistic choice when designing a propeller. The advance ratio and pitch are obtained for an isolated propeller at maximum efficiency at $T_{C,des}$ ($\frac{1}{2}T_{C,des}$ for a single propeller). The $T_{C,prop-on}$ typically differs about 1% with respect to $T_{C,des}$.
- **Swirl multiplication factor**
  The swirl multiplication factor SMF changes the amount of swirl in the propeller slipstream. At $T_{C,des}$, the propeller always operates at maximum efficiency for a given thrust level. To determine the influence of swirl, the calculated swirl at maximum efficiency is multiplied with SMF. In reality a change is swirl is obtained by a change in efficiency and thus power. This would potentially also change the propeller circulation distribution and thus the swirl distribution. However, this direct approach of influencing swirl was thought to make it easier to analyze the results. Thus, the SMF represents a direct change in propeller power and efficiency. The lower and upper bound of SMF are 0.5 and 2 respectively, giving a wide range for the propeller swirl. It must be noted that values of $SMF < 1$ might be hard, if not impossible, to obtain, since this would effectively call for a very efficient propeller.
- **Design lift coefficient**
  The design lift coefficient $C_{L,des}$ was included to see if the effect of thrust is relative with respect to the lift. $C_{L,des}$ varies from 0.2 to 0.8. $C_{L,des}$ is obtained by changing the wing angle of attack and calculating the lift curve slope for the propeller-wing system and interpolating to $C_{L,des}$.
- **Aspect ratio**
  Aspect ratio A has been included to still slightly change the spanwise lift distribution. The bounds are 7 and 16, the same as for metamodels 1 and 2.

Table 8.4: Design parameters and bounds for metamodel 3

	lower bound	upper bound
$T_{C,des}$	0.00	0.12
SMF	0.5	2.0
$C_{L,des}$	0.2	0.8
A	7	16

8.3.2. Metamodel set-up

The performance parameters evaluated using metamodel 3 are largely the same as for metamodel 1 and 2. The performance parameters include: ΔC_D, C_D, ΔC_L, T_C, η_T and $\Delta\eta_T$. Here η_T and $\Delta\eta_T$ are the total efficiency and the change in total efficiency respectively. Since the thrust and propeller swirl are design parameters, a measure to evaluate the total system efficiency is needed. For the wing this measure is the lift-to-drag ratio L/D and for the propeller this is the propeller efficiency η. By multiplying the two, total system efficiency η_T is obtained. Furthermore, the swirl multiplication factor is included as a multiplier on propeller power. It is assumed that the amount of swirl is proportional to the propeller power. This is based on the blade element momentum theory, where both power and swirl are proportional to the tangential induction factor a' [51]. This gives the definition of η_T, given in Equation 8.1. To calculate the change in total efficiency $\Delta\eta_T$, an initial value for η_T must be calculated. To do this Equation 8.1 is used with the values for the isolated propeller and isolated wing. Note that changes in thrust and changes in power are proportional to each other, so $\Delta\eta$ mainly captures the change in lift-to-drag ratio with the propeller efficiency as multiplication factor.

$$\eta_T = \eta L/D = \frac{T_C}{P_C SMF}\frac{C_L}{C_D} \tag{8.1}$$

Next, the degree of the response surfaces N_{deg} and the number of sampling points N_{pts} must be determined. In Figure 8.52 the influence of the number of degrees of the polynomials on the R^2 is investigated. It can be seen that for most parameters, $N_{deg} = 2$ gives the highest value of R^2. For $\Delta\eta_T$, R^2 will even decrease if N_{deg} is further increased. Only for ΔC_L and η_T, further increasing N_{deg} is beneficial, thus $N_{deg} = 3$ and $N_{deg} = 4$ were chosen for these parameters respectively. In Figure 8.53 the convergence of R^2 for the number of sampling points N_{pts} can be seen. R^2 values are divided by their respective R^2 value for the maximum number of sampling points. It can be seen that for all parameters, except η_T, about 150 sampling points would already suffice, since the increase in R^2 beyond that is relatively small. The convergence behaviour of η_T is slower, about 400 points are needed before an increase in the number of points yields little benefit. Since 700 points were sampled, this is the number of points that has been used to construct the response surface, which is shown to be more than sufficient.

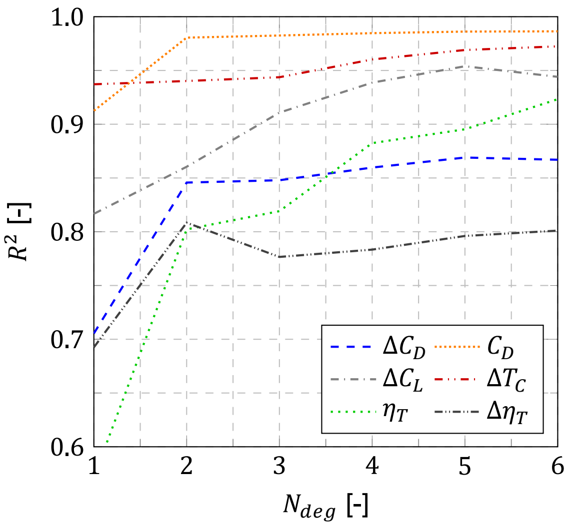

Figure 8.52: R^2 for different number of degrees of the polynomial response surface for metamodel 3

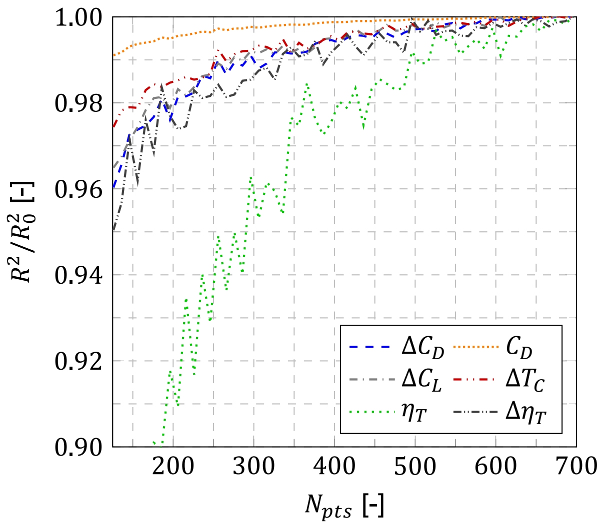

Figure 8.53: R^2 for different number of sampling points for metamodel 3

8.3.3. Metamodel quality

In Table 8.5 a summary of the quality evaluation of metamodel 3 can be found. When looking at the R^2 value it can be seen that they are all relatively high. This suggests that there are clear trends in the data, which can be explained using a polynomial function. The R^2 for ΔC_D and $\Delta\eta_T$ are the lowest, 0.846 and 0.808 respectively. This suggests that the drag prediction contains noise. However, it is expected that this noise cancels out by fitting a polynomial function through the data and the major trends in the data are captured. Furthermore, the maximum residual for 90% of the points is typically an order of magnitude lower than the range of the parameter. This also suggests that major trends in the data should be captured by the response surface.

Next, the residuals are examined. For most of the response surfaces the residuals show expected behaviour. An example is shown in Figure 8.54. Here two sets of data are used to validate the response surface. One is obtained using random sampling throughout the design space, while the second set

Table 8.5: Summary of the response surface results for metamodel 3

	min	max	range	N_{deg}	R^2	residual (90% of points)
ΔC_D	-0.0110	0.00209	0.01312	2	0.846	0.00089
C_D	0.0037	0.0426	0.0389	2	0.981	0.00116
ΔC_L	-0.0105	0.0718	0.082	3	0.911	0.0066
ΔT_C	-0.00103	0.00132	0.00235	2	0.940	0.00015
η_T	-2.35	60.87	63.22	4	0.882	4.06
$\Delta\eta_T$	-2.37	22.07	24.44	2	0.808	1.59

samples in areas with a low density of sampling points. It can be seen that the behaviour of all data sets is very similar. Only the validation data set for low density areas shows a consistent higher residual. Furthermore, in Figure 8.55 it is shown that there is a slight bias in the residuals, meaning that there is still some behaviour that could not be explained by the response surface. However, the bias seems not too concerning, as the slope of the trend line is relatively low.

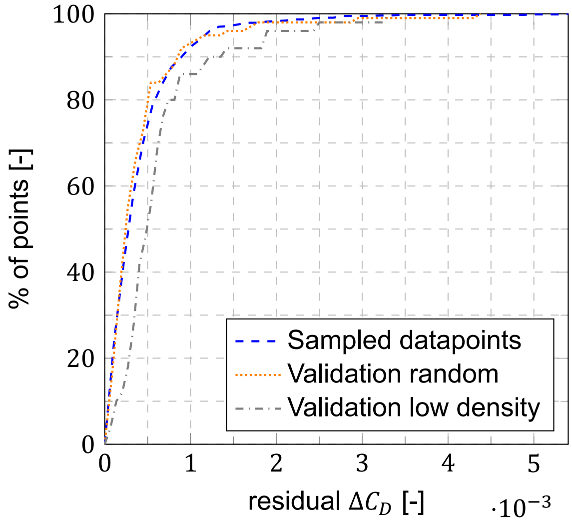

Figure 8.54: Comparison of residual of ΔC_D for metamodel 3

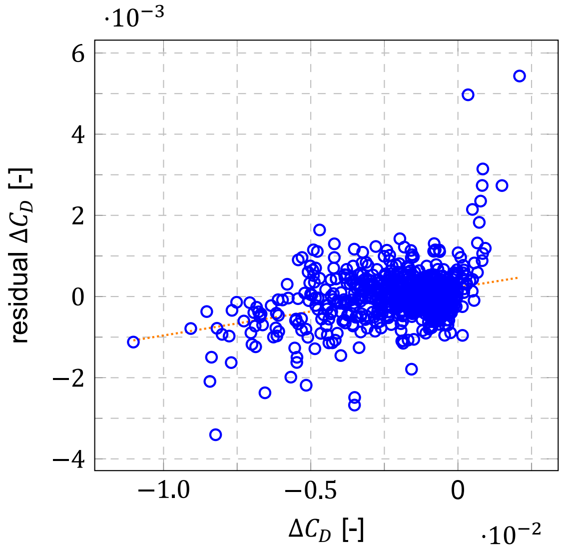

Figure 8.55: Bias of the residuals of ΔC_D for metamodel 3

Only for the change in thrust ΔT_C some unexpected behaviour is found when looking at the residuals. In Figure 8.56 it can be seen that the response surface is in good agreement with the behaviour found by randomly sampled points. However, the residual in low density areas is substantially higher. For the sampling used here, low density areas are mostly found near the edges of the design space. This is further investigated using Figure 8.57. Here two peculiarities are seen. There is a cluster of points in the lower left corner. Furthermore, the main cluster of points shows a high positive residual around $\Delta T_C = 0$. By closer investigation it was found that both phenomena are caused by points sampled for a low $T_{C,des}$. The cluster in the lower left corner represents points close to the design space boundary. The peak in residual is due to points with $T_{C,des} < 0.02$. At low $T_{C,des}$, the model has trouble finding operating settings for maximum efficiency. Thus, many points with low $T_{C,des}$ show a low efficiency, around 20% instead of 80% for higher thrust settings. This leads to different propeller-wing interaction and thus this behaviour is not well captured by the response surface. This behaviour at low $T_{C,des}$ values must be taken into account when analyzing the data.

8.3.4. Results

This section presents the results obtained with metamodel 3.

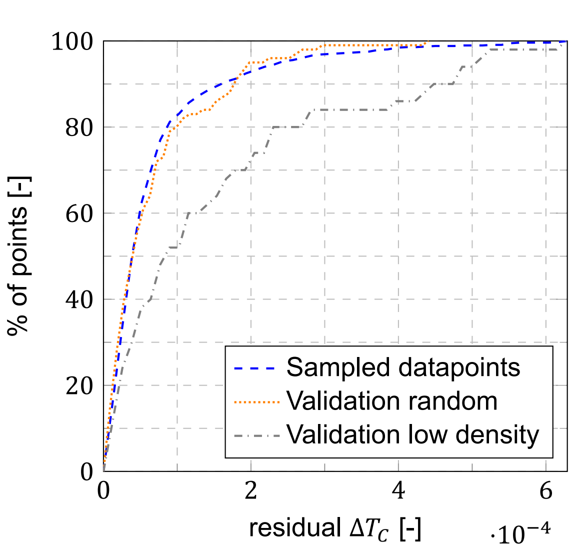

Figure 8.56: Comparison of residual for ΔT_C for metamodel 3

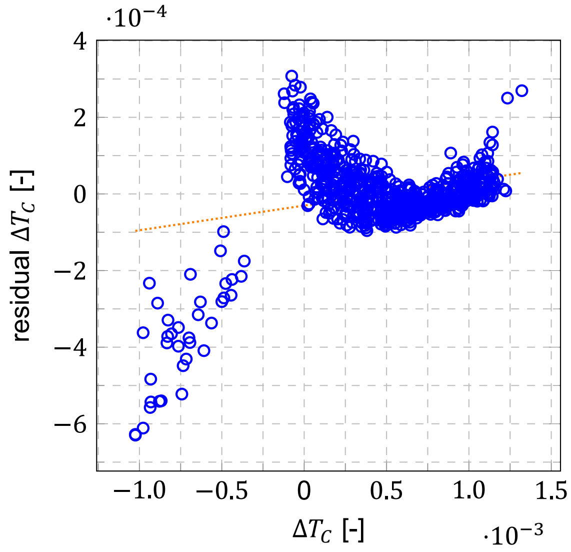

Figure 8.57: Bias of the residuals of ΔT_C for metamodel 3

Change in drag

In Figure 8.58 it is shown how ΔC_D is dependent on $T_{C,des}$ and SMF. It can be seen that depending on the amount of swirl, ΔC_D and $T_{C,des}$ are negatively correlated. The slope of this correlation depends on SMF, where the slope becomes more negative with increasing SMF. This relationship seems straightforward. ΔC_D is highly dependent on the vertical induced velocities by the propeller slipstream. The vertical induced velocity is mainly dependent on the tangential velocity, which increases with increasing $T_{C,des}$ and increasing SMF. It can be seen that there is still some spread in the data. This is mainly caused by the design lift coefficient ΔC_L, as shown in Figure 8.59. For constant thrust, ΔC_D decreases (becomes more negative) with increasing $C_{L,des}$.

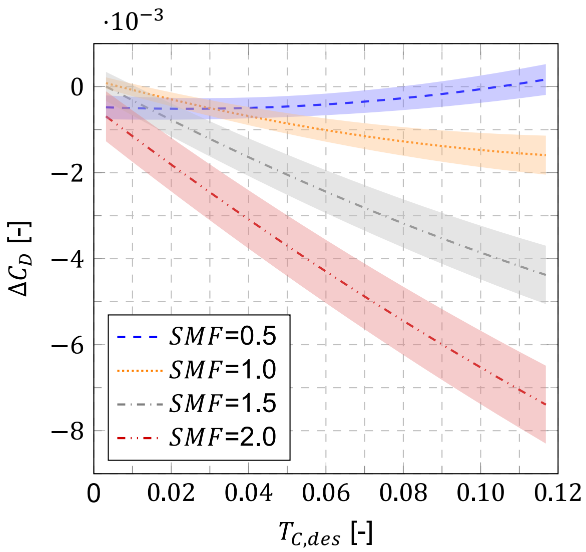

Figure 8.58: The effect of $T_{C,des}$ and SMF on ΔC_D

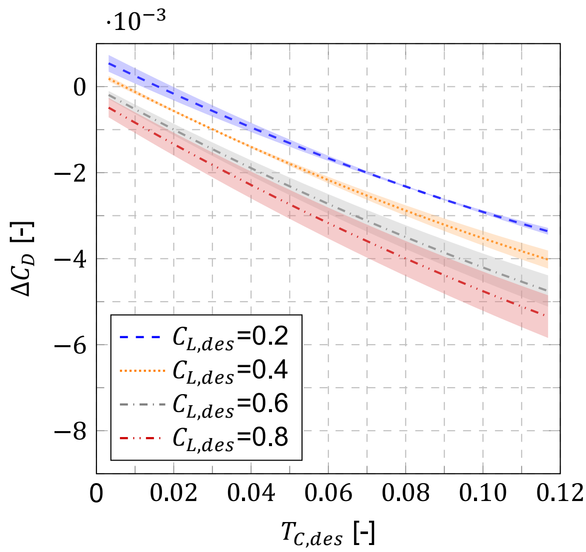

Figure 8.59: The effect of $T_{C,des}$ and $C_{L,des}$ on ΔC_D for SMF = 1.5

Drag

In Figures 8.60 and 8.61 it can be seen that the drag coefficient C_D and change in drag coefficient ΔC_D are positively correlated. It can be seen that C_D starts at an initial drag value at $\Delta C_D = 0$ and decreases with ΔC_D. The initial drag value depends on the wing design, which is in this case represented by the design lift coefficient $C_{L,des}$ and aspect ratio A. The influence of $C_{L,des}$ is the strongest, giving increasing C_D with increasing $C_{L,des}$. This is expected, as tip vortices are stronger for increasing C_L. Finally, with increasing A, C_D will decrease. This is again dependent on the strength of the wingtip vortices. Then, by increasing $T_{C,des}$ and SMF a more negative ΔC_D can be obtained, as shown in Figures 8.58 and 8.59. However, the effects of this are still relatively low with respect to the effects of wing design.

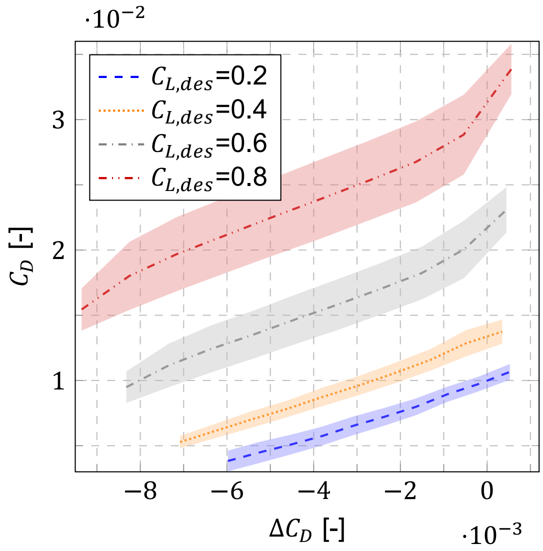

Figure 8.60: Correlation between C_D and ΔC_D for constant $C_{L,des}$

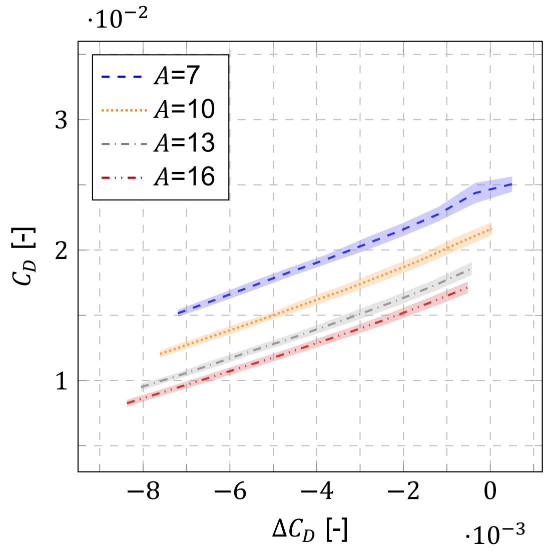

Figure 8.61: Correlation between C_D and ΔC_D for constant A at $C_{L,des} = 0.6$

Change in lift

In Figures 8.62 and 8.63 the influence of the design parameters on ΔC_L is investigated. It can be seen that with increasing swirl multiplication factor SMF and increasing thrust coefficient $T_{C,des}$, the change in lift increases. With increasing thrust, both induced axial and tangential velocity are increased on the wing, while with increasing SMF, only induced tangential velocity is increased. Both design parameters still result in a significant increase in lift. However, it can be seen that after some point, the rate of change decreases. When increasing SMF from 1.5 to 2.0, the gain in ΔC_L is very small. The same holds for a thrust increase for $T_{C,des}$ above 0.06. For both high $T_{C,des}$ and high SMF, the increased tangential velocities will lead to a very high angle of attack on the part of the wing inside the propeller slipstream. This part of the wing enters the stall region and no further increase in lift is predicted with increasing angle of attack. Thus, increasing SMF and $T_{C,des}$ is beneficial for the gain in lift, until the wing enters the non-linear regime. This behaviour has not been seen for ΔC_D since the change in drag is driven by potential flow phenomena in the numerical model. It is expected that in reality, the pressure drag would increase when wing sections reach high angles of attack, but this is not captured by the numerical model.

Change in thrust

In Figure 8.64 is can be seen that the change in thrust and design thrust coefficient are almost linearly proportional to each other. It can be seen that the line does not go exactly through the origin. However, in Figure 8.57 it was shown that the residual was large and showed strange behaviour for low values of $T_{C,des}$. It is believed that this behaviour led to some modelling error in the response surface and that ΔT_C should be linearly proportional to $T_{C,des}$. This would mean that the change in thrust scales with dynamic pressure on the propeller blades. The propeller sees mainly upwash from the wing, which causes a difference in thrust on the advancing and retreating side of the propeller disk. The net effect of this is an increase in thrust or positive ΔT_C. To increase $T_{C,des}$, rotational speed is increased, leading to increased dynamic pressure on the blades. The difference in thrust due to upwash scales with this dynamic pressure, giving a ΔT_C proportional to $T_{C,des}$. However, an increase in thrust does not lead to better propeller efficiency, since it was found that thrust and power scale proportional to each other. Furthermore, in Figure 8.64 it can be seen that, for the chosen range of $C_{L,des}$, the ΔT_C is relatively independent of $C_{L,des}$. On a last note, it can also be seen that for a tractor configuration, the impact of the wing on the propeller is relatively low, ΔT_C is typically in the order of 1% of $T_{C,des}$.

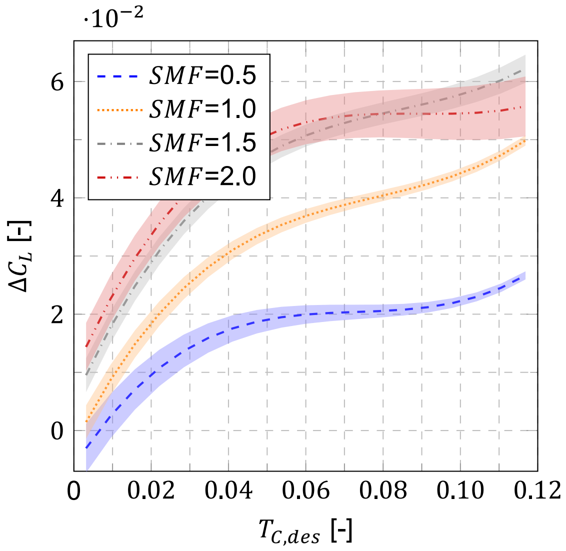

Figure 8.62: The effect of $T_{C,des}$ and SMF on ΔC_L for $C_{L,des} = 0.4$

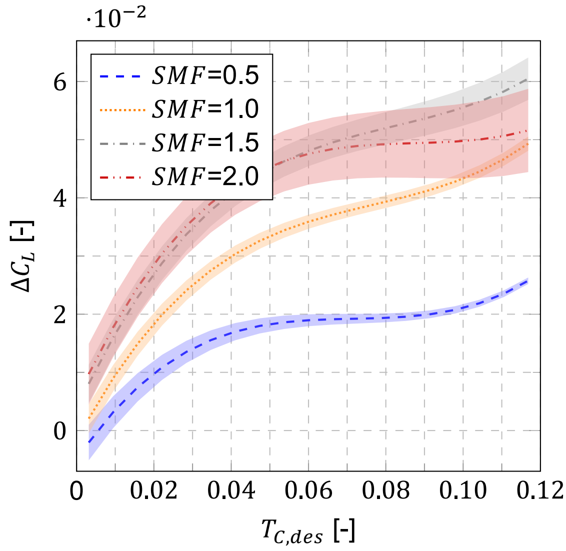

Figure 8.63: The effect of $T_{C,des}$ and SMF on ΔC_L for $C_{L,des} = 0.6$

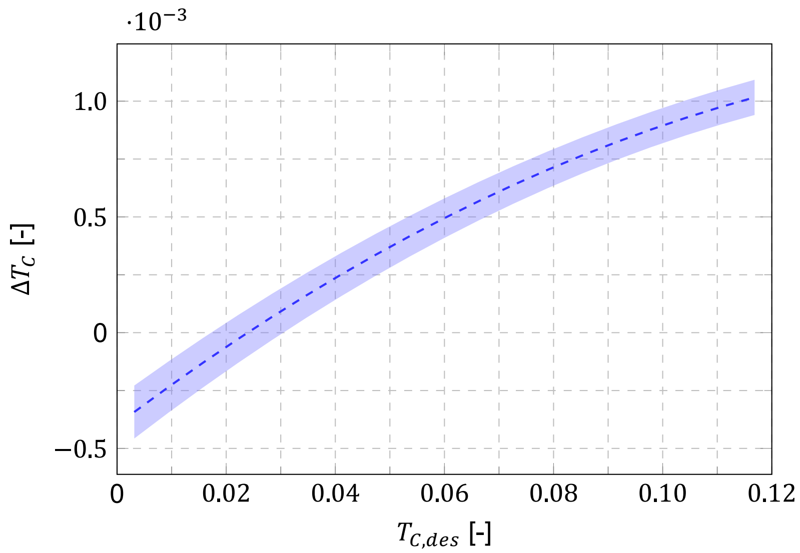

Figure 8.64: The effect of $T_{C,des}$ on ΔT_C

System efficiency

The definition of the system efficiency η_T has been given in Equation 8.1. η_T is dependent on the thrust, swirl multiplication factor, lift and drag, represented by T_C, SMF, C_L and C_D respectively. The results of the analysis of system efficiency are shown in Figure 8.65. This figure is independent of C_L, because it was found that there is no clear influence of C_L on the behaviour of the system efficiency. Furthermore, increasing aspect ratio will increase η_T, but this effect is relatively small compared to the effects of the propeller thrust and swirl. When looking at the effect of thrust on system efficiency, it can be seen that system efficiency increases with increasing $T_{C,des}$ up to around $T_{C,des} = 0.03$ for this specific propeller-wing combination. The lift-to-drag ratio keeps increasing with increasing thrust, as shown in Figure 8.67. The propeller efficiency increases up to $T_{C,des} = 0.03$ and decreases after that, as shown in Figure 8.68. This results in a plateau in η_T with respect to $T_{C,des}$ after $T_{C,des} = 0.03$. Only for $SMF = 2.0$ it can be seen that the increase in L/D is larger than the decrease in propeller efficiency. However, this still results in a lower η_T, compared to lower SMF values. With increasing SMF, it can be seen that system efficiency decreases. Thus, it is concluded that a propeller operating at maximum efficiency gives the best system performance.

In Figure 8.66 the results for the change in system efficiency $\Delta\eta_T$ are shown for $C_{L,des} = 0.6$. Since thrust and power scale proportionally, the change in system efficiency $\Delta\eta_T$ is determined by the change in lift-to-drag ratio scaled with the propeller efficiency. It can be seen that the gain due to propeller-wing interaction in system efficiency increases with increasing $T_{C,des}$. Furthermore, increasing swirl also leads to more benefit from interaction. It can be seen that the slope of the $\Delta\eta_T$-$T_{C,des}$ relation at constant SMF increases with SMF. Increasing SMF decreases propeller efficiency, thus the increase in lift-to-drag ratio for increasing $T_{C,des}$ is higher for higher SMF. In other words, for the same increase in $T_{C,des}$, a bigger increase in lift-to-drag ratio is achieved for a higher SMF. However, increasing SMF leads to a worse system performance, as shown in Figure 8.65.

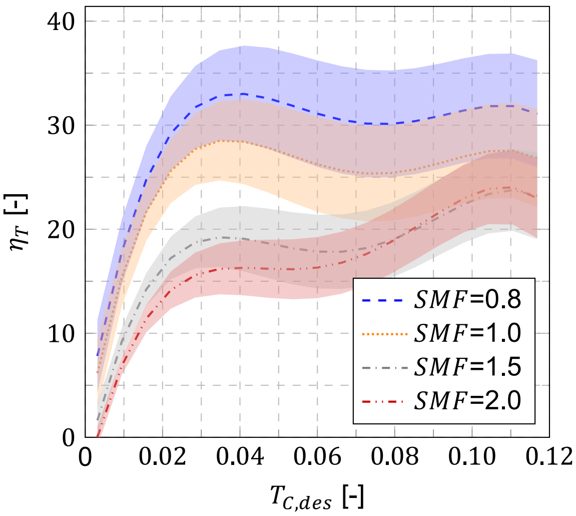

Figure 8.65: The effect of $T_{C,des}$ and SMF on η_T

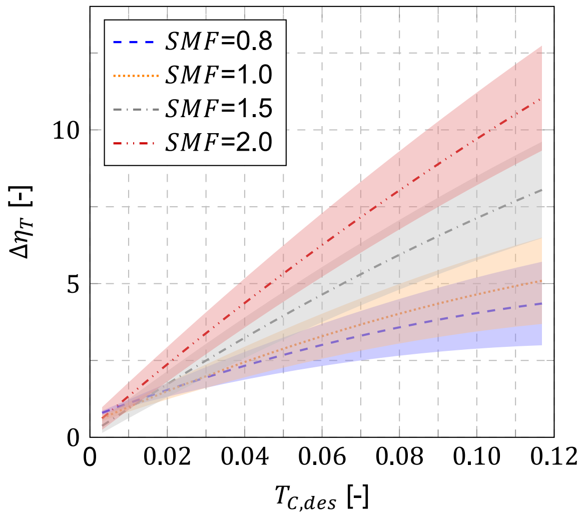

Figure 8.66: The effect of $T_{C,des}$ and SMF on $\Delta\eta_T$ for $C_{L,des} = 0.6$

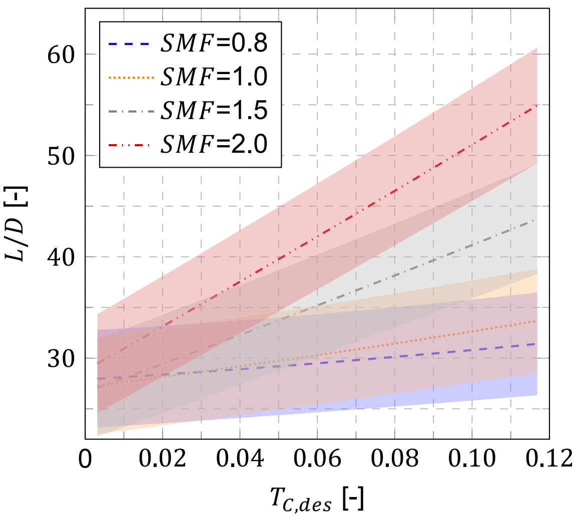

Figure 8.67: The effect of $T_{C,des}$ and SMF on L/D

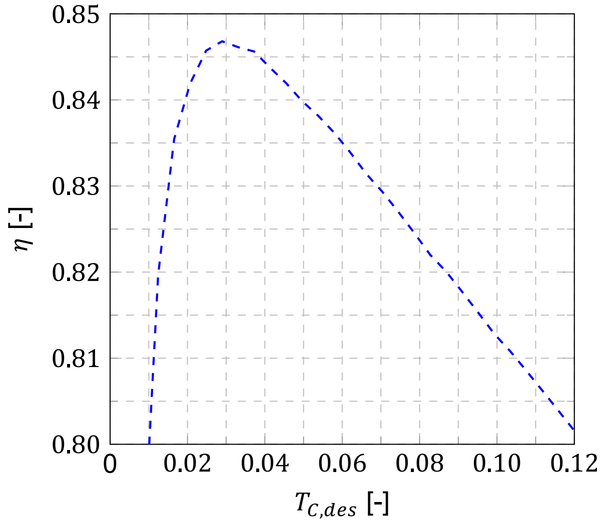

Figure 8.68: The maximum propeller efficiency for different $T_{C,des}$

Lift-drag interaction

In Figures 8.69 and 8.70 the effects of $C_{T,des}$ and SMF on the relation between ΔC_L and ΔC_D can be seen. It can be seen that increasing thrust moves the design space to higher ΔC_L and lower ΔC_D. This is consistent with the findings from metamodel 1 and metamodel 2. Changing the swirl in the propeller slipstream has the same effect. While increasing $T_{C,des}$ mainly influences ΔC_L, increasing the swirl mainly influences ΔC_L as well as ΔC_D significantly. This shows that drag is more sensitive to tangential velocities than to axial velocities.

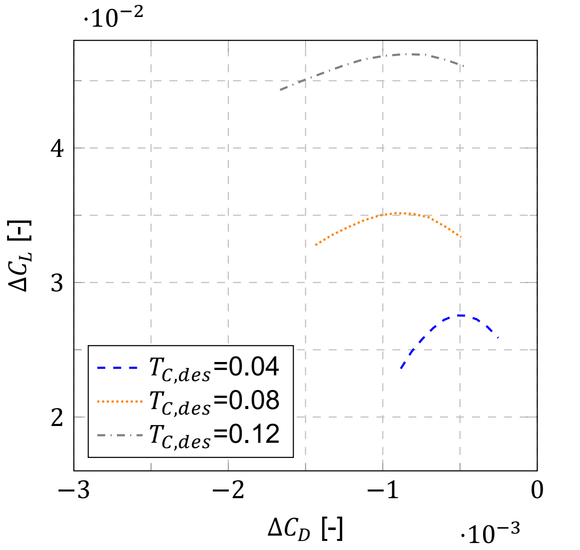

Figure 8.69: Correlation between ΔC_L and ΔC_D for constant $T_{C,des}$ at SMF = 0.8 and $C_{L,des}$ = 0.6

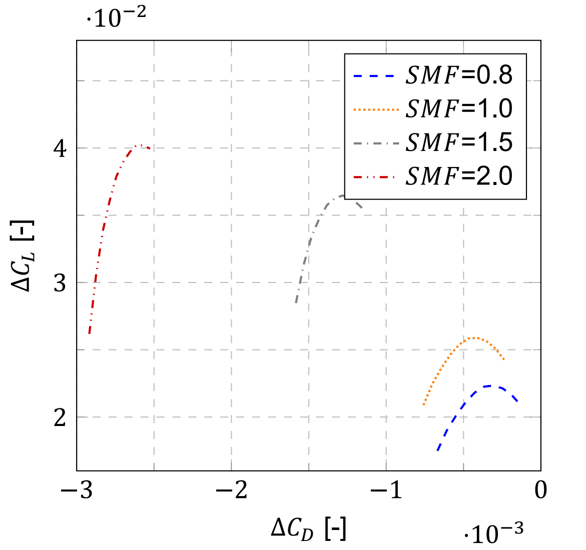

Figure 8.70: Correlation between ΔC_L and ΔC_D for constant SMF at $T_{C,des}$ = 0.04 and $C_{L,des}$ = 0.6

9

Conclusions and recommendations

This chapter presents the conclusions based on the conducted research in Section 9.1. This is followed by recommendations for future research in Section 9.2.

9.1. Conclusions

The research aim and objectives were defined in Section 1.2 of Chapter 1. The aim of the research was to quantify the sensitivity of the aerodynamic efficiency of the whole propeller-wing system for the main design parameters for a wingtip-mounted tractor propeller-wing system by means of a low-order numerical model. This has been achieved by researching sub-objectives. The results of relating to these sub-objectives will be discussed in the next paragraphs.

Firstly, a numerical model is created to analyze propeller-wing interaction. This model consists of two parts: a wing model and a propeller model. Both models are based on potential flow methods, enhanced with viscous polars from 2D airfoil analysis. Since the propeller and wing model are dependent on each other, a solution for the propeller-wing system is obtained iteratively. The numerical propeller-wing model was validated using experimental data. The main trends in the data could be predicted by the numerical model, however some discrepancies were found. The propeller performance showed an offset. This could be corrected for by a adjustment in pitch of $1.2°$. By investigating the isolated propeller, it was found that this offset was caused by low Reynolds numbers on the propeller blades. At lower Reynolds numbers, viscous effects are more prominent and thus airfoil performance is harder to predict using numerical models. Furthermore, the drag of the propeller-wing system was underestimated. This is believed to be the result of the nacelle. The nacelle is modelled in the numerical model as a wing extension with the same airfoil as the rest of the wing. Since the nacelle will produce more profile drag than the wing airfoil, the drag is under predicted. Lastly, for the propeller-wing system the increase in lift curve slope with decreasing advance ratio was under predicted by the numerical model. Possible causes for this are the modelling of the propeller slipstream and not taking into account interaction effects with the nacelle in the numerical model.

To investigate the influence of wing spanwise lift distribution on the propeller-wing interaction, the influence of aspect ratio and outboard wing twist have been investigated. By changing aspect ratio and outboard wing twist, the strength of the wingtip vortex changes. It was found that this has little influence on the propeller-wing interaction mechanisms, as the changes in system lift and drag were largely independent of aspect ratio and outboard wing twist. The wing lift distribution does have a large influence on the final drag value of the system. Since changes in drag due to propeller-wing interaction are relatively small compared to the total drag, in the order of 10% of total drag, the total drag is mainly determined by the clean wing drag, which is dependent on the wing spanwise lift distribution. Thus, a high aspect ratio and low outboard twist are desired. Furthermore, it was found that the change in lift to drag ratio is mainly determined by the drag values. With a lower total drag, the same change in drag, gives a larger change in lift-to-drag ratio. Since the same change in drag is achievable for all investigated spanwise lift distributions, a wing with low drag would benefit most from propeller-wing interaction in terms of lift-to-drag ratio.

The influence of the linear and angular momentum distribution of the propeller has been investigated by changing the thrust and the propeller swirl. The change of thrust was achieved by changing blade pitch and advance ratio to obtain maximum efficiency at the desired thrust coefficient. The propeller swirl was changed by calculating the swirl for the propeller at maximum efficiency and multiplying it with a factor. It was found that with increasing thrust and increasing swirl, more beneficial propeller-wing interaction could be obtained. This means a higher increase in lift and a higher (in magnitude) decrease in drag. This would benefit the lift-to-drag ratio. However, if thrust and swirl are increased beyond a certain point, it was observed that the change in lift became constant. This has been attributed to non-linear effects. At these high thrust and swirl values, the angle of attack for the part of the wing inside the propeller slipstream becomes very large and makes the wing stall. While this behaviour was not observed for drag, it is expected that in reality pressure drag will increase at high angles of attack, diminishing the benefit of propeller-wing interaction. Finally, a system efficiency parameter was defined as the propeller efficiency times the lift-to-drag ratio. It was found that the highest value of this system efficiency is simply obtained for a maximum propeller efficiency. In other words, the increase in lift-to-drag ratio obtained by decreasing propeller efficiency is relatively low. To conclude, the propeller should be designed for maximum efficiency, as added swirl in the propeller slipstream decreases propeller efficiency and the corresponding increase in wing efficiency is lower in comparison to the decrease in propeller efficiency.

Next, the main design parameters for a wingtip-mounted propeller system were investigated. These were: D/b, x/c and z/D. For D/b it was found that it mainly affects the propeller-wing interaction with respect to drag. A larger D/b is beneficial for the drag, since a larger D/b results in a larger wing area with upwash, leading to a decrease in induced drag. This relation no longer holds for small propellers with high thrust. For these propellers another mechanism dominates. With increasing diameter, the propeller induced velocities decrease, which usually leads to a small penalty in performance. However, for small propellers this decrease is more rapidly, since propeller induced velocities scale quadratically with diameter. Thus, the effect of decreased propeller induced velocity on the wing is dominating and it leads to less performance benefits. For x/c it was found that it influences both the change in lift and the change in drag. An increase in x/c will be disadvantageous for lift, but beneficial for drag. With increasing x/c, induced velocities are increased, but the induced angle of attack is reduced, thus less lift is created. This leads to a weaker wingtip vortex, decreasing the drag. Next, z/D influences mostly the lift. The results suggest that a propeller position where the wing sees maximum radial velocities is the most beneficial. Thus, high propeller positions are desired and for this high position, the area of the wing inside the propeller slipstream needs to be maximized. Lastly, if the circulation of the wing inside the propeller slipstream is relatively strong, then a low propeller position is beneficial for the thrust. Below the wing the propeller will see a higher angle of attack due to wing circulation. However, it was found that this does not lead to a better propeller efficiency, as this thrust increase is paired with a proportional increase in power.

Finally, the interaction between performance parameters has been investigated. It was found that for a given lift coefficient, clean wing drag should be minimized to get the best system performance. This is due to the fact that benefits in drag due to propeller-wing interaction are almost an order of magnitude smaller than the total drag. To get the highest increase in lift due to interaction, z/D and x/c need to be considered. To get the highest decrease in drag due to interaction, D/b and x/c should be used. x/c is the one variable that leads to a trade-off between lift and drag. Furthermore, thrust can be increased to increase lift and decrease drag. However, this only leads to a better system performance if the change in thrust leads to a higher propeller efficiency, or if the decrease in efficiency leads to a higher relative increase in lift-to-drag ratio. However, for the used geometry, it was found that if propeller efficiency decreases when thrust is increased, the magnitude of the lift-to-drag ratio increase was not sufficient to lead to an increase in system efficiency. Lastly, for a tractor propeller system, the achievable change in thrust due to interaction is relatively small, about 1% of the total thrust. Again, this change in thrust is not paired with a change in propeller efficiency.

To conclude, for a tractor propeller-wing system, propeller-wing interaction has mainly effect on the wing performance. The relative change in drag due to propeller-wing interaction found in this research was typically around 10%. The relative change in thrust would be around 1% and this would not lead to a change in propeller efficiency. Furthermore, it was found that for the best propeller-wing system performance, propeller and wing should both be optimized separately. The wing lift distribution has little effect on the performance increase due to propeller-wing interaction. Furthermore, decreasing propeller efficiency would lead to an increase in wing efficiency through interaction, but this increase is typically low compared to the decrease in propeller efficiency and leads to an overall lower system efficiency. Thus, to obtain the best performance, the wing should maximize lift-to-drag ratio and the propeller should maximize its efficiency. Finally, by fine tuning the relative position and size of the wing and propeller, performance can be somewhat enhanced by maximizing interaction.

9.2. Recommendations

This research has investigated the aerodynamic performance of a tractor propeller-wing system. However, there are still aspects of wingtip-mounted propeller-wing interaction that are left to be investigated. This section deals with recommendations for future work regarding this topic.

- The numerical model could be further improved. During the validation, effects of the nacelle were found that were not captured by the numerical model and during the numerical experiments, no nacelle was modelled. By adjusting the wing model, it might be possible to include some effects of the nacelle. Possibly a potential flow solver is needed to model the nacelle. This would make the results more representative, since in a practical wingtip-mounted propeller design, a nacelle must be present.
- The radial distribution of propeller circulation has not been investigated. Fine tuning the propeller radial distributions for propeller-interaction might lead to enhanced system performance and is thus worth investigating. However, a metamodel that would thoroughly investigate the effects of the radial circulation distribution has not been made, as it would require too many design parameters. This would have increased the number of dimensions of the problem, leading to high computational times. Creating such a metamodel could not be achieved within the time constraints of this project.
- The change in drag due to propeller-wing interaction was found not to be dependent on the vertical propeller position. However, it is also suspected that this could possibly be due to noise in the data, since the drag is rather sensitive to small changes in propeller deflection, averaging out any effects due to vertical propeller position. Thus, it is recommended to further investigate the effects of z/D, possibly by removing slipstream deflection. This would simplify the interaction and make the effects of z/D more direct, which could lead to better insights of the influence of z/D on drag.

Bibliography

[1] J. D. Anderson Jr. *Introduction to flight*. McGraw-Hill, 7 edition, 2012. ISBN 978-007-108605-9.

[2] W. F. Durand. Experimental research on air propellers. Technical Report NACA-TR-141, National Advisory for Aeronautics (NACA), 1917.

[3] C. Rohrbach and F. B. Metzger. The prop-fan - a new look in propulsors. In *11th Propulsion Conference, Joint Propulsion Conferences*, Anaheim, CA, United States, Sep 1975. doi: 10.2514/6.1975-1208.

[4] IATA. Fact sheet - climate change & CORISA, May 2018.

[5] NASA. NASA facts - green aviation: Safeguarding our future on earth, 2015.

[6] J. B. Whitlow and G. K. Siever. Fuel savings potential of the NASA advanced turboprop program. Technical Report NASA-TM-83736, NASA Lewis Research Center. Cleveland, OH, United States, Sep 1984.

[7] I. M. Goldsmith. A study to define the research and technology requirements for advanced turbo/propfan transport aircraft. Technical Report NASA-CR-166138, NASA Ames Research Center. Mountain View, CA, United States, Feb 1981.

[8] R. Vos and M. F. M. Hoogreef. System-level assessment of tail-mounted propellers for regional aircraft. In *31st Congress of the International Council of the Aeronautical Sciences*, Belo Horizonte, Brazil, Sep 2018.

[9] B. Magliozzi, D. B. Hanson, and R. Amiet. Propeller and propfan noise. *Aeroacoustics of Flight Vehicles: Theory and Practice. Volume 1: Noise Sources*, 1:1–64, Aug 1991. NASA-RP-1258-VOL-1.

[10] M. Voskuijl, J. van Bogaert, and A. G. Rao. Analysis and design of hybrid electric regional turboprop aircraft. *CEAS Aeronautical Journal*, 9:15–25, May 2018. doi: 10.1007/s13272-017-0272-1.

[11] A. M. Stoll, J. Bevirt, and M. D. Moore. Drag reduction through distributed electric propulsion. In *14th AIAA Aviation Technology, Integration, and Operations Conference, AIAA AVIATION Forum, (AIAA 2014-2851)*, Jun 2014. doi: 10.2514/6.2014-2851.

[12] L. R. Miranda and J. E. Brennan. Aerodynamic effects of wingtip-mounted propellers and turbines. In *4th Applied Aerodynamics Conference, Fluid Dynamics and Co-located Conferences*, Jun 1986. doi: 10.2514/6.1986-1802.

[13] I. Kroo. Propeller-wing integration for minimum induced loss. *Journal of Aircraft*, 23(7):561–565, Aug 1986. doi: 10.2514/3.45344.

[14] M. D. Moore and B. Fredericks. Misconceptions of electric propulsion aircraft and their emergent aviation markets. In *52nd Aerospace Sciences Meeting, AIAA SciTech Forum, (AIAA 2014-0535)*, Jan 2014. doi: 10.2514/6.2014-0535.

[15] J. L. Felder, G. V. Brown, H. DaeKim, and J. Chu. Turboelectric distributed propulsion in a hybrid wing body aircraft. In *20th International Society for Airbreathing Engines (ISABE 2011)*. NASA Glenn Research Center. Cleveland, OH, United States, Sep 2011.

[16] J. R. Chambers. *Cave of the Winds - The Remarkable History of the Langley Full-Scale Wind Tunnel*. National Aeronautics and Space Administration (NASA), 2014. ISBN 978-1-62683-016-5.

[17] J. P. Reeder and G. W. Brewer. NACA full-scale wind-tunnel test of Vought-Sikorsky V-173 airplane. Technical report, National Advisory for Aeronautics (NACA), 1942.

[18] R. H. Lange, B. W. Cocke Jr., and A. J. Proterra. Langley full-scale tunnel investigation of a 1/3-scale model of the Chance Vought XF5U-1 airplane. Technical Report NACA-RM-L6I19, National Advisory for Aeronautics (NACA). Langley Field, VA, United States, 1946.

[19] M. H. Snyder Jr. *Effect of a wingtip mounted propeller on wing lift induced drag and shed vortex pattern*. PhD thesis, Department of Aeronautical Engineering Wichita State University, 1968.

[20] M. H. Snyder Jr. and G. W. Zumwalt. Effects of wingtip-mounted propellers on wing lift and induced drag. *Journal of Aircraft*, 6(5):392–397, 1969. doi: 10.2514/3.44076.

[21] J. C. Patterson Jr. and S. G. Flechner. An exploratory wind-tunnel investigation of the wake effect of a panel tip-mounted fan-jet engine on the lift-induced vortex. Technical Report NASA-TN-D-5729, NASA Langley Research Center. Hampton, VA, United States, May 1970.

[22] J. C. Patterson Jr. and G. R. Bartlett. Evaluation of installed performance of a wing-tip-mounted pusher turboprop on a semispan wing. Technical Report NASA-TP-2739, NASA Langley Research Center. Hampton, VA, United States, 1987.

[23] J. C. Patterson Jr. and G. R. Bartlett. Effect of a wing-tip mounted pusher turboprop on the aerodynamic characteristics of a semi-span wing. In *21st Joint Propulsion Conference, Joint Propulsion Conferences*, Jul 1985. doi: 10.2514/6.1985-1286.

[24] J. L. Loth and F. Loth. Induced drag reduction with wing tip mounted propellers. In *2nd Applied Aerodynamics Conference, Fluid Dynamics and Co-located Conferences*, Aug 1984. doi: 10.2514/6.1984-2149.

[25] M. M. Munk. The minimum induced drag of aerofoils. Technical Report NACA-TR-121, NACA, 1923.

[26] N. K. Borer, M. D. Patterson, J. K. Viken, M. D. Moore, S. Clarke, M. E. Redifer, R. J. Christie, A. M. Stoll, A. Dubois, and J. Bevirt. Design and performance of the NASA SCEPTOR distributed electric propulsion flight demonstrator. In *16th AIAA Aviation Technology, Integration, and Operations Conference*, Jun 2016. doi: 10.2514/6.2016-3920.

[27] K. A. Deere, J. K. Viken, S. A. Viken, M. B. Carter, M. R. Wiese, and N. L. Farr. Computational analysis of a wing designed for the X-57 distributed electric propulsion aircraft. In *AIAA Aviation Forum 2017*, Jun 2017. doi: 10.2514/6.2017-3923.

[28] L. L. M. Veldhuis. *Propeller wing aerodynamic interference*. PhD thesis, Delft University of Technology, Jun 2005.

[29] L. L. M. Veldhuis. Review of propeller-wing aerodynamic interference. In *24th Congress of International Council of the Aeronautical Sciences (ICAS)*, Yokohama, Japan, Aug 2004.

[30] T. Sinnige, D. Ragni, A. M. N. Malgoezar, G. Eitelberg, and L. L. M. Veldhuis. APIAN-INF: an aerodynamic and aeroacoustic investigation of pylon-interaction effects for pusher propellers. *CEAS Aeronautical Journal*, 9(2):291–306, Jun 2018. doi: 10.1007/s13272-017-0247-2.

[31] T. Sinnige, K. P. Lynch, D. Ragni, G. Eitelberg, and L. L. M. Veldhuis. Aerodynamic and aeroacoustic effects of pylon trailing edge blowing on pusher propeller installation. In *21st AIAA/CEAS Aeroacoustics Conference, AIAA AVIATION Forum, (AIAA 2015-2356)*, Jun 2015. doi: 10.2514/6.2015-2356.

[32] T. Sinnige, A. M. N. Malgoezar, D. Ragni, M. Snellen, G. Eitelberg, and L. L. M. Veldhuis. APIAN-INF: A low-speed aerodynamic and aeroacoustic investigation of pylon – pusher propeller interaction effects. In *CEAS 2015: 5th CEAS Air and Space Conference ”Challenges in European Aerospace”*, Sep 2015. ISBN 978-1-906913-20-5.

[33] T. Sinnige, R. de Vries, B. Della Corte, F. Avallone, D. Ragni, G. Eitelberg, and L. L. M. Veldhuis. Unsteady pylon loading caused by propeller-slipstream impingement for tip-mounted propellers. *Journal of Aircraft*, 55(4):1605–1618, Jul 2018. doi: 10.2514/1.C034696.

[34] L. L. M. Veldhuis, T. C. A. Stokkermans, T. Sinnige, and G. Eitelberg. Analysis of swirl recovery vanes for increased propulsive efficiency in tractor propeller aircraft. In *30th Congress of International Council of the Aeronautical Sciences*. International Council of the Aeronautical Sciences, 2016. ISBN 978-393218285-3.

[35] Q. Li, K. Öztürk, T. Sinnige, D. Ragni, Y. Wang, G. Eitelberg, and L. L. M. Veldhuis. Towards optimum swirl recovery vanes for propeller propulsion systems. In *35th AIAA Applied Aerodynamics Conference, AIAA AVIATION Forum, (AIAA 2017-3571)*, Jun 2017. doi: 10.2514/6.2017-3571.

[36] T. Sinnige, J. J. van Kuijk, K. P. Lynch, D. Ragni, G. Eitelberg, and L. L. M. Veldhuis. The effects of swirl recovery vanes on single-rotation propeller aerodynamics and aeroacoustics. In *21st AIAA/CEAS Aeroacoustics Conference, AIAA AVIATION Forum, (AIAA 2015-2358)*, Jun 2015. doi: 10.2514/6.2015-2358.

[37] L. L. M. Veldhuis, M. Kotsonis, E. van Berkel, and G. Eitelberg. Non-uniform inflow effects on propeller performance. In *31st AIAA Applied Aerodynamics Conference, Fluid Dynamics and Co-located Conferences, (AIAA 2013-2801)*, Jun 2013. doi: 10.2514/6.2013-2801.

[38] T. Sinnige, D. Ragni, G. Eitelberg, and L. L. M. Veldhuis. Pusher-propeller installation effects in angular inflow. In *22nd AIAA/CEAS Aeroacoustics Conference, (AIAA 2016-2875)*, 2016. doi: 10.2514/6.2016-2875.

[39] N. van Arnhem, T. Sinnige, T. C. A. Stokkermans, G. Eitelberg, and L. L. M. Veldhuis. Aerodynamic interaction effects of tip-mounted propellers installed on the horizontal tailplane. In *2018 AIAA Aerospace Sciences Meeting, AIAA SciTech Forum, (AIAA 2018-2052)*, 2018. doi: 10.2514/6.2018-2052.

[40] T. C. A. Stokkermans, N. van Arnhem, T. Sinnige, and L. L. M. Veldhuis. Validation and comparison of RANS propeller modeling methods for tip-mounted applications. *AIAA Journal*, 57(2):566–580, Feb 2019. doi: 10.2514/1.J057398.

[41] T. Sinnige, N. van Arnhem, T. C. A. Stokkermans, G. Eitelberg, and L. L. M. Veldhuis. Wingtip-mounted propellers: Aerodynamic analysis of interaction effects and comparison with conventional layout. *Journal of Aircraft*, 56(1), Jan 2019. doi: 10.2514/1.C034978.

[42] M. Dimchev. *Experimental and numerical study on wingtip mounted propellers for low aspect ratio UAV design*. Master's thesis, Delft University of Technology, 2012.

[43] A. A. Candade. *Horizontal Tailplane-Tip Mounted Tractor Propeller Interaction Effects*. Master's thesis, Delft University of Technology, 2015.

[44] B. Nootebos. *Aerodynamic Analysis and Optimisation of Wingtip-Mounted Pusher Propellers*. Master's thesis, Delft University of Technology, 2018.

[45] J. Katz and A. Plotkin. *Low-speed Aerodynamics, From Wing Theory to Panel Methods*. McGraw-Hill Inc., 1991. ISBN 0-07-050446-6.

[46] J. D. Anderson Jr. *Fundamentals of Aerodynamics*. McGraw-Hill, 5 edition, 2011. ISBN 978-1-259-01028-6.

[47] L. Ting and C. H. Liu. Thin airfoil in nonuniform parallel streams. *Journal of Aircraft*, 6(2):173–175, 1969. doi: 10.2514/3.44030.

[48] R. Nederlof. *Improved modeling of propeller-wing interactions with a lifting-line approach*. Master's thesis, Delft University of Technology, 2020.

[49] S. C. Rethorst. Aerodynamic of nonuniform flows as related to an airfoil extending through a circular jet. *Journal of the Aeronautical Sciences*, 25(1):11–28, Jan 1958. doi: 10.2514/8.7479.

[50] S. C. Rethorst. *Characteristics of an airfoil extending through a circular jet*. PhD thesis, California Institute of Technology, 1956.

[51] T. Burton, N. Jenkins, D. Sharpe, and E. Bossanyi. *Wind Energy Handbook*. John Wiley & Sons, Ltd, second edition, 2011. ISBN 978-0-470-69975-1.

[52] H. Glauert. *Airplane Propellers. In: Aerodynamic Theory Volume IV*. Springer, 1935. ISBN 978-3-642-89630-9.

[53] S. Goldstein. On the vortex theory of screw propellers. *Proceedings of the Royal Society of London. Series A, Containing Papers of a Mathematical and Physical Character*, 123(792):440–465, Apr 1929. doi: 10.1098/rspa.1929.0078.

[54] A. Betz. Schraubenpropeller mit geringstem Energieverlust. Mit einem Zusatz von L. Prandtl. *Nachrichten von der Gesellschaft der Wissenschaften zu Göttingen, Mathematisch-Physikalische Klasse*, 1919:193–217, 1919.

[55] W. Z. Shen, R. Mikkelsen, and J. N. Sørensen. Tip loss corrections for wind turbine computations. *Wind Energy*, 8(4):457–475, Mar 2005. doi: 10.1002/we.153.

[56] Q. R. Wald. The aerodynamics of propellers. *Progress in Aerospace Sciences*, 42(2):85–128, Feb 2006. doi: 10.1016/j.paerosci.2006.04.001.

[57] J. T. Conway. Analytical solutions for the actuator disk with variable radial distribution of load. *Journal of Fluid Mechanics*, 297:327–355, Aug 1995. doi: 10.1017/S0022112095003120.

[58] H. S. Ribner. Formulas for propellers in yaw and charts on the side-force derivative. Technical Report NACA-TR-819, NACA. Langley Memorial Aeronautical Laboratory. Langley Field, VA, United States, 1943.

[59] H. S. Ribner. Propellers in yaw. Technical Report NACA-TR-820, NACA. Langley Aeronautical Lab. Langley Field, VA, United States, 1945.

[60] B. Ortun, R. Boisard, and I. Gonzalez-Martino. Assessment of propeller 1P loads predictions. *International Journal of Engineering Systems Modelling and Simulation*, 4(1/2):36–46, Jan 2012. doi: 10.1504/IJESMS.2012.044842.

[61] J. De Young. Propeller at high incidence. *Journal of Aircraft*, 2(3):241–250, May 1965. doi: 10.2514/3.43646.

[62] K. Tehrani. *Propellers in yawed flow at low speeds*. Master's thesis, University of California, 2006.

[63] R. P. Coleman, A. M. Feingold, and C. W. Stempin. Evaluation of the induced-velocity field of an idealized helicopter rotor. Technical Report NACA-ARR-L5E10, NACA. Langley Memorial Aeronautical Laboratory. Langley Field, VA, United States, 1945.

[64] D. L. Whitfield, T. W. Swafford, J. M. Janus, R. A. Mulac, and D. M. Belk. Three-dimensional unsteady euler solutions for propfans and counter-rotating propfans in transonic flow. In *19th AIAA, Fluid Dynamics, Plasma Dynamics, and Lasers Conference*, Honolulu, HI, United States, Jun 1987. doi: 10.2514/6.1987-1197.

[65] N. van Arnhem, R. de Vries, T. Sinnige, R. Vos, G. Eitelberg, and L. L. M. Veldhuis. (in press) Engineering method to estimate the blade loading of propellers in nonuniform flow. *AIAA Journal*, Oct 2020. doi=10.2514/1.J059485.

[66] H. S. Ribner. Notes on the propeller and slipstream in relation to stability. Technical Report NACA-ARR-L4I12A, NACA. Langley Aeronautical Lab. Langley Field, VA, United States, 1944.

[67] L. Heidelberg and R. Woodward. Advanced turboprop wing installation effects measured by unsteady blade pressure and noise. In *11th Aeroacoustics Conference*, Sunnyvale, CA, United States, Oct 1987. doi: 10.2514/6.1987-2719.

[68] F. M. Catalano. On the effects of an installed propeller slipstream on wing aerodynamic characteristics. *Acta Polytechnica, Journal of Advanced Engineering*, 44(3):8–14, 2004. ISSN 1210-2709.

[69] S. J. Miley, R. M. Howard, and B. J. Holmes. Wing laminar boundary layer in the presence of a propeller slipstream. *Journal of Aircraft*, 25(7):606–611, Jul 1988. doi: 10.2514/3.45630.

[70] T. C. A. Stokkermans. *Design and Analysis of Swirl Recovery Vanes for an Isolated and a Wing Mounted Tractor Propeller*. Master's thesis, Delft University of Technology, 2015.

[71] H. K. Epema. *Wing Optimisation for Tractor Propeller Configurations*. Master's thesis, Delft University of Technology, 2017.

[72] C. Alba. *A Surrogate-Based Multi-Disciplinary Design Optimization Framework Exploiting Wing-Propeller Interaction*. Master's thesis, Delft University of Technology, 2017.

[73] J. T. Goates. *DEVELOPMENT OF AN IMPROVED LOW-ORDER MODEL FOR PROPELLER-WING INTERACTIONS*. Master's thesis, Utah State University, 2018.

[74] P. Della Vecchia, M. Daniele, F. Nicolosi, and A. De Marco. Numerical analysis of propeller effects on wing aerodynamic: tip mounted and distributed propulsion. *Transportation Research Procedia*, 29:106–115, Oct 2018. doi: 10.1016/j.trpro.2018.02.010.

[75] L. L. M. Veldhuis. Optimization of tractor propeller-wing configurations. *Proceedings of the Institution of Mechanical Engineers Part G Journal of Aerospace Engineering*, 209(37):215–226, Jul 1995. doi: 10.1243/PIME_PROC_1995_209_292_02.

[76] M. Drela. QPROP formulation. MIT Aero & Astro, Jun 2006.

[77] S. van der Meer. *Numerical Assessment of Directional Stability and Control with Tip-mounted Propellers*. Master's thesis, Delft University of Technology, 2020.

[78] N. van Arnhem. *Design and Analysis of an Installed Pusher Propeller with Boundary Layer Inflow*. Master's thesis, Delft University of Technology, 2015.

[79] B. Chandrasekaran. Method for the prediction of the installation aerodynamics of a propfan at subsonic speeds. Technical Report NASA-CR-3887, NASA Langley Research Center. Hampton, VA, United States, Apr 1985.

[80] J. L. van Ingen. The eN method for transition prediction: Historical review of work at TU Delft. In *38th Fluid Dynamics Conference and Exhibit*, Seattle, WA, United States, Jun 2018. doi: 10.2514/6.2008-3830.

[81] H. Snel. Review of the present status of rotor aerodynamics. *Wind Energy*, 1:46–69, Apr 1998. doi: 10.1002/(SICI)1099-1824(199804)1:1+<46::AID-WE3>3.0.CO;2-9.

[82] D. Yorita, K. Asai, C. Klein, C. Henne, and S. Schaber. Transition detection on rotating propeller blades by means of temperature sensitive paint. In *50th AIAA Aerospace Sciences Meeting including the New Horizons Forum and Aerospace Exposition*, Nashville, TN, United States, Jan 2012. doi: 10.2514/6.2012-1187.

[83] A. Weiss, A. D. Gardner, T. Schwermer, C. Klein, and M. Raffel. On the effect of rotational forces on rotor blade boundary-layer transition. *AIAA JOURNAL*, 57(1):252–266, Dec 2019. doi: 10.2514/1.J057036.

[84] L. Koomen. *Wing Optimization for Wingtip-Mounted Tractor Propellers*. Master's thesis, Delft University of Technology, 2018.

[85] L. R. Miranda, R. D. Elliot, and W. M. Baker. A generalized vortex lattice method for subsonic and supersonic flow applications. Technical Report NASA-CR-2865, Lockheed-California Co. Burbank, CA, United States, Dec 1977.

[86] I. Kroo. Drag due to lift: Concepts for prediction and reduction. *Annual Review of Fluid Mechanics*, 33:587–617, Jan 2001. doi: 10.1146/annurev.fluid.33.1.587.

[87] L. L. M. Veldhuis and P. M. Heyma. Aerodynamic optimisation of wings in multi-engined tractor propeller arrangements. *Aircraft Design*, 3(3):129–149, Sep 2000. doi: 10.1016/S1369-8869(00)00010-0.

[88] R. K. Prabhu. *Studies on the interference of wings and propeller slipstreams*. PhD thesis, Indian Institute of Science, 1984.

[89] B. Horsten and L. L. M. Veldhuis. A new hybrid method to correct for wind tunnel wall and support interference on-line. *World Academy of Science, Engineering and Technology*, 58:507–514, Oct 2009. ISSN 1307-6892.

[90] R. M. Howard, S. J. Miley, and B. J. Holmes. An investigation of the effects of the propeller slipstream on a laminar wing boundary layer. *SAE Transactions*, 94(4):474–485, 1985.

[91] S. J. Miley, R. M. Howard, and B. J. Holmes. Wing laminar boundary layer in the presence of a propeller slipstream. *Journal of Aircraft*, 25(7):606–611, Jul 1988. doi: 10.2514/3.45630.

[92] F. Catalano. On the effects of an installed propeller slipstream on wing aerodynamic characteristics. In *22nd Congress of International Council of the Aeronautical Sciences (ICAS 2000)*, Harrogate, United Kingdom, Aug 2000.

[93] I. Samuelsson. Low speed wind tunnel investigation of propeller slipstream aerodynamic effects on different nacelle/wing combinations. In *16th Congress of the International Council of the Aeronautical Sciences*, Jerusalem, Israel, Aug 1987.

[94] J. Morgado, R. Vizinho, M. A. R. Silvestre, and J. C. Páscoa. XFOIL vs CFD performance predictions for high lift low Reynolds number airfoils. *Aerospace Science and Technology*, 52:207 – 214, May 2016. doi: 10.1016/j.ast.2016.02.031.

[95] O. Gur and A. Rosen. Propeller performance at low advance ratio. *Journal of Aircraft*, 42(2):435–441, Mar 2005. doi: 10.2514/1.6564.

[96] Q. Li, K. Öztürk, T. Sinnige, D. Ragni, G. Eitelberg, L. L. M. Veldhuis, and Y. Wang. Design and experimental validation of swirl-recovery vanes for propeller propulsion systems. *AIAA Journal*, 56(12):4719–4729, Dec 2018. doi: 10.2514/1.J057113.

[97] N. van Arnhem, R. Vos, and L. L. M. Veldhuis. Aerodynamic loads on an aft-mounted propeller induced by the wing wake. In *AIAA Scitech 2019 Forum*, San Diego, CA, United States, Jan 2019. doi: 10.2514/6.2019-1093.

[98] T. Stokkermans, B. Soemarwoto, M. Voskuijl, R. Fukari, L. L. M. Veldhuis, and P. Eglin. Aerodynamic installation effects of lateral rotors on a novel compound helicopter configuration. In *Annual Forum Proceedings - AHS International*, May 2018.

[99] R. H. Myers, D. C. Montgomery, and C. M. Anderson-Cook. *Response Surface Methodology: Process and Product Optimization Using Designed Experiments*. John Wiley & Sons, 2009. ISBN 9780470174463.

[100] T. W. Simpson, J. D. Peplinski, P. N. Koch, and J. K. Allen. On the use of statistics in design and the implications for deterministic computer experiments. In *DETC97*, Sacramento, CA, United States, Sep 1997.

[101] M. D. McKay, R. J. Beckman, and W. J. Conover. A comparison of three methods for selecting values of input variables in the analysis of output from a computer code. *Technometrics*, 21(2):239–245, May 1979. doi: 10.2307/1268522.

[102] A. Giunta, S. Wojtkiewicz, and M. Eldred. Overview of modern design of experiments methods for computational simulations. In *41st Aerospace Sciences Meeting and Exhibit*, Reno, NV, United States, Jan 2003. doi: 10.2514/6.2003-649.

[103] R. R. Barton. Metamodeling: a state of the art review. In *Winter Simulation Conference*, Lake Buena Vista, FL, United States, Dec 1994. doi: 10.1109/WSC.1994.717134.

[104] L. Schueremans and D. van Gemert. Benefit of splines and neural networks in simulation based structural reliability analysis. *Structural Safety*, 27(3):246–261, Jul 2005. doi: 10.1016/j.strusafe.2004.11.001.

[105] J. Sacks, W. J. Welch, T. J. Mitchell, and H. P. Wynn. Design and analysis of computer experiments. *Statistical Science*, 4(4):409–423, Nov 1989. doi: 10.1214/ss/1177012413.

[106] N. Cressie. Spatial prediction and ordinary kriging. *Mathematical Geology*, 20(4):405–421, May 1988. doi: 10.1007/BF00892986.